Università
degli Studi di
Messina

Dipartimento di Scienze Matematiche e Informatiche,
Scienze Fisiche e Scienze della Terra

Dottorato di Ricerca in Fisica, XXXVIII ciclo (PHYS-04/A)

Ultrastrongly coupled light-matter systems: quantum phase transitions, spectral properties and effective models

Daniele Lamberto

Ph.D. Coordinator:
Prof. Vincenza Crupi

Supervisor:
Prof. Salvatore Savasta

Academyc year 2024–2025

A coloro che amo,
e per i quali vivo.

To the ones I love,
and for whom I live.

Abstract

The interaction of light and matter is a fundamental aspect in many fields of physics. In recent years, there has been a growing interest in the study of light-matter systems in the ultrastrong coupling (USC) regime, where the coupling strength between light and matter is comparable to the characteristic frequencies of the system, or even larger than them. This regime has enabled the prediction, and subsequently their experimental exploration, of many new physical phenomena, such as the presence of virtual photons in the system's ground state, the modification of the system's spectral properties, and processes that do not conserve the number of excitations, which are forbidden in the weak and strong coupling regimes. These phenomena have potential applications in many fields, including quantum information, quantum technologies, as well as in the study of fundamental aspects of quantum mechanics. Nevertheless, many questions remain open, both from a theoretical and experimental perspective.

In this thesis, we investigate the properties of ultrastrongly coupled light-matter systems, focusing on quantum phase transitions, spectral properties, and effective models. We employ a combination of analytical and numerical techniques to study these systems, such as perturbative expansions, mean-field theory, and exact diagonalization. These results are relevant for understanding the behavior of light-matter systems in the USC regime, especially in cavity and circuit quantum electrodynamics (QED) settings. Indeed, many of the results presented here concern the spectral properties of these systems, either weakly or strongly coupled to an external bath.

This thesis is structured as follows. In Chapter 1, we provide an overview of the current state of the art and introduce the necessary theoretical framework employed for describing light-matter interactions, with a particular focus on the USC regime and the models typically used to describe these systems. We also introduce the concept of quantum phase transitions (QPTs) and discuss their relevance in the context of light-matter systems.

After presenting these introductory topics, in Chapter 2, we explore in detail one of the most fundamental models in quantum optics, the quantum Rabi model (QRM) and its generalizations, both in cavity and circuit QED implementations. This model describes the interaction between a two-level system and a single mode of the electromagnetic field, and is commonly used to effectively describe light-matter interactions in the USC regime. In particular, we analyze its spectral properties, such as coherent and incoherent emission spectra, in the USC regime and how they differ between various implementations. We then investigate the influence of higher energy levels of the matter subsystem, which are obviously neglected in a two-level description of the matter subsystem (or qubit, in circuit QED systems), on the system's behavior in the USC regime. This will lead us to the derivation of an effective Hamiltonian, the renormalized QRM (RQRM), that incorporates the effects of these higher-energy levels into the system's parameters while still retaining a two-level description of the matter component (qubit).

Subsequently, in Chapter 3, this analysis is extended to the study of systems composed of multiple two-level emitters coupled to a single mode of the electromagnetic field, which can be described by an extended Dicke model and, in the thermodynamic limit, by the Hopfiled model. We explore the evolution of the system properties, such as energy levels and emission spectra, as a function of the number of emitters, and how the results expected in the thermodynamic limit are effectively recovered.

Chapter 4 is dedicated to the study of QPTs in ultrastrongly coupled light-matter systems. In particular, we focus on the role of the electrostatic interactions between the emitters, which are often neglected in simpler models, and the impact they have on the system's behavior. We show that these interactions can significantly alter the occurrence and nature of QPTs. To this end, we investigate two realistic and specific arrangements of the emitters: a three-dimensional lattice of spatially separeted and highly localized dipoles and a two-dimensional layer of such dipoles embedded in a cavity. We analyze how the geometry of the emitter arrangement influences the system's properties, and we identify the conditions under which a QPT can occur. This results can be placed in the context of a long-standing debate about the occurrence of a superradiant phase transition (SPT) in such systems, which has been the subject of much theoretical investigation in recent years.

Finally, Chapter 5 is devoted to the study of the open Dicke model, and specifically to the impact of external baths on the occurrence of the SPT in equilibrium conditions. We will find that our results differ significantly from previous works studying the open Dicke model in effective driven-dissipative systems. Specifically, we analyze how the presence of these baths modifies the critical point, as well as the macroscopic occupations in the superradiant phase. We also investigate the role of different types of baths, both ohmic and non-ohmic, and their influence on the system's behavior. In the end, we present coherent emission spectra for the open Dicke model for these types of baths and analyze their features in relation to the usual interpretations for systems that do not exhibit QPTs.

List of Publications

[1] A. Sergi, D. Lamberto, A. Migliore, and A. Messina, “Quantum-Classical Hybrid Systems and Ehrenfest’s Theorem”, Entropy **25**, 602 (2023).

[2] D. Lamberto, O. Di Stefano, S. Hughes, F. Nori, and S. Savasta, “Quantum phase transitions in many-dipole light-matter systems”, Phys. Rev. Res. **7**, 013271 (2025).

[3] S. Napoli, A. Mercurio, D. Lamberto, A. Zappalà, O. Di Stefano, and S. Savasta, “Circuit QED spectra in the ultrastrong coupling regime: How they differ from cavity QED”, Phys. Rev. Res. **7**, 033037 (2025).

[4] D. Lamberto, A. Mercurio, O. D. Stefano, V. Savona, and S. Savasta, “Renormalization and low-energy effective models in cavity and circuit quantum electrodynamics”, Commun. Phys. **8**, 430 (2025).

[5] A. Zappalà, A. Mercurio, D. Lamberto, S. Napoli, O. Di Stefano, and S. Savasta, “From Few to Many Emitters Cavity QED: Energy Levels and Emission Spectra From Weak to Deep-Strong Coupling”, arXiv:2506.18763 (2025), to appear on Phys. Rev. A.

[6] C. Bonizzoni, D. Lamberto, S. Napoli, S. Gunzler, D. Rieger, F. Santanni, A. Ghirri, W. Wernsdorfer, S. Savasta, and M. Affronte, “Observation of Perfect Absorption in Hyperfine Levels of Molecular Spins with Hermitian Subspaces”, arXiv:2505.05966 (2025), to appear on Nature Communications.

[7] D. Lamberto, G. Orlando, and S. Savasta, “Superradiant Quantum Phase Transition in Open Systems: System-Bath Interaction at the Critical Point”, arXiv:2411.16514 (2025).

[8] R. Stassi, S. Abo, D. Lamberto, Y.-H. Chen, A. Miranowicz, S. Savasta, and F. Nori, “Noise Protected Logical Qubit in a Open Chain of Superconducting Qubits with Ultrastrong Interactions”, arXiv:2509.17903 (2025).

Contents

Chapter 1

Introduction to light-matter interaction

In this chapter, we introduce all the fundamental concepts of light-matter interaction, which form the basis for the topics presented in the following chapters. We begin by discussing the notion of matter in condensed matter physics, the basic principles of electromagnetic radiation, and the mechanisms through which these two entities interact. Along the way, we introduce several fundamental effective models and the regimes of cavity quantum electrodynamics (QED), which forms the theoretical framework that provides the basic quantum description of light-matter interaction. The chapter then proceeds to introduce the concept of quantum phase transition, which will be a central theme in the context of this thesis.

The chapter starts with a discussion about the concept of matter, first from a classical perspective and then within a quantum mechanical framework, focusing on the effective modeling of atoms and molecules through widely used approximations, such as the two-level approximation. We then proceed to the description of the electromagnetic field, beginning with its classical formulation via Maxwell's equations, and subsequently moving to its quantization, which naturally leads to the concept of photons. Using these notions, we address light-matter interaction, first from a classical standpoint and subsequently within quantum mechanics. Particular attention is given to gauge invariance, a fundamental principle that guarantees the consistency and validity of theoretical models.

Next, we present commonly employed effective models and regimes of cavity QED, with a particular focus on the ultrastrong coupling regime (USC). Many of these models will reappear and be analyzed in detail later in the thesis. Finally, the following section is devoted to the basics of quantum phase transitions, with particular emphasis on their relevance in the context of light-matter interaction, which is a key aspect of this thesis.

Altogether, this chapter aims to provide all the basic concepts for the study of more complex systems and advanced phenomena, such as emission processes and scattering in light-matter systems, which will be addressed in the subsequent chapters.

1.1 What is matter?

Although seemingly straightforward, the concept of matter in physics is more subtle and multifaceted than it might appear at first glance. From a naive and non-rigorous perspective, matter can be described as the substance that makes up the physical world around us. Its constituent are the atoms, which represent the basic building blocks of all matter. Atoms themselves consist of a nucleus, made up of protons and neutrons, surrounded by electrons that occupy discrete energy levels or orbitals. In condensed matter physics, the term “matter” usually refers to ensembles of atoms bounded together, whose arrangements and interactions define the physical properties of the different materials [9–12]. Under suitable conditions, these arrangements may change as well as their defining properties, giving rise to the notion of *phase transition*. Familiar examples of phase transitions include the transition from different states of matter, such as solid, liquid, and gas [12–15]. However, phase transitions can also occur in more complex systems. Typical examples in condensed matter physics are superconductors and magnets, driven by either thermal fluctuations, external fields, or other types of fluctuations. In section 1.5, we will focus specifically on *quantum phase transitions*, which are instead driven by quantum fluctuations and may thus occur also at zero temperature [16, 17]. Such transitions are characterized by a qualitative change in the ground state of the system and often lead to new emergent phenomena, *e.g.* macroscopic condensates in the superradiant phase of the Dicke model [18–22].

Returning to the notion of matter, its definition becomes even more puzzling when we enter the realm of quantum mechanics (which is the primary focus of this thesis), where the very concepts of particles and interactions acquire a deeper level of complexity. Indeed, in classical physics, matter can be pragmatically defined as whatever possesses mass and occupies space. However, this definition fails if we move to the relativistic regime, where mass and energy are two sides of the same coin, as expressed by Einstein’s celebrated equation $E = mc^2$. The situation becomes even more intricate in the context of quantum mechanics, where particles exhibit wave-like behavior and are described by wave functions that do not have a well-defined position or momentum until a measurement is performed [23, 24]. In this context, matter is more appropriately described in terms of wave functions and quantum states, which give rise also to phenomena with no classical counterpart. Notable examples include the superposition principle, whereby a particle can exist in multiple states simultaneously until a measurement is performed, and quantum entanglement, where correlations persist between particles regardless of their spatial separation or direct interaction. Such phenomena challenge our classical intuition and require a refined definition of matter consistent with the principles of quantum mechanics.

It is worth noting that the seemingly straightforward definition of matter as a collection of atoms is itself somewhat incomplete, as it does not specify the inclusion of the interactions binding those atoms together. A simple yet illustrative example is the hydrogen atom: it consists of a nucleus (a single proton, if we disregard its substructure) and an electron. The two constituents are held together by their electrostatic interaction, and thus the definition of matter must encompass not only the particles themselves, with their mass and charge, but also the interactions that binds them. The same reasoning extends to more complex systems, such as molecules or larger structures, which are built by atoms connected by electrostatic forces between their constituent particles.

For these reasons, throughout this thesis we shall adopt a consistent and general definition of matter as the collection of all massive (possibly charged) particles together with the electrostatic interactions among them. Although this clarification may appear trivial, or even pedantic, it will prove essential in distinguishing the degrees of freedom associated with matter from those belonging to the electromagnetic field. Indeed, overlooking this distinction can lead to ambiguities, even in recent literature, as it will be discussed in Chapter 4.

1.1.1 Quantum harmonic oscillator

A fundamental model in physics, describing the motion of a particle in a quadratic potential, is the harmonic oscillator. Owing to its simplicity and versatility, this model finds applications across a wide variety of physical systems, both in cases where the potential is exactly quadratic (such as an LC circuit) and in situations where it provides an accurate approximation, for instance within the linear response regime. Its relevance becomes even more pronounced in quantum mechanics, where it represents a cornerstone for the understanding of more complex phenomena, including the quantization of the electromagnetic field (see Section 1.2.2).

Let us consider the prototypical case of a classical particle of mass m confined in a one-dimensional harmonic potential $V(x) = kx^2/2$, where k is the spring constant. Hence, the equation of motion for the harmonic oscillator is written as

$$m\frac{d^2x}{dt^2} + kx = 0 \,, \tag{1.1}$$

where x is the displacement of the particle from its equilibrium position. The solution to this equation is given by

$$x(t) = A\cos(\omega t + \phi)\ , \tag{1.2}$$

where A is the amplitude of the oscillation, $\omega = \sqrt{k/m}$ is the angular frequency, and ϕ is the phase. By simple algebra, we can show that, in the complex domain, the solution can be also written as $x(t) = Ae^{i(\omega t+\phi)}$.

The equation of motion in Eq. (1.1) can be derived from the Lagrangian of the system [25], which reads

$$\mathcal{L} = T\left(\dot{x}\right) - V(x) = \frac{1}{2}m\dot{x}^2 - \frac{1}{2}kx^2\ , \tag{1.3}$$

where $T\left(\dot{x}\right) = m\dot{x}^2/2$ is the kinetic energy of the system. We indicated with $\dot{x}$ the time derivative of the position x, *i.e.* $\dot{x} = dx/dt$, as it is customary in the Lagrangian formalism. The equations of motion can be derived from the Lagrangian using the Euler-Lagrange equations.

Through a Legendre transform, we can also derive the Hamiltonian of the system from the Lagrangian. The Hamiltonian is particularly useful in the quantum mechanical description of a system and it is defined as

$$H = p\,\dot{x} - \mathcal{L} = \frac{p^2}{2m} + \frac{1}{2}kx^2\ , \tag{1.4}$$

where $p = \partial\mathcal{L}/\partial\dot{x} = m\dot{x}$ is the momentum of the particle. The Hamiltonian describes the total energy of the system (kinetic plus potential energies), which is conserved in time, as the Lagrangian does not explicitly depend on t.

In the quantum mechanical description, the position and momentum are promoted to operators satisfying the canonical commutation relation $[\hat{x}, \hat{p}] = i\hbar$, where $\hbar$ is the reduced Planck's constant. Therefore, the Hamiltonian itself is promoted to an operator preserving the same form as in Eq. (1.4), *i.e.*

$$\hat{H} = \frac{\hat{p}^2}{2m} + \frac{1}{2}k\hat{x}^2\ . \tag{1.5}$$

In order to calculate the energy eigenvalues and eigenstates of the harmonic oscillator, we can rewrite this Hamiltonian in terms of the so-called *creation* and *annihilation* operators, which are defined as

$$\hat{a} = \sqrt{\frac{m\omega}{2\hbar}}\left(\hat{x} + i\frac{\hat{p}}{m\omega}\right)\ , \qquad \hat{a}^\dagger = \sqrt{\frac{m\omega}{2\hbar}}\left(\hat{x} - i\frac{\hat{p}}{m\omega}\right)\ , \tag{1.6}$$

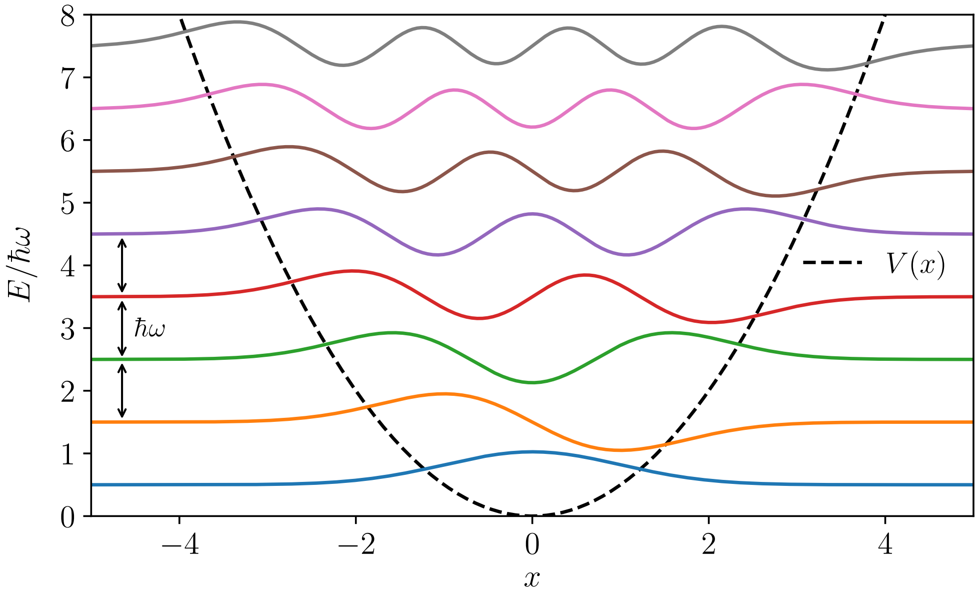

Figure 1.1: Eigenstates of a one-dimensional harmonic oscillator, each shifted by its corresponding energy eigenvalue. In black, the quadratic potential $V(x)$. Parameters used: $m = 1$, $k = 1$.

where $\omega = \sqrt{k/m}$ is the angular frequency of the oscillator. The creation and annihilation operators satisfy the bosonic commutation relation $[\hat{a}, \hat{a}^\dagger] = 1$. In terms of these operators, the Hamiltonian in Eq. (1.5) can be rewritten as

$$\hat{H} = \hbar\omega \left(\hat{a}^\dagger \hat{a} + \frac{1}{2} \right) \ . \tag{1.7}$$

We observe that this Hamiltonian is diagonal in the basis of the eigenstates of the number operator $\hat{n} = \hat{a}^\dagger \hat{a}$, which counts the number of excitations in the system. The eigenvalues of the Hamiltonian are thus given by $E_n = \hbar\omega\,(n + 1/2)$, where $n = 0, 1, 2, \dots$ is the quantum number associated with the number of excitations. Notice that the ground state energy is $\hbar\omega/2$, which is a consequence of the Heisenberg uncertainty principle. By construction, the eigenvalues of the harmonic oscillator are equally spaced, with a spacing of $\hbar\omega$, as shown in Fig. 1.1. The eigenstates of Hamitlonian in Eq. (1.7) are given by the Fock states $|n\rangle$, which are defined as the eigenstates of the number operator $\hat{n}$ associated to the eigenvalue n, *i.e.* $\hat{n}\,|n\rangle = n\,|n\rangle$. The Fock states can be expressed in terms of the creation operator as

$$|n\rangle = \frac{1}{\sqrt{n!}} \left(\hat{a}^\dagger \right)^n |0\rangle \ , \tag{1.8}$$

where $|0\rangle$ is the vacuum state, defined as the state with no excitations ($\hat{a}\,|0\rangle = 0$) or, analogously, as the lowest state of the energy spectrum.

As a final note, we introduce the so-called *coherent states*, which are defined as the eigenstates of the annihilation operator $\hat{a}$, *i.e.* $\hat{a}\,|\alpha\rangle = \alpha\,|\alpha\rangle$. Notice that α is a complex number, since $\hat{a}$ is not Hermitian. Coherent states can be expressed in terms of the Fock states as

$$|\alpha\rangle = e^{-\frac{|\alpha|^2}{2}} \sum_{n=0}^{\infty} \frac{\alpha^n}{\sqrt{n!}}\,|n\rangle \ . \tag{1.9}$$

The importance of coherent states lies in the fact that they are the closest quantum states to classical states, as they exhibit minimum uncertainty. These states are widely used, especially in quantum optics and quantum information theory, as they provide a bridge between classical and quantum descriptions [26–29].

1.1.2 A simple atomic model: the double-well potential

Although the harmonic oscillator constitutes a fundamental model in physics, the description of many quantum systems requires more elaborate potentials that incorporate some degree of nonlinearity. A simple yet important example is the double-well potential, which serves as a minimal model for systems with two stable states. It can, for instance, be used as a toy model of an atom, where the two wells represent the states (ground and excited) of interest. The *quartic* double-well potential is given by

$$V(x) = \alpha x^4 - \beta x^2 \ , \tag{1.10}$$

with $\alpha, \beta > 0$. Given that the potential is even, *i.e.* $V(x) = V(-x)$, it has two symmetric minima at $x = \pm\sqrt{\beta/2\alpha}$, which correspond to the two stable states of the system. It can be easily shown that the anharmonicity of the system can be tuned through the dimensionless parameter $\gamma = m\beta^3/(\hbar^2\alpha^2)$. For small values of γ, the potential displays weak anharmonicity, meaning that the third energy level remains relatively close in the spectrum. In contrast, in the limit $\gamma \to \infty$, the system effectively reduces to an ideal two-level system, as the third energy level is pushed to infinity. In Fig. 1.2(a,b), we show the potential in Eq. (1.10) together with the first three energy eigenvalues of the system, E_i, calculated by diagonalizing the Hamiltonian

$$\hat{H} = \frac{\hat{p}^2}{2m} + V(\hat{x}) = \frac{\hat{p}^2}{2m} + \alpha\hat{x}^4 - \beta\hat{x}^2 \ , \tag{1.11}$$

where $\hat{p}$ and $\hat{x}$ are the momentum and position operators, respectively. In this example, the anharmonicity of the system is approximately $\omega_{21}/\omega_{10} \approx 15$, where $\omega_{ij} = (E_i - E_j)/\hbar$ is the frequency associated with the transition between the energy

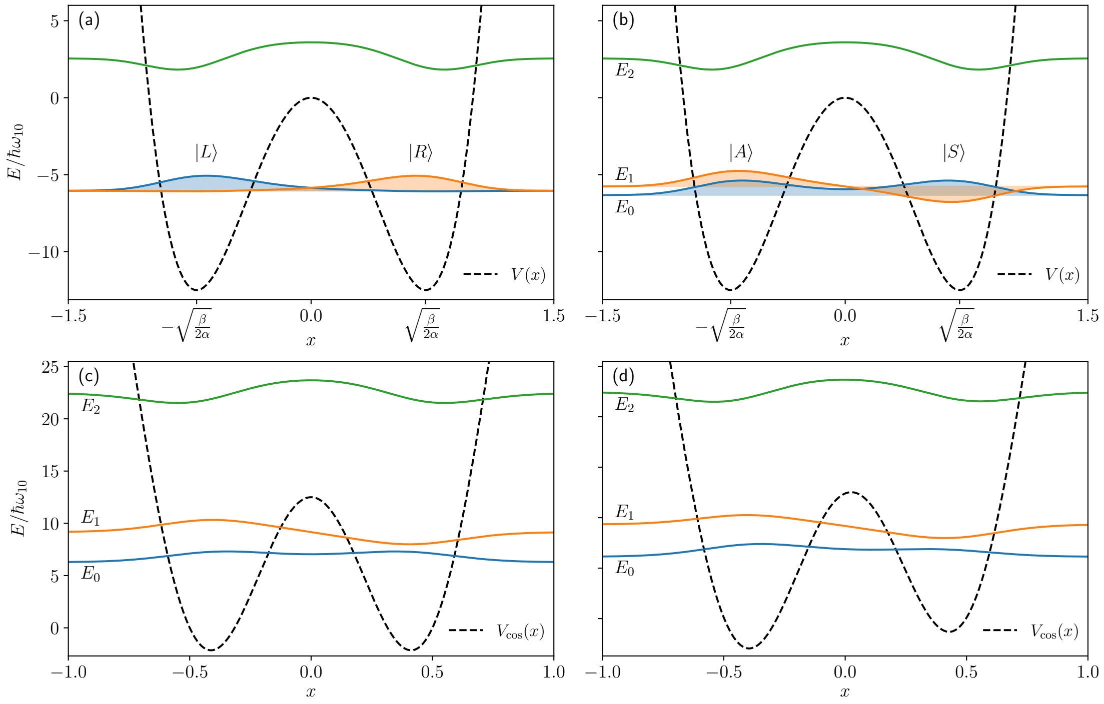

Figure 1.2: Eigenstates and potential shapes for the double-well potentials in Eqs. (1.10) and (1.14). **(a,b)** The quartic double-well potential $V(x)$ in Eq. (1.10) with (a) the ground states of the two wells, $|L\rangle$ and $|R\rangle$, and (b) the first three energy eigenstates. The ground and first excited states are a symmetric and antisymmetric superpositions of the two-wells states, as given in Eq. (1.12). **(c,d)** The Josephson potential in Eq. (1.14) and first three energy eigenstates for (c) $x_0 = 1/2$ and (d) $x_0 = 12/25$, corresponding to the symmetric and asymmetric conditions, respectively. Each energy eigenstate is shifted by its corresponding energy eigenvalue E_i. Parameters used: $m = 1$, $\alpha = 50$, $\gamma = 50$.

levels E_i and E_j. Indeed, given the high energy barrier, the system dynamics can be adequately described by a two-dimensional Hilbert space spanned by the two degenerate ground states in the two wells, indicated with $|L\rangle$ and $|R\rangle$ (see Fig. 1.2(a)). The ground and the first excited states of this double-well system are given by the symmetric and antisymmetric superpositions of the two ground states in each well, respectively, *i.e.*

$$|0\rangle = \frac{1}{\sqrt{2}}\left(|L\rangle + |R\rangle\right) \ , \qquad |1\rangle = \frac{1}{\sqrt{2}}\left(|L\rangle - |R\rangle\right) \ , \tag{1.12}$$

as shown in Fig. 1.2(b) (where the states are labeled $|S\rangle \equiv |0\rangle$ and $|A\rangle \equiv |1\rangle$, to better emphasize the symmetry).

The Hamiltonian of the system in the two-level approximation reads

$$\hat{H} = \frac{\hbar\Delta}{2}\hat{\sigma}_z \ , \tag{1.13}$$

where $\hat{\sigma}_z = |1\rangle\langle 1| - |0\rangle\langle 0|$ is the Pauli operator associated with the two-level system, and $\Delta = (E_1 - E_0)/\hbar$ is the frequency of the transition between the ground and the first excited states. Physically, Δ is associated with the tunneling rate between the two wells, which is a key feature of the double-well potential. The Hamiltonian in Eq. (1.13), describing an effective two-level system, is a fundamental model in quantum mechanics and is widely used to describe various physical systems, ranging from atoms and molecules to superconducting qubits.

For future applications in circuit QED, it is convenient to consider an alternative double-well potential to the quartic one introduced in Eq. (1.10). Specifically, this potential combines the usual quadratic term with the so-called *Josephson potential* used to model Josephson junction, *i.e.*

$$V_{\cos}(x) = \beta x^2 - \frac{\gamma}{4}\cos\left[2\pi(x - x_0)\right] \ , \tag{1.14}$$

which is commonly employed to describe the dynamics of superconducting qubits, the building blocks of circuit QED, quantum computing, and quantum information processing [30–33]. A distinctive property of $V_{\cos}(x)$ is that the $\mathbb{Z}_2$ parity symmetry can be easily broken by tuning the parameter x_0, which in experimental realizations corresponds to the so-called *flux bias*. In particular, for $x_0 = 1/2$, corresponding to a phase shift of π (which is usually referred to as the *symmetry point* or *sweet spot*), the potential is symmetric and displays a pronounced double-well structure for small values of x. By contrast, for $x_0 \neq 1/2$ the parity symmetry is broken and the two wells have different depths.

The Hamiltonian of the system in the two-level approximation can be written in a similar form as in Eq. (1.13), but with an additional term accounting for the possible symmetry breaking, namely

$$\hat{H} = \frac{\hbar\Delta}{2}\hat{\sigma}_z + \frac{\hbar\epsilon}{2}\hat{\sigma}_x \ , \tag{1.15}$$

where ϵ is the detuning parameter, representing the energy difference between the ground states of the two wells in absence of tunneling. This Hamiltonian can be straightforwardly diagonalized, yielding the eigenvalues $\pm\sqrt{\Delta^2 + \epsilon^2}/2$.

From a formal point of view, both Hamiltonians in Eqs. (1.13) and (1.15) can be obtained by applying to the full Hamiltonian of the systems the projection operator $\hat{\mathcal{P}} = |0\rangle\langle 0| + |1\rangle\langle 1|$, which, by construction, projects the Hilbert space onto the two-dimensional subspace spanned by the ground and first excited states.

1.2 What is light?

In contrast to the notion of matter, whose definition has demonstrated to be rather subtle and multifaceted, the concept of light is comparatively more intuitive, though no less fascinating. Indeed, the question “What is light?” has been subject of fascination and inquiry for centuries. Different views on the answer have emerged over time, reflecting the evolving understanding of light’s nature. Most notably, the dualism between light as a wave and light as a particle has been a central theme in the history of physics. In modern terms, light is understood as a quantum electromagnetic field, whose excited states can be described as a stream of discrete quanta, called photons. This dual description is essential for explaining a wide range of physical phenomena and is fundamental for much of contemporary physics. In what follows, we will briefly review both the classical and quantum mechanical descriptions of light, highlighting the key concepts and theories that have shaped our modern understanding. For a more comprehensive and detailed discussion on the topic, the reader is referred to classical textbooks on quantum optics, such as Refs. [26–28].

1.2.1 Classical description and Maxwell’s equations

The classical description of light is intrisically linked to the notions of electromagnetic waves, as the term “light” refers to an electromagnetic radiation propagating through space and time.[1] To describe the electromagnetic waves, we rely on Maxwell’s equations, which are a set of four fundamental equations that govern the behavior of the electric and magnetic fields. In the vacuum, these equations can be written in their *local* (differential) form as [34, 35]

$$\nabla \cdot \mathbf{E} = \frac{\rho}{\epsilon_0} \,, \tag{1.16a}$$

$$\nabla \cdot \mathbf{B} = 0 \,, \tag{1.16b}$$

$$\nabla \times \mathbf{E} = -\frac{\partial \mathbf{B}}{\partial t} \,, \tag{1.16c}$$

$$\nabla \times \mathbf{B} = \mu_0 \left(\mathbf{J} + \epsilon_0 \frac{\partial \mathbf{E}}{\partial t} \right) \,, \tag{1.16d}$$

where $\mathbf{E}$ and $\mathbf{B}$ are the electric and magnetic fields, respectively, ρ is the total charge density, and $\mathbf{J}$ is the total current density. The constants μ_0 and ϵ_0 are the permeability and permittivity of free space, respectively.

---

[1] In the past, the term “light” only referred to the visible spectrum, having wavelengths between $400-700$ nm. However, nowadays, the term “light” refers more broadly to electromagnetic radiation of any wavelength, whether visible or not.

We notice how the two fields are coupled together, and, by taking the curl of Eq. (1.16c) and substituting it in Eq. (1.16d), we can derive the wave equation for the electric field (in absence of charges and currents, *i.e.* $\rho = 0$ and $\mathbf{J} = 0$):

$$\nabla^2 \mathbf{E} - \mu_0 \epsilon_0 \frac{\partial^2 \mathbf{E}}{\partial t^2} = 0 \ , \tag{1.17}$$

which describes the propagation of a wave with speed $c = 1/\sqrt{\mu_0 \epsilon_0}$. Analogous treatment can be performed for the magnetic field, leading to the same result. In addition, the two field are perpendicular to the diretion of propagation and to each other and oscillate in phase. Notably, one of the most important discoveries in the history of physics is that the speed of light in vacuum is a universal constant, approximally equal to 3×10^8 m/s, and it is independent of the observer's frame of reference. This invariance is a cornerstone of Einstein's theory of relativity, which revolutionized our understanding of space and time.

The set of Eqs. (1.16) can be rewritten by the introduction of the scalar and vector potentials, $\phi(\mathbf{r}, t)$ and $\mathbf{A}(\mathbf{r}, t)$, respectively, defined by

$$\mathbf{B} = \nabla \times \mathbf{A} \ , \qquad \mathbf{E} = -\nabla \phi - \frac{\partial \mathbf{A}}{\partial t} \ . \tag{1.18}$$

These potentials are not unique, and different choices can lead to the same physical predictions, as only the fields $\mathbf{E}$ and $\mathbf{B}$ are physically meaningful and observable. This possibility to freely choose the potentials is known as *gauge freedom*, and it allows us to simplify calculations by choosing a gauge that is convenient for the problem at hand. In particular, given that the gradient of any scalar field is irrotational, we can artbitrarly choose a smooth scalar function $\chi(\mathbf{r}, t)$ and redefine both potentials as

$$\mathbf{A}' = \mathbf{A} - \nabla \chi \ , \qquad \phi' = \phi + \frac{\partial \chi}{\partial t} \ , \tag{1.19}$$

This transformation leaves the electric and magnetic fields unchanged, as can be easily verified by substituting Eq. (1.19) into Eq. (1.18).

Sometimes χ itself is referred to as *gauge transformation*, given that the choice of the scalar function χ uniquely defines the gauge we are working in. Given the arbitrariness of the gauge transformation, a common choice is for the vector potential to satisfy the condition $\nabla \cdot \mathbf{A} = 0$, which is known as the *Coulomb gauge*. Another particularly common gauge, that will be extensively employed in this thesis, is the so-called *multipolar gauge*, which however does not possess this property. As it will be discussed in the next section, these gauges are particularly useful in the context of QED and, in particular, cavity QED. We stress that the Coulomb gauge is the only gauge such that the vector potential $\mathbf{A}$ is purely transverse, *i.e.* it satisfies the condition $\nabla \cdot \mathbf{A} = 0$.[2] In this gauge, the scalar potential ϕ is related to the charge density ρ through Poisson's equation, and the vector potential $\mathbf{A}$ is related to the current density $\mathbf{J}$ through a non-homogeneous wave equation, *i.e.*

$$\nabla^2 \phi = -\frac{\rho}{\epsilon_0} \,, \tag{1.20a}$$

$$\nabla^2 \mathbf{A} - \mu_0 \epsilon_0 \frac{\partial^2 \mathbf{A}}{\partial t^2} = -\mu_0 \mathbf{J} + \mu_0 \epsilon_0 \nabla \left(\frac{\partial \phi}{\partial t} \right) \,. \tag{1.20b}$$

In absence of charges and currents, Eq. (1.20a) admits the trivial solution $\phi = 0$, which, in turn, leads to the homogeneous wave equation for the vector potential $\mathbf{A}$:

$$\left(\nabla^2 - \frac{1}{c^2} \frac{\partial^2}{\partial t^2} \right) \mathbf{A} = 0 \,. \tag{1.21}$$

Therefore, in the Coulomb gauge, by calculating the vector potential $\mathbf{A}$, we can straightforwardly obtain the electric and magnetic fields through Eqs. (1.18). The total energy stored in the electromagnetic field is given by

$$E = \frac{1}{2} \int_V d^3 r \left(\epsilon_0 |\mathbf{E}|^2 + \frac{1}{\mu_0} |\mathbf{B}|^2 \right) \,, \tag{1.22}$$

where the volume of integration V can be chosen to be the entire space, as in the case of open fields considered in standard QED, or a finite region of interest in which the field is present, such as a cavity or a waveguide (typical cases of cavity and circuit QED systems).

To solve Eq. (1.21), we must specify the boundary conditions to be satisfied by the field. Let us consider the case of an electromagnetic field within a cube of side L, and impose periodic boundary conditions on the vector potential $\mathbf{A}$. The continuum limit can be taken by letting $L \to \infty$. The solution to Eq. (1.21) can be found by separation of variables, which yields, considering the periodic boundary conditions, to the following decomposition of the vector potential

$$\mathbf{A}(\mathbf{r}, t) = \sum_{\mathbf{k},\lambda} A_{\mathbf{k}\lambda}(t) \mathbf{f}_{\mathbf{k}\lambda}(\mathbf{r}) + h.c. \,, \tag{1.23}$$

where $\mathbf{k}$ is the wave vector and λ is the polarization index, which can take values corresponding to the two transverse polarizations of the electromagnetic

---

[2] Any field $\mathbf{F}$ can be decomposed into a longitudinal and a transverse part, $\mathbf{F} = \mathbf{F}^{\parallel} + \mathbf{F}^{\perp}$, satisfying the conditions $\nabla \times \mathbf{F}^{\parallel} = 0$ and $\nabla \cdot \mathbf{F}^{\perp} = 0$, respectively. The nomenclature longitudinal and transverse refers to the direction of the field with respect to the direction of propagation of the wave. Specifically, if these conditions are expressed in the Fourier space, the longitudinal part is parallel to the wave vector $\mathbf{k}$ since it satisfies $\mathbf{k} \times \mathbf{F}^{\parallel} = 0$, while the transverse part is orthogonal to the wave vector as $\mathbf{k} \cdot \mathbf{F}^{\perp} = 0$.

wave. The spatial solutions, which are mutually orthonormalized, have the form $\mathbf{f}_{\mathbf{k}\lambda}(\mathbf{r}) = \mathbf{e}_{\mathbf{k}\lambda} e^{i\mathbf{k}\cdot\mathbf{r}}$, where $\mathbf{e}_{\mathbf{k}\lambda}$ are unit vectors that define the polarization of the wave. Given the trasversality of the field, these vectors satisfy the orthonomality conditions $\mathbf{k}\cdot\mathbf{e}_{\mathbf{k}\lambda} = 0$ and $\mathbf{e}_{\mathbf{k}\lambda}\cdot\mathbf{e}_{\mathbf{k}\lambda'} = \delta_{\lambda\lambda'}$, for $\lambda, \lambda' = 1, 2$. The wave vector $\mathbf{k}$ is quantized due to the periodic boundary conditions, taking values of the form $\mathbf{k} = 2\pi(n_x, n_y, n_z)/L$, where n_x, n_y, and n_z are integers. On the other hand, the time-dependent coefficients $\mathbf{A}_{\mathbf{k}\lambda}(t)$ must each one satisfy the differential equation

$$\left(c^2k^2 + \frac{d^2}{dt^2}\right) A_{\mathbf{k}\lambda}(t) = 0 \ , \tag{1.24}$$

where $k = |\mathbf{k}|$ is the magnitude of the wave vector. This is the equation of an harmonic oscillator, with angular frequency $\omega_k = ck$, whose solution is given by

$$A_{\mathbf{k}\lambda}(t) = A_{\mathbf{k}\lambda} e^{-i\omega_k t} \ . \tag{1.25}$$

Therefore, having an expansion for $\mathbf{A}(\mathbf{r}, t)$, the Fourier expansions of the electric and magnetic fields follow from Eq. (1.18), leading to

$$\mathbf{E}(\mathbf{r}, t) = \sum_{\mathbf{k},\lambda} \left(i\omega_k A_{\mathbf{k}\lambda} e^{-i\omega_k t} \mathbf{f}_{\mathbf{k}\lambda}(\mathbf{r}) + h.c.\right) \ , \tag{1.26a}$$

$$\mathbf{B}(\mathbf{r}, t) = \sum_{\mathbf{k},\lambda} \left(i\mathbf{k} \times A_{\mathbf{k}\lambda} e^{-i\omega_k t} \mathbf{f}_{\mathbf{k}\lambda}(\mathbf{r}) + h.c.\right) \ . \tag{1.26b}$$

Analogously, the energy stored in the electromagnetic field can be expressed in terms of the Fourier coefficients. It is useful to introduce dimensionless amplitudes $a_{\mathbf{k}\lambda}$, obtained by rescaling the Fourier coefficients as $A_{\mathbf{k}\lambda} = \sqrt{\hbar/2\epsilon_0 V\omega_k}\, a_{\mathbf{k}\lambda}$. Substituting this definition into Eq. (1.22), we obtain the energy in terms of $a_{\mathbf{k}\lambda}$ as

$$E = \frac{\hbar}{2} \sum_{\mathbf{k},\lambda} \omega_k \left(a_{\mathbf{k}\lambda} a^*_{\mathbf{k}\lambda} + a^*_{\mathbf{k}\lambda} a_{\mathbf{k}\lambda}\right) \ . \tag{1.27}$$

We notice that, in the classical scenario, the Fourier coefficients $a_{\mathbf{k}\lambda}$ are c-numbers, and thus commute with each other, allowing us to rewrite the term in parentheses as $2|a_{\mathbf{k}\lambda}|^2$. However, as it will be discussed in the next subsection, in the quantum mechanical description, the Fourier coefficients are promoted to operators that satisfy the bosonic commutation relations. Hence, we prefer to leave the term in parentheses as it is, to avoid confusion between the classical and the quantum mechanical cases. By introducing the real vairables $q_{\mathbf{k}\lambda}$ and $p_{\mathbf{k}\lambda}$, defined as

$$q_{\mathbf{k}\lambda} = \sqrt{\frac{\hbar}{2\omega_k}} \left(a_{\mathbf{k}\lambda} + a^*_{\mathbf{k}\lambda}\right) \ , \qquad p_{\mathbf{k}\lambda} = i\sqrt{\frac{\hbar\omega_k}{2}} \left(a^*_{\mathbf{k}\lambda} - a_{\mathbf{k}\lambda}\right) \ , \tag{1.28}$$

the energy in Eq. (1.27) can be rewritten as

$$E = \frac{1}{2} \sum_{\mathbf{k},\lambda} \left(p^2_{\mathbf{k}\lambda} + \omega_k^2 q^2_{\mathbf{k}\lambda} \right) \ . \tag{1.29}$$

This expression explicitly shows that the electromagnetic field can be described as an infinite collection of independent harmonic oscillators, each associated with a different wave vector $\mathbf{k}$ and polarization λ, and with $q_{\mathbf{k}\lambda}$ and $p_{\mathbf{k}\lambda}$ playing the role of position and momentum operators, respectively.

1.2.2 Quantization of the electromagnetic field

The quantization of the electromagnetic field is a fundamental step in the development of QED. The way to achieve this quantization is evident from the final expression in Eq. (1.29) of the previous subsection, which can be interpreted as the Hamiltonian of a collection of independent harmonic oscillators with unitary masses. Indeed, for each wave vector $\mathbf{k}$ and polarization λ, Eq. (1.29) is formally equivalent to the Hamiltonian of an harmonic oscillator in Eq. (1.4), whose quantization has been already discussed in Section 1.1.1.

The quantization of the electromagnetic field Hamiltonian can be achieved by promoting the position and momentum operators $q_{\mathbf{k}\lambda}$ and $p_{\mathbf{k}\lambda}$ to quantum mechanical operators that satisfy the canonical commutation relations $[\hat{q}_{\mathbf{k}\lambda}, \hat{p}_{\mathbf{k}'\lambda'}] = i\hbar\delta_{\mathbf{k}\mathbf{k}'}\delta_{\lambda\lambda'}$. This is analogous to promoting the Fourier coefficients $a_{\mathbf{k}\lambda}$ to bosonic operators $\hat{a}_{\mathbf{k}\lambda}$, satisfying $[\hat{a}_{\mathbf{k}\lambda}, \hat{a}^\dagger_{\mathbf{k}'\lambda'}] = \delta_{\mathbf{k}\mathbf{k}'}\delta_{\lambda\lambda'}$ and $[\hat{a}_{\mathbf{k}\lambda}, \hat{a}_{\mathbf{k}'\lambda'}] = 0$. The Hamiltonian of the electromagnetic field in terms of creation and annihilation operators can then be written as

$$\hat{H} = \hbar \sum_{\mathbf{k},\lambda} \omega_k \left(\hat{a}^\dagger_{\mathbf{k}\lambda} \hat{a}_{\mathbf{k}\lambda} + \frac{1}{2} \right) \ . \tag{1.30}$$

We notice that, given the presence of the zero-point energy term, this Hamiltonian is not bounded from below, which is a consequence of the infinite number of harmonic oscillators (or *modes*) in the electromagnetic field. However, this term can be neglected in most physical situations, as it does not affect the dynamics of the system. Indeed, as long as the processes considered describe the exchange of energy between the field and some other system, it is only energy differences that matter, in which case the zero-point energy can be directly omitted from the Hamiltonian. Analogously to the standard quantum harmonic oscillator, the eigenstates of the Hamiltonian in Eq. (1.30) are the Fock states, which are defined as the eigenstates of the number operator $\hat{n}_{\mathbf{k}\lambda} = \hat{a}^\dagger_{\mathbf{k}\lambda}\hat{a}_{\mathbf{k}\lambda}$, *i.e.* $\hat{n}_{\mathbf{k}\lambda} |n_{\mathbf{k}\lambda}\rangle = n_{\mathbf{k}\lambda} |n_{\mathbf{k}\lambda}\rangle$, where $n_{\mathbf{k}\lambda}$ is the number of quanta (called *photons*) with wave vector $\mathbf{k}$ and polarization λ.

The quantized vector potential and the electric and magnetic fields are thus expressed in terms of the creation and annihilation operators as

$$\hat{\mathbf{A}}(\mathbf{r},t) = \sum_{\mathbf{k},\lambda} \sqrt{\frac{\hbar}{2\epsilon_0 V \omega_k}} \left(\hat{a}_{\mathbf{k}\lambda} e^{i(\mathbf{k}\cdot\mathbf{r}-\omega_k t)} + \hat{a}^{\dagger}_{\mathbf{k}\lambda} e^{-i(\mathbf{k}\cdot\mathbf{r}-\omega_k t)} \right) \mathbf{e}_{\mathbf{k}\lambda} \ , \tag{1.31a}$$

$$\hat{\mathbf{E}}(\mathbf{r},t) = \sum_{\mathbf{k},\lambda} i \sqrt{\frac{\hbar\omega_k}{2\epsilon_0 V}} \left(\hat{a}_{\mathbf{k}\lambda} e^{i(\mathbf{k}\cdot\mathbf{r}-\omega_k t)} - \hat{a}^{\dagger}_{\mathbf{k}\lambda} e^{-i(\mathbf{k}\cdot\mathbf{r}-\omega_k t)} \right) \mathbf{e}_{\mathbf{k}\lambda} \ , \tag{1.31b}$$

$$\hat{\mathbf{B}}(\mathbf{r},t) = \sum_{\mathbf{k},\lambda} i \sqrt{\frac{\hbar}{2\epsilon_0 V \omega_k}} \left(\hat{a}_{\mathbf{k}\lambda} e^{i(\mathbf{k}\cdot\mathbf{r}-\omega_k t)} - \hat{a}^{\dagger}_{\mathbf{k}\lambda} e^{-i(\mathbf{k}\cdot\mathbf{r}-\omega_k t)} \right) \mathbf{k} \times \mathbf{e}_{\mathbf{k}\lambda} \ . \tag{1.31c}$$

We notice that the quantized modes of the field are transverse. This will have important consequences when considering the interaction between light and matter, as discussed in Section 1.3.

As a final note, it is possible to perform the quantization of the electromagnetic field within a finite volume, such as a cavity or a waveguide, by imposing appropriate boundary conditions on the vector potential $\mathbf{A}$. Namely, it must be chosen such that the electric field vanishes at the boundaries of the cavity. The specific form of the boundary conditions depends on the geometry of the cavity or waveguide.

1.3 Light-matter interaction

The interaction between light and matter lies at the heart of a wide range of physical phenomena, from atomic and molecular spectroscopy to quantum optics to quantum information processing. Understanding this interaction is not only crucial for describing fundamental processes, such as absorption, emission, and scattering of radiation, but also for explaining emergent collective effects in many-body systems and for developing new technological applications. In this section, we provide a brief overview of both the classical and quantum mechanical descriptions of light-matter interaction, with particular emphasis on the principle of gauge invariance, which plays a central role in many aspects of QED and will be especially relevant in the context of this thesis.

1.3.1 General Lagrangian and gauge transformations

The description of light-matter interaction is based on the coupling between the electromagnetic field and the electric dipole moment of the matter system. As a simple illustrative example, let us consider a single particle with charge Q and mass m moving in an electromagnetic field described by the vector potential $\mathbf{A}(\mathbf{r},t)$ and the scalar potential $\phi(\mathbf{r},t)$, within the non-relativistic limit. In particular, we will consider the case of an hydrogen atom, where the electron (with charge $Q=-e$) moves bounded to a proton fixed at the origin of the coordinate system. The Lagrangian of the system can be written as [36–38]

$$\mathcal{L}=\frac{1}{2}m\dot{\mathbf{q}}^2+\int\mathscr{L}d\mathbf{r}\ , \tag{1.32}$$

where $\dot{\mathbf{q}}$ is the velocity of the particle and $\mathscr{L}$ is the Lagrangian density of the electromagnetic field, given by

$$\mathscr{L}=\frac{1}{2}\epsilon_0\left(\left(\dot{\mathbf{A}}+\nabla\phi\right)^2-c^2(\nabla\times\mathbf{A})^2\right)+\mathbf{J}\cdot\mathbf{A}-\rho\phi\ . \tag{1.33}$$

The first term in Eq. (1.32) represents the kinetic energy of the particle, while the terms in Eq. (1.33) describe the contributions of the electric and magnetic fields to the Lagrangian density, as well as the interaction between the particle and the electromagnetic field, respectively. The current density $\mathbf{J}(\mathbf{r})$ and the charge density $\rho(\mathbf{r})$ can be expressed as

$$\mathbf{J}(\mathbf{r})=-e\dot{\mathbf{q}}\delta(\mathbf{r}-\mathbf{q})\ ,\qquad \rho(\mathbf{r})=-e\delta(\mathbf{r}-\mathbf{q})+e\delta(\mathbf{r})\ , \tag{1.34}$$

where $\delta(\mathbf{r}-\mathbf{q})$ and $\delta(\mathbf{r})$ are the Dirac delta functions, ensuring that the electron is in the position $\mathbf{q}(t)$ at time t, while the proton is fixed at the origin. The current and charge densities clearly satisfy the continuity equation

$$\dot{\rho}+\nabla\cdot\mathbf{J}=0\ , \tag{1.35}$$

which is a fundamental requirement for the conservation of charge in electromagnetism. It can be easily verified that the Lagrangian in Eq. (1.32) leads to the correct equations of motion for the particle and the electromagnetic field, which are given by the Lorentz force law and Maxwell's equations, respectively.

It is natural to choose $\mathbf{q}$ and $\mathbf{A}$ as the canonical coordinates of the particle and the electromagnetic field, respectively, while the scalar potential ϕ can be determined from the equations of motion. Furthermore, as it will be demonstrated shortly, it is possible to eliminate the explicit presentce of the scalar potential from the Hamiltonian of the system. The conjugate momenta to $\mathbf{q}$ and $\mathbf{A}$ are

$$\mathbf{p}=\frac{\partial\mathcal{L}}{\partial\dot{\mathbf{q}}}=m\dot{\mathbf{q}}-e\mathbf{A}(\mathbf{q})\ , \tag{1.36a}$$

$$\mathbf{\Pi}(\mathbf{r})=\frac{\partial\mathscr{L}}{\partial\dot{\mathbf{A}}(\mathbf{r})}=\epsilon_0\left(\dot{\mathbf{A}}(\mathbf{r})+\nabla\phi(\mathbf{r})\right)=-\epsilon_0\mathbf{E}\ . \tag{1.36b}$$

The Hamiltonian of the system can be obtained by performing a Legendre transformation of the Lagrangian in Eq. (1.32), leading to

$$H = \mathbf{p}\cdot\dot{\mathbf{q}} + \int \mathbf{\Pi}(\mathbf{r})\cdot\dot{\mathbf{A}}(\mathbf{r})d\mathbf{r} - \mathcal{L}\ . \tag{1.37}$$

By substituting the expressions for the conjugate momenta given in Eqs. (1.36a) and (1.36b) and the explicit form of the Lagrangian, we obtain

$$H = \frac{1}{2m}\left(\mathbf{p}+e\mathbf{A}\right)^2 + \frac{1}{2}\int\left(\frac{\mathbf{\Pi}^2}{\epsilon_0}+\frac{\mathbf{B}^2}{\mu_0}\right)d\mathbf{r}\ . \tag{1.38}$$

In this expression, an additional term equal to $\int\left(\nabla\cdot\mathbf{\Pi}+\rho\right)\phi d\mathbf{r}$ has been omitted, as the quantity in parentheses is zero due to Maxwell's equations. Therefore, as discussed above, the scalar potential ϕ can be eliminated from the Hamiltonian description of the system. We highlight that the dynamical variables of the system, satisfying the Poisson braket relations (and later, after the quantization, the canonical commutation relations), are $(\mathbf{q},\mathbf{p})$ and $(\mathbf{A},\mathbf{\Pi})$.

Although the Hamiltonian in Eq. (1.38) closely resembles the Coulomb-gauge Hamiltonian of QED (which will be introduced shortly), it is important to notice that no gauge has been specified yet since the vector potential $\mathbf{A}$ is still a generic function of space and time and no division into longitudinal and transverse components has been made. To further elucidate this point, let us introduce a general gauge transformation of the potentials, as discussed in Section 1.2.1. Specifically, the vector potential $\mathbf{A}$ and the scalar potential ϕ are redefined as

$$\mathbf{A}'(\mathbf{r}) = \mathbf{A}(\mathbf{r}) - \nabla\chi(\mathbf{r})\ , \qquad \phi'(\mathbf{r}) = \phi(\mathbf{r}) + \dot{\chi}(\mathbf{r})\ , \tag{1.39}$$

where $\chi(\mathbf{r})$ is an arbitrary smooth scalar function (for the sake of simplicity, we are omitting the time dependence). In the most general case, the function $\chi(\mathbf{r})$ can also depend on the vector potential at a general position. Accordingly we introduce a gauge density $\tilde{\chi}$ such that

$$\chi(\mathbf{r},t) = \int \tilde{\chi}(\mathbf{r},\mathbf{r}',\mathbf{A}(\mathbf{r}'))d\mathbf{r}'\ . \tag{1.40}$$

Therefore, the new Lagrangian $\mathcal{L}'$ can be written in terms of the old potentials as

$$\begin{aligned}\mathcal{L}' &= \mathcal{L} - \int \mathbf{J}(\mathbf{r})\cdot\nabla\chi(\mathbf{r})d\mathbf{r} - \int \rho(\mathbf{r})\dot{\chi}(\mathbf{r})d\mathbf{r} \\ &= \mathcal{L} + e\dot{\mathbf{q}}\cdot\nabla\chi(\mathbf{q}) - \int \dot{\mathbf{A}}(\mathbf{r})\left(\int\frac{\partial\tilde{\chi}\left(\mathbf{r},\mathbf{r}'\right)}{\mathbf{A}(\mathbf{r})}\rho(\mathbf{r}')d\mathbf{r}'\right)d\mathbf{r}\ .\end{aligned} \tag{1.41}$$

If we continue to take $\mathbf{q}$ and $\mathbf{A}$ as the dynamical variables, the conjugate momenta to these variables are now given by

$$\mathbf{p}' = \frac{\partial \mathcal{L}'}{\partial \dot{\mathbf{q}}} = m\dot{\mathbf{q}} - e\mathbf{A}'(\mathbf{q}) + e\nabla\chi(\mathbf{q}) \ , \tag{1.42a}$$

$$\mathbf{\Pi}'(\mathbf{r}) = \frac{\partial \mathcal{L}'}{\partial \dot{\mathbf{A}}(\mathbf{r})} = \epsilon_0 \left(\dot{\mathbf{A}}(\mathbf{r}) + \nabla\phi(\mathbf{r})\right) - \mathbf{P}(\mathbf{r}) \ , \tag{1.42b}$$

where we defined $\mathbf{P}(\mathbf{r})$, which can be identified as the polarization density, as

$$\mathbf{P}(\mathbf{r}) = \int \frac{\partial \tilde{\chi}\left(\mathbf{r},\mathbf{r}'\right)}{\partial \mathbf{A}(\mathbf{r})} \rho(\mathbf{r}')d\mathbf{r}' \ . \tag{1.43}$$

Comparing Eqs. (1.42a) and (1.42b) with Eqs. (1.36a) and (1.36b), we notice that the conjugate momenta have been modified by the gauge transformation, obtaining the relations

$$\mathbf{p}' = \mathbf{p} + e\nabla\chi(\mathbf{q}) \ , \tag{1.44a}$$

$$\mathbf{\Pi}'(\mathbf{r}) = \mathbf{\Pi}(\mathbf{r}) - \mathbf{P}(\mathbf{r}) \ . \tag{1.44b}$$

Following the same procedure as above, we can obtain the Hamiltonian of the system in terms of the transformed conjugate momenta, which reads

$$H' = \frac{1}{2m}\left(\mathbf{p}' + e\mathbf{A} - e\nabla\chi\right)^2 + \frac{1}{2}\int \left(\frac{\left(\mathbf{\Pi}' + \mathbf{P}\right)^2}{\epsilon_0} + \frac{\mathbf{B}^2}{\mu_0}\right) d\mathbf{r} \ . \tag{1.45}$$

We stress that the new set of dynamical variables is now $(\mathbf{q}, \mathbf{p}')$ and $(\mathbf{A}, \mathbf{\Pi}')$, which satisfy the Poisson bracket relations in classical mechanics, and later, after the quantization, the canonical commutation relations $[\hat{q}_i, \hat{p}'_j] = i\hbar\delta_{ij}$ and $[\hat{A}_i(\mathbf{r}), \hat{\Pi}'_j(\mathbf{r}')] = i\hbar\delta_{ij}\delta(\mathbf{r}-\mathbf{r}')$, respectively. It can be shown that the Hamiltonian in Eq. (1.45) leads to the same equations of motion as the Hamiltonian in Eq. (1.38), which is a consequence of the gauge invariance of the theory.

If we now wish to consider a specific gauge, such as the Coulomb gauge, it is convenient to decompose the vector potential $\mathbf{A}$ into a longitudinal and a transverse part, as discussed in Section 1.2.1. In particular, we can write

$$\mathbf{A}(\mathbf{r}) = \mathbf{A}^{\parallel}(\mathbf{r}) + \mathbf{A}^{\perp}(\mathbf{r}) \ , \tag{1.46}$$

where the longitudinal part $\mathbf{A}^{\parallel}(\mathbf{r})$ is irrotational, $\nabla \times \mathbf{A}^{\parallel}(\mathbf{r}) = 0$, and the transverse part $\mathbf{A}^{\perp}(\mathbf{r})$ is solenoidal, $\nabla \cdot \mathbf{A}^{\perp}(\mathbf{r})$. It is now clear that the gauge transformation in Eq. (1.39) can be interpreted as a transformation of the longitudinal part of the vector potential, while leaving the transverse part unchanged.[3] In the following subsection, we will discuss two of the most commonly used gauges in the context of light-matter interaction in condensed matter physics: the Coulomb gauge and the Power-Zienau-Woolley (PZW) gauge.

1.3.2 Coulomb gauge

In the Coulomb gauge, the vector potential is purely transverse. This gauge is particularly useful and intuitive as the vector potential itself only contains the dynamical degrees of freedom of the electromagnetic field (transverse modes). The gauge transformation required to realize this choice must satisfy

$$\nabla \chi_{\mathrm{C}}(\mathbf{r}) = \mathbf{A}^{\parallel}(\mathbf{r}) \ , \tag{1.47}$$

such that the transformed vector potential $\mathbf{A}_{\mathrm{C}}(\mathbf{r})$ (the subscript C is used instead of the general notation $\mathbf{A}'(\mathbf{r})$ to indicate that the quantity is specific to the Coulomb gauge) has the equivalent properties

$$\mathbf{A}_{\mathrm{C}}(\mathbf{r}) = \mathbf{A}^{\perp}_{\mathrm{C}}(\mathbf{r}) \, , \qquad \mathbf{A}^{\parallel}_{\mathrm{C}}(\mathbf{r}) = 0 \, , \qquad \nabla \cdot \mathbf{A}_{\mathrm{C}}(\mathbf{r}) = 0 \ . \tag{1.48}$$

It can be shown that the generator of the Coulomb gauge transformation can be expressed as

$$\chi_{\mathrm{C}}(\mathbf{r}) = \frac{1}{4\pi} \int \mathbf{A}(\mathbf{r}') \cdot \left(\nabla' \frac{1}{|\mathbf{r} - \mathbf{r}'|} \right) d\mathbf{r}' \ , \tag{1.49}$$

where ∇' indicates the gradient with respect to the variable $\mathbf{r}'$. Substituting Eq. (1.49) into the definition of $\mathbf{P}(\mathbf{r})$ in Eq. (1.43), we obtain

$$\mathbf{P}_{\mathrm{C}}(\mathbf{r}) = \frac{1}{4\pi} \nabla \left(\int \frac{\rho(\mathbf{r}')}{|\mathbf{r} - \mathbf{r}'|} \right) d\mathbf{r}' \ . \tag{1.50}$$

Being the gradient of a scalar function, $\mathbf{P}_{\mathrm{C}}(\mathbf{r})$ is a longitudinal vector field, and it satisfies the condition $\nabla \cdot \mathbf{P}_{\mathrm{C}}(\mathbf{r}) = -\rho(\mathbf{r})$. By comparison with the Maxwell's equations, we can identify $\mathbf{P}_{\mathrm{C}}(\mathbf{r})$ as the longitudinal component of the electric polarization density, satisfying

$$\mathbf{P}_{\mathrm{C}}(\mathbf{r}) = -\epsilon_0 \mathbf{E}^{\parallel}(\mathbf{r}) \ . \tag{1.51}$$

The momentum conjugate to the vector potential in the Coulomb gauge, from Eqs. (1.42b) and (1.44b) is given by

$$\mathbf{\Pi}_{\mathrm{C}}(\mathbf{r}) = -\epsilon_0 \mathbf{E} + \epsilon_0 \mathbf{E}^{\parallel}(\mathbf{r}) = -\epsilon_0 \mathbf{E}^{\perp}(\mathbf{r}) \ , \tag{1.52}$$

---

[3] This is a consequence of the fact that the curl of the gradient of any scalar function $v(\mathbf{r})$ is zero by definition, *i.e.* $\nabla \times \nabla v(\mathbf{r}) = 0$. Thus, any additional term to the vector potential (that is proportional to the gradient of the scalar potential) can only modify the longitudinal part of the vector potential, while leaving the transverse part unchanged.

and, hence, is a purely transverse vector field.

The Hamiltonian of the system in the Coulomb gauge can be derived from the general expression in Eq. (1.45), leading to

$$H_{\mathrm{C}} = \frac{1}{2m}\left(\mathbf{p}_{\mathrm{C}} + e\mathbf{A}_{\mathrm{C}}\right)^2 + \frac{1}{2}\int\left(\frac{\mathbf{\Pi}_{\mathrm{C}}^2}{\epsilon_0} + \frac{\mathbf{B}^2}{\mu_0}\right)d\mathbf{r} + \frac{1}{2\epsilon_0}\int \mathbf{P}_{\mathrm{C}}^2 d\mathbf{r}\ , \tag{1.53}$$

where we used the property that the integral of the product between any longitudinal and transverse vector fields is zero. The last term in Eq. (1.53) can be identified as the Coulomb energies of the charged particles in the system. Indeed, in the case of the hydrogen atom, $\mathbf{P}_{\mathrm{C}}(\mathbf{r})$ can be evaluated as

$$\mathbf{P}_{\mathrm{C}}(\mathbf{r}) = -\frac{e}{4\pi}\nabla\left(\frac{1}{|\mathbf{q}-\mathbf{r}|} - \frac{1}{|\mathbf{r}|}\right)\ , \tag{1.54}$$

which leads to the Coulomb energy term

$$\frac{1}{2\epsilon_0}\int \mathbf{P}_{\mathrm{C}}^2 d\mathbf{r} = -\frac{e^2}{4\pi\epsilon_0|\mathbf{q}|}\ , \tag{1.55}$$

corresponding to the interaction between the electron and the proton in the hydrogen atom. We notice that the contributions due to the charged particles (infinte) self-energies have been omitted in this last integral.

1.3.3 Power-Zienau-Woolley gauge

Another commonly used gauge in the context of light-matter interaction is the Power-Zienau-Woolley (PZW) gauge [39, 40], or *multipolar gauge*, which is particularly useful for describing bounded systems. The main feature of this gauge is that, while in the Coulomb gauge $\mathbf{P}_{\mathrm{C}}(\mathbf{r})$ has been indentified as the longitudinal component of the polarization density, in the multipolar gauge $\mathbf{P}_{\mathrm{M}}(\mathbf{r})$ contains both the longitudinal and the transverse components of the polarization density.

The vector field $\mathbf{P}_{\mathrm{M}}(\mathbf{r})$ can be expressed as

$$\mathbf{P}_{\mathrm{M}}(\mathbf{r}) = -e\int_0^1 \mathbf{q}\delta(\mathbf{r}-\lambda\mathbf{q})d\lambda\ . \tag{1.56}$$

It can be shown that $\nabla\cdot\mathbf{P}_{\mathrm{M}}(\mathbf{r}) = -\rho(\mathbf{r})$, thus having the same longitudinal part as the Coulomb gauge, *i.e.* $\mathbf{P}_{\mathrm{M}}^{\parallel}(\mathbf{r}) = \mathbf{P}_{\mathrm{C}}(\mathbf{r})$, but different transverse part. Another useful relation that can be easily derived is

$$\dot{\mathbf{P}}_{\mathrm{M}}(\mathbf{r}) = \mathbf{J}(\mathbf{r}) - \nabla\times\mathbf{M}\ , \tag{1.57}$$

where $\mathbf{M}(\mathbf{r})$ is the magnetization density, defined as

$$\mathbf{M}(\mathbf{r}) = -\dot{\mathbf{q}} \times \boldsymbol{\theta}(\mathbf{r},\mathbf{q}) \ , \quad \text{with} \quad \boldsymbol{\theta}(\mathbf{r},\mathbf{q}) = -e\int_0^1 \lambda\mathbf{q}\delta(\mathbf{r}-\lambda\mathbf{q})d\lambda \, . \tag{1.58}$$

Equations (1.56) and (1.58) show that $\mathbf{P}_\mathrm{M}(\mathbf{r})$ and $\mathbf{M}(\mathbf{r})$ can be indentified as the polarization and magnetization densities of the system, respectively. It can be shown that the generator of the PZW gauge transformation is given by

$$\chi_\mathrm{M}(\mathbf{r}) = -\int\int_0^1 \mathbf{A}(\mathbf{r}')\cdot\mathbf{r}\,\delta(\mathbf{r}'-\lambda\mathbf{r})d\lambda d\mathbf{r}' \ , \tag{1.59}$$

and it satisfies the condition

$$\nabla\chi_\mathrm{M}(\mathbf{r}) = \mathbf{A}(\mathbf{r}) - \frac{1}{e}\int \boldsymbol{\theta}(\mathbf{r},\mathbf{r}') \times \mathbf{B}(\mathbf{r}')d\mathbf{r}' \, . \tag{1.60}$$

From Eq. (1.39), we can therefore conclude that the vector potential in the PZW gauge is given by

$$\mathbf{A}_\mathrm{M}(\mathbf{r}) = \frac{1}{e}\int \boldsymbol{\theta}(\mathbf{r},\mathbf{r}') \times \mathbf{B}(\mathbf{r}')d\mathbf{r}' \ , \tag{1.61}$$

which has a non-zero longitudinal part, in contrast to the Coulomb gauge.

The conjugate momentum to the vector potential in the PZW gauge can be expressed as

$$\boldsymbol{\Pi}_\mathrm{M}(\mathbf{r}) = -\epsilon_0\mathbf{E} - \mathbf{P}_\mathrm{M}(\mathbf{r}) = -\mathbf{D}(\mathbf{r}) \ , \tag{1.62}$$

where $\mathbf{D}(\mathbf{r})$ is the electric displacement field, as defined in the Maxwell's equations. It can be readily verified that $\boldsymbol{\Pi}_\mathrm{M}(\mathbf{r})$ is a purely transverse vector field, consistently with the well-known transversality of the electric displacement field.

The Hamiltonian of the system in the PZW gauge can be derived from the general expression in Eq. (1.45), leading to

$$\begin{aligned} H_\mathrm{M} &= \frac{1}{2m}\left(\mathbf{p}_\mathrm{M} + e\mathbf{A}_\mathrm{M}\right)^2 + \frac{1}{2}\int\left(\frac{\left(\boldsymbol{\Pi}_\mathrm{M}+\mathbf{P}_\mathrm{M}\right)^2}{\epsilon_0} + \frac{\mathbf{B}^2}{\mu_0}\right)d\mathbf{r} \\ &= \frac{\mathbf{p}_\mathrm{M}^2}{2m} + \frac{1}{2}\int\left(\frac{\boldsymbol{\Pi}_\mathrm{M}^2}{\epsilon_0} + \frac{\mathbf{B}^2}{\mu_0}\right)d\mathbf{r} \\ &\quad + \frac{1}{\epsilon_0}\int \mathbf{P}_\mathrm{M}\cdot\boldsymbol{\Pi}_\mathrm{M}d\mathbf{r} + \frac{1}{2\epsilon_0}\int\mathbf{P}_\mathrm{M}^2 d\mathbf{r} - \int \mathbf{B}\cdot\mathcal{M}d\mathbf{r} + \frac{1}{2m}\left(\int\boldsymbol{\theta}\times\mathbf{B}d\mathbf{r}\right)^2 , \end{aligned} \tag{1.63}$$

where we defined the magnetization operator $\mathcal{M} = \left(\boldsymbol{\theta}\times\mathbf{p}_\mathrm{M} - \mathbf{p}_\mathrm{M}\times\boldsymbol{\theta}\right)/2m$. In classical mechanics the two contributions in this definition of the magnetization operator are equal, whereas in quantum mechanics they differ due to the non-commutativity of $\mathbf{p}_\mathrm{M}$ and $\boldsymbol{\theta}$. The first and second terms of the last line of Eq. (1.63) correspond to the standard interaction and *self-polarization* terms, respectively. On the other hand, the third and fourth terms are present due to the interaction with the magnetic field. In cavity QED, however, these magnetic contributions are typically neglected, as atoms are usually located in regions where the magnetic field vanishes or is strongly suppressed, such as at the center of a cavity.

It should be noted that the longitudinal part of the vector potential $\mathbf{A}^{\|}(\mathbf{r})$ in the PZW gauge does not play any role as a dynamical variable, as it does not affect the commutation relations due to the transversality of $\mathbf{\Pi}_\mathrm{M}(\mathbf{r})$, while the magnetic field $\mathbf{B}(\mathbf{r})$ can be determined only from the transverse part of the vector potential, as $\mathbf{B}(\mathbf{r}) = \nabla \times \mathbf{A}_\mathrm{M}(\mathbf{r})$.

1.3.4 Quantum mechanical description of light-matter interaction

As briefly mentioned in the previous subsections, the quantum mechanical description of light-matter interaction is based on the classical counterpart, which is then quantized by promoting the dynamical variables to operators and imposing the canonical commutation relations. In this section, we outline the quantization procedure and, in particular, highlight the correspondence between gauge transformations and unitary transformations, a central aspect of quantum mechanics.

The canonical quantization is performed by promoting the classical dynamical variables to operators and requiring the following commutation relations between the position and momentum operators of the particle, as well as between the vector potential and its conjugate momentum of the electromagnetic field:

$$[\hat{q}_i, \hat{p}_j] = i\hbar\delta_{ij} \ , \tag{1.64a}$$

$$[\hat{A}_i(\mathbf{r}), \hat{\Pi}_j(\mathbf{r}')] = i\hbar\delta^{\perp}_{ij}(\mathbf{r}-\mathbf{r}') \ , \tag{1.64b}$$

while all the other commutators vanish. Here, $\delta^{\perp}_{ij}(\mathbf{r}-\mathbf{r}')$ is the transverse delta function[4], reflecting the fact that only the transverse components of the fields possess dynamical degrees of freedom, as testified by the transversality of $\hat{\Pi}$. It is important to emphasize that the commutation relations in Eqs. (1.64a) and (1.64b) hold in any gauge, provided the appropriate definition of the conjugate momentum is employed. In particular, as discussed in the previously, in the Coulomb gauge the conjugate momentum to the vector potential corresponds to the transverse part of the electric field, while in the multipolar gauge it corresponds to the electric displacement field.

---

[4] The longitudinal and transverse delta functions are strictly linked to the decomposition of a vector field into longitudinal and transverse components. See Ref. [37] for a detailed discussion.

A direct consequence is that the creation and annihilation operators used to describe the electromagnetic field are *not* physical observables, since their definition depends on the chosen gauge. Specifically, in the Coulomb gauge they are related to the transverse component of the electric field, whereas in the multipolar gauge they are linked to the electric displacement field. By contrast, physical observables such as the fields themselves or the total energy remain gauge-invariant quantities. This point, while seemingly straightforward, is crucial: it is common practice to associate the creation and annihilation operators with the transverse modes of the free electromagnetic field, and thus with photons. However, this identification is strictly valid only in the Coulomb gauge, where the vector potential is purely transverse and the conjugate momentum is indeed the transverse part of the electromagnetic field. This subtle but important distinction will play a central role in Chapter 4.

We now establish the connection between the gauge transformations discussed in the previous subsections and the more familiar unitary transformations of quantum mechanics. In particular, we demonstrate that by introducing suitable unitary operators it is possible to implement gauge transformations, thus obtaining equivalent Hamiltonians in different gauges.

The evolution of the system in a given gauge can be described by solving the Schrödinger equation

$$i\hbar\frac{\partial}{\partial t}\left|\psi(t)\right\rangle = \hat{H}\left|\psi(t)\right\rangle \ , \tag{1.65}$$

where $\hat{H}$ is the Hamiltonian of the system in the chosen gauge, as given in Eq. (1.38). By applying a unitary transformation $\hat{U}$ to both the wavefunctions and the Hamiltonian, we obtain a transformed Schrödinger equation in the new gauge, given by

$$i\hbar\frac{\partial}{\partial t}\left|\psi_U(t)\right\rangle = i\hbar\frac{\partial}{\partial t}\hat{U}\left|\psi(t)\right\rangle = \hat{U}\hat{H}\hat{U}^\dagger\hat{U}\left|\psi(t)\right\rangle = \hat{H}_U\left|\psi_U(t)\right\rangle \ , \tag{1.66}$$

where $\hat{H}_U = \hat{U}\hat{H}\hat{U}^\dagger$ is the Hamiltonian in the new gauge and $\left|\psi_U(t)\right\rangle$ are the corresponding rotated states. The unitary operator $\hat{U}$ can be identified with the gauge transformation operator, as it transforms the wavefunctions and the dynamical variables of the system in a way that preserves the physical observables.

As an example, let us demonstrate how the multipolar gauge Hamiltonian in Eq. (1.63) can be obtained from the general Hamiltonian by performing a suitable unitary transformation defined by the operator

$$\hat{U}_{\rm M} = \exp\left(\frac{i}{\hbar}e\hat{\chi}_{\rm M}(\mathbf{q})\right) \ , \tag{1.67}$$

where $\chi_{\rm M}(\mathbf{q})$ is the generator of the PZW gauge transformation, given in Eq. (1.59). As $\chi_{\rm M}(\mathbf{q})$ depends only on $\mathbf{q}$ and $\mathbf{A}$, it can be easily verified that it commutes with both these operators, *i.e.* $[\hat{U}_{\mathrm{M}}, \hat{q}_i] = 0$ and $[\hat{U}_{\mathrm{M}}, \hat{A}_i(\mathbf{r})] = 0$, while shifting the conjugate momenta. In particular, to compute the action of the unitary operator on these conjugate momenta, we can use the Baker-Campbell-Hausdorff formula, which leads to the relations

$$\hat{\mathbf{p}}_{\mathrm{M}} = \hat{U}_{\mathrm{M}}\hat{\mathbf{p}}\hat{U}_{\mathrm{M}}^{\dagger} = \mathbf{p} - e\frac{\partial\hat{\chi}_{\mathrm{M}}(\mathbf{q})}{\partial\mathbf{q}} = \hat{\mathbf{p}} - e\nabla\hat{\chi}_{\mathrm{M}} \ , \tag{1.68a}$$

$$\hat{\mathbf{\Pi}}_{\mathrm{M}}(\mathbf{r}) = \hat{U}_{\mathrm{M}}\hat{\mathbf{\Pi}}(\mathbf{r})\hat{U}_{\mathrm{M}}^{\dagger} = \hat{\mathbf{\Pi}}(\mathbf{r}) - e\frac{\partial\hat{\chi}_{\mathrm{M}}(\mathbf{q})}{\partial\mathbf{A}(\mathbf{r})} = \hat{\mathbf{\Pi}}(\mathbf{r}) + \hat{\mathbf{P}}_{\mathrm{M}}(\mathbf{r}) \ . \tag{1.68b}$$

Hence, the new rotated Hamiltonian can be written as

$$\hat{H}_{\mathrm{M}} = \hat{U}_{\mathrm{M}}\hat{H}\left(\mathbf{q}, \mathbf{p}, \mathbf{A}, \mathbf{\Pi}\right)\hat{U}_{\mathrm{M}}^{\dagger} = \hat{H}\left(\mathbf{q}, \mathbf{p}_{\mathrm{M}}, \mathbf{A}, \mathbf{\Pi}_{\mathrm{M}}\right) \ , \tag{1.69}$$

which is the same as the Hamiltonian in Eq. (1.63), thus proving the equivalence between the two approaches.

Analogously, we can define the unitary operator for the Coulomb gauge as

$$\hat{U}_{\mathrm{C}} = \exp\left(\frac{i}{\hbar}e\hat{\chi}_{\mathrm{C}}(\mathbf{q})\right) \ , \tag{1.70}$$

where $\chi_{\mathrm{C}}(\mathbf{q})$ is the generator of the Coulomb gauge transformation, given in Eq. (1.49). Proceding similarly, we obtain the new Hamiltonian in the Coulomb gauge which coincides with the one in Eq. (1.53). The procedure outlined above can be generalized to any gauge transformation in quantum mechanics, and it proves useful and widely used in many applications.

1.4 Regimes in effective models of cavity QED

The interaction between light and matter, as described in the previous sections, can be rather complex, especially when attempting to describe realistic systems where multiple degrees of freedom, dissipation mechanisms, and strong correlations are simultaneously present. A direct treatment of the full quantum electrodynamical problem is in most cases intractable, both analytically and numerically, due to the presence of several coupled degrees of freedom, infinite dimensionality of the Hilbert space and the need to account for different energy and time scales. To make progress, it is therefore common to employ effective models that retain the essential physical ingredients while neglecting unnecessary microscopic details. These simplified descriptions not only provide analytical tractability but also offer physical insight and reliable predictions, while simultaneously highlighting the predominant mechanisms in the different regimes.

In cavity QED, paradigmatic examples include the Jaynes-Cummings model, the Tavis-Cummings model for multiple emitters, and the quantum Rabi model (QRM), which accounts for nonperturbative effects. Within these frameworks, one can explore different coupling regimes, ranging from weak to strong and ultrastrong coupling, each characterized by qualitatively distinct physical behavior. As we will see, the appropriate choice of effective model is closely tied to the regime under consideration and is fundamental for a consistent description of cavity QED phenomena [41, 42].

1.4.1 Weak and strong coupling regimes: the rotating wave approximation

As discussed in Section 1.1.2, one of the basic methodologies to model light-matter interaction is to describe the matter subsystem as a two-level system (representing, for instance, an atom or a quantum emitter), which subsequently couples to one or more modes of the electromagnetic field. When restricted to a single field mode, this approach leads to the QRM [43], defined by the Hamiltonian

$$\hat{H}_{\text{Rabi}} = \hbar\omega_c \hat{a}^\dagger \hat{a} + \frac{\hbar\omega_0}{2}\hat{\sigma}_z + \hbar g \left(\hat{a} + \hat{a}^\dagger\right)\left(\hat{\sigma}_- + \hat{\sigma}_+\right) \ , \tag{1.71}$$

where $\hat{a}$ ($\hat{a}^\dagger$) is the annihilation (creation) operator of the cavity mode with frequency ω_c, $\hat{\sigma}_z$ and $\hat{\sigma}_\pm$ are the Pauli matrices describing the two-level system with transition frequency ω_0, and g denotes the light-matter coupling strength. The QRM captures the essential physics of light-matter interaction for systems in which the cavity frequency is nearly or perfectly resonant with the atomic transition considered. A more detailed discussion of the QRM and its properties is provided in Section 2.1.

However, the full QRM is not always necessary to describe the system accurately. In many experimental setups, the light-matter coupling strength g is much smaller than both the cavity and atomic frequencies, *i.e.* $g \ll \omega_c, \omega_0$. In this regime, the rotating wave approximation (RWA) can be employed, which consists in neglecting the so-called counter-rotating terms, $\hat{a}\hat{\sigma}_-$ and $\hat{a}^\dagger\hat{\sigma}_+$, in the interaction Hamiltonian. These terms describe processes where both the atom and the cavity mode are simultaneously excited or de-excited, which are highly off-resonant and thus have a negligible effect on the system dynamics when g is small compared to the bare frequencies. The remaining interaction terms, $\hat{a}^\dagger\hat{\sigma}_-$ and $\hat{a}\hat{\sigma}_+$, are commonly referred to as corotating terms since, in the interaction picture, they remain stationary, in contrast to the counter-rotating terms, which oscillate at much higher frequencies. Physically, these corotating terms describe energy-conserving processes in which an excitation is coherently exchanged between the atom and the cavity mode. By applying the RWA to the QRM, we obtain the Jaynes-Cummings model [44], described by the Hamiltonian

$$\hat{H}_{\mathrm{JC}} = \hbar\omega_c \hat{a}^\dagger \hat{a} + \frac{\hbar\omega_0}{2}\hat{\sigma}_z + \hbar g \left(\hat{a}\hat{\sigma}_+ + \hat{a}^\dagger \hat{\sigma}_-\right) \ . \tag{1.72}$$

The Jaynes-Cummings model has been extensively studied and successfully applied in the interpretation of experimental results, providing crucial insights into the physics of cavity QED. Its main strength lies in the analytical solvability, which allows for a detailed understanding of fundamental phenomena such as vacuum Rabi oscillations and Rabi splitting [45].

In particular, to block-diagonalize the Jaynes-Cummings Hamiltonian, it is useful to introduce the total excitation number operator $\hat{N}_{\mathrm{exc}} = \hat{a}^\dagger \hat{a} + \hat{\sigma}_+\hat{\sigma}_-$, which commutes with the Hamiltonian, *i.e.* $[\hat{H}_{\mathrm{JC}}, \hat{N}_{\mathrm{exc}}] = 0$. As the total number of excitations in the system is conserved, we can diagonalize the Hamiltonian in subspaces with fixed excitation number. The eigenstates of the Jaynes-Cummings Hamiltonian can thus be expressed as superpositions of states with a definite number of photons and atomic excitations, namely

$$|n,+\rangle = \cos(\theta_n/2)\,|e, n-1\rangle + \sin(\theta_n/2)\,|g, n\rangle \ , \tag{1.73}$$

$$|n,-\rangle = -\sin(\theta_n/2)\,|e, n-1\rangle + \cos(\theta_n/2)\,|g, n\rangle \ , \tag{1.74}$$

where $|g\rangle$ and $|e\rangle$ are the ground and excited states of the two-level system, respectively, $|n\rangle$ is the Fock state with n photons in the cavity mode, and $\theta_n = \arctan(2g\sqrt{n}/\delta)$ is the mixing angle, with $\delta = \omega_0 - \omega_c$ being the detuning between the atom and the cavity mode. The corresponding eigenenergies are given by

$$E_{n,\pm} = n\hbar\omega_c \pm \frac{\hbar}{2}\sqrt{\delta^2 + 4g^2 n} \ , \tag{1.75}$$

for $n \geq 1$, while the ground state of the system is simply $|g, 0\rangle$ with energy $E_0 = -\hbar\omega_0/2$.

Given the analytical solvability of the model, its dynamics is straightforward to compute. For instance, if the system is initially prepared in the state $|e, 0\rangle$, the time evolution leads to the so-called Rabi oscillations between the states $|e, 0\rangle$ and $|g, 1\rangle$ with a frequency $\Omega_R = \sqrt{\delta^2 + 4g^2}$. However, the main obstacle to the experimental observation of Rabi oscillations is the presence of dissipation mechanisms, such as spontaneous emission and cavity losses, which can dampen the oscillations and lead to decoherence. This is usually referred to as *weak coupling regime*, and it is characterized by the condition $g < \gamma, \kappa$, where γ and κ are the atomic and cavity decay rates, respectively (see Fig. 1.3(a)). In this regime, the dynamics of the system is dominated by dissipation, and coherent phenomena such as Rabi oscillations are typically not observable. On the other hand, when

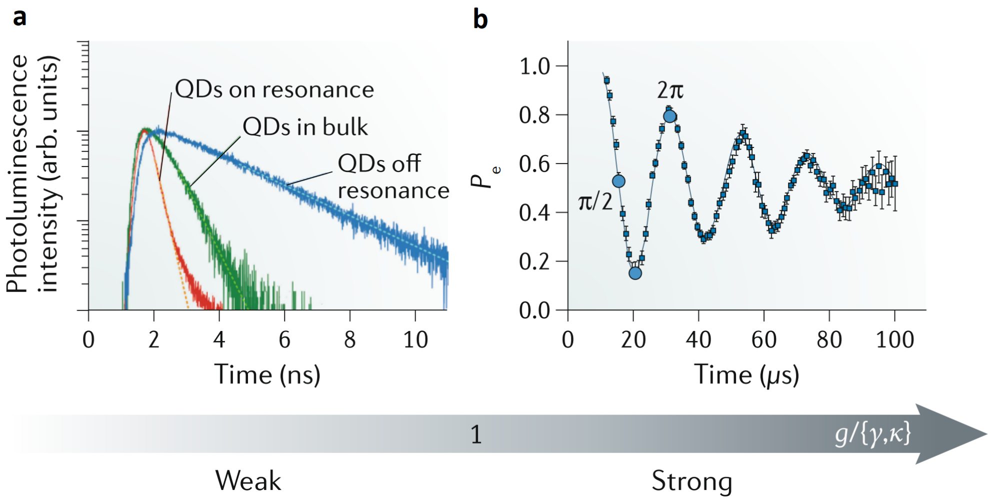

Figure 1.3: Scale of the coupling strength g relative to the cavity and atomic decay rates, κ and γ, defining the weak and strong coupling regimes in cavity QED. **(a)** In the weak coupling regime, dissipation dominates the dynamics. Experimental data of single quantum dots (QDs) interacting with a photonic nanocavity [46]. If the QDs are resonant with the cavity frequency they decay faster, demonstrating the Purcell effect [47]. **(b)** In the strong coupling regime, coherent exchange of excitations between the atom and the cavity mode can occur before dissipation takes over. Experimental data of Rydberg atoms interacting with a superconducting microwave cavity [48]. Figure reproduced with permission from Ref. [41].

the coupling strength g exceeds both γ and κ, the system enters the *strong coupling regime*, where coherent exchange of excitations between the atom and the cavity mode can occur before dissipation takes over (see Fig. 1.3(b)). In 1983 the first experimental observation of the Rabi oscillations was reported by Haroche and coworkers [49], using Rydberg atoms.

1.4.2 Ultrastrong and deep-strong coupling regimes: beyond the rotating wave approximation

While the ratio $g/\{\gamma, \kappa\}$ remains the key parameter to study the coherence of the system, defining the weak and strong coupling regimes, it is important to emphasize that the previous discussion so far assumes $g \ll \omega_c, \omega_0$, such that the RWA is safely applicable. However, if the coupling strength g is increased even further, becoming comparable to the bare frequencies, the counter-rotating terms in the quantum Rabi Hamiltonian can no longer be neglected, and the full model must be considered. This regime is known as the *ultrastrong coupling regime* (USC), which is conventionally identified by the condition $0.1 \lesssim g/\omega_c \lesssim 1$ [41, 42]. It should be emphasized that, since the Hamiltonian depends continuously on the coupling strength (and hence the intensity of higher-order processes), the distinction between different regimes is gradual, and the previous bounds are just historical conventions rather than strict physical thresholds. In the USC regime, the properties of the system change both quantitatively and qualitatively, as the light-matter interaction becomes nonperturbative and the ground state of the system acquires a nontrivial structure, containing virtual photons and atomic excitations. Moreover, the total excitation number is no longer conserved, as the counter-rotating terms allow for processes between states with different numbers of excitations. However, it is still possible to demonstrate that the parity of the excitations is a conserved quantity. Indeed, by defining the parity operator as

$$\hat{\Pi} = \exp\left[i\pi\left(\hat{a}^\dagger\hat{a} + \hat{\sigma}_-\hat{\sigma}_+\right)\right] = (-1)^{\hat{a}^\dagger\hat{a}+\frac{1}{2}(1+\hat{\sigma}_z)}\,, \tag{1.76}$$

we can verify that it commutes with the quantum Rabi Hamiltonian in Eq. (1.71), *i.e.* $[\hat{H}_{\mathrm{Rabi}}, \hat{\Pi}] = 0$. Therefore, this model possesses a discrete $\mathbb{Z}_2$ symmetry, which has been shown to be sufficient for the model to be integrable [50]. The additional higher-order processes allowed in USC lead to a breakdown of the simple picture of Rabi oscillations and vacuum Rabi splitting, and new phenomena emerge, such as the Bloch-Siegert shift [51].

Although achieving such high coupling strengths is challenging, nowadays, the USC regime has been experimentally realized in various systems, including superconducting circuits [30], semiconductor microcavities [53], and organic molecules [54]. Two main strategies are typically employed to enhance the coupling strength: (i) increase the number of emitters N coupled to the same mode, since the collective coupling strength scales as $g\sqrt{N}$ [18], or (ii) use different platforms where the coupling strength is not limited by the smallness of the fine structure constant as in the natural atoms case, such as superconducting circuits or confined structures with very small mode volumes [41, 42]. Fig. 1.4 shows the scale of the coupling strength g relative to the cavity frequency ω_c, defining the ultrastrong and deep-strong coupling regimes in cavity QED, along with some experimental realizations. In particular, Fig. 1.4(a) shows experimental data from Ref. [30], where a superconducting qubit was coupled to coplanar-waveguide resonator, achieving a coupling strength of $g/\omega_c = 0.12$.

If the coupling strength is pushed even further, exceeding the bare frequencies of the system, we enter the so-called *deep-strong coupling regime* (DSC), defined by the condition $g/\omega_c \gtrsim 1$ [41, 42]. In this regime, the light-matter interaction dominates the dynamics, and the system exhibits highly nontrivial behavior. A typical signature of the DSC regime is the significant splitting between the upper and lower polaritons, which is larger than the bare frequencies themselves, as

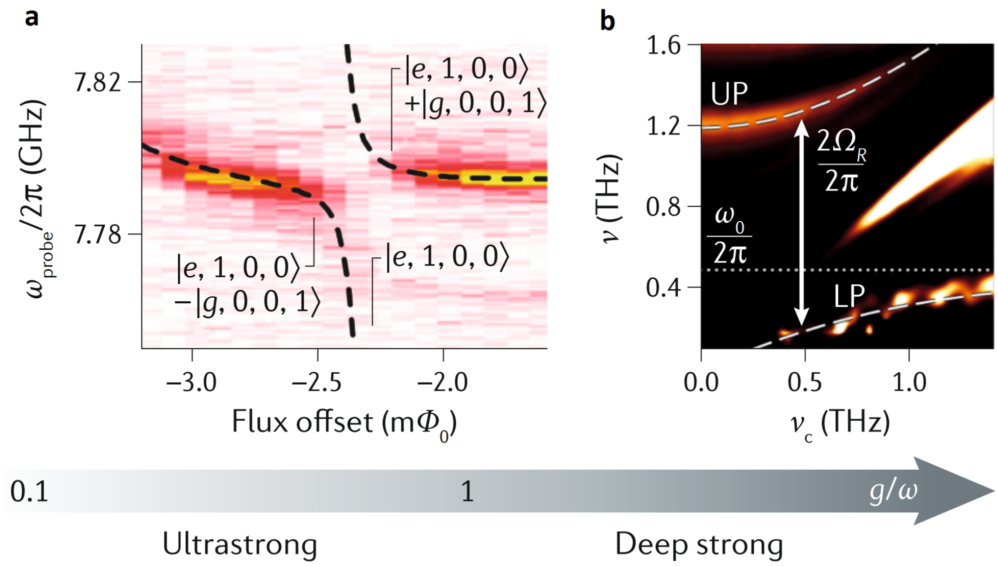

Figure 1.4: Scale of the coupling strength g relative to the cavity frequency ω_c, defining the ultrastrong and deep-strong coupling regimes in cavity QED. **(a)** In the ultrastrong coupling regime, processes that do not conserve the number of excitations are allowed, as illustrated by the avoided level crossing. Experimental data from Ref. [30] **(b)** In the deep-strong coupling regime, the splitting between the upper and lower polaritons, which is a measure of the coupling strength, becomes considerable. Experimental data from Ref. [52], where a record high coupling strength of $g/\omega_c = 1.43$ was achieved. Figure reproduced with permission from Ref. [41].

shown in Fig. 1.4(b). Furthermore, in the DSC regime, the so-called light-matter decoupling effect can occur, where the system effectively behaves as if the light and matter subsystems are decoupled, despite the highly strong interaction between them [55, 56].

The novel effects enabled by the USC and DSC regimes have attracted considerable attention in recent years, both for their fundamental interest and for their potential applications [54, 57–71]. On the fundamental side, they provide a unique testbed to explore light-matter interaction in a genuinely nonperturbative regime, where entirely new quantum phenomena can arise. On the applied side, these regimes open promising perspectives for quantum information processing, quantum simulation, and emerging quantum technologies.

1.5 Quantum phase transitions in light-matter models

Some effective models used to describe light-matter interaction predict a qualitative change in the ground-state properties when the coupling strength exceeds a critical value. Typical examples include the QRM and its generalization to multiple emitters, known as the Dicke model [18]. This phenomenon is referred to as a quantum phase transition (QPT), which occurs at zero temperature and is driven by quantum fluctuations, in contrast to classical phase transitions that occur at finite temperature and are driven by thermal fluctuations [16, 17]. QPTs are typically characterized by a non-analytic behavior of the ground-state energy and a change in the order parameter.

In this section, we briefly present the basics concepts regarding QPTs that will be relevant for the following chapters. In particular, we first outline the main differences and similiarities between classical and quantum phase transitions. We then schematically discuss two representative examples of QPTs in models widely used in quantum optics, namely the QRM and the Dicke model. We will highlight the main features of these transitions, such as the critical points, the order parameters, and the nature of the phases involved.

1.5.1 Basics of quantum phase transitions

Unlike classical phase transitions, which occur at finite temperatures and are usually driven by thermal fluctuations, QPTs are governed by quantum fluctuations originating from the Heisenberg uncertainty principle. They take place at zero temperature ($T = 0$) when a non-thermal control parameter of the Hamiltonian, such as an external magnetic field or pressure, exceeds a critical value. At this point, the ground state of the system undergoes a qualitative change of its properties, such as in the nature of the correlations, thus leading to different phases [16, 17].

Let us consider a general Hamiltonian $\hat{H}(g)$ depending on a control parameter g, which could represent, for instance, the coupling strength in a light-matter system. Since our focus is on ground-state properties, we study the behaviour of the ground-state energy $E_0(g)$ as a function of the parameter g. For finite systems, $E_0(g)$ is typically analytic, except at isolated points corresponding to level crossings, as schematically shown in Fig. 1.5(a). This scenario can occur only when the bare Hamiltonian $\hat{H}_0 = \hat{H}(0)$ is coupled to a conserved quantity $\hat{H}_1$, i.e. $\hat{H}(g) = \hat{H}_0 + g\hat{H}_1$ with $[\hat{H}_0, \hat{H}_1] = 0$, so that $\hat{H}_0$ and $\hat{H}_1$ can be simultaneously diagonalized. In this case, it is possible to find a set of eigenfunctions that do not depend on g, while the eigenvalues can still depend on it. In this situation,

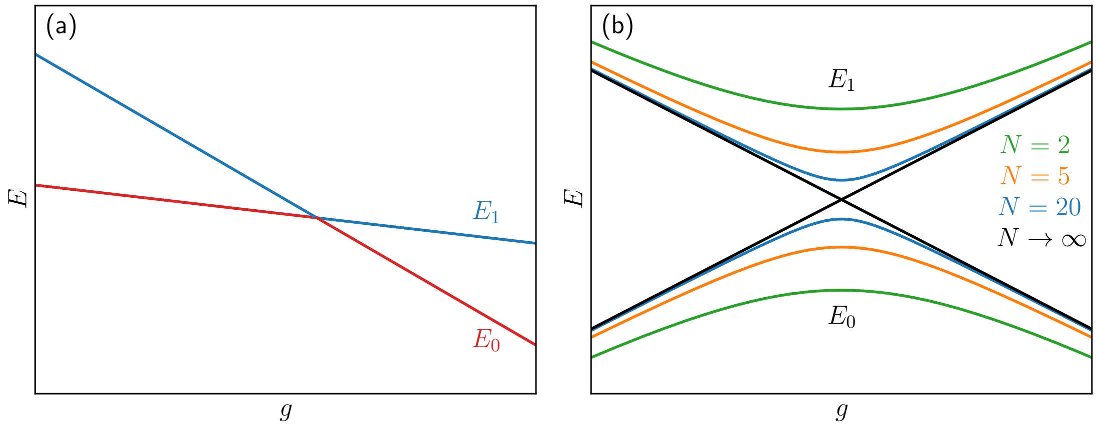

Figure 1.5: Schematic representation of level crossings leading to a quantum phase transition, in arbitrary units. **(a)** True level crossing, where the ground-state energy $E_0(g)$ (red line) is non-analytic at the critical point g_c due to the crossing with an excited state $E_1(g)$ (blue line). **(b)** Effective level crossing in the thermodynamic limit, where the ground-state energy $E_0(g)$ is non-analytic at the critical point g_c only in the limit $N \to \infty$, where N is a relevant quantity pushed to the thermodynamic limit. For finite N, the ground-state energy is analytic, as the crossing is avoided.

an excited level may cross the ground state at some g_c, thus becoming the new ground state. By contrast, in systems where some relevant quantity is pushed to the thermodynamic limit, avoided level crossings can sharpen into effective level crossings, thus producing non-analyticities in $E_0(g)$, as shown in Fig. 1.5(b). These singular points, independently if they arise from true level crossings or from avoided level crossings in the thermodynamic limit, are identified as QPTs, with the latter mechanism being the most common.

Most of the QPTs that are studied in the literature are second-order transitions, which are characterized by the continuous vanishing of a characteristic energy scale of fluctuations above the ground state near the critical point. More specifically, denoting by Δ a characteristic excitation energy of the ground state of the system (e.g. the gap to the first excited state), one finds that as $g \to g_c$ it vanishes as

$$\Delta \sim J|g - g_c|^{z\nu};\,, \tag{1.77}$$

where J is a microscopic energy scale, ν the correlation-length exponent, and z the dynamical critical exponent. Simultaneously, second-order QPT have a characteristic correlation length scale ξ that diverges as

$$\xi \sim |g - g_c|^{-\nu};\,. \tag{1.78}$$

These relations establish a universal connection between the critical exponents, which is a defining property of critical phenomena. Universality plays a central role in the theory of QPTs, and more generally phase transitions: different microscopic Hamiltonians can share identical critical exponents and scaling forms, provided they belong to the same universality class.

We emphasize that, since all the properties discussed so far refer to the ground state of the system, true QPTs can occur only at zero temperature. However, experiments inevitably probe systems at finite T, even if very low. Therefore, it is crucial to understand how the singularities at $T = 0$ influence the properties of the system at $T > 0$. There are two main possibilities: the singularity exists only at $T = 0$, and for any $T > 0$ all quantities are analytic in g, or a line of classical second-order phase transitions (for which the thermodynamic free energy is not continuous) extends from the quantum critical point to finite temperatures. In the latter case, near this line, the relevant degrees of freedom fluctuate at frequencies ω_{rel} such that $\hbar\omega_{\text{rel}} \ll k_B T$. Under these conditions, a classical description becomes applicable. In this sense, the quantum critical point can be regarded as the zero-temperature limit of a line of classical critical points, and hence classical and quantum criticality are continuously connected. The Dicke model provides a paradigmatic example of this scenario, as its classical critical point (at finite temperature) is continuously linked to its quantum counterpart.

1.5.2 Quantum phase transitions in quantum Rabi and Dicke models

Let us now analyze two models widely employed in quantum optics that can exhibit a QPT, namely the QRM and the Dicke model. Both these models are particularly relevant in cavity QED, as they describe the interaction between a bosonic mode and one or more two-level systems, respectively.

We begin with the QRM, whose Hamiltonian has been introduced in Eq. (1.71). While a detailed study about the properties of this model will be presented in Chapter 2, here we briefly outline the conditions under which it exhibits a QPT. It has been shown that the QRM undergoes a second-order QPT in the limit where the ratio between the atomic and cavity frequencies diverges, *i.e.* $\omega_0/\omega_c \to \infty$ [72, 73]. Although the QRM obviously does not possess a true thermodynamic limit (as there is only one two-level system), the parameter ω_0/ω_c plays the role of an effective one, allowing the spectral gap to the first excited state to close in this limit. The critical coupling is found at $g_c = \sqrt{\omega_c\omega_0}/2$, and the order parameter can be identified with the coherence of the bosonic mode, $\langle \hat{a} \rangle$. In the normal phase ($g < g_c$), this expectation value is zero, while for $g > g_c$ it becomes finite, signaling a spontaneous breaking of the $\mathbb{Z}_2$ symmetry of the Hamiltonian and the ground state becomes double degenerate. Since the cavity field acquires a macroscopic expectation value, this QPT can be classified as a so-called *superradiant phase transition*, similiarly to the Dicke model that will be discussed shortly. It can be shown that the critical exponents associated with this transition are $z\nu = 1/2$ and $\nu = 1/4$, which are respectively associated to the vanishing of the excitation energy and to the divergence of the position quadrature of the bosonic field [72].

We now investigate the Dicke model, which describes the interaction between a single bosonic mode and N identical two-level systems. A full analysis of this model will be provided in Chapter 5, while here we restrict ourselves to a brief overview about its QPT. The Hamiltonian of the Dicke model is given by [18, 19, 21, 74]

$$\hat{H}_{\text{Dicke}} = \hbar\omega_c \hat{a}^\dagger \hat{a} + \hbar\omega_0 \hat{J}_z + \frac{\hbar g}{\sqrt{N}} \left(\hat{a} + \hat{a}^\dagger\right) \left(\hat{J}_+ + \hat{J}_-\right) , \tag{1.79}$$

where $\hat{J}_z = \sum_{i=1}^{N} \hat{\sigma}_z^{(i)}/2$ and $\hat{J}_\pm = \sum_{i=1}^{N} \hat{\sigma}_\pm^{(i)}$ are collective spin operators that describe the ensemble of two-level systems. The factor $1/\sqrt{N}$ in the coupling term ensures a well-defined thermodynamic limit. This Hamiltonian exhibits a $\mathbb{Z}_2$ symmetry, since it commutes with the parity operator which, in presence of multiple two-level systems, can be defined as $\hat{\Pi} = \exp\left[i\pi\left(\hat{a}^\dagger\hat{a} + \hat{J}_z + N/2\right)\right]$. In the thermodynamic limit, $N \to \infty$, the Dicke model presents a second-order QPT which occurs at the critical coupling strength $g_c = \sqrt{\omega_c\omega_0}/2$, identical to that of the QRM. The order parameter can again be identified with the coherence of the bosonic mode, $\langle\hat{a}\rangle$, which vanishes in the normal phase ($g < g_c$) and becomes finite in the superradiant phase ($g > g_c$), signaling a spontaneous breaking of the $\mathbb{Z}_2$ parity symmetry of the Hamiltonian. The critical exponents associated with this transition are found to be $z\nu = 1/2$ and $\nu = 1/4$ [21]. We notice that these values are identical to those of the QRM, showing that the two models belong to the same universality class.

CHAPTER 2

One-atom models in cavity and circuit QED: renormalization and spectral properties

In this chapter we focus on the interaction between a single emitter and a single-mode electromagnetic resonator. Our primary interest is in a fundamental model of light-matter interaction, extensively employed in both cavity and circuit QED: the quantum Rabi model (QRM). We begin by introducing the model and discussing the gauge ambiguities that arise when truncating the matter system to its two lowest energy levels.

Subsequently, we analyze the spectral properties of the QRM, with particular attention to the modifications in the emission spectra that arise when different forms of coupling to the external environment are considered. These distinctions become especially relevant in the ultrastrong coupling (USC) and deep strong coupling (DSC) regimes, where the light-matter interaction strength constitutes a significant fraction of, or even exceeds, the bare frequencies of the system.

We then turn to the validity of the two-level approximation and of the QRM itself. In particular, we highlight the necessity of renormalizing the QRM in order to incorporate the effects of higher-energy levels of the matter system, which are usually neglected in the two-level truncation. To this end, we develop a framework for deriving renormalized QRMs (RQRMs), applicable to both cavity and circuit QED, which provides an accurate description of the system even in the USC and DSC regimes. Finally, we investigate key properties of these RQRMs, such as gauge invariance.

The structure of the chapter is as follows. In Section 2.1, we introduce the QRM Hamiltonian in both the Coulomb and multipolar gauges, and discuss the gauge ambiguities that arise when truncating the matter system to its two lowest energy levels. In Section 2.2, we analyze the spectral properties of the QRM under different forms of coupling to the external environment, emphasizing the differences that emerge in the USC and DSC regimes. In Section 2.3, we present the renormalization procedure for the QRM, develop the general framework for constructing RQRMs in both cavity and circuit QED, and analyze their properties. The content of this chapter is based on the original works in Refs. [3, 4].

2.1 The quantum Rabi model and the breakdown of gauge invariance

The quantum Rabi model (QRM) [43, 48, 75] is a cornerstone in quantum optics, condensed matter physics, and both cavity and circuit QED, providing a fundamental yet simple model for describing light-matter interactions at the quantum level. The QRM describes the interaction between a two-level system (TLS) and a single mode of the electromagnetic field. The QRM Hamiltonian can be derived from the minimal coupling Hamiltonian in Eq. (1.53) or Eq. (1.63) by truncating the matter system to its two lowest energy levels, in the dipole approximation. The validity of this two-level truncation is generally justified when the resonance frequency of the cavity mode is close to the atomic transition of interest, and the light-matter coupling strength remains small compared to the bare frequencies of the system. However, as we will discuss, this approximation becomes problematic in the USC regime, where the coupling strength approaches a significant fraction of these frequencies, or in presence of large detunings between the cavity and TLS frequencies.

In particular, it has been shown [76–81] that the QRM obtained from the two-level truncation of the Coulomb-gauge Hamiltonian is not equivalent to the one derived in the multipolar gauge, and moreover, its predictions deteriorate more rapidly with increasing coupling strength. This discrepancy reflects a fundamental *gauge-invariance breakdown* that arises when the full light-matter Hamiltonian is truncated. Moreover, in the USC and DSC regimes, the standard QRM also faces several complications in the theory of photodetection [82, 83] and in the description of the system's coupling to the external environment [84–86].

The two-level truncation is formally implemented by projecting the Hamiltonian onto the subspace spanned by the two lowest-energy eigenstates of the matter system, *i.e.* by applying the projection operator $\hat{\mathcal{P}} = |0\rangle\langle 0| + |1\rangle\langle 1|$. A crucial point is that the position and momentum operators of the matter subsystem do not commute with the projection operator. Consequently, truncating *before* or *after* applying the minimal coupling replacement $\hat{p} \to \hat{p} - q\hat{A}$ (in the Coulomb gauge) yields different effective Hamiltonians.

If the truncation is performed first and applied consistently, namely by replacing the matter operators with their two-level counterparts both in the Hamiltonians and in the associated unitary transformations, it has been demonstrated [87] that it is possible to introduce a unitary transformation in the truncated Hilbert space that maps the multipolar gauge QRM Hamiltonian to a modified version of the Coulomb-gauge QRM, which, by construction, preserves the energy spectrum. Furthermore, this procedure is also consistent with lattice gauge principles (that, however, are beyond the scope of this thesis), which require that any truncation or approximation must be carried out carefully and, above all, consistently [77]. This has been a key step in resolving the gauge issue which arises in truncated Hilbert spaces, as it shows that gauge-invariant formulations, and thus physically consistent predictions, can be consistently obtained even in truncated models, provided that gauge transformations are implemented consistently. However, by performing the truncation before the minimal coupling replacement, the resulting QRM Hamiltonian exhibits reduced accuracy as the coupling strength increases [88]. To achieve a more faithful description of the system in the USC regime, it is therefore necessary to apply the two-level truncation *after* performing the minimal coupling replacement. This approach, however, comes at the expense of explicitly breaking gauge invariance. In the following sections, we will present and compare results obtained within both approaches.

2.1.1 The quantum Rabi Hamiltonian

Let us start by introducing the QRM Hamiltonians in both the Coulomb and multipolar gauges [76]. As discussed in Section 1.1.2, when restricted to a one dimension, a single electric dipole can be modeled as an effective particle of mass m moving in a double-well potential $V(x)$, where x is the distance between the two charges, q and $-q$, forming the dipole. The two lowest energy eigenstates, $|0\rangle$ and $|1\rangle$ (or $|g\rangle$ and $|e\rangle$, for ground and excited states, respectively), are separated by an energy gap ω_{10}. The dipole is coupled to a single mode of an electromagnetic resonator with frequency ω_c and corresponding annihilation (creation) operator $\hat{a}$ ($\hat{a}^\dagger$). The light-matter interaction can be described in the Coulomb gauge by the Hamiltonian in Eq. (1.53). We first perform the dipole approximation, which consists in assuming that the spatial variation of the electromagnetic field over the extent of the dipole is negligible, *i.e.* $\hat{A}(\hat{r}) \approx \hat{A}(0) = A_0(\hat{a} + \hat{a}^\dagger)$, where A_0 is the amplitude of the vector potential, which can thus be considered constant in the region of interest. This approximation is sometimes also referred to as the long-wavelength approximation, as it is valid when the wavelength of the electromagnetic field is much larger than the size of the dipole. The resulting Hamiltonian reads

$$\begin{aligned}\hat{H}_{\rm C} &= \hbar\omega_c \hat{a}^\dagger\hat{a} + \frac{(\hat{p}-q\hat{A})^2}{2m} + V(\hat{x}) \\ &= \hbar\omega_c \hat{a}^\dagger\hat{a} + \frac{\hat{p}^2}{2m} + V(\hat{x}) - \frac{qA_0}{m}\hat{p}(\hat{a}+\hat{a}^\dagger) + \frac{q^2A_0^2}{2m}(\hat{a}+\hat{a}^\dagger)^2\,, \end{aligned} \tag{2.1}$$

where we have used the fact that $\hat{p}$ and $\hat{A} \equiv \hat{A}(0)$ commute, as they act on different Hilbert spaces. The last term in Eq. (2.1) is the so-called *diamagnetic* A^2 term, which plays a crucial role in ensuring the stability of the system and preventing unphysical predictions, such as superradiant phase transitions in the thermodynamic limit, as discussed in Chapter 4 and Refs. [89–92]. We notice that the minimal coupling replacement in Eq. (2.1) can be formally obtained by applying a suitable unitary transformation $\hat{U}$ to the free matter Hamiltonian $\hat{H}_{\rm mat} = \hat{p}^2/2m + V(\hat{x})$, namely $\hat{U}\hat{H}_{\rm mat}\hat{U}^\dagger$, where

$$\hat{U} = \exp\left(iq\hat{x}\hat{A}/\hbar\right) = \exp\left(iqA_0\hat{x}(\hat{a}+\hat{a}^\dagger)/\hbar\right)\,. \tag{2.2}$$

Indeed, by applying the Baker-Campbell-Hausdorff formula, it is possible to show that $\hat{U}\hat{p}\hat{U}^\dagger = \hat{p} - q\hat{A}$ and $\hat{U}\hat{x}\hat{U}^\dagger = \hat{x}$. Therefore, the Hamiltonian in Eq. (2.1) can be equivalently written as

$$\hat{H}_{\rm C} = \hat{H}_{\rm ph} + \hat{U}\hat{H}_{\rm mat}\hat{U}^\dagger\,, \tag{2.3}$$

where $\hat{H}_{\rm ph} = \hbar\omega_c\hat{a}^\dagger\hat{a}$ is the free photonic Hamiltonian.

We subsequently project the Hamiltonian in Eq. (2.1) onto the subspace spanned by the two lowest energy states of the unperturbed matter system by applying the projection operator $\hat{\mathcal{P}}$. Hence, we obtain (from now on, we will use the calligraphic font to denote operators belonging to the two-dimensional subspace)

$$\hat{\mathcal{H}}_{\rm C} = \hat{\mathcal{P}}\hat{H}_{\rm C}\hat{\mathcal{P}} = \hbar\omega_c\hat{a}^\dagger\hat{a} + \frac{\hbar\omega_{10}}{2}\hat{\sigma}_z - \hbar g_{10}^{\rm C}(\hat{a}+\hat{a}^\dagger)\hat{\sigma}_x + \hbar D(\hat{a}+\hat{a}^\dagger)^2\,, \tag{2.4}$$

where ω_{jk} and $g_{jk}^{\rm C} = \omega_c q A_0 \langle j|\hat{p}|k\rangle/\hbar$ are the transition frequencies and light-matter coupling strengths (in the Coulomb gauge), respectively, concerning the transitions between the states $|j\rangle$ and $|k\rangle$. Furthermore, we have introduced the diamagnetic constant $D = q^2A_0^2/2\hbar m$ and the Pauli operators $\hat{\sigma}_x = |1\rangle\langle 0| + |0\rangle\langle 1|$ and $\hat{\sigma}_z = |1\rangle\langle 1| - |0\rangle\langle 0|$, acting on the two-dimensiona Hilbert space. We notice that the coupling strength $g_{10}^{\rm C}$ can be either positive or negative, depending on the sign of the momentum matrix element $\langle 1|\hat{p}|0\rangle$ and the charge q. Thus, moving forward, we will always implicitly consider $|g_{jk}|$ in defining the regimes of light-matter interaction, if not explicitly stated contrarly.

Sometimes it is useful to incorporate the diamagnetic term into the bare photonic Hamiltonian through a Bogoliubov transformation [93]. Specifically, by introducing new bosonic operators $\hat{c}$ and $\hat{c}^\dagger$ and renormalized cavity frequency $\tilde{\omega}_c = \sqrt{\omega_c^2 + 4D^2}$, we can rewrite the QRM in Eq. (2.4) as

$$\hat{\mathcal{H}}_{\mathrm{C}} = \hbar\tilde{\omega}_c \hat{c}^\dagger \hat{c} + \frac{\hbar\omega_{10}}{2}\hat{\sigma}_z - \hbar\tilde{g}_{10}^{\mathrm{C}}(\hat{c} + \hat{c}^\dagger)\hat{\sigma}_x \,, \tag{2.5}$$

where $\tilde{g}_{10}^{\mathrm{C}} = g_{10}^{\mathrm{C}}\sqrt{\omega_c/\tilde{\omega}_c}$ is the renormalized coupling strength.

The QRM Hamiltonian in the multipolar gauge can be derived in an analogous way, starting from the Hamiltonian in Eq. (1.63) and applying the dipole approximation. Equivalently, it can be obtained by performing a unitary transformation of the Hamiltonian in Eq. (2.1) with the same operator $\hat{U}$ in Eq. (2.2). The resulting Hamiltonian, commonly referred to as the *dipole gauge Hamiltonian*, reads

$$\begin{aligned}
\hat{H}_{\mathrm{D}} &= \hat{U}^\dagger \hat{H}_{\mathrm{C}} \hat{U} = \hat{U}^\dagger \hat{H}_{\mathrm{ph}} \hat{U} + \hat{H}_{\mathrm{mat}} \\
&= \hbar\omega_c \left(\hat{a}^\dagger - i\frac{qA_0}{\hbar}\hat{x}\right)\left(\hat{a} + i\frac{qA_0}{\hbar}\hat{x}\right) + \frac{\hat{p}^2}{2m} + V(\hat{x}) \\
&= \hbar\omega_c \hat{a}^\dagger \hat{a} + \frac{\hat{p}^2}{2m} + V(\hat{x}) - iq\omega_c A_0 \hat{x}\omega_c\left(\hat{a} - \hat{a}^\dagger\right) + \frac{\omega_c q^2 A_0^2}{\hbar}\hat{x}^2 \,.
\end{aligned} \tag{2.6}$$

The structure of Eq. (2.6) shows that, in the dipole gauge, the Hamiltonian can be interpreted as if the minimal coupling replacement were applied directly to the photonic operators, *i.e.* $\hat{a} \to \hat{a} + iqA_0\hat{x}/\hbar$. This contrasts with the Coulomb gauge, where the minimal coupling substitution instead is performed on the anharmonic subsystem, *i.e.* on the matter operators. The last term in Eq. (2.6) is the so-called *self-polarization* P^2 term, which, similarly to the diamagnetic term in the Coulomb gauge, plays a crucial role in ensuring the stability of the system. We notice that the unitary transformation in Eq. (2.2) does not change the spectrum of the Hamiltonian. Therefore, the Hamiltonians in Eqs. (2.3) and (2.6) are equivalent and lead to the same physical predictions. However, this equivalence is lost when performing the two-level truncation, as we will see in the following.

As discussed at the beginning of this section, the two-level truncation can be carried out either before or after applying the minimal coupling substitution via the unitary transformation $\hat{U}$. Moreover, if the minimal coupling is performed first, the truncation itself may be carried out with respect to different states. In particular, three distinct procedures can be identified for deriving a dipole-gauge QRM, each yielding a different effective Hamiltonian:

- **Truncation before the minimal coupling replacement:** The two-level truncation is performed directly on the matter operators, *i.e.* directly replacing the matter operators with their two-level counterparts, such as $\hat{x} \to$

$x_{10}\hat{\sigma}_x$. This implies that the unitary transformation $\hat{U}$ must also be truncated consistently, *i.e.*

$$\hat{U} \to \hat{\mathcal{U}} = \exp\left(i\,\frac{qA_0x_{10}}{\hbar}\hat{\sigma}_x(\hat{a}+\hat{a}^\dagger)\right) = \exp\left(i\,\frac{g_{10}^{\mathrm{D}}}{\omega_c}\hat{\sigma}_x(\hat{a}+\hat{a}^\dagger)\right)\,, \tag{2.7}$$

where $g_{jk}^{\mathrm{D}} = \omega_c qA_0 \langle j|\hat{x}|k\rangle/\hbar$ are the coupling strengths in the dipole gauge, as it will be clear shortly. With this procedure, the last term of Eq. (2.6) becomes proportional to the identity operator, as $\hat{x}^2 \to x_{10}^2\hat{\sigma}_x^2 = x_{10}^2\hat{I}$, and can be thus neglected. Specifically, the resulting Hamiltonian reads

$$\begin{aligned}\hat{\mathcal{H}}_{\mathrm{D}}^{(1)} &= \hat{\mathcal{U}}^\dagger\hat{H}_{\mathrm{ph}}\hat{\mathcal{U}} + \hat{\mathcal{H}}_{\mathrm{mat}}\\ &= \hbar\omega_c\hat{a}^\dagger\hat{a} + \frac{\hbar\omega_{10}}{2}\hat{\sigma}_z - i\hbar g_{10}^{\mathrm{D}}(\hat{a}-\hat{a}^\dagger)\hat{\sigma}_x\,,\end{aligned} \tag{2.8}$$

where $\hat{\mathcal{H}}_{\mathrm{mat}} = \hat{\mathcal{P}}\hat{H}_{\mathrm{mat}}\hat{\mathcal{P}} = (\hbar\omega_{10}/2)\,\hat{\sigma}_z$ is the truncated matter Hamiltonian, as in Eq. (1.13). But why should we consider this approach in which the truncation is performed before the minimal coupling replacement? The answer lies in the fact that the resulting Hamiltonian in Eq. (2.8) has been widely employed in the literature, especially in the context of cavity QED, as it represents the simplest and historically most common form of the QRM (up to a unitary transformation $\hat{a} \to i\hat{a}$). Moreover, as mentioned above, this procedure is consistent with lattice gauge principles [77]. Following this philosophy, the Coulomb-gauge QRM Hamiltonian can be obtained by applying the unitary transformation $\hat{\mathcal{U}}$ to the truncated matter Hamiltonian, thus performing the minimal coupling replacement directly in the truncated Hilbert space, *i.e.* $\hat{\mathcal{H}}_{\mathrm{C}}^{(1)} = \hat{\mathcal{U}}\hat{\mathcal{H}}_{\mathrm{mat}}\hat{\mathcal{U}}^\dagger + \hat{H}_{\mathrm{ph}}$, as shown in Ref. [77]. Although this formulation has the important advantage of ensuring gauge invariance, it turns out to yield less accurate predictions in the USC regime compared to the other approaches.

- **Truncation after the minimal coupling replacement:** The two-level truncation is performed after applying the unitary transformation $\hat{U}$, which has led to the Hamiltonian in Eq. (2.6). Thus, the resulting dipole-gauge QRM Hamiltonian reads

$$\begin{aligned}\hat{\mathcal{H}}_{\mathrm{D}}^{(2)} &= \hat{\mathcal{P}}\hat{H}_{\mathrm{D}}\hat{\mathcal{P}}\\ &= \hbar\omega_c\hat{a}^\dagger\hat{a} + \frac{\hbar\omega_{10}}{2}\hat{\sigma}_z - i\hbar g_{10}^{\mathrm{D}}(\hat{a}-\hat{a}^\dagger)\hat{\sigma}_x + \frac{\hbar(G_{11}-G_{00})}{2\omega_c}\hat{\sigma}_z\\ &= \hbar\omega_c\hat{a}^\dagger\hat{a} + \frac{\hbar\bar{\omega}_{10}}{2}\hat{\sigma}_z - i\hbar g_{10}^{\mathrm{D}}(\hat{a}-\hat{a}^\dagger)\hat{\sigma}_x\,,\end{aligned} \tag{2.9}$$

where $G_{jk} = \sum_l g_{jl} g_{lk} \equiv \omega_c^2 q^2 A_0^2 \langle j|\hat{x}^2|k\rangle /\hbar^2$, and the renormalized frequency $\bar{\omega}_{10} = \omega_{10} + (G_{11} - G_{00})/\omega_c$. We point out that the truncation has been carried out with respect to the bare states of the matter Hamiltonian. The last term in Eq. (2.8), containing the parameters G_{jk}, arises from the projection of the self-polarization term onto the two-dimensional subspace, as $\hat{\mathcal{P}}\hat{x}^2\hat{\mathcal{P}} \neq (\hat{\mathcal{P}}\hat{x}\hat{\mathcal{P}})^2$. Due to the parity of the potential describing the electriv dipole selection rules (no transition can occur between orbitals of the same parity), it follows that $\langle 0|\hat{x}|0\rangle = \langle 1|\hat{x}|1\rangle = 0$, and thus $\hat{\mathcal{P}}\hat{x}\hat{\mathcal{P}} = x_{10}\hat{\sigma}_x$. Therefore, by construction, this implies that only the elements having the same parity contribute to the $\hat{x}^2$ matrix elements, leading to $\hat{\mathcal{P}}\hat{x}^2\hat{\mathcal{P}} \propto \hat{\sigma}_z$. This approach is the most consistent with the phylosophy of two-level truncation, as it takes into account the effects of the self-polarization term. Furthermore, it has been demonstrated that this approach leads to more accurate predictions in the USC regime compared to the other methods [88].

- **Truncation with respect to dressed states:** The two-level truncation is still performed after the application of the unitary transformation $\hat{U}$, but on the dressed states of the matter system, which are obtained by diagonalizing the matter Hamiltonian with the inclusion of the self-polarization term. Specifically, we first define the effective potential $V_{\text{eff}}(x) = V(x) + \omega_c q^2 A_0^2/\hbar x^2$, which includes the effects of the self-polarization term directly into the potential. We then diagonalize the effective matter Hamiltonian $\hat{H}_{\text{mat}}^{\text{eff}} = \hat{p}^2/2m + V_{\text{eff}}(\hat{x})$ to obtain the dressed states $|j'\rangle$ and corresponding energies $\hbar\omega_j'$. Finally, we perform the two-level truncation by projecting the Hamiltonian in Eq. (2.6) onto the subspace spanned by the two lowest dressed states, *i.e.* by applying the projection operator $\hat{\mathcal{P}}' = |0'\rangle\langle 0'| + |1'\rangle\langle 1'|$. The resulting Hamiltonian reads

$$\hat{\mathcal{H}}_{\text{D}}^{(3)} = \hat{\mathcal{P}}'\hat{H}_{\text{D}}\hat{\mathcal{P}}' = \hbar\omega_c\hat{a}^\dagger\hat{a} + \frac{\hbar\omega_{10}'}{2}\hat{\sigma}_z' - i\hbar g_{10}'^{\text{D}}(\hat{a} - \hat{a}^\dagger)\hat{\sigma}_x' \,, \tag{2.10}$$

  where $\omega_{10}' = \omega_1' - \omega_0'$, $g_{jk}'^{\text{D}} = \omega_c q A_0 \langle j'|\hat{x}|k'\rangle /\hbar$, and $\hat{\sigma}_x'$ and $\hat{\sigma}_z'$ are the Pauli operators acting on the dressed states. This approach, although leading to more accurate results compared to the first method, it has been demonstrated to perform worstly than the second if the two bare frequencies are detuned [88].

The three different procedures for deriving a dipole-gauge QRM lead to different Hamiltonians, which, by construction, are not equivalent. Furthermore, it has been demonstrated that the second approach leads to more accurate predictions in the USC regime compared to the other two, especially if the two bare frequencies are detuned [88]. Nontheless, each of these Hamiltonians performs better than the Coulomb-gauge QRM in Eq. (2.4), which, as stated above, leads to inaccurate predictions much faster than the dipole-gauge ones as the coupling strength increases [76, 87]. This discrepancy arises because the interaction term in the Coulomb-gauge light-matter Hamiltonian in Eq. (2.1) depends on the momentum operator $\hat{p}$, whereas in the dipole gauge in Eq. (2.6), it depends on the position operator $\hat{x}$. Since the matrix elements of $\hat{p}$ grow significantly faster than those of $\hat{x}$ increasing the system's nonlinearity, as given by the relation $\langle j|\hat{p}|k\rangle = im\omega_{jk}\langle j|\hat{x}|k\rangle$, the Coulomb gauge is less suitable to perform accurate truncation in the non-perturbative regime $g \gtrsim 0.1$ [76]. This analysis is consistent with Refs. [77, 87], which attributed the poorer accuracy in the Coulomb gauge to the non-locality of the truncated potential.

2.1.2 Symmetry-breaking quantum Rabi Hamiltonian

In the previous section, we have introduced the QRM Hamiltonians in both the Coulomb and dipole gauges, derived by considering a symmetric double-well potential modeling the electric dipole. However, especially in the context of circuit QED, it is common to consider asymmetric potentials, leading to additional terms in the quantum Rabi Hamiltonians which break the $\mathbb{Z}_2$ symmetry of the models. Indeed, when asymmetries are present in the potential, both the position and momentum operators acquire non-zero matrix elements between states of the same parity. This stands in contrast to the symmetric case of cavity QED, where such matrix elements vanish due to parity selection rules.

Let us consider a simple example which is widely employed in circuit QED, namely a single-junction fluxonium qubit [94–97], as shown in Fig. 2.1. Such circuital element is composed by a Cooper-pair box, with a Josephson junction with energy E_J and a capacitance C_J, shunted by a large inductance L. The fluxonium qubit can be modeled as a particle of mass C_J moving in a potential given by the sum of a cosine potential, arising from the Josephson junction, and a parabolic potential, arising from the inductive shunt. The external flux $\phi_{\rm ex}$ threading the loop formed by the inductance and the Josephson junction allows to tune the asymmetry of the potential. The Hamiltonian of this system can be formally derived by applying the circuit quantization rules [94, 95], where the flux at the node $\hat{\phi}$ and the corresponding charge $\hat{Q}$ are the conjugate variables, *i.e.* $[\hat{\phi}, \hat{Q}] = i\hbar$. This choice corresponds to the so-called *flux gauge*. The resulting Hamiltonian reads

$$\hat{H}_{\rm flux} = \frac{\hat{Q}^2}{2C_J} + \frac{\hat{\phi}^2}{2L} - E_J \cos\left(\frac{\hat{\phi} - \phi_{\rm ex}}{\phi_0}\right), \tag{2.11}$$

where $\phi_0 = \hbar/2e$ is the reduced superconducting flux quantum. As it can be easily observed, for $\phi_{\rm ex}/\phi_0 = k\pi$ (with $k \in \mathbb{Z}$), the potential is symmetric, whereas

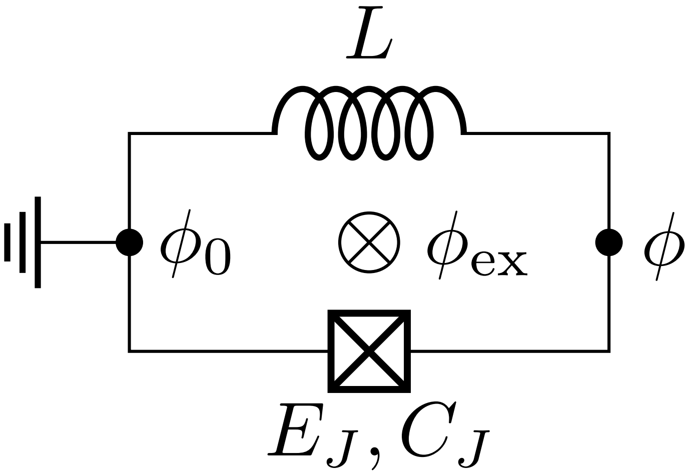

Figure 2.1: Schematic representation of single-junction fluxonium qubit, composed by an inductively shunted Cooper-pair box with an applied external flux ϕ_{ex}. The Josephson junction has energy E_J and capacitance C_J. The groung node ϕ_0 is chosen as the reference point for the electric potential.

for $\phi_{\text{ex}}/\phi_0 \neq k\pi$, it becomes asymmetric. The eigenstates of the fluxonium qubit can be obtained by numerically diagonalizing the Hamiltonian in Eq. (2.11). It is customary to express this Hamiltonian in the basis of two states with persistent supercurrents flowing in opposite directions (clockwise and counterclockwise) around the qubit loop, $|L\rangle_{\text{q}}$ and $|R\rangle_{\text{q}}$, respectively. This naturally leads to the two-level truncation of the Hamiltonian, resulting in

$$\hat{\mathcal{H}}_{\text{flux}} = -\frac{\hbar}{2}\left(\Delta\hat{\sigma}_x + \epsilon\hat{\sigma}_z\right) , \tag{2.12}$$

where Δ and ϵ are the tunneling amplitude and energy bias between the two persistent-current states, respectively, tunable through the external flux ϕ_{ex}. We note that the Pauli matrices are written with respect to the persisten currents basis chosen, differently from the common convention of cavity QED in which $\hat{\sigma}_x$ is associated to the transition operator. This choice is made to be consistent with the literature on circuit QED. The Hamiltonian in Eq. (2.12) can be easily diagonalized, leading to the eigenstates $|0\rangle$ and $|1\rangle$, which are superpositions of the persistent-current states. The Hamiltonian in Eq. (2.12) can be rewritten in the energy eigenbasis as

$$\hat{\mathcal{H}}_{\text{flux}} = \frac{\hbar\omega_{10}}{2}\hat{\sigma}_z , \tag{2.13}$$

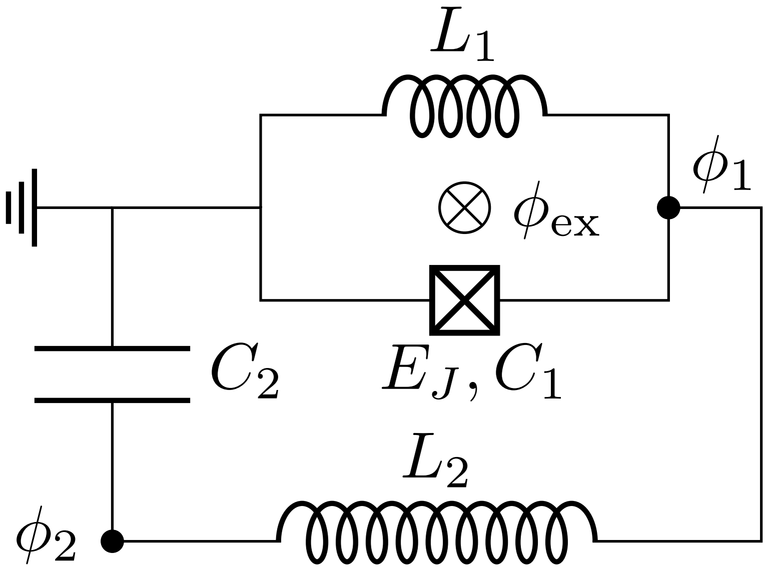

Figure 2.2: Schematic representation of a single-junction fluxonium qubit coupled to an electromagnetic resonator. The coupling can be capacitive (Coulomb gauge) or inductive (multipolar gauge).

where $\omega_{10} = \sqrt{\Delta^2 + \epsilon^2}$ is the transition frequency between the two lowest energy states, and the Pauli operators are now expressed in the new basis of eigenstates. The relation between the two bases is given by a rotation around the y axis of an angle θ defined by $\cos\theta = \epsilon/\omega_{10}$ and $\sin\theta = \Delta/\omega_{10}$.

When the fluxonium qubit is coupled to a single mode of an electromagnetic resonator (see Fig. 2.2), their interaction can be effectively described by the QRM Hamiltonian with additional terms due to the breaking of the $\mathbb{Z}_2$ symmetry of the model. This model will be discussed in more detail in Section 2.3.2, where we will see that the presence of these additional terms has significant implications for the renormalization of the QRM Hamiltonians. Here, we will simply present the resulting Hamiltonian in the full Hilbert space and its truncated version, derived by following analogous procedure as in Section 2.1.1.

The Hamiltonian of the fluxonium qubit coupled to a single-mode electromagnetic resonator, which is modeled as an LC circuit, reads

$$\hat{H}_{\text{fl-res}} = \frac{\hat{Q}_1^2}{2C_1} + \frac{\hat{\phi}_1^2}{2L_1} - E_J \cos\left(\frac{\hat{\phi}_1 - \phi_{\text{ext}}}{\phi_0}\right) + \frac{\hat{Q}_2^2}{2C_2} + \frac{(\hat{\phi}_2 - \hat{\phi}_1)^2}{2L_2}\,, \tag{2.14}$$

where the subscripts 1 and 2 refer to the fluxonium qubit and the resonator variables, respectively. We then perform the two-level truncation by projecting the

Hamiltonian in Eq. (2.14) onto the subspace spanned by the two lowest energy eigenstates of the fluxonium qubit, as done in Eq. (2.13). This is equivalent to applying the projection operator $\hat{\mathcal{P}}$ to the interacting Hamiltonian in the full Hilbert space, *i.e.* $\hat{\mathcal{H}}_{\text{fl-res}} = \hat{\mathcal{P}}\hat{H}_{\text{fl-res}}\hat{\mathcal{P}}$. Such procedure is analogous to the second approach for deriving the dipole-gauge QRM Hamiltonian in Eq. (2.9). The canonical variables of the electromagnetic resonator can be expressed in terms of bosonic operators defined as $\hat{a} = (\omega_c\hat{\phi}_2 + i\hat{Q}_2)/\omega_c\phi_{\text{zpf}}$, where $\omega_c = 1/\sqrt{L_2C_2}$ and $\phi_{\text{zpf}} = \sqrt{\hbar/2C_2\omega_c}$ are the resonator frequency and the zero-point fluctuations of the flux, respectively. The resulting Hamiltonian reads

$$\hat{\mathcal{H}}_{\text{fl-res}} = \hbar\omega_c\hat{a}^\dagger\hat{a} + \hbar\frac{\bar{\omega}_{10}}{2}\hat{\sigma}_z + \hbar\frac{G_{01}}{\omega_c}\hat{\sigma}_x - \hbar\left(\frac{g_{11}-g_{00}}{2}\hat{\sigma}_z + g_{01}\hat{\sigma}_x\right)\left(\hat{a}+\hat{a}^\dagger\right) , \quad (2.15)$$

where $\omega_c = 1/\sqrt{L_2C_2}$ is the resonator frequency, and

$$g_{jk} = \frac{\phi_{\text{zpf}}\phi_{jk}}{\hbar L_2} , \qquad G_{jk} = \frac{\hbar L_2\omega_c}{2\phi_{\text{zpf}}^2}\sum_l g_{jl}g_{lk} = \frac{\omega_c}{2\hbar L_2}\Phi_{jk} , \quad (2.16)$$

with $\phi_{ij} = \langle i|\,\hat{\phi}_1\,|j\rangle$ and $\Phi_{ij} = \langle i|\,\hat{\phi}_1^2\,|j\rangle = \sum_k \phi_{ik}\phi_{kj}$. The renormalized qubit frequency is given, as above, by $\bar{\omega}_{10} = \omega_{10} + (G_{11} - G_{00})/\omega_c$. We point out that in Eq. (2.15) some higher-order terms have been neglected, as it is customary in the literature [98, 99]. However, these terms can be included straightforwardly if needed, as discussed in Section 2.3.2. The third term, proportional to $\hat{\sigma}_x$, arises from the projection of the $\hat{\phi}_1^2$ term onto the two-dimensional subspace, analogously to the self-polarization term in the dipole-gauge QRM in Eq. (2.9). In many works and experimental realizations, this term is neglected due to its smallness compared to the other terms. We observe that the interaction Hamiltonian contains an additional term proportional to $\hat{\sigma}_z$ compared to Eq. (2.34), which arises from the non-zero diagonal matrix elements of the flux operator due to the asymmetry of the potential, as discussed above.

The Hamiltonian in Eq. (2.15) has been used in a wide range of theoretical and experimental works in the context of circuit QED [97–101], where it has been used to describe the interaction between a fluxonium or flux qubit and a single mode of an electromagnetic resonator in the USC regime, both theoretically and experimentally.

2.2 Spectral properties of the quantum Rabi model in the USC regime

In this section, we discuss the coherent and incoherent emission spectra of the QRM Hamiltonians in both cavity and circuit QED. In order to allow the measurement

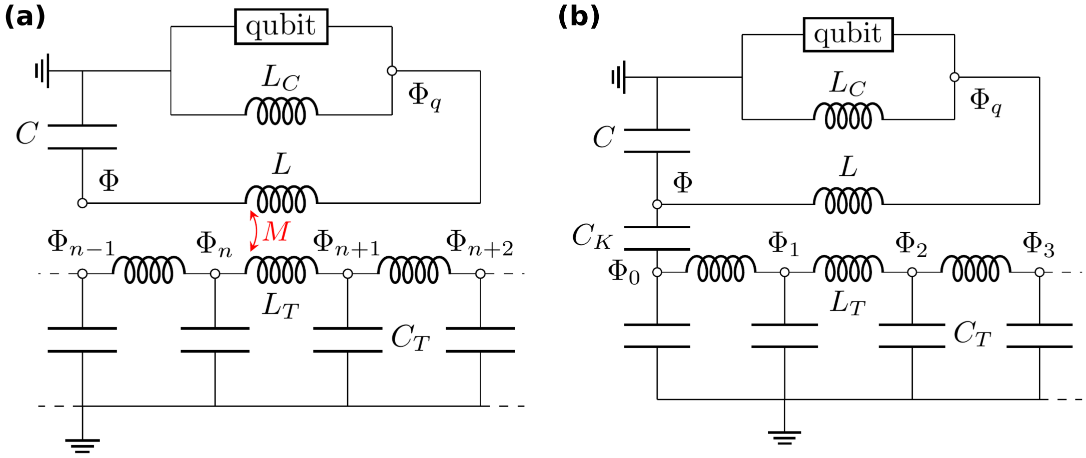

Figure 2.3: **(a,b)** Schematic representation of a flux qubit galvanically coupled to an electromagnetic resonator, which is in turn coupled to an external transmission line (TL). The coupling between the resonator and the TL can either be (a) mutual inductive or (b) capacitive.

of these spectra experimentally, the system must be coupled to an external environment, which is typically modeled as a thermal bath of harmonic oscillators. We will show that the form of the coupling between the circuit Hamiltonians and the environment plays a crucial role, giving rise to distinct spectral features. These differences become particularly pronounced in the USC and DSC regimes. The discussion presented here is based on the results of Ref [3], where detailed derivations and a thorough analysis of the various coupling mechanisms and their impact on the emission spectra can be found.

Let us consider a flux qubit [102] galvanically coupled to an electromagnetic resonator [98–100, 103–106], as in the system described in Section 2.1.2. To enable the measurement of emission spectra, the resonator is further coupled to an external transmission line (TL). This configuration provides significant flexibility, both in tuning the system parameters and in selecting the system-reservoir coupling mechanism. In particular, the coupling between the resonator and the TL can be either inductive or capacitive, as illustrated in Fig. 2.3. In the following, we will analyze how these two distinct coupling mechanisms influence the emission spectra of the system, and we will highlight their similarities and differences with a typical cavity QED scenario.

As discussed above, the Hamiltonian of the flux qubit coupled to a single-mode electromagnetic resonator can be described by the QRM Hamiltonian supplemented with additional terms arising from the breaking of the $\mathbb{Z}_2$ symmetry.

In the qubit eigenbasis, and after expading the electromagnetic resonator in terms of bosonic operators, the resulting two-level Hamiltonian takes a form analogous to the one in Eq. (2.15). For convenience, we rewrite it here in a more compact notation, neglecting the self-polarization term and adopting natural units ($\hbar = 1$):

$$\hat{\mathcal{H}}_{\text{fl-res}} = \omega_r \hat{a}^\dagger \hat{a} + \frac{\omega_0}{2}\hat{\sigma}_z + \omega_r \eta\, \tilde{\hat{\sigma}}_x \left(\hat{a} + \hat{a}^\dagger\right) , \tag{2.17}$$

where $\omega_r \approx 1/\sqrt{(L_C + L)C}$ and $\omega_0 = \sqrt{\Delta^2 + \epsilon^2}$ are the resonator (renormalized by the coupler L_C) and qubit (see Eq. (2.13)) frequencies, respectively. The parameter $\eta = L_C I_p \Phi_{\text{zpf}}/L\omega_r$ is the normalized coupling strength, with I_p being the persistent critical current flowing in the qubit loop. For the sake of compactness, we defined $\tilde{\hat{\sigma}}_x = \cos\theta \hat{\sigma}_x + \sin\theta \hat{\sigma}_z$, with $\cos\theta = \epsilon/\omega_0$ and $\sin\theta = \Delta/\omega_0$. It is worth stressing that whatever variation of the applied flux, which is proportional to ϵ, would modify the resonance frequency ω_r of the LC circuit, and, as a consequence, both the zero-point fluctuations Φ_{zpf} and the normalized coupling η. However, in this theoretical framework, ω_r and Φ_{zpf} are assumed to be independent from ϵ. A thorough analysis of this aspect can be found in Refs. [99, 107].

We now consider the coupling between this system and an external TL, which can be either inductive or capacitive. In the first case (see Fig. 2.3a), where the coupling is realized through a mutual inductance M, the total Hamiltonian reads

$$\hat{\mathcal{H}}_{\text{M}} = \hat{\mathcal{H}}_{\text{fl-res}} + \hat{\mathcal{H}}_{\text{TL}} + \hat{\mathcal{V}}_{\text{M}} , \tag{2.18}$$

where $\hat{\mathcal{H}}_{\text{fl-res}}$ is given in Eq. (2.17) and

$$\hat{\mathcal{H}}_{\text{TL}} = \int_0^\infty \omega \hat{b}^\dagger_\omega \hat{b}_\omega \, d\omega \tag{2.19}$$

is the Hamiltonian of the TL, modeled as an infinite bath of harmonic oscillators with bosonic operators $\hat{b}_\omega$ and $\hat{b}^\dagger_\omega$, satisfying the commutation relation $[\hat{b}_\omega, \hat{b}^\dagger_{\omega'}] = \delta(\omega - \omega')$. The mutual interaction term between the resonator and the TL reads

$$\hat{\mathcal{V}}_{\text{M}} = i\hat{X}_M \int_0^\infty g(\omega) \left(\hat{b}^\dagger_\omega - \hat{b}_\omega\right) d\omega , \tag{2.20}$$

where $\hat{X}_M = \hat{\Phi}_L/\Phi_{\text{zpf}} = \hat{a} + \hat{a}^\dagger - 2\eta\tilde{\hat{\sigma}}_x$ is the system operator coupling the system with the TL, being $\hat{\Phi}_L = \hat{\Phi} - \hat{\Phi}_q$ the flux operator across the inductor of the resonator. $g(\omega) = \sqrt{\gamma_r \omega / 2\pi\omega_r}$ represents the coupling strength between the resonator and the mode of frequency ω of the TL.[1]

---

[1] The infinite transmission line can be modeled as a lumped element circuit composed by an infinite series of LC circuits, and, subsequently, the continuum limit of this configuration can be implemented by increasing the number of sites to the infinity while reducing their mutual distance. In this framework, the damping rate can be expressed as $\sqrt{\gamma_r/2\pi} = \alpha\Phi_{\text{zpf}}\Lambda\sqrt{\omega_r}/v_0$, where $\Lambda = \sqrt{Z_0}/4\pi$ (Z_0 is the TL impedance) and $\alpha = M/Ll_T$. $v_0 = 1/\sqrt{l_T c_T}$ is the propagation velocity of the light in the TL, with $l_T = L_T/\Delta x$ and $c_T = C_T/\Delta x$ being the inductance and capacitance per unit length, respectively, with Δx being the distance between two sites.

In the second case (see Fig. 2.3b), where the coupling is realized through a capacitance C_K, the total Hamiltonian $\hat{\mathcal{H}}_{\mathrm{C}}$ has similiar form as in Eq. (2.18), but in this case the interaction term between the resonator and the TL reads

$$\hat{\mathcal{V}}_{\mathrm{C}} = i\hat{X}_C \int_0^{\infty} g(\omega)\left(\hat{b}^{\dagger}_{\omega} - \hat{b}_{\omega}\right) d\omega\,, \tag{2.21}$$

where the system operator coupling the system with the TL is now $\hat{X}_C = i(\hat{a}-\hat{a}^{\dagger})$, and $g(\omega)$ is defined as above.[2] Furthermore, it can be demostrated that the input-output relations for the two different coupling mechanisms, mutual inductive and capacitive, respectively, read

$$\hat{V}^{\pm}_{M,\mathrm{out}}(x,t) = \hat{V}^{\pm}_{\mathrm{in}}(x,t) - \frac{M}{2L}\,\dot{\hat{\Phi}}^{\pm}_{L}(x,t), \tag{2.22a}$$

$$\hat{V}^{\pm}_{C,\mathrm{out}}\left(t - \frac{x}{v_0}\right) = \hat{V}^{\pm}_{\mathrm{in}}\left(t + \frac{x}{v_0}\right) + Z_0\frac{C_K}{C}\,\dot{\hat{Q}}^{\pm}\left(t - \frac{x}{v_0}\right). \tag{2.22b}$$

The superscripts ± denote the positive and negative frequency components of the voltage operator $\hat{V}(x,t)$.

The difference in the system operator $\hat{X}$ coupling the system with the TL, and consequently the input-output relations in Eqs. (2.22) above, has significant implications for the emission spectra of the system, especially in the USC and DSC regimes, as we will see shortly. Detailed derivations of the previous Hamiltonians and input-output relations can be found in Ref. [3].

For completeness, we also consider the case of a cavity QED system, composed by a two-level atom coupled to a single mode of an electromagnetic resonator, which is in turn coupled to an external reservoir. In this case, a similar analysis can be performed, where the coupling operator $\hat{X}$ corresponds to the electric field, whose representation depends on the gauge choice. Specifically, in the Coulomb gauge, the system operator coupling the system with the reservoir is $\hat{X}_{\mathrm{Coul}} = i(\hat{a}-\hat{a}^{\dagger})$, whereas in the dipole gauge, it is $\hat{X}_D = \hat{a}+\hat{a}^{\dagger} - 2\eta\hat{\sigma}_x$, where $\eta = g/\omega_c$ is the normalized coupling strength, with g being the coupling strength between the atom and the resonator.

2.2.1 Incoherent emission spectra

In this section, we will focus on the incoherent emission spectra of the system, which can be calculated by considering the coupling between the system and the external TL. In particular, we will consider incoherent thermal-like excitation of the qubit, in absence of any coherent drive on the system, $\left\langle \hat{V}^{\pm}_{\mathrm{in}} \right\rangle = 0$. Therefore,

---

[2] In this case, namely a semi-infinite TL coupled capacitively, the damping rate can be expressed as $\sqrt{\gamma_r} = C_K\omega_r/\sqrt{v_0 c_T C}$.

the voltage measured at the output of the TL will be solely determined by the system operator (see Eqs. (2.22)), namely

$$\dot{\hat{\Phi}} \propto \dot{\hat{X}}_M = i\left(\hat{a}^\dagger - \hat{a}\right) - 2\eta\frac{\omega_0}{\omega_r}\sin\theta\hat{\sigma}_y\,, \tag{2.23a}$$

$$\dot{\hat{Q}} \propto \dot{\hat{X}}_C = -\left(\hat{a} + \hat{a}^\dagger + 2\eta\hat{\tilde{\sigma}}_x\right)\,, \tag{2.23b}$$

in the inductive and capacitive coupling cases, respectively.

The dynamics of the system can be described by the use of a generalized master equation [85], which is suitable for the USC regime. Specifically, the master equation for the density matrix $\hat{\rho}(t)$ of the system reads

$$\dot{\hat{\rho}} = -i\left[\hat{\mathcal{H}}_{\text{fl-res}}, \hat{\rho}\right] + \mathcal{L}_{\text{GME}}\hat{\rho}\,, \tag{2.24}$$

where $\hat{\mathcal{H}}_{\text{fl-res}}$ is given in Eq. (2.17), and $\mathcal{L}_{\text{GME}}$ is the Liouvillian superoperator, which takes into account the dissipation and decoherence processes of the system or eventual additional dissipation channels. The explicit form of $\mathcal{L}_{\text{GME}}$ can be found in Refs. [3, 85]. We assume that the interaction between the qubit and its reservoir occurs through the operator $\hat{\tilde{\sigma}}_x$, for both the inductive and capacitive coupling cases.

Once the steady-state density matrix $\hat{\rho}_{\text{ss}}$ is obtained by solving (numerically) the master equation in Eq. (2.24), the power spectrum can be calculated as the Fourier transform of the two-time correlation function of the output field operator $\hat{X}$, as given by the Wiener-Khinchin theorem [108, 109]. The system operator $\hat{X}$ is given by $\hat{X}_M$, $\hat{X}_C$, or $\hat{X}_D$, in the case of inductive and capacitive coupling in circuit QED and dipole gauge in cavity QED, respectively. We point out that in the cavity QED case, given the gauge invariance of the physical observables (specifically, of the electric field), the emission spectrum must be the same independently from the gauge choice if the observables are correctly considered [81]. Therefore, we will only present the results for the dipole gauge.

The power spectrum reads [28, 29, 83, 110, 111]

$$S(\omega) = \frac{1}{2\pi}\int_{-\infty}^{\infty} d\tau\, e^{i\omega\tau}\langle\dot{\hat{X}}^-(t)\dot{\hat{X}}^+(t+\tau)\rangle_{\text{ss}}\,, \tag{2.25}$$

where $\langle\cdots\rangle_{\text{ss}} = \text{Tr}\left\{\hat{\rho}_{\text{ss}}(\cdots)\right\}$, and $\hat{X}^+$ ($\hat{X}^-$) is the positive (negative) frequency component of the operator $\hat{X}$, which can be obtained by expressing $\hat{X}$ in the basis of the eigenstates of the system Hamiltonian $\hat{\mathcal{H}}_{\text{fl-res}}$ and retaining only the terms which lower (raise) the energy of the system [82, 112]. Namely, if we denote the eigenstates and eigenvalues of the system Hamiltonian as $|j\rangle$ and ω_j, respectively, such that $\hat{\mathcal{H}}_{\text{fl-res}} \left| j \right\rangle = \omega_j \left| j \right\rangle$, then the positive frequency component of the operator $\hat{X}$ reads

$$\hat{X}^+ = \sum_{j,k>j} X_{jk} \left| j \right\rangle\!\left\langle k \right| \,, \tag{2.26}$$

where $X_{jk} = \left\langle j \right| \hat{X} \left| k \right\rangle$ are the matrix elements of the operator $\hat{X}$ in the eigenbasis of the system Hamiltonian. The negative frequency component $\hat{X}^-$ is simply given by the Hermitian conjugate of $\hat{X}^+$. The two-time correlation function in Eq. (2.25) can be calculated by using the quantum regression theorem [83, 110, 111], which allows to express it in terms of single-time expectation values. Moreover, we point out that the power spectrum in Eq. (2.25) is calculated in the steady-state regime, thus the time shifts and spatial dependence in the input-output relations in Eqs. (2.22) can be neglected. An explicit calculation of the emission spectrum in Eq. (2.25) shows that it depends on the transition matrix elements of the operator $\hat{X}$, *i.e.*

$$S(\omega) \propto \sum_{j \neq k} |\dot{X}_{jk}|^2 \, \rho_{\text{ss},kk} \, \frac{\lambda_{jk}^{(R)}}{\left(\omega - \lambda_{jk}^{(I)}\right)^2 + \left(\lambda_{jk}^{(R)}\right)^2} \,, \tag{2.27}$$

where $\lambda_{jk}^{(R)}$ and $\lambda_{jk}^{(I)}$ are the real and imaginary parts of the eigenvalues of the Liouvillian superoperator $\mathcal{L}_{\text{GME}}$, respectively, and $\rho_{\text{ss},kk} = \left\langle k \right| \hat{\rho}_{\text{ss}} \left| k \right\rangle$ is the steady-state population of the state $\left| k \right\rangle$. Eq. (2.27) can be interpreted as a sum of Lorentzian profiles spanning all the possible transitions between the eigenstates of the system Hamiltonian, weighted by the corresponding transition matrix elements and steady-state populations.

The incoherent emission spectra presented in this section are calculated numerically by assuming a finite effective temperature for the qubit reservoir, $T_q/\omega_r \neq 0$ (in natural units, $k_B = 1$), while the photonic reservoir is assumed to be at zero temperature, $T_r = 0$. The numerical simulations are performed by using *QuantumToolbox.jl* [113], which is a Julia package designed for quantum physics simulations, closely emulating the popular Python QuTiP package [114, 115].

The system incoherent excitation through the qubit reservoir is able to populate the low energy excited states of the system $\left| \tilde{n}_\pm \right\rangle$, which in turn decay towards the lower energy states. In the QRM, beyond the strong-coupling regime, the eigenstates do not exhibit the simple structure of the Jaynes-Cummings (JC) model. Therefore, we use a generalized notation for these states by introducing a tilde [83, 84]. In particular, the system energy states are labeled so that in the small η limit $\left| \tilde{n}_\pm \right\rangle$ coincides with the corresponding JC state $\left| n_\pm \right\rangle$.

Fig. 2.4(a,b) present the resulting emission steady-state spectra as a function of the system coupling rate η. Specifically, Fig. 2.4(a) shows the case of capacitive coupling with the TL, as given in Eq. (2.21), while Fig. 2.4(b) displays the

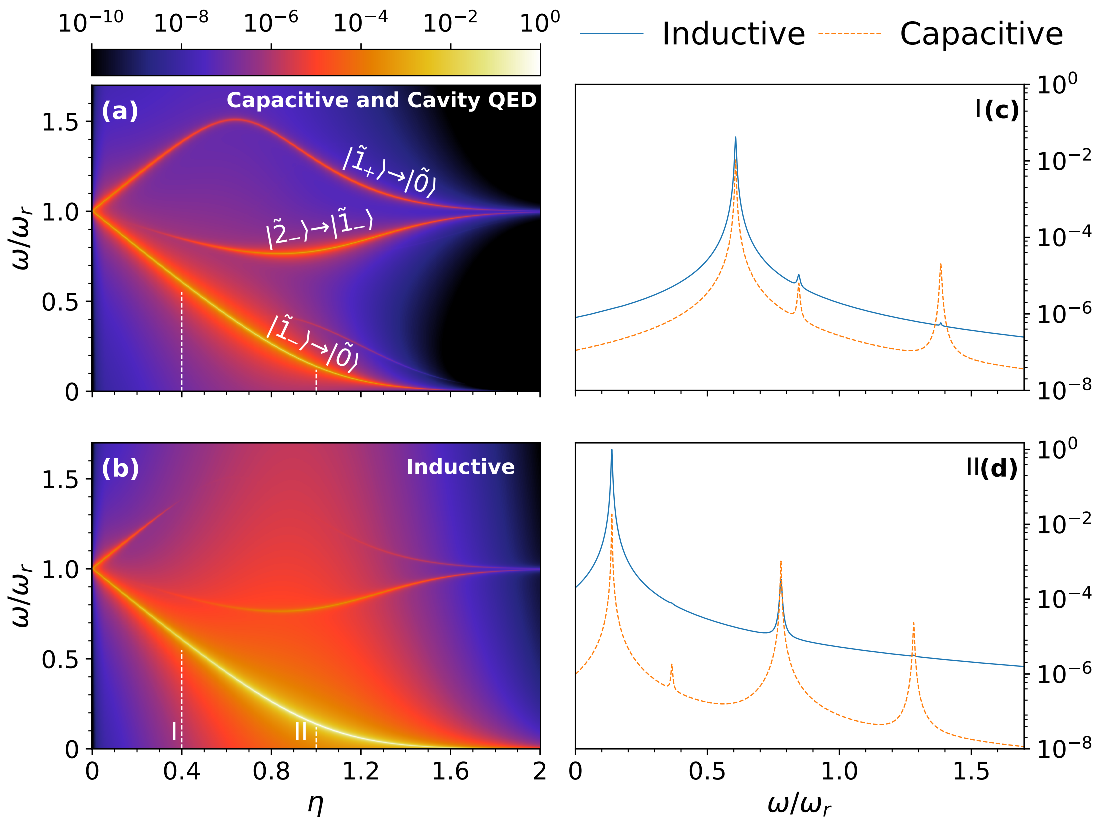

Figure 2.4: Logarithmic emission spectra obtained for $T_q/\omega_r = 0.1$, $\Delta/\omega_r = 1$, $\epsilon = 0$, and $\gamma_q/\Delta = 10 \cdot \gamma_r/\omega_r = 10^{-2}$. **(a,b)** Logarithmic spectra as a function of η at the steady state $\hat{\rho}_{ss}$ for (a) the system capacitively coupled to the TL (coinciding with the spectra in the cavity QED case) and (b) for the mutual inductive coupling. The spectra are normalized with respect to the absolute maximum value. **(c,d)** Vertical cuts of the colormaps for (c) $\eta = 0.4$ and (d) $\eta = 1$.

spectra obtained for the inductive coupling with the input-output TL, given in Eq. (2.20). Both panels clearly highlight (in ascending order of frequency) the transitions $|\tilde{1}_-\rangle \to |\tilde{0}\rangle$, $|\tilde{2}_-\rangle \to |\tilde{1}_-\rangle$, and $|\tilde{1}_+\rangle \to |\tilde{0}\rangle$. As expected, the $|\tilde{1}_-\rangle \to |\tilde{0}\rangle$ transition line, corresponding to the transition from the lower ibridazed state of one excitation (at $\eta = 0$) to the ground state, is the most intense for any values of η at such low effective temperature, being the lowest energy transition allowed in the system. The other transitions tend to become brighter at increasing coupling strength, until the light-matter decoupling occurs in the DSC limit [55, 56, 116]. Figures 2.4(c) and (d) display the spectra obtained fixing specific values of the normalized coupling, namely $\eta = 0.4$ and $\eta = 1$, respectively. We observe that the

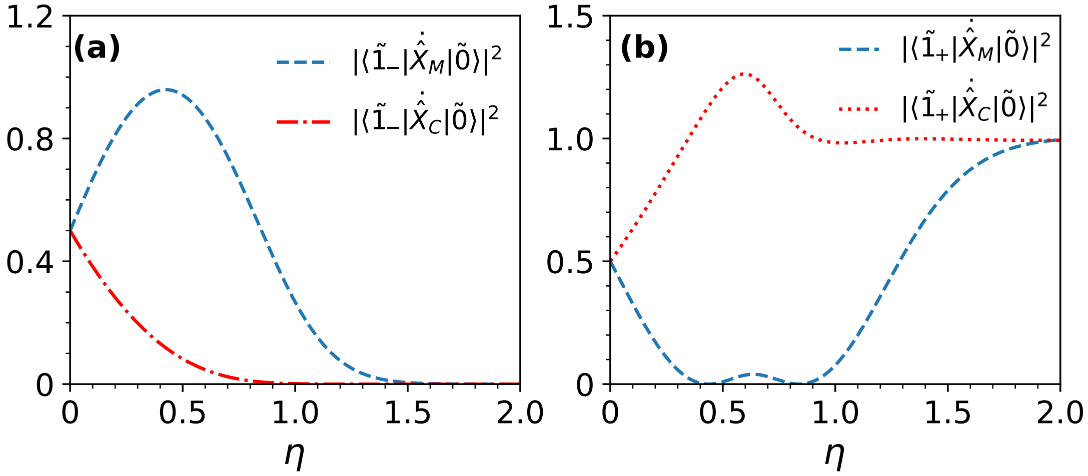

Figure 2.5: **(a,b)** Squared modulus of two transition matrix elements as a function of η, for the trasitions (a) $|\tilde{1}_-\rangle \to |\tilde{0}\rangle$ and (b) $|\tilde{1}_+\rangle \to |\tilde{0}\rangle$. For $\epsilon = 0$, the operator associated with the electric field in the dipole gauge has the same expression as $\dot{\hat{X}}_C$, up to a phase rotation. Consequently, the matrix elements of $\hat{X}_D$ coincide with those of $\dot{\hat{X}}_C$ (red curves). This observation is crucial in explaining why the emission spectra of the capacitive coupling scheme match those of the cavity QED model in Fig. 2.4(a). The parameters used for the calculations are the same as in Fig. 2.4.

mutual inductive spectra exhibit a quenching of the $|\tilde{1}_+\rangle \to |\tilde{0}\rangle$ spectral line when the coupling ranges roughly from 0.4 to 1, as visible in Fig. 2.4(b). This different behaviour between the two spectra is determined by the matrix elements of the corresponding system observables coupled to the output channels, as expressed in Eq. (2.27).

Figure 2.5 shows the squared modulus of the system matrix elements determining the output emission associated to the transitions $|\tilde{1}_-\rangle \to |\tilde{0}\rangle$ and $|\tilde{1}_+\rangle \to |\tilde{0}\rangle$, as a function of the normalized coupling strength η. These matrix elements explain the behavior observed above, namely the quenching of the $(\tilde{1}_+, \tilde{0})$ spectral line in the mutual inductive coupling case, as validated by the vanishing of the matrix element $\left|\langle\tilde{1}_+|\, \dot{\hat{X}}_M \,|\tilde{0}\rangle\right|^2$ in Fig. 2.5(b) approximately in the range $0.4 \lesssim \eta \lesssim 1$.

The results presented above are clear evidence how the calculated spectra are influenced by the observable coupled to the output port. This influence, however, becomes evident only in the USC or DSC regime. It is also interesting to compare these findings for circuit QED systems (for zero flux offset, $\epsilon = 0$) with the corresponding spectra for a cavity QED model. Specifically, we consider an atom

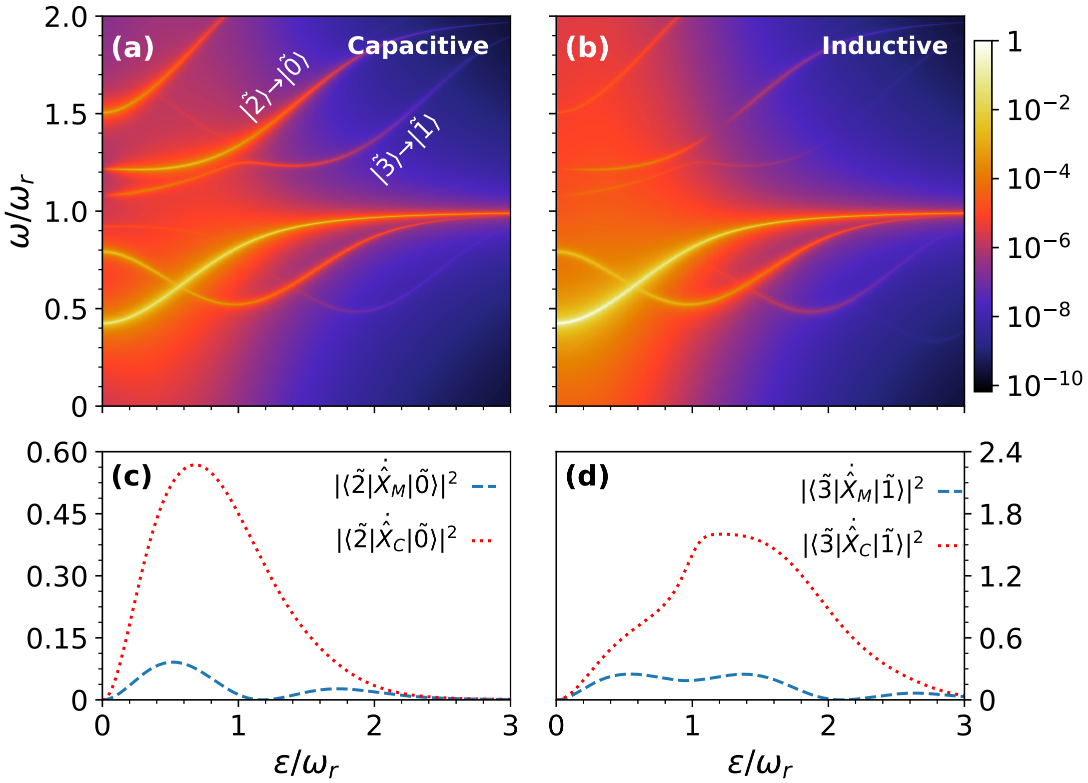

Figure 2.6: Logarithmic emission spectra obtained for $T_q/\omega_r = 0.15$, $\Delta/\omega_r = 1$, $\eta = 0.6$, and $\gamma_q/\Delta = 10 \cdot \gamma_r/\omega_r = 10^{-2}$. **(a,b)** Logarithmic spectra as a function of the flux offset ϵ at the steady state $\hat{\rho}_{ss}$ for (a) the system capacitively coupled to the TL and (b) for the mutual inductive coupling. The spectra are normalized with respect to the absolute maximum value. **(c,d)** Matrix elements of $\dot{\hat{X}}_C$ and $\dot{\hat{X}}_M$ for the transitions (c) $|\tilde{2}\rangle \to |\tilde{0}\rangle$ and (d) $|\tilde{3}\rangle \to |\tilde{1}\rangle$.

interacting with the cavity field via standard dipolar coupling [36, 37, 81, 83, 87, 117], and where the photodetection rate is proportional to the expectation value of the product of the negative and positive electric-field operators [112]. This implies that the correct observable coupled to the external environment is the electric field operator, which, in the dipole gauge, is given by $\hat{X}_D = \hat{a} + \hat{a}^\dagger - 2\eta\hat{\sigma}_x$. The resulting incoherent emission spectra are also shown in Fig. 2.4(a). Indeed, it turns out that the dipolar cavity QED spectra coincide with the circuit QED ones computed for the capacitive coupling to the output TL. This behavior can be understood by observing that, applying a phase rotation $\hat{a} \to i\hat{a}$ ($\hat{a}^\dagger \to -i\hat{a}^\dagger$) to the cavity QED Hamiltonian and to the electric-field operator $\hat{X}_D$, we obtain the circuit QED

Hamiltonian and the output operator proportional to $\dot{\hat{Q}}$ in Eq. (2.23b). We can interpret this correspondence, noting that the output capacitive coupling carries on the information of the electric field.

For completeness, we also report the incoherent emission spectra obtained for a finite flux offset ($\epsilon \neq 0$), which breaks the parity symmetry of the system Hamiltonian. In particular, in Fig. 2.6 we present incoherent emission spectra as functions of the flux offset ϵ for a fixed normalized coupling strength $\eta = 0.6$. We consider an effective temperature of the qubit $T_q/\omega_r = 0.15$. Note that we have switched the notation of the energy eigenstates from $|\tilde{n}_\pm\rangle$ to $|\tilde{n}\rangle$, labeled in order of increasing energy, as the JC notation cannot be used anymore. For non-zero flux offset, the spectra exhibit additional spectral lines corresponding to transitions that were previously forbidden due to parity conservation. Specifically, we can observe the presence of the $|\tilde{2}\rangle \to |\tilde{0}\rangle$ and $|\tilde{3}\rangle \to |\tilde{1}\rangle$ transitions, which are now allowed due to the broken symmetry. This behavior is illustrated by the matrix elements in Fig. 2.6(c,d), which clearly show that the quantities $\left|\langle\tilde{2}|\,\dot{\hat{X}}_C\,|\tilde{0}\rangle\right|^2$ and $\left|\langle\tilde{3}|\,\dot{\hat{X}}_M\,|\tilde{1}\rangle\right|^2$ vanish for $\epsilon = 0$ and become non-zero as soon as $\epsilon \neq 0$. Moreover, we observe that these matrix elements explain the different intensities of the lines highlighted above in the spectra of Fig. 2.6(a,b). Obviously, in this case, it is meaningless to compare the spectra obtained for the circuit QED system with those of the cavity QED model, as the latter always preserves the parity symmetry.

2.2.2 Coherent emission spectra

In this section, we examine the coherent emission spectra of the system. Specifically, we will focus on reflection spectra, which can be measured by applying a weak coherent drive to the system through the input TL and subsequently measuring the output through the same port. In the USC regime, the time dependence of the driving Hamiltonian, involving the operators coupled to the TL, cannot be eliminated through a unitary transformation, due to the presence of counter-rotating terms [118]. This limitation prevents the existence of a stationary steady state, resulting in a periodic time-dependent density matrix $\hat{\rho}_{ss}(t)$. The period $T = 2\pi/\omega_d$ only depends on the frequency of the input signal $\omega_d/2\pi$. This behavior aligns with the Floquet formalism [119], as discussed in Refs. [107, 120, 121]. Consequently, the steady state can be expressed as a Fourier series

$$\hat{\rho}_{ss}(t) = \sum_{k=-\infty}^{+\infty} \hat{\rho}^{(k)} e^{ik\omega_d t}\,, \tag{2.28}$$

where k is an integer number. By employing this expansion and using the formalism of generalized master equation, the different Fourier components of the density matrix can be determined. In particular, when computing the expectation value of a positive-frequency operator, e.g., $\langle \hat{X}^+ \rangle$ at the drive frequency ω_d, the $k = -1$ contribution is the only relevant term. This can be understood by simply observing that, when calculating the expectation value of a positive-frequency operator, only the terms oscillating at the negative frequency of the drive will result in a time-independent contribution. For a driving tone in a coherent state, the frequency-dependent reflection S_{11}^M for the mutual inductive coupling can be directly obtained from Eq. (2.22a), yielding

$$S_{11}^M = \left| \frac{\left\langle \hat{V}^+_{M\text{out}} \right\rangle}{\left\langle \hat{V}^+_{\text{in}} \right\rangle} \right| = \left| 1 - \frac{\sqrt{2\pi}}{|b_{\text{in}}|} \sqrt{\frac{\omega_d\, \gamma_m}{\omega_r}}\; \text{Tr}\left\{ \hat{X}_M^+\, \hat{\rho}^{(-1)} \right\} \right|, \tag{2.29}$$

where $|b_{\text{in}}|^2$ represents the photon rate of the coherent drive, and γ_m denotes the damping rate of the input-output port. It is important to note that Eq. (2.29) describes a one-port excitation-detection configuration from the perspective of the circuit QED system (reflection). However, from the standpoint of the TL, this setup can also be interpreted as a two-port scheme, since the signal is detected on the side opposite to the input. In this section, we will also compare our spectra with those reported in Refs. [99, 100]. Since Ref. [100] treats $\hat{a} + \hat{a}^\dagger$ as the system operator coupled to the input-output port, it is instructive to also evaluate the reflection spectrum using a trace over $(\hat{a} + \hat{a}^\dagger)^+$, rather than $\hat{X}_M^+$ as in our primary analysis. We therefore define

$$\bar{S}_{11} = \left| 1 - \frac{\sqrt{2\pi}}{|b_{\text{in}}|} \sqrt{\frac{\omega_d\, \gamma_m}{\omega_r}}\; \text{Tr}\left[(\hat{a} + \hat{a}^\dagger)^+ \hat{\rho}^{(-1)} \right] \right|. \tag{2.30}$$

Similarly, starting from Eq. (2.22b), the reflection in the capacitive coupling scheme can be written as

$$S_{11}^C = \left| \frac{\left\langle \hat{V}^+_{C\text{out}} \right\rangle}{\left\langle \hat{V}^+_{\text{in}} \right\rangle} \right| = \left| 1 + \frac{\sqrt{2\pi}}{|b_{\text{in}}|} \sqrt{\frac{\omega_d\, \gamma_c}{\omega_r}}\; \text{Tr}\left\{ \hat{X}_C^+\, \hat{\rho}^{(-1)} \right\} \right|, \tag{2.31}$$

where γ_c is the damping rate of the input-output port. A similar method to derive a semi-analytical expression of the coherent spectra as well as the relationship between the matrix elements of the output operators and the spectral amplitude can be found in Ref. [107]. In the following, we will present coherent reflection spectra calculated using Eq. (2.29) and Eq. (2.31), with parameters which are very similar to those in Ref. [100], namely $\eta = 1.01$ and $\Delta/\omega_r = 0.69$.

Figure 2.7(a) shows the reflection for the mutual inductive coupling with the TL (S_{11}^M) as function of ω_d/ω_r and ϵ/ω_r. The transitions $|\tilde{1}\rangle \to |\tilde{0}\rangle$, $|\tilde{2}\rangle \to |\tilde{0}\rangle$, and

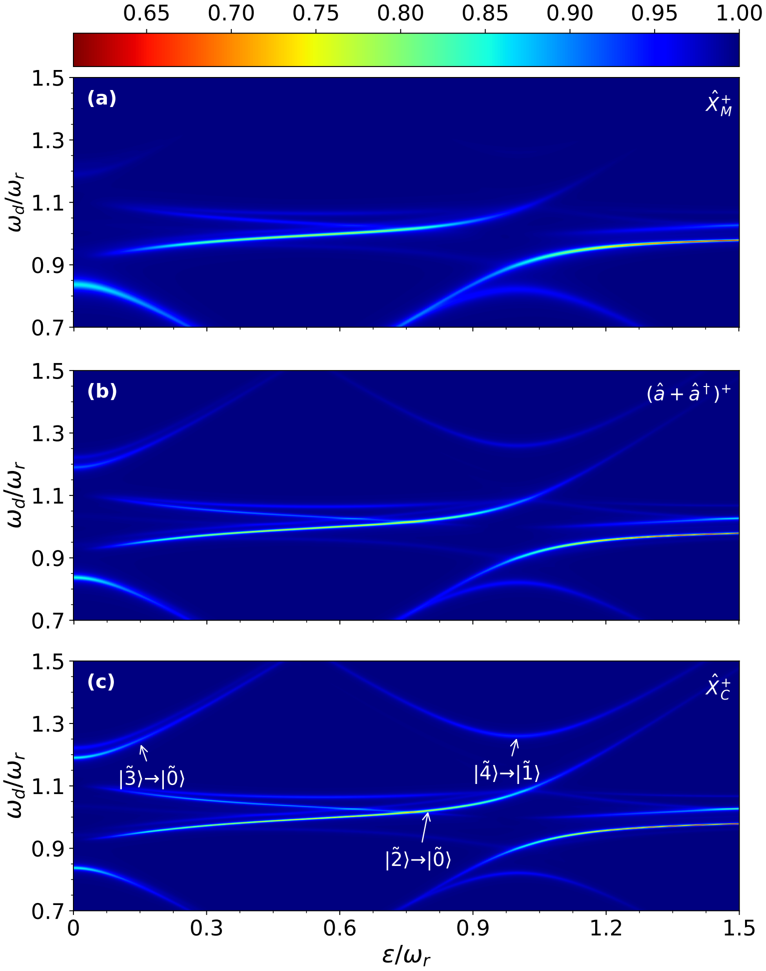

Figure 2.7: **(a-c)** Coherent reflection spectra as a function of the flux offset ϵ for (a) the mutual inductive coupling $S_{11}^M(\omega_d)$, (b) using $\hat{a}+\hat{a}^\dagger$ as the coupling system operator $\bar{S}_{11}(\omega_d)$, and (c) the capacitive coupling $S_{11}^C(\omega_d)$. Transitions discussed in the main text are explicitly labeled. The colormap is normalized such that the maximum value is 1, and the minimum corresponds to the lowest value across all spectra. The parameters used for the calculations are $\eta = 1.01$, $\Delta/\omega_r = 0.69$, $\gamma_m/\omega_r = \gamma_c/\omega_r = 10^{-3}$, $\gamma_q/\omega_r = 0.005$ and $T_r/\omega_r = T_q/\omega_r = 0.55$. In order to also excite higher energy levels, $|b_{\text{in}}|$ is set to 0.03.

$|\tilde{2}\rangle \to |\tilde{1}\rangle$ are those with the lowest reflection (the highest reduction of the input signal). As discussed above, a complete comparison between different models also requires computing $\bar{S}_{11}$, obtained by considering the coupling system operator as $\hat{a}+\hat{a}^\dagger$, which is included in Fig. 2.7(b). Moreover, in Fig. 2.7(c), we display the

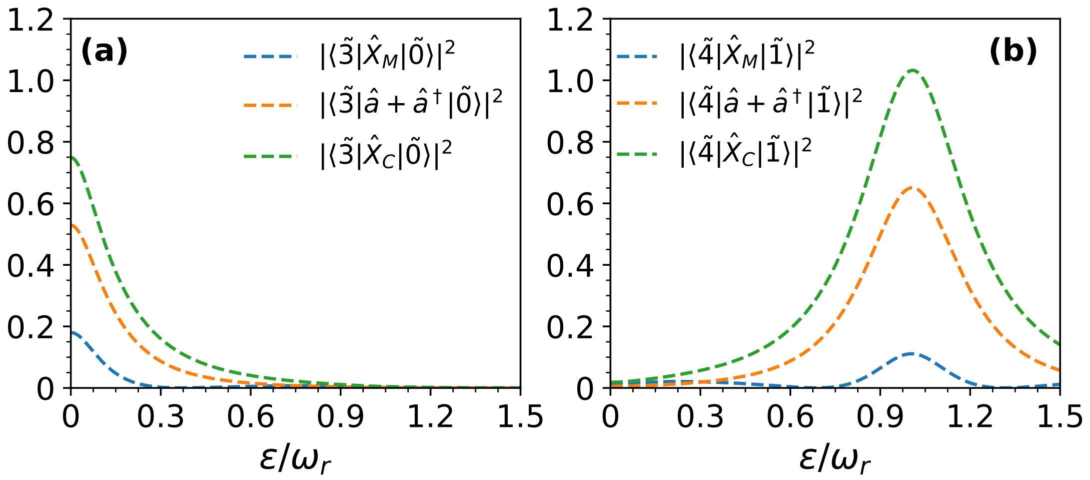

Figure 2.8: Squared modulus of the transition matrix elements as a function of ϵ/ω_r for the transitions **(a)** $|\tilde{3}\rangle \to |\tilde{0}\rangle$ and **(b)** $|\tilde{4}\rangle \to |\tilde{1}\rangle$, for different system operators.

reflection spectra (S_{11}^C) for the system capacitively coupled to the TL. The main differences between the three panels of Fig. 2.7 can be traced back to the spectral lines associated to the transitions $|\tilde{2}\rangle \to |\tilde{0}\rangle$, $|\tilde{3}\rangle \to |\tilde{0}\rangle$ and $|\tilde{4}\rangle \to |\tilde{1}\rangle$.

Specifically, the $|\tilde{2}\rangle \to |\tilde{0}\rangle$ transition is visible up to $\epsilon/\omega_r = 1.5$ in both $\bar{S}_{11}$ and S_{11}^C spectra. However, this spectral line quenches for $\epsilon/\omega_r \geq 1.2$ in the S_{11}^M reflection spectra (see Fig. 2.7(a)). The $|\tilde{3}\rangle \to |\tilde{0}\rangle$ spectral line displays a greater reduction of the input signal (i.e., lower reflection) in Fig. 2.7(c) compared to Fig. 2.7(b), while almost disappearing in Fig. 2.7(a) with complete quenching observed for $\epsilon/\omega \geq 0.3$. Finally, the $|\tilde{4}\rangle \to |\tilde{1}\rangle$ transition is not visible in Fig. 2.7(a), while it is present in both Fig. 2.7(b,c). All the previous observations are supported by the matrix elements shown in Fig. 2.8, which display the squared modulus of the transition matrix elements associated with the output operators $\dot{\hat{X}}_M$, $\dot{\hat{X}}_C$, and $\hat{a} + \hat{a}^\dagger$ for the corresponding transistion. Unfortunately, this spectral region was not reported in Ref. [100], although the spectra presented therein show excellent agreement in the accessible range. In summary, the results in Fig. 2.7 show that the coherent spectra calculated using $\hat{a} + \hat{a}^\dagger$ as system operator coupled to the output port, *i.e.* ($\bar{S}_{11}$), can differ significantly in the USC and DSC regimes from those associated with $\hat{X}_M$ or $\hat{X}_C$, which account for the inductive or capacitive coupling between the resonator and the TL, respectively.

The differences observed between circuit and cavity QED spectra (both coherent and incoherent), even at zero flux offset, ultimately stem from the distinct forms of the light-matter coupling Hamiltonian (or Lagrangian). In cavity

QED, the interaction Lagrangian takes the form of a coordinate-momentum coupling, namely between the field coordinate $\hat{A}$ and the matter momentum $\hat{p}$ in the Coulomb gauge, and conversely in the dipole gauge (see Section 1.3). In contrast, in the circuit QED systems considered here, the corresponding interaction term is of the coordinate-coordinate type, as the system is quantized in the flux gauge, or equivalently, momentum-momentum in the so-called charge gauge [94, 95, 97].

These results further confirm the findings presented in Section 2.2.1 for the incoherent emission spectra, highlighting the importance of correctly identifying the coupling mechanism between the system and the external environment, especially in the USC and DSC regimes.

2.3 Renormalization of the quantum Rabi model

In the previous section, we have shown how the emission spectra of a circuit QED system in the USC and DSC regimes depend on the specific system operator coupled to the external environment. However, additional inaccuracies may also arise from the modelling of the system Hamiltonian itself, due to neglecting the higher energy levels of the artificial (or natural) atom when approximating it as a two-level system. These higher levels can effectively renormalize key system parameters, such as the qubit and resonator frequencies and the light-matter coupling strength, with significant consequences for the dynamics, energy spectrum, and measurable observables, particularly in the USC and DSC regimes.

We begin by analyzing the paradigmatic case of cavity QED, where a natural atom interacts with a single cavity mode, which can be modeled by the standard QRM. We then extend the analysis to circuit QED, focusing on a flux qubit coupled to an electromagnetic resonator, which requires the inclusion of symmetry-breaking terms in the QRM Hamiltonian.

To systematically capture the influence of higher atomic levels while retaining analytical tractability, we propose a framework based on the Schrieffer-Wolff transformation, which yields effective low-energy Hamiltonians. This approach leads to the formulation of the *Renormalized Quantum Rabi Model* (RQRM), an extension of the QRM that incorporates the effects of high-energy states while still retaining a two-level description for the qubit. We also highlight the connections between our method and alternative theoretical techniques, such as the resolvent approach. Finally, we investigate two central aspects of the RQRM: its gauge invariance properties and its implications for physical observables.

The original results presented in this section are based on Ref. [4], where additional discussions and a detailed analysis of the renormalization effects in both cavity and circuit QED systems are reported.

2.3.1 Renormalization in cavity QED

Let us consider a single electric dipole of charge q and mass m in a one-dimensional potential, which interacts with a single cavity mode with frequency ω_c. In the electric-dipole approximation, the radiation wavelength is much larger than the atomic size, allowing us to neglect the spatial dependence of the vector potential, i.e. $\hat{A} = A_0 \left(\hat{a} + \hat{a}^\dagger\right)$, where A_0 is the zero-point fluctuation amplitude and $\hat{a}$ $\left(\hat{a}^\dagger\right)$ is the annihilation (creation) operator of the electromagnetic mode. As outlined in Section 2.1, the Hamiltonian of the system can be expressed in different gauges, such as the Coulomb gauge or the dipole gauge. In the Coulomb gauge, the Hamiltonian reads (see Eq. (2.1))

$$\hat{H}_C = \omega_c \, \hat{a}^\dagger \hat{a} + \frac{\left(\hat{p} - q\hat{A}\right)^2}{2m} + V(\hat{x}) \,, \tag{2.32}$$

where $\hat{x}$ and $\hat{p}$ are the position and momentum operators of the dipole, respectively, and $V(\hat{x})$ is the confining potential.

On the other hand, in the dipole gauge, the Hamiltonian reads (see Eq. (2.6))

$$\begin{aligned} \hat{H}_\mathrm{D} &= \frac{\hat{p}^2}{2m} + V(\hat{x}) + \hbar\omega_c \left(\hat{a}^\dagger - i\frac{qA_0}{\hbar}\hat{x}\right)\left(\hat{a} + i\frac{qA_0}{\hbar}\hat{x}\right) \\ &= \frac{\hat{p}^2}{2m} + V(\hat{x}) + \hbar\omega_c\hat{a}^\dagger\hat{a} - iq\omega_c A_0 \hat{x}\omega_c \left(\hat{a} - \hat{a}^\dagger\right) + \frac{\omega_c q^2 A_0^2}{\hbar}\hat{x}^2 \,. \end{aligned} \tag{2.33}$$

We remind that the two Hamiltonians $\hat{H}_C$ and $\hat{H}_D$ are connected by a unitary transformation, *i.e.* $\hat{H}_D = \hat{U}\hat{H}_C\hat{U}^\dagger$, where $\hat{U} = \exp\left(-iqA_0\hat{x}(\hat{a} + \hat{a}^\dagger)/\hbar\right)$. However, as discussed in Section 2.1, when the dipole is truncated to a two-level system, the resulting QRM Hamiltonians in the two gauges are no longer unitaryly equivalent, thus leading to different physical predictions. Given that the interaction term in the dipole gauge Hamiltonian is directly proportional to the dipole operator, it results to be more suitable for a two-level truncation, while the Coulomb gauge provides less accurate results given that the interaction term is proportional to the momentum $\hat{p}$, whose matrix elements grow significantly faster compared to $\hat{x}$ for increasing system's nonlinearity (see Section 2.1.1). For these reasons, in the following we will focus on studying and renormalizing the QRM within the dipole gauge.

The QRM Hamiltonian in the dipole gauge can be obtained from Eq. (2.33) by applying the projection operator $\hat{\mathcal{P}} = \sum_{n=0}^{1} |n\rangle\langle n|$, where $|n\rangle$ are the eigenstates of the *bare* atomic Hamiltonian $\hat{H}_\mathrm{a} = \hat{p}^2/2m + V(\hat{x})$. For the atomic potential, we will consider a quartic double-well potential as in Eq. (1.10), namely $V(\hat{x}) = \alpha\hat{x}^4 - \beta\hat{x}^2$, with $\alpha, \beta > 0$. By tuning the dimensionless anharmonicity parameter $\gamma = m\beta^3/(\hbar\alpha)^2$, we can control the system's nonlinearity, with larger values of γ

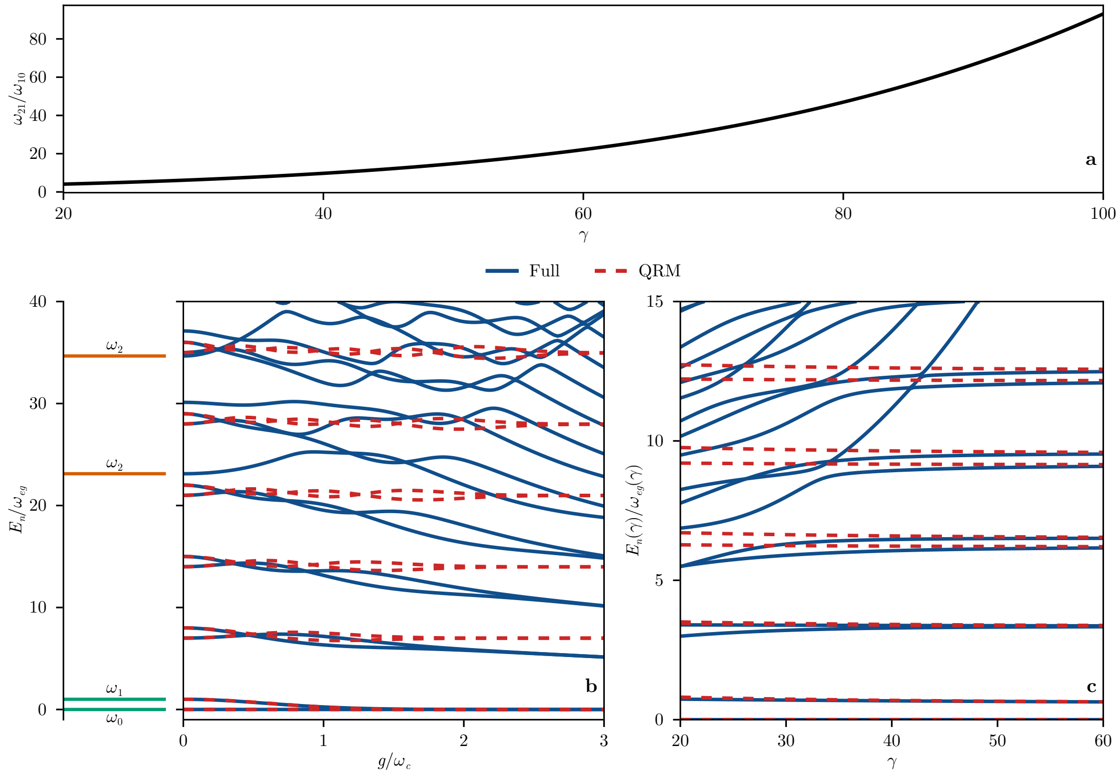

Figure 2.9: **(a)** Plot of the frequency ratio ω_{21}/ω_{10} as a function of the anharmonicity γ, highlighting its monotonic increase. **(b)** (Left panel) Bare atomic energy levels. (Right panel) Energy levels comparison between the full model in Eq. (2.33) and the QRM in Eq. (2.34), as functions of the normalized coupling strength g/ω_c. As shown, when the anharmonicity is insufficient compared to the detuning, the third atomic level ω_2 significantly affects the spectral properties, making the two level approximation meaningless. **(c)** Energy levels comparison as a function of the anharmonicity, showing progressive convergence as the anharmonicity increases. The parameters used are: (b) $m = 1$, $\gamma = 60$, and $\omega_c = 7\omega_{10}$; (c) $m = 1$, $g = 1.5\,\omega_{10}$, and $\omega_c = 3\omega_{10}$.

corresponding to a more pronounced double-well shape. The standard QRM in the dipole gauge is then obtained as

$$\hat{\mathcal{H}}_{\mathrm{D}} = \hat{\mathcal{P}}\hat{H}_{\mathrm{D}}\hat{\mathcal{P}} = \frac{\hbar\bar{\omega}_{10}}{2}\hat{\sigma}_z + \hbar\omega_c\hat{a}^\dagger\hat{a} - i\hbar g_{01}\hat{\sigma}_x(\hat{a} - \hat{a}^\dagger)\,, \tag{2.34}$$

where $\bar{\omega}_{10} = \omega_{10} + (G_{11} - G_{00})/\omega_c$ is the two-level resonance frequency renormalized by the truncation of the $\hat{x}^2$ contribution, as $G_{jk} = \sum_l g_{jl}g_{lk} \equiv \omega_c^2 q^2 A_0^2 \langle j|\hat{x}^2|k\rangle/\hbar^2$. The terms $g_{jk} = \omega_c q A_0 \langle j|\hat{x}|k\rangle/\hbar$ are the light-matter coupling strengths between the atomic states $|j\rangle$ and $|k\rangle$. We notice that Eq. (2.34) is analogous to Eq. (2.9).

Before proceeding with the renormalization analysis, it is important to assess the validity of the two-level approximation. Specifically, when the anharmonicity of the atomic potential is too small (compared to the detuning between the cavity and the two-level transition frequency), higher atomic levels can significantly influence the system's spectrum even at low energies, leading to a breakdown of the two-level approximation. In Fig. 2.9, we present a systematic analysis of this aspect. As previously discussed, increasing the anharmonicity parameter γ leads to an increase in the frequency ratios ω_{jk}/ω_{10}. Of particular interest are the ratios involving transitions from the two lowest-energy levels to higher excited states, as these mostly determine the validity of the two-level truncation itself and of the dispersive regime, which is crucial in the derivation of the renormalized QRM, as we will see shortly. For illustrative purposes, Fig. 2.9(a) displays the growth of the ratio ω_{21}/ω_{10} with increasing γ. Fig. 2.9(b) illustrates how the two-level approximation breaks down when the system's anharmonicity is small compared to the detuning between the cavity and the two-level transition frequency, $\omega_c - \omega_{10}$. In this regime, the third atomic level (ω_2, shown in the left panel) starts to significantly influence the hybridized energy levels, as evidenced by the growing discrepancies between the full model and the standard QRM, even at low excitation energies. Fig. 2.9(c) confirms the gradual improvement in the validity of the two-level approximation as the anharmonicity increases. As expected, the lowest-energy levels converge more rapidly, while higher-energy levels require larger values of γ to achieve a comparable level of accuracy.

Let us now delve into the renormalization of the QRM, and its importance in accurately describing the system's spectral properties. Specifically, the standard QRM in Eq. (2.34) is well-known to closely match the full model when $\bar{\omega}_{10} \simeq \omega_c$ or for weak coupling strengths [122, 123]. However, when these conditions are not met, its accuracy progressively worsens [76, 88]. To address these limitations, we now ask whether an improved version of the QRM can be developed, still within a two-level description, leading us to the introduction of the RQRM. To this end, we first apply a Schrieffer-Wolff (SW) transformation [124, 125] to the full Hamiltonian in Eq. (2.34), and subsequently project it onto the two-level subspace. The chosen generator of the SW transformation is chosen such that it effectively treats the high-energy subspace as a perturbation, while the two-level subspace is handled non-perturbatively, marking a clear difference from the traditional SW approach. A detailed point-by-point derivation of the RQRM is provided in the Appendix A, as well as a detailed discussion on the differences between this approach and traditional perturbative methods (as standard SW). Indeed, the application of this SW procedure is possible because the higher-energy atomic levels are in the so-called *dispersive regime* with the cavity, characterized

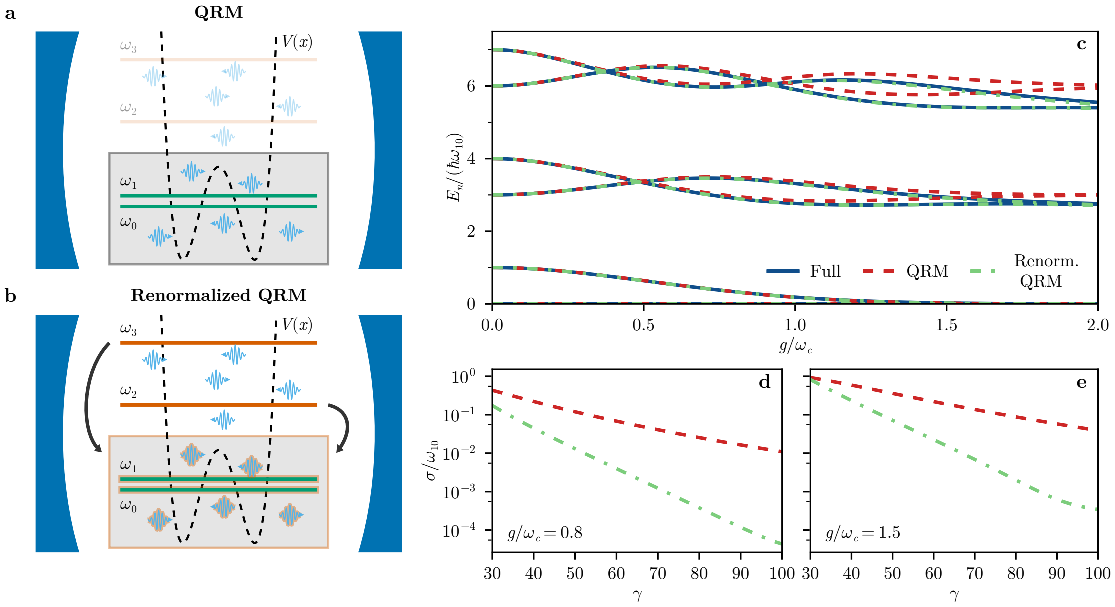

Figure 2.10: We consider a single electron in a one-dimensional double-well potential, interacting with a cavity mode. **(a)** Standard procedure for obtaining the QRM from the full Hamiltonian, which consists of simply projecting in the low-energy subspace of the atomic eigenstates. **(b)** Renormalization of the QRM, which takes into account the interaction of photons with the higher-energy atomic levels, providing more accurate results while still manteining a two-level description. **(c)** Comparison of the eigenvalues in the full model (blue solid), the standard QRM (red dashed), and the RQRM (green dash-dotted). The RQRM provides more accurate results, even for strong coupling strengths. Parameters used: $m = 1$, $\gamma = 60$, and $\omega_c = 3\omega_{10}$. **(d,e)** Mean square error of the eigenvalues of the first 5 excited states with respect to the full model, as a function of the anharmonicity parameter γ, for (d) $g/\omega_c = 0.8$ and (e) $g/\omega_c = 1.5$.

by the propterty $|g_{jk}/(\omega_{jk} - \omega_c)| \ll 1$. This condition is satisfied for large enough atomic anharmonicities, which ensure that the transitions from the two lowest energy levels to the higher ones are not resonant with the cavity frequency, i.e. $|\omega_{jk}| \gg \omega_c$. This approach allows for a fully non-perturbative treatment of the interactions belonging to the two-level subspace of the QRM, while effectively dressing both the two-level system and the cavity field parameters by the contributions of higher atomic levels (see Fig. 2.10(a,b)). The resulting Hamiltonian, *i.e.* the RQRM in cavity QED, reads

$$\begin{aligned}\hat{\mathcal{H}}_{\mathrm{D}}^{\mathrm{eff}} = \frac{\hbar\tilde{\omega}_{10}}{2}\hat{\sigma}_z + \hbar\omega_c\hat{a}^\dagger\hat{a} + \hbar\left(B_+ + B_-\hat{\sigma}_z\right)\left(\hat{a} - \hat{a}^\dagger\right)^2 \\ - i\hbar\tilde{g}_{01}\hat{\sigma}_x\left(\hat{a} - \hat{a}^\dagger\right) - D_{01}\hat{\sigma}_y\left(\hat{a} + \hat{a}^\dagger\right)\,,\end{aligned} \tag{2.35}$$

with $\tilde{\omega}_{10} = \bar{\omega}_{10} + 2A_-$ and $\tilde{g}_{01} = g_{01} + C_{01}$ being the renormalized two-level resonance frequency and coupling strength, respectively. The whole derivation of Eq. (2.35) can be found in Appendix A. The coefficients $A_\pm$, $B_\pm$, C_{01} and D_{01} are the renormalization parameters defined in Eqs. (A.23-A.26), which depend on the microscopic details of the high energy states and effectively account for the virtual transitions (up to the first order) between the two-level subspace and higher energy states. Notably, the RQRM in Eq. (2.35) provides a significantly more accurate description of the full system without requiring explicit enlargement of the Hilbert space.

Figure 2.10(c) shows a comparison of the eigenvalues of the first 5 excited states obtained from the full model $\hat{H}_{\mathrm{D}}$ in Eq. (2.33) (solid blue line), the standard QRM in Eq. (2.34) (red dashed), and the RQRM in Eq. (2.35) (green dash-dotted). The results confirm that the RQRM yields more accurate predictions than the standard QRM, which diverges at relatively high coupling strengths. The coupling strength $g = |g_{01}|$ was varied through A_0, which proportionally scales all the other coupling strengths g_{jk} as well. In Fig. 2.10(d-e), we show the mean square error with respect to the full model $\sigma = \sqrt{\sum_{j=1}^{N}\left(E_j - E_j^{\mathrm{full}}\right)^2/N}$ of the eigenvalues of the first $N = 5$ excited states of the full light-matter system. We compare the QRM with the RQRM as a function of the anharmonicity parameter γ for two different coupling strengths, namely $g/\omega_c = 0.8$ and $g/\omega_c = 1.5$. We observe that the RQRM not only provides more accurate results (green line is always significantly lower than the red one), but also scales better with increasing anharmonicity (higher slope of the green curve).

A detailed analysis of the coefficients in Eq. (2.35) and their dependence on the system parameters reveals that some of the renormalization terms become negligible for high anharmonicity, specifically the B_- and D_{01} terms (see Appendix A). Therefore, we can write a simplified version of the RQRM, which is given by

$$\hat{\mathcal{H}}_{\mathrm{D}}' = \frac{\hbar\tilde{\omega}_{10}}{2}\hat{\sigma}_z + \hbar\omega_c\hat{a}^\dagger\hat{a} + \hbar B_+\left(\hat{a} - \hat{a}^\dagger\right)^2 - i\hbar\tilde{g}_{01}\hat{\sigma}_x\left(\hat{a} - \hat{a}^\dagger\right)\,. \tag{2.36}$$

We now perform a Bogolioubov transformation on the above Hamiltonian, which allows us to diagonalize the purely photonic terms. The resulting Hamiltonian reads

$$\hat{\mathcal{H}}_{\mathrm{D}}' = \frac{\hbar\tilde{\omega}_{10}}{2}\hat{\sigma}_z + \hbar\tilde{\omega}_c\hat{b}^\dagger\hat{b} - i\hbar\tilde{g}_{01}\sqrt{\frac{\omega_c}{\tilde{\omega}_c}}\hat{\sigma}_x\left(\hat{b} - \hat{b}^\dagger\right)\,, \tag{2.37}$$

where $\tilde{\omega}_c = \sqrt{\omega_c^2 - 4B_+\omega_c}$ is the renormalized cavity frequency, and the momentum is rescaled as $\hat{b} - \hat{b}^\dagger = \sqrt{\tilde{\omega}_c/\omega_c}(\hat{a} - \hat{a}^\dagger)$. Remarkably, Eq. (2.37) preserves a QRM-like structure with renormalized frequencies and coupling, although in general providing slightly less accurate results with respect to Eq. (2.35).

One important question arises: why does the standard QRM still provide a reasonable fit of the experimental data in many USC and DSC experiments (*e.g.*, Refs. [99, 100]), despite the influence of higher atomic levels? The answer lies in the form of Eq. (2.37) itself. Indeed, in many experimental settings, the system parameters are fixed, and the renormalization effects can be effectively absorbed into the fitted constants, as showed by the renormalized parameters in Eq. (2.37). In other words, when fitting the experimental data with the standard QRM, the fitted parameters already include the renormalization effects through effective scaling factors that remain indistinguishable in experimental fits. However, as illustrated in Fig. 2.10(c), such a fit procedure breaks down when varying the coupling strength g (or other system parameters) in a wide range. In such cases, the renormalization of the system frequencies, depending on g, plays a crucial role and must be incorporated for an accurate description over all the range, as is done in the RQRM.

2.3.2 Renormalization in circuit QED

The renormalization of the QRM is not limited to cavity QED systems, but it is equally (if not more) relevant in circuit QED setups, where artificial atoms (superconducting qubits) are coupled to electromagnetic resonators. To illustrate our approach, we focus on a specific example involving the fluxonium qubit [96].

In particular, we study a fluxonium-resonator system [97, 127] represented in Fig. 2.11(a), bearing in mind that the same procedure can be applied to other circuits, once the corresponding Hamiltonian is derived. The fluxonium qubit is characterized by higher anharmonicity when compared to other devices, such as the transmon qubit, making it an ideal candidate for the study of the renormalization of the QRM. Specifically, the system under study is composed by a Josephson junction with energy E_J and capacitance C_1 in parallel with a inductance L_1, forming the fluxonium qubit, which is then coupled in series to an L_2C_2 resonator. An external flux ϕ_{ext} is threading the qubit loop formed by the Josephson junction and the inductance L_1.

The corresponding Hamiltonian is obtained through the usual quantization procedure [94, 95], already introduced in Section 2.1.2. In the so-called flux gauge, the node flux variables are chosen as the canonical coordinates, while their conjugate

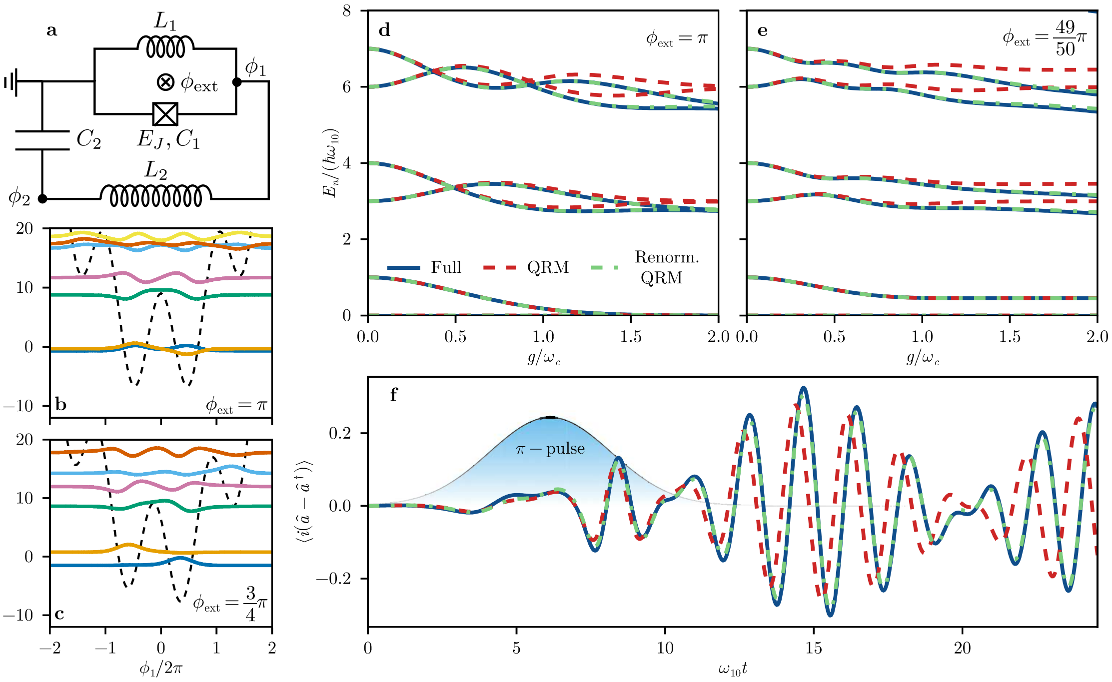

Figure 2.11: **(a)** Circuital realization of a fluxonium qubit, defined by a Josephson junction with energy E_J and a capacitance C_1 in parallel with a inductance L_1, galvanically coupled to a LC resonator. **(b,c)** First eigenstates of the fluxonium qubit for (b) $\phi_{\text{ext}} = \pi$ and (c) $\phi_{\text{ext}} = 3\pi/4$. The dashed black line correspond to the potential. **(d,e)** Comparison of the eigenvalues between the full model (solid blue line), the standard QRM (dashed green line), and the RQRM (dotted red line), as a function of the normalized coupling g/ω_c, and for (d) $\phi_{\text{ext}} = \pi$ and (e) $\phi_{\text{ext}} = 49\pi/50$. As for the natural atoms case, the RQRM provides better results. **(f)** Time evolution of $\left\langle i(\hat{a} - \hat{a}^\dagger)\right\rangle$ after a π-pulse on the qubit, for $\phi_{\text{ext}} = 49\pi/50$. Also in this case, the RQRM provides a better agreement with the full model. The parameters used in this Figure are: $E_C = q^2/(2C_1) = 2.5$ GHz, $E_L = (\hbar/2q)^2/L_1 = 0.5$ GHz, $E_J = 9$ GHz, and $\omega_c = 3\omega_{10}$, which reproduce typical experimental values for fluxonium qubits [96, 126]. For the π-pulse, we used $\omega_{\text{dr}} = E_{10}$, $\sigma_{\text{dr}} = 50/(E_{21} - E_{10})$ and $t_0 = 3\sigma_{\text{dr}}$ (see main text).

momenta correspond to the node charges. The resulting Hamiltonian reads

$$\begin{aligned}
\hat{H}_{\text{fl-res}} &= \frac{\hat{Q}_1^2}{2C_1} + \frac{\hat{Q}_2^2}{2C_2} + \frac{\hat{\phi}_1^2}{2L_1} + \frac{\left(\hat{\phi}_2 - \hat{\phi}_1\right)^2}{2L_2} - E_J \cos\left(\frac{\hat{\phi}_1 - \phi_{\text{ext}}}{\phi_0}\right) \\
&= \hat{H}_{\text{flux}}\left(\hat{\phi}_1, \hat{Q}_1\right) + \hat{H}_{\text{res}}\left(\hat{\phi}_2 - \hat{\phi}_1, \hat{Q}_2\right) ,
\end{aligned} \tag{2.38}$$

where $\hat{H}_{\text{flux}}$ and $\hat{H}_{\text{res}}$ are the fluxonium and resonator bare Hamiltonians, given by

$$\hat{H}_{\text{flux}}\left(\hat{\phi}_1, \hat{Q}_1\right) = \frac{\hat{Q}_1^2}{2C_1} + \frac{\hat{\phi}_1^2}{2L_1} - E_J \cos\left(\frac{\hat{\phi}_1 - \phi_{\text{ext}}}{\phi_0}\right), \tag{2.39}$$

$$\hat{H}_{\text{res}}\left(\hat{\phi}_2, \hat{Q}_2\right) = \frac{\hat{Q}_2^2}{2C_2} + \frac{\hat{\phi}_2^2}{2L_2}, \tag{2.40}$$

respectively, with $\phi_0 = \hbar/2e$ being the reduced flux quantum and ϕ_i (Q_i) the flux (charge) variables of the *i-th* node. Equation (2.40) can be rewritten by the introduction of the bosonic operator $\hat{a} = (\omega_c\hat{\phi}_2 + i\hat{Q}_2)/\omega_c\phi_{\text{zpf}}$, where $\omega_c = 1/\sqrt{L_2C_2}$ is the frequency of the resonator and $\phi_{\text{zpf}} = \sqrt{\hbar/2C_2\omega_c}$ is the zero-point fluctuation amplitude of the flux variable, which leads to $\hat{H}_{\text{res}} = \hbar\omega_c\hat{a}^\dagger\hat{a}$.

The Hamiltonian in Eq. (2.38) exhibits a striking similarity to the cavity-QED Hamiltonian in Eq. (2.33), with the flux variable $\hat{\phi}_1$ playing the role of the dipole position operator $\hat{x}$, and the resonator flux $\hat{\phi}_2$ playing the role of the vector potential $\hat{A}$. Indeed, as discussed in Section 2.1.1, Eq. (2.33) can be obtained by performing a minimal coupling replacement on the harmonic subsystem, *i.e.* on the photonic operators, defined by $\hat{a} \to \hat{a} + iqA_0\hat{x}/\hbar$ [81, 128]. Analogously, Eq. (2.38) presents a minimal coupling replacement on the resonator variables, specifically $\hat{\phi}_2 \to \hat{\phi}_2 - \hat{\phi}_1$. The primary distinction between the two cases lies in the nature of the coupling. In the former, the interaction term is of the form coordinate-momentum $(\hat{x}\,\hat{E})$, while in the latter it involves the two fluxes, which correspond to the generalized coordinates in the flux gauge. Therefore, the two Hamiltonians can be mapped into each other by the unitary transformation $\hat{T} = \exp\left(i\pi\hat{a}^\dagger\hat{a}/2\right)$, which effectively swaps the roles of the position and momentum operators of the harmonic subsystem (see Appendix Section A.3 for details). Consequently, the same procedure and part of the results of the previous section can be applied here.

First, we derived the Hamiltonian for the QRM by projecting the full Hamiltonian in the low-energy subspace of the fluxonium qubit, which results in

$$\begin{aligned}\hat{\mathcal{H}}_{\text{fl-res}} = \hbar\omega_c\hat{a}^\dagger\hat{a} + \frac{\hbar\bar{\omega}_{10}}{2}\hat{\sigma}_z + \hbar\frac{G_{01}}{\omega_c}\hat{\sigma}_x \\ - \hbar\left(\frac{g_{11}+g_{00}}{2}\hat{I} + \frac{g_{11}-g_{00}}{2}\hat{\sigma}_z + g_{01}\hat{\sigma}_x\right)\left(\hat{a}+\hat{a}^\dagger\right),\end{aligned} \tag{2.41}$$

where

$$g_{jk} = \frac{\phi_{\text{zpf}}\phi_{jk}}{\hbar L_2}, \quad G_{jk} = \frac{\hbar L_2\omega_c}{2\phi_{\text{zpf}}^2}\sum_l g_{jl}g_{lk} = \frac{\omega_c}{2\hbar L_2}\Phi_{jk}, \tag{2.42}$$

with $\phi_{ij} = \langle i|\,\hat{\phi}_1\,|j\rangle$ and $\Phi_{ij} = \langle i|\,\hat{\phi}_1^2\,|j\rangle = \sum_k \phi_{ik}\phi_{kj}$. The renormalized qubit frequency $\bar{\omega}_{10} = \omega_{10} + (G_{11} - G_{00})/\omega_c$ has the same definition as in the cavity

QED case. Three additional terms emerge in Eq. (2.41) due to the breaking of $\mathbb{Z}_2$ symmetry, originating from the external flux ϕ_{ext}. These additional terms vanish when $\phi_{\text{ext}}/\phi_0 = k\pi$ (with $k \in \mathbb{Z}$), where the symmetry is restored. We notice that Eq. (2.41) is analogous to Eq. (2.15), where we retained all the terms arising from the two-level projection, without neglecting any of them. Namely, these additional terms are the third and the fourth of Eq. (2.41). In particular, the third term arises from the projection of $\hat{\phi}_1^2$ onto the unperturbed fluxonium states, similarly to the self-polarization term of the cavity QED case, while the fourth term is usually neglected since, near the symmetry point, $g_{11} \approx -g_{00}$. Even though these terms are often disregarded, we retain them here for the sake of completeness.

Following our approach, outlined in the previous subsection, we now proceed to renormalize the QRM Hamiltonian in Eq. (2.41) by applying a SW transformation to the full Hamiltonian in Eq. (2.38), and subsequently projecting it onto the two-level subspace of the fluxonium qubit. A detailed derivation of the RQRM in circuit QED is provided in Appendix Section A.3. The resulting renormalized Hamiltonian, *i.e.* the RQRM in circuit QED, is given by

$$\begin{aligned}
\hat{\mathcal{H}}^{\text{eff}}_{\text{fl-res}} = \hbar\omega_c \hat{a}^\dagger \hat{a} + \frac{\hbar\tilde{\omega}_{10}}{2}\hat{\sigma}_z + \hbar\left(\frac{G_{01}}{\omega_c} + A_{10} + A_{01}\right)\hat{\sigma}_x \\
-\hbar\left(\frac{\tilde{g}_{11}+\tilde{g}_{00}}{2}\hat{I} + \frac{\tilde{g}_{11}-\tilde{g}_{00}}{2}\hat{\sigma}_z + \tilde{g}_{01}\hat{\sigma}_x\right)\left(\hat{a}+\hat{a}^\dagger\right) \\
-\hbar\left(B_+\hat{I} + B_-\hat{\sigma}_z + 2B_{01}\hat{\sigma}_x\right)\left(\hat{a}+\hat{a}^\dagger\right)^2 \\
+i\hbar\left(A_{10}-A_{01}\right)\hat{\sigma}_y\left(\hat{a}^2 - \hat{a}^{\dagger 2}\right) - i\hbar D_{01}\hat{\sigma}_y\left(\hat{a}-\hat{a}^\dagger\right) ,
\end{aligned} \tag{2.43}$$

with $\tilde{\omega}_{10} = \bar{\omega}_{10} + 2A_-$ and $\tilde{g}_{jk} = g_{jk} + C_{jk}$. The Hamiltonian in Eq. (2.43) is the Circuit QED version of the RQRM. It is worth noting that all the coefficients are the same as those in the natural atom case in Eq. (2.35), defined explicitly in the Appendix Section A.2, with the only difference lying in the definitions of the coupling coefficients g_{jk} and G_{jk}. Notably, in the case of cavity QED, where the system's Hamiltonian presents the $\mathbb{Z}_2$ parity symmetry, the coupling g_{ij} vanishes between states of the same parity (namely, $g_{ij} = 0$ for $i + j$ even), in contrast to the circuit QED Hamiltonian, where this symmetry is broken (thus $g_{ij} \neq 0$ for $i+j$ even). This is a direct consequence of the fact that the fluxonium potential is not symmetric when $\phi_{\text{ext}}/\phi_0 \neq k\pi$ (with $k \in \mathbb{Z}$), thus giving rise to the additional terms in Eq. (2.43).

Figure 2.11(b,c) shows the shapes of the fluxonium potential (already defined in Eq. (1.14)) and the respective eigenstates for (b) the symmetric and (c) asymmetric cases, with values of the flux offset corresponding to $\phi_{\text{ext}}/\phi_0 = \pi$ and $\phi_{\text{ext}}/\phi_0 = 3\pi/4$, respectively. Fig. 2.11(d,e) show the comparison of the eigenvalues of the first 5 excited states obtained from the full model in Eq. (2.38) (blue solid), the standard QRM in Eq. (2.41) (red dashed), and the RQRM in Eq. (2.43) (green dash-dotted), as a function of the normalized coupling g/ω_c, and for both (d) the symmetric and (e) asymmetric cases. Figure 2.11(f) shows the time evolution of the expectation value $\langle i(\hat{a}-\hat{a}^\dagger)\rangle$, considering the system initially in its ground state and applying a π-pulse on the qubit, in presence of symmetry breaking.[3] All these results demonstrate that the RQRM provides significantly more accurate results than the standard QRM, even in absence of parity symmetry in the anharmonic potential, as explicitly demonstrated in Fig. 2.11(e), while still retaining a two-level description and analytical tractability. Furthermore, the RQRM performs better also in describing the system dynamics (see Fig. 2.11(f)) and its impact on the observables. In particular, the impact of the renormalization on the observables will be further examined in the following subsections.

2.3.3 Gauge invariance of the RQRM

In the previous subsections, we derived the RQRM in the dipole (flux) gauge for cavity (circuit) QED system. However, as discussed in Section 2.1.1, the choice of gauge can significantly impact the results when the Hilbert space is truncated to a two-level description. This naturally raises the question of whether the renormalization procedure we employed preserves gauge invariance.

Gauge invariance in truncated models is a subtle and complex issue that has been the subject of extensive debate in recent years [77, 78, 87, 129, 130], as also mentioned in Section 2.1. One of the most important drawbacks in models that do not preserve gauge invariance is that they may lead to incorrect physical predictions. A striking example is provided by the Dicke model, where an infinite collection two-level systems coupled to light was originally predicted to undergo a second-order phase transition to a photon condensate [18–21, 74, 131, 132]. However, it was later shown that this phase transition is actually forbidden if the so-called $\hat{\mathbf{A}}^2$ term, which ensures the gauge invariance of the model, is not neglected [92, 133]. More generally, photon condensation has been shown to be forbidden by the gauge invariance itself, both in truncated systems [89] and in the full Hilbert space [90, 91, 134]. Nonetheless, this point remains a topic of ongoing debates in the literature, with some works suggesting that a phase transition could occur in specific conditions if the electrostatic interactions are taken into account [78, 129, 130]. This issue will be addressed in detail in Chapter 4. In the

---

[3] The π-pulse is modeled as a Gaussian drive on the qubit, described by the Hamiltonian $\hat{H}_{\rm dr}(t) = \left(\hbar\pi/\sigma_{\rm dr}\sqrt{2\pi}\right)\, e^{-(t-t_0)^2/2\sigma_{\rm dr}} \cos(\omega_{\rm dr} t)\ \hat{\phi}_1$, where $\omega_{\rm dr}$ is the drive frequency and $\sigma_{\rm dr}$ is the pulse width. The time evolution is computed by solving the time-dependent Schrödinger equation with the total Hamiltonian $\hat{H}_{\rm tot}(t) = \hat{H}_{\text{fl-res}} + \hat{H}_{\rm dr}(t)$. For the QRM and RQRM cases, the drive term is projected onto the two-level subspace, i.e. $\hat{\mathcal{H}}_{\rm dr}(t) = \hat{\mathcal{P}}\hat{H}_{\rm dr}(t)\hat{\mathcal{P}}$. The parameters used for the pulse are specified in the caption of Fig. 2.11.

remainder of this subsection, we focus on the single-atom case and explicitly derive the RQRM in a gauge-invariant form for the cavity QED setting, highlighting the implications of this result.

To facilitate the discussion about gauge invariance, as it is customary in literature [78, 88], we can introduce a gauge parameter η which gives rise to a continuous family of η-dependent Hamiltonians $\hat{H}^{(\eta)}$ in the full Hilbert space interpolating between the Coulomb and the dipole gauges, spanned by the unitary transformation $\hat{U}^{(\eta)} = \exp\Big(i\eta q\hat{x}\hat{A}/\hbar\Big)$. Explicitly, in the long-wavelength approximation, *i.e.* for a spatially constant vector potential, we have

$$\hat{H}^{(\eta)} = \hat{U}^{(1-\eta)}\hat{H}_{\rm a}\hat{U}^{(1-\eta)\dagger} + \hat{U}^{(\eta)}\hat{H}_{\rm ph}\hat{U}^{(\eta)}\,, \tag{2.44}$$

where $\hat{H}_{\rm a} = \hat{p}^2/(2m) + V(\hat{x})$ and $\hat{H}_{\rm ph} = \hbar\omega_c\hat{a}^\dagger\hat{a}$ are the usual bare atomic and photonic Hamiltonians, respectively. For $\eta = 0$, we recover the Coulomb gauge Hamiltonian ($\hat{H}_{\rm C} = \hat{H}^{(0)}$) with the usual minimal coupling replacement applied to the matter variables, whereas for $\eta = 1$ we obtain the dipole gauge Hamiltonian ($\hat{H}_{\rm D} = \hat{H}^{(1)}$), showing that in this case the minimal coupling is applied to the photonic term[4].

When truncating to the atomic low-energy subspace, gauge invariance breaks down, since $\hat{\mathcal{H}}_{\rm C} = \hat{\mathcal{P}}\hat{H}_{\rm C}\hat{\mathcal{P}}$ and $\hat{\mathcal{H}}_{\rm D} = \hat{\mathcal{P}}\hat{H}_{\rm D}\hat{\mathcal{P}}$ are no longer linked by any unitary transformation. This issue was resolved by applying the minimal coupling replacement directly in the projected Hilbert space [79, 80, 87]. Indeed, analogously to the case of the full models, we can define a unitary transformation directly in the truncated Hilbert space similarly to Eq. (2.7), namely $\hat{\mathcal{U}}^{(\eta)} = \exp\Big[i\eta q\hat{\mathcal{P}}\hat{x}\hat{\mathcal{P}}\hat{A}\Big] = \exp\big[i\eta g_{01}\hat{\sigma}_x(\hat{a}+\hat{a}^\dagger)/\omega_c\big]$, which interpolates between the Coulomb and dipole gauges as

$$\hat{\mathcal{H}}^{(\eta)} = \hat{\mathcal{U}}^{(1-\eta)}\hat{\mathcal{H}}_{\rm a}\hat{\mathcal{U}}^{(1-\eta)\dagger} + \hat{\mathcal{U}}^{(\eta)\dagger}\hat{\mathcal{H}}_{\rm ph}\hat{\mathcal{U}}^{(\eta)}\,, \tag{2.45}$$

where $\hat{\mathcal{H}}_{\rm a} = \hat{\mathcal{P}}\hat{H}_{\rm a}\hat{\mathcal{P}} = \hbar\omega_{10}\hat{\sigma}_z/2$. This procedure restores a discrete form of gauge invariance directly within the truncated space [77, 87].

Following the same reasoning, the RQRM in Eq. (2.37) can be interpreted in a gauge-preserving form, since

$$\hat{\mathcal{H}}'_{\rm D} = \hat{\mathcal{H}}'_{\rm a} + \hat{\mathcal{U}}'^{(1)\dagger}\hat{\mathcal{H}}'_{\rm ph}\hat{\mathcal{U}}'^{(1)}\,, \tag{2.46}$$

where the renormalized atomic and photonic Hamiltonians are, respectively,

$$\hat{\mathcal{H}}'_{\rm a} = \frac{\hbar\tilde{\omega}_{10}}{2}\hat{\sigma}_z\,, \qquad \hat{\mathcal{H}}'_{\rm ph} = \hbar\tilde{\omega}_c\hat{b}^\dagger\hat{b}\,, \tag{2.47}$$

---

[4] Notice that, by definition, $\hat{U}^{(0)} = \hat{I}$

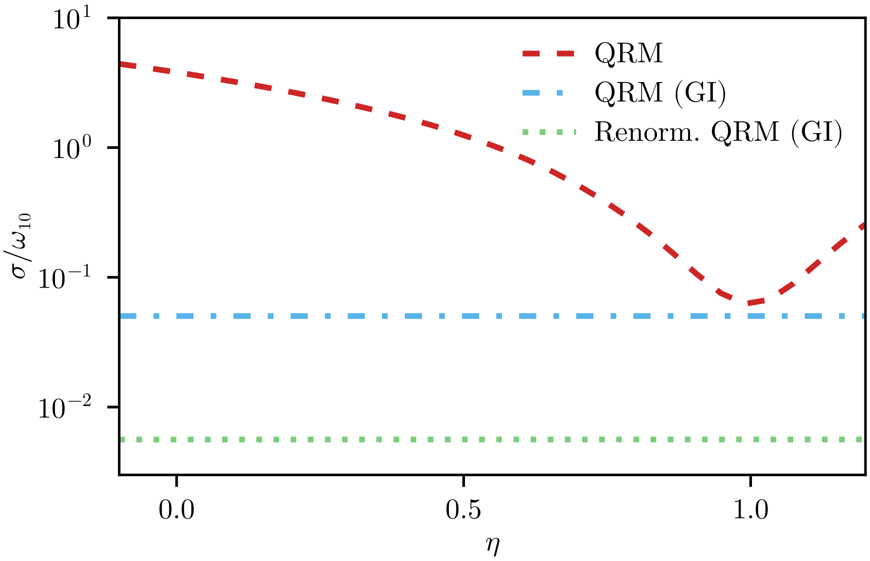

Figure 2.12: Mean square error of the eigenvalues of the first 5 excited states with respect to the full model, as a function of the gauge parameter η, for $g/\omega_c = 0.8$, $m = 1$, $\gamma = 60$, and $\omega_c = 3\omega_{10}$. The QRM (red dashed) breaks gauge invariance, showing that the dipole gauge ($\eta = 1$) is the most accurate. On the other hand, the gauge invariant RQRM, $\hat{\mathcal{H}}'^{(\eta)}$, in Eq. (2.49) (green dotted) is not only gauge invariant but also provides more accurate results. For completeness, we also compare these models with the gauge-preserving QRM, $\hat{\mathcal{H}}^{(\eta)}$, in Eq. (2.45) (blue dash-dotted), which, however, does not take into account the renormalization of the higher energy levels, as testified by its lower accuracy.

and the renormalized (η-dependent) unitary operator is

$$\hat{\mathcal{U}}'^{(\eta)} = \exp\left[i\eta \frac{\tilde{g}_{01}}{\tilde{\omega}_c} \sqrt{\frac{\omega_c}{\tilde{\omega}_c}} \hat{\sigma}_x \left(\hat{b} + \hat{b}^\dagger \right) \right] . \tag{2.48}$$

Consequently, the η-interpolated RQRM becomes

$$\hat{\mathcal{H}}'^{(\eta)} = \hat{\mathcal{U}}'^{(1-\eta)} \hat{\mathcal{H}}'_{\text{a}} \hat{\mathcal{U}}'^{(1-\eta)\dagger} + \hat{\mathcal{U}}'^{(\eta)\dagger} \hat{\mathcal{H}}'_{\text{ph}} \hat{\mathcal{U}}'^{(\eta)} . \tag{2.49}$$

Figure 2.12 shows the mean square error on the energies of the first five excited states, compared to those obtained from the full model as a function of the gauge parameter η, for $g/\omega_c = 0.8$. While the standard QRM breaks gauge invariance (with dipole gauge being the most accurate), the QRM derived by gauge principles in Eq. (2.44), $\hat{\mathcal{H}}^{(\eta)}$, and RQRM in Eq. (2.49), $\hat{\mathcal{H}}'^{(\eta)}$, ensure gauge invariance, with the latter providing a better accuracy.

2.3.4 Higher-order corrections to the RQRM

The effective Hamiltonians both in cavity and circuit QED, in Eq. (2.35) and Eq. (2.43) respectively, are obtained by performing a SW transformation up to the second order in the $g_{jk}/(\omega_{jk}-\omega_c)$ expansion, as detailed in Appendix Section A.1. This leads to an improvement in the accuracy, as can be seen from Fig. 2.10(c-e) and Fig. 2.11(d-f). One may wonder whether higher-order corrections can further improve the accuracy of the renormalization procedure. Notice that, even expanding the series of the SW to higher orders, the original eigenvalues are not recovered because the unitary transformation $\hat{H} \to e^{-\hat{S}}\hat{H}e^{\hat{S}}$ preserves the spectrum of the Hamiltonian only if no projection is performed.

In order to quantify the impact of higher-order corrections on the renormalization, here we adopt another widely used framework in the context of condensed matter physics, namely the resolvent (or Green's function) method [38, 135, 136]. In particular, we focus on the cavity QED model, but the same analysis can be applied to other cases. To apply the resolvent method, we start by considering the eigenvalue equation of the full Hamiltonian in the dipole gauge, *i.e.*

$$\hat{H}_{\mathrm{D}} |\psi_{\mathrm{D}}\rangle = E |\psi_{\mathrm{D}}\rangle \ . \tag{2.50}$$

It is possible to derive an eigenvalue equation for an effective Hamiltonian, which is defined in the projected subspace, such that

$$\hat{\mathcal{H}}^{(\mathrm{res.})}_{\mathrm{D}}(E) |\psi_{\mathrm{D}}\rangle = E |\psi_{\mathrm{D}}\rangle \ , \tag{2.51}$$

where E is the same eigenvalue as in the full case in Eq. (2.50). The energy-dependent effective Hamiltonian is given by

$$\hat{\mathcal{H}}^{(\mathrm{res.})}_{\mathrm{D}}(E) = \hat{P}\hat{H}_{\mathrm{D}}\hat{P} + \hat{P}\hat{H}_{\mathrm{D}}\hat{Q}\frac{1}{E - \hat{Q}\hat{H}_{\mathrm{D}}\hat{Q}}\hat{Q}\hat{H}_{\mathrm{D}}\hat{P} \, , \tag{2.52}$$

where $\hat{Q} = \hat{I} - \hat{P}$ is the projector on the subspace complementary to $\hat{P}$.

Equation (2.51), by construction, gives the exact eigenvalues in the low-energy subspace. However, the implicit dependence of the effective Hamiltonian on the eigenvalue E may make the problem highly challenging. Nonetheless, the resolvent $\hat{G}_{\mathrm{QQ}}(E) \equiv (E - \hat{Q}\hat{H}_{\mathrm{D}}\hat{Q})^{-1}$ can be expanded in series by using the operator property $(A-B)^{-1} = A^{-1}\sum_{n=0}^{\infty}(BA^{-1})^n$, with $A = -\hat{Q}\hat{H}_{0'}\hat{Q}$ and $B = \hat{Q}\hat{H}^{\mathrm{H}}_{\mathrm{int,D}}\hat{Q} - E$. Here, $\hat{H}_{0'}$ and $\hat{H}_{\mathrm{int,D}}$ are defined in Appendix Section A.2. By substituting this series expansion for the resolvent $\hat{G}_{\mathrm{QQ}}(E)$ into Eq. (2.51), and subsequently truncating the series up to the *M-th* order, we derive a polynomial expression in E for the effective Hamiltonian. This reformulation simplifies the initial task into solving a polynomial eigenvalue problem. The order of the polynomial in the variable E,

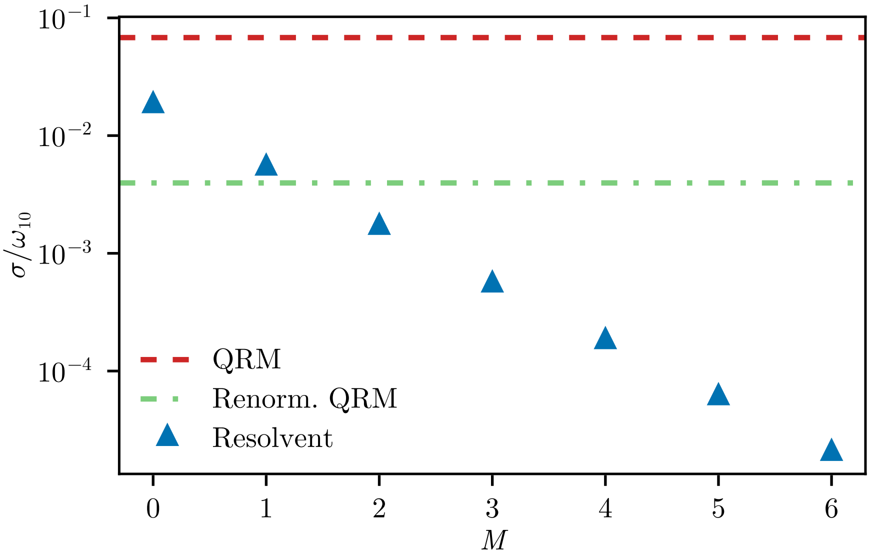

Figure 2.13: Mean square error of the first 5 excited states with respect to the full model, as a function of the order of the resolvent expansion. The error decreases exponentially with the order of the series M, showing the convergence of the resolvent method. To make a comparison, we show also the QRM and RQRM errors. We used the same parameters as in Fig. 2.10(c) with $g/\omega_c = 0.8$.

determined by the self-energy, corresponds to the order M at which the series is truncated. In the limit of $M \to \infty$, we recover the exact solution.

Figure 2.13 shows the mean square error of the first 5 excited states with respect to the full model, as a function of the order of the resolvent expansion. We observe that the error decreases exponentially with M, showing the convergence of the method. As a comparison, we plot also the QRM (red line) and RQRM (green line) errors. While the resolvent method provides higher accuracy, it remains purely numerical. In contrast, the SW approach developed in the previous subsections enables the analytical derivation of an effective Hamiltonian, *i.e.* the RQRM, which already provides a significant improvement in accuracy.

2.3.5 Impact of the renormalization on the observables

In the previous subsections, we have established that the renormalization significantly improves the energy spectrum of the system. However, a comprehensive understanding requires also examining how renormalization influences other physical quantities. In the following, taking the cavity QED case as an example, we analyze how the renormalization affects both photonic and atomic observables and matrix elements.

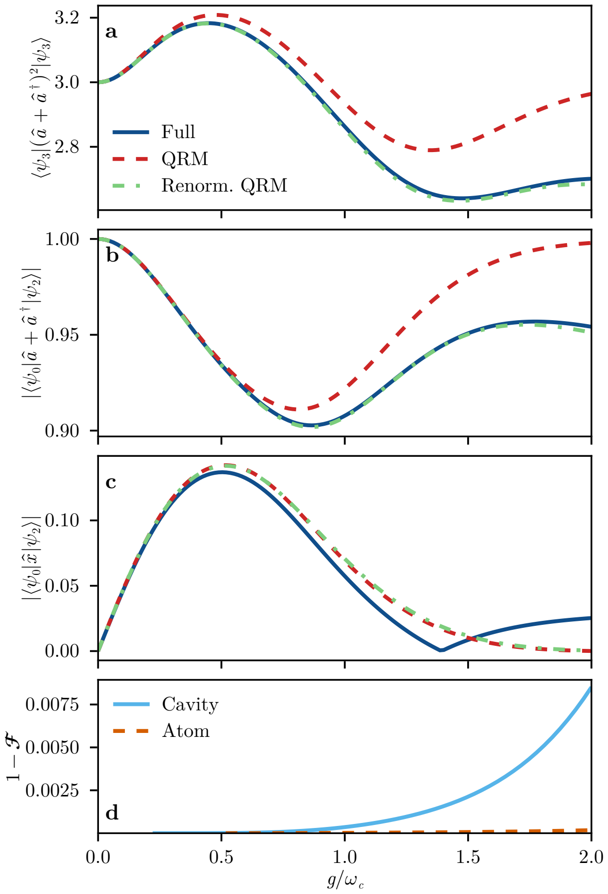

Figure 2.14: **(a)** Expectation value of $(\hat{a}+\hat{a}^\dagger)^2$ on the third excited state of the full model (blue solid), QRM (red dashed) and the RQRM (green dash-dotted), as a function of the coupling strength g/ω_c. The renormalized QRM provides more accurate results, even for strong coupling strengths. **(b,c)** Matrix elements of (b) the cavity field $\hat{a}+\hat{a}^\dagger$ and (c) the atomic position operator $\hat{x}$, between the ground and the second excited, as a function of g/ω_c. While in the panel (b) the renormalization improves the accuracy, in the panel (c) it does not. This behavior can be explained by (**d**) the infidelity of the second excited state of the RQRM with respect to the QRM, as a function of g/ω_c, for both the reduced density matrix of the cavity (solid light blue) and the atom (dashed orange).

Figure 2.14(a) shows the expectation value $\langle\psi_3|\,(\hat{a}+\hat{a}^\dagger)^2\,|\psi_3\rangle$ on the third excited state, as a function of the coupling strength g/ω_c. The RQRM provides more accurate predictions, even for large coupling strengths. A similar improvement is observed in Fig. 2.14(b), which displays the matrix element $|\,\langle\psi_0|(\hat{a}+\hat{a}^\dagger)|\psi_2\rangle\,|$, between the ground and the second excited states. Although not directly observable, this quantity is closely related to dissipation rates and line broadening, which play an important role in experimental realizations [84, 85, 137].

Interestingly, Fig. 2.14(c) reveals that renormalization does not improve the accuracy of the matrix element $|\langle\psi_0|\hat{x}|\psi_2\rangle|$, and of many other matter observables. This behavior can be in part understood by observing Fig. 2.14(d), which shows the infidelity $1-\mathcal{F}$ of $|\psi_2\rangle$ between the standard QRM and the RQRM, for the reduced density matrices of the cavity and atom, as a function of g/ω_c. More specifically, the fidelity $\mathcal{F}$ is calculated as:

$$\mathcal{F} = \mathrm{Tr}\left[\sqrt{\sqrt{\hat{\rho}_\mu}\hat{\sigma}_\mu\sqrt{\hat{\rho}_\mu}}\right] , \tag{2.53}$$

where $\hat{\rho}_\mu$ and $\hat{\sigma}_\mu$ are the reduced density matrices for the renormalized and standard QRM, respectively, with μ indicating either the cavity or atom subsystems. The plot reveals that the renormalization does not significantly change the atomic subsystem, compared to the standard QRM, explaining the behavior in Fig. 2.14(c). On the contrary, the degrees of freedom of the cavity are strongly affected by the renormalization to more accurately reproduce the full model. In fact, the operator $\hat{x}$ includes contributions from higher energy levels that cannot be reproduced by the corresponding operator projected into a two-level Hilbert space. Furthermore, the two-level truncation inherently discretizes space [77], introducing intrinsic inaccuracies in atomic observables that persist even after renormalization. These differences explain the contrasting behaviors observed between panels (a,b) and panel (c).

CHAPTER 3

The Dicke and Hopfield models: from few-atom to effective bosonic models

In the previous chapter, we discussed in detail the physics of a single atom interacting with a single mode of the electromagnetic field, from the derivation of the quantum Rabi model to its spectral properties and the renormalization of its parameters. A natural question that follows is how this picture changes when not just one, but several atoms interact with the same field mode. Moreover, one may wonder what happens when the number of atoms becomes very large, approaching the thermodynamic limit.

These questions form the subject of the present chapter, where we will introduce two cornerstone models of quantum optics: the Dicke model and the Hopfield model. Both have been extensively studied in the literature and have historically provided crucial insights into the collective behavior of light-matter systems. The Dicke model has been firstly introduced for the description of a collection of two-level atoms coupled to a single electromagnetic mode, while the Hopfield model has been independently developed for describing the interaction between two bosonic modes, one representing the electromagnetic field and the other the collective excitations of the polarization density. In the following, we will show how the usual Dicke model must be extended to include the self-polarization term (in the dipole gauge) when describing systems whose interactions are through electric dipoles. This additional term is essential to ensure the physical consistency of the model in the ultrastrong and deep strong coupling regimes, as well as to guarantee its gauge invariance. Furthermore, we will demonstrate how this extended Dicke model naturally converges to the Hopfield model in the thermodynamic limit, through the analysis of both the energy spectrum and the emission properties of the system, considering both collective as well as individual reservoirs.

Specifically, we will begin by studying the interaction between a few two-level atoms and a single electromagnetic mode, with particular attention to the resulting energy spectrum and emission properties. We will then extend the analysis to systems composed of many atoms, where collective phenomena emerge, including the appearance of effective bosonic modes that describe the collective excitations of the atomic ensemble. Finally, we will address the thermodynamic limit, in which the number of atoms tends to infinity, and examine how this limit naturally leads to an effective bosonic description provided by the Hopfield model. Subsequently, we will examine the differences that emerge when the self-polarization term in the dipole-gauge Hamiltonian is either included or neglected. While this term is typically omitted in the standard Dicke model, its presence is essential to guarantee gauge invariance and ensure the stability of the system in the USC and DSC regimes. Moreover, as we will show in Section 3.2, it is precisely this term that governs the convergence of the extended Dicke model to the Hopfield model in the thermodynamic limit. Finally, we will analyze how different forms of coupling to the external environment, namely different dissipation channels, influence the emission properties of the system. In particular, we will compare two distinct scenarios: one where each atom interacts *individually* with its own independent bath, and another where all atoms couple *collectively* to a common bath. As we will see, the choice between individual and collective dissipation channels results in qualitatively distinct emission features.

In this chapter, we will not take into account electrostatic interactions between atoms. These interactions have been at the center of an extensive debate in the literature, particularly in connection with superradiant phase transitions, since they can substantially alter the system's behavior. For the sake of simplicity, however, we will assume that the atoms are sufficiently far apart so that their electrostatic interactions can be safely neglected. This assumption is well justified in many experimental settings, where individual atoms are placed inside a cavity or resonator and their mutual distance is large enough. A detailed discussion of the role of electrostatic interactions, and of how they may affect the system properties, will be provided in Chapter 4.

This chapter is organized as follows. In Section 3.1, we investigate the interaction between a small number of two-level systems and a single bosonic mode, focusing on the evolution of the energy spectrum as a function of the coupling strength and the number of atoms. Particular attention will be given to the role of the self-polarization term, and to the differences that arise when this term is included or neglected. In Section 3.2, we extend the discussion to ensembles composed of many atoms, where collective phenomena emerge and the system approaches the Hopfield model in the thermodynamic limit. Finally, in Section 3.3, we analyze the emission spectra of both few- and many-atom systems, emphasizing the influence of different dissipation channels. The results presented in this chapter are based on Ref. [5], where a detailed analysis of the energy spectrum and emission properties of few-atom to many-atom systems, from the weak to the DSC regimes, is presented.

3.1 Few atoms interacting with a bosonic mode

In this section, we investigate the interaction between a few two-level atoms and a single mode of the electromagnetic field. This scenario is particularly insightful, as it already reveals the onset of collective atomic behavior, such as the enhancement of the effective light-matter coupling strength and the subsequent reduction of the energy gaps in the level anticrossings, allowing us to examine how these collective effects modify the system's properties. The analysis presented here will serve as a foundation for the study of many-atom systems in the following section. This study is also of direct experimental relevance in both cavity and circuit QED. In particular, circuit QED platforms enable the engineering of setups where a small number of artificial atoms (superconducting qubits) are coupled to a single resonator mode, making them ideal testbeds for exploring the physics of few-emitter systems.

Our analysis will focus in particular on the energy spectrum and emission properties of the system across different coupling regimes, ranging from weak to USC and DSC, as the number of emitters increases. Special attention will be devoted to the role of the self-polarization term in the dipole gauge Hamiltonian. Although often neglected, this term, which plays the same role as the A^2 contribution in the Coulomb gauge, is crucial for ensuring the physical consistency of the model and the stability of the system in the USC and DSC regimes.

Finally, we will examine how different types of dissipation channels affect the emission properties. Specifically, we will compare the case where each atom couples *individually* to its own independent resorvoir with the case where all atoms interact *collectively* with a common resorvoir, highlighting the different spectral features that arise in the two scenarios.

3.1.1 The Hamiltonian in dipole and Coulomb gauges

Let us consider a system composed of N identical two-level systems (TLSs) interacting with a single bosonic mode. This framework can describe either natural atoms, in the two-level approximation, interacting with a single-mode cavity or superconducting qubits coupled to a resonator. In the present chapter, we will not take into account the contributions of the electrostatic interactions between the atoms, which will be discussed in detail in Chapter 4. In cavity QED, this assumption is justified when the atoms are sufficiently far apart from each other, such that the dipole-dipole interactions can be neglected. In the case of superconducting qubits, this assumption is equivalent to consider configurations where the qubits are not directly coupled to each other, but only interacting via the common mode of the resonator.

The total Hamiltonian of the system in the dipole gauge can be derived by generalizing the single-atom Hamiltonian in Eq. (2.6). Namely, in the dipole approximation and two-level truncation, the resulting Hamiltonian for N atoms reads

$$\hat{\mathcal{H}}_{\mathrm{D}} = \hbar\omega_c \hat{a}^\dagger \hat{a} + \frac{\hbar}{2}\sum_i^N \omega_a^{(i)} \hat{\sigma}_z^{(i)} - i\hbar\lambda\omega_c(\hat{a} - \hat{a}^\dagger)\sum_i^N \hat{\sigma}_x^{(i)} + \hbar\lambda^2\omega_c\left(\sum_i^N \hat{\sigma}_x^{(i)}\right)^2 , \quad (3.1)$$

where $\hat{a}$ ($\hat{a}^\dagger$) is the annihilation (creation) operator of the bosonic mode with frequency ω_c, and $\hat{\sigma}_\alpha^{(i)}$ (with $\alpha = x, y, z$) are the Pauli operators for the i-th TLS with transition frequency $\omega_a^{(i)}$. The parameter $\lambda = \eta/\sqrt{N}$ is the effective single-atom coupling, where η is the collective normalized coupling strength, defined as $\eta = g/\omega_c$. We are implicitly assuming that all atoms are coupled with the same strength to the bosonic mode, which is a valid assumption if they are located within a region of space much smaller than the wavelength of the mode.

If all the atoms are identical, as we are assuming here, $\omega_a^{(i)} = \omega_a$ for all i, and thus we can introduce the collective spin operators $\hat{J}_\alpha = \frac{1}{2}\sum_i^N \hat{\sigma}_\alpha^{(i)}$, which satisfy the angular momentum commutation relations $[\hat{J}_\alpha, \hat{J}_\beta] = i\epsilon_{\alpha\beta\gamma}\hat{J}_\gamma$, where $\epsilon_{\alpha\beta\gamma}$ is the Levi-Civita symbol. The total spin operator is given by $\hat{\mathbf{J}}^2 = \hat{J}_x^2 + \hat{J}_y^2 + \hat{J}_z^2$, with eigenvalues $j(j+1)$, where j can take values from 0 (or 1/2) to $N/2$, depending on whether N is even or odd. The Dicke states, which are the simultaneous eigenstates of $\hat{\mathbf{J}}^2$ and $\hat{J}_z$, are denoted as $|j, m\rangle$, where m is the eigenvalue of $\hat{J}_z$ and can take values from $-j$ to j in integer steps. With these definitions, the Hamiltonian in Eq. (3.1) can be rewritten as

$$\hat{\mathcal{H}}_{\mathrm{D}} = \hbar\omega_c \hat{a}^\dagger \hat{a} + \hbar\omega_a \hat{J}_z - i2\hbar\lambda\omega_c(\hat{a} - \hat{a}^\dagger)\hat{J}_x + 4\hbar\lambda^2\omega_c \hat{J}_x^2 \, . \quad (3.2)$$

The Hamiltonian in Eq. (3.2) can be regarded as an extended version of the well-known Dicke Hamiltonian [18, 22], as it includes the transverse self-polarization term $\propto \hat{J}_x^2$. This additional contribution is essential for a consistent description of the system in the non-perturbative USC and DSC regimes. For convenience, in the following we will refer to the Hamiltonian in Eq. (3.2) as *extended Dicke model*, while using the nomenclature *standard Dicke model* (or simply *Dicke model*) for the case when the $\hat{J}_x^2$ term is omitted. As we will show in Section 3.2, the $\hat{J}_x^2$ term also plays a crucial role in ensuring the gauge invariance of the model and dictates the convergence to the Hopfield model in the thermodynamic limit.

To obtain a unitary equivalent Hamiltonian in the Coulomb gauge, we apply the unitary transformation $\hat{\mathcal{U}} = \exp\left(-2i\lambda(\hat{a}+\hat{a}^\dagger)\hat{J}_x\right)$, defined directly in the truncated Hilbert space of the TLSs [77, 87, 128]. This procedure preserves the gauge invariance of the model, as discussed in Section 2.1.1. Similiarly to the single-atom case, the bosonic operators are not gauge invariant, transforming as $\hat{a} \to \hat{\mathcal{U}}\hat{a}\hat{\mathcal{U}}^\dagger = \hat{a} + 2i\lambda\hat{J}_x$. The resulting Hamiltonian in the Coulomb gauge reads

$$\hat{\mathcal{H}}_\mathrm{C} = \hbar\omega_c\hat{a}^\dagger\hat{a} + \hbar\omega_a\left[\hat{J}_z\cos\big(2\lambda(\hat{a}^\dagger+\hat{a})\big) + \hat{J}_y\sin\big(2\lambda(\hat{a}^\dagger+\hat{a})\big)\right]. \tag{3.3}$$

3.1.2 Energy spectrum: the importance of the self-polarization term

In this section, we will study the energy spectrum of the Hamiltonians in Eqs. (3.2) and (3.3), focusing in particular on the differences that arise when including or omitting the self-polarization term.

Let us first define the basic nomenclature of the energy levels of the system. In the absence of light-matter interaction ($\lambda = 0$), the eigenstates of the system are simply given by the tensor product of the Fock states of the bosonic mode and the Dicke states of the atomic ensemble, *i.e.* $|n\rangle \otimes |j,m\rangle$, where n is the number of photons in the mode, and j and m are the quantum numbers associated to the collective spin operators, as defined in Section 3.1.1.

However, when the light-matter interaction is turned on ($\lambda \neq 0$), the eigenstates of the system are no longer separable, and they become entangled states of the bosonic mode and the atomic ensemble. In particular, if we consider weak coupling strengths, the counter-rotating terms in the Hamiltonian can be neglected (rotating wave approximation, RWA), and thus we recover the well-known Tavis-Cummings model [138]. In this case, the eigenstates of the system can be classified according to the total number of excitations, which is a conserved quantity for the model's Hamiltonian, defined as the eigenvalue of the operator $\hat{N}_\mathrm{exc} = \hat{a}^\dagger\hat{a} + \hat{J}_z + j$. In this case, the eigenstates eigenstates of the Hamiltonian can be written as superpositions of states with the same total number of excitations.

If the coupling strength is increased even more, the counter-rotating terms can no longer be neglected, and the total number of excitations is no longer a conserved quantity, and thus the eigenstates of the system can no longer be classified accordingly, as they become more complex entangled states of the bosonic mode and the atomic ensemble. However, the parity of the total number of excitations, defined as the eigenvalue of the operator $\hat{\Pi} = \exp\left(i\pi\hat{N}_\mathrm{exc}\right)$, remains a conserved quantity even in the USC and DSC regimes. This means that the eigenstates of the system can be classified according to their parity, being either even or odd.

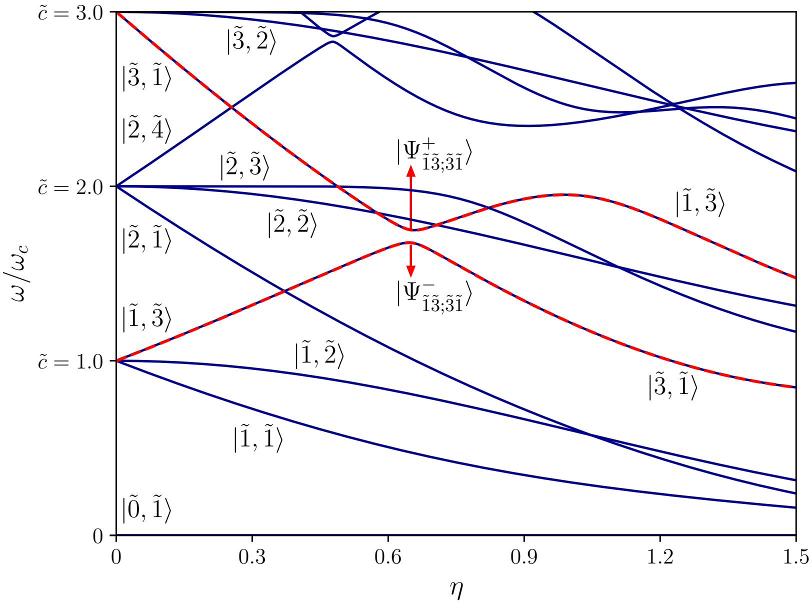

Figure 3.1: Energy states, and their corresponding labeling, of the extended Dicke Hamiltonian in Eq. (3.2) for $N = 2$ TLSs, as a function of the normalized coupling strength $\eta = \lambda\sqrt{N}$. The energy levels are labeled using the notation $\left|\tilde{c}, \tilde{k}\right\rangle$, where $\tilde{c}$ is the excitation number of the multiplet at $\eta = 0$ and $\tilde{k}$ indicates the levels in ascending order of energy within each multiplet. Two levels, $\left|\tilde{1}, \tilde{3}\right\rangle$ and $\left|\tilde{3}, \tilde{1}\right\rangle$, are highlighted in red to evidence an avoided level crossing occurring at approximately $\eta \sim 0.65$. On the right of the anti-crossing, the energy levels exchange character, and thus, we effectively swap the labels of the two states.

In the following, we will label the eigenstates of the system as $\left|\tilde{c}, \tilde{k}\right\rangle$, where $\tilde{c}$ indicates the total number of excitations in the RWA limit, and $\tilde{k}$ is an index that orders the states within each excitation manifold according to their energy, starting from the lowest one (indicated by 1). For example, the ground state of the system will be denoted as $\left|\tilde{0}, \tilde{1}\right\rangle$, while the first excited state will be $\left|\tilde{1}, \tilde{1}\right\rangle$, and so on (see Fig. 3.1). Notice that some ambiguity in labeling the energy levels persists in the vicinity of the anti-crossing regions. When two levels exhibit a small (with respect to the bare resonance frequencies) avoided level crossing, we label them describing explicitly the superposition at the anticrossing and nearby it. Outside the avoided level crossing region, we choose to label the states as if they would cross. As a result, to the right of the anti-crossing, the labels of the states are exchanged with respect to the left.

An example of this labeling scheme is shown in Fig. 3.1, where we plot the energy levels of the extended Dicke Hamiltonian in Eq. (3.2) for $N = 2$ TLSs as a function of the normalized coupling strength η. The two levels $\left|\tilde{1},\tilde{3}\right\rangle$ and $\left|\tilde{3},\tilde{1}\right\rangle$ are highlighted in red to evidence an avoided level crossing occurring at approximately $\eta \sim 0.65$. This anti-crossing is characterized by the formation of hybridized superposition states, denoted as $\left|\Psi^{\pm}_{\tilde{1}\tilde{3};\tilde{3}\tilde{1}}\right\rangle$. At the anti-crossing, the energy levels exchange character, and thus, we effectively swap the labels of the two states.

Let us now analyze the energy spectrum of the system as a function of the normalized coupling strength $\eta = \lambda\sqrt{N}$, comparing the results obtained with the extended Dicke Hamiltonian in Eq. (3.2) (including the self-polarization term) and the standard Dicke Hamiltonian (without the self-polarization term). In Fig. 3.2, we plot the energy levels of both Hamiltonians for $N = 1, 2, 3$ TLSs, as a function of η on a logarithmic scale, for the resonant case $\omega_a = \omega_c$. The energy levels are plotted up to the third excitation manifold, considering the ground state energy as reference. As we can see from Fig. 3.2, the energy spectra of the two Hamiltonians are very similar in the weak and strong coupling regimes, while significant differences arise in the USC and DSC regimes, especially for increasing number of TLSs. In particular, for $N = 1$ TLS in Fig. 3.2(a), the two Hamiltonians coincide as the self-polarization term reduces to a constant energy shift, since $\hat{J}_x^2 = \hat{\sigma}_x^2/4 = \hat{I}/4$ (see discussion in Section 2.1.1). However, in Fig. 3.2(b,c), we observe that dropping the self-polarization term significantly alters the behavior of the energy levels. In the absence of this term, the energy levels diverge and do not approach the light-matter decoupling as $\eta \gg 1$, with the exception of a couple of levels for each multiplet, which become degenerate in the DSC regime.

On the contrary, in the DSC regime, the energy levels of the extended Dicke Hamiltonian in Eq. (3.2) correctly approach the light-matter decoupling [55, 56], where the bosonic mode and the atomic ensemble behave as two independent systems. In this limit, the energy levels tend to those of a bare quantum harmonic oscillator with frequency ω_c, *i.e.* $E_n = n\hbar\omega_c$. Indeed, for $\lambda \gg 1$, the $\hat{J}_z$ term can be regarded as a small perturbation of the system's Hamiltonian. In this limit, the eigenstates of the system become 2^N-fold degenerate and can be approximated as displaced harmonic oscillator states, with displacements determined by the collective spin state of the atomic ensemble. More specifically, the Hamiltonian in Eq. (3.2) can be split as the sum of two contributions, namely $\hat{\mathcal{H}}_{\mathrm{D}} = \hat{\mathcal{H}}'_0 + \hat{\mathcal{H}}'_1$, where

$$\hat{\mathcal{H}}'_0 = \hbar\omega_c\hat{a}^\dagger\hat{a} + 2i\hbar\lambda\omega_c\hat{J}_x\left(\hat{a}^\dagger - \hat{a}\right) + 4\hbar\lambda^2\omega_c\hat{J}_x^2 = \hbar\omega_c\hat{\mathcal{A}}^\dagger\hat{\mathcal{A}}\,, \tag{3.4}$$

$$\hat{\mathcal{H}}'_1 = \hbar\omega_a\hat{J}_z\,, \tag{3.5}$$

with $\hat{\mathcal{A}} = \hat{a} + 2i\lambda\hat{J}_x$ being the shifted bosonic operator, satisfying the canonical commutation relation $[\hat{\mathcal{A}}, \hat{\mathcal{A}}^\dagger] = 1$. Hence, the Hamiltonian $\hat{\mathcal{H}}'_0$ describes a dis-

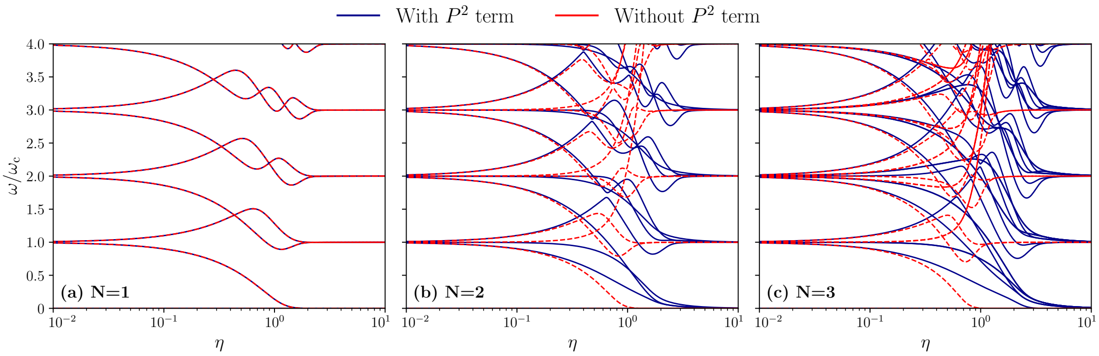

Figure 3.2: Comparison between the lowest energy eigenvalues of the generalized Dicke Hamiltonian in Eq. (3.2) (blue solid lines) and those of the standard Dicke Hamiltonian, without the self-energy polarization term (red dashed lines). The energy levels are shown as a function of the normalized coupling strength $\eta = \lambda\sqrt{N}$ on a logarithmic scale for **(a)** $N = 1$, **(b)** $N = 2$, and **(c)** $N = 3$ TLSs, for the resonant case $\omega_a = \omega_c$. The energy levels are displayed considering the ground state energy as reference.

placed harmonic oscillator with frequency ω_c, shifted by an amount depending on $\hat{J}_x$. The remaining term $\hat{\mathcal{H}}'_I = \hbar\omega_a\hat{J}_z$ can be safely treated as a perturbation in the limit $\lambda \gg \omega_a$, ω_c, since its matrix elements between the eigenstates of $\hat{\mathcal{H}}'_0$ scale as $\exp\{(-2\lambda^2)\}$. A detailed derivation of this result, together with the nomenclature of the energy levels, can be found in Ref. [5].

As a final note, we observe that the matter-decoupling is not recovered in the standard Dicke Hamiltonian, precisely for the absence the self-polarization term, which is essential to reconstruct in $\hat{\mathcal{H}}'_0$ the shifted bosonic operator $\hat{\mathcal{A}}$, leading to the displaced harmonic oscillator.

Finally, let us present the energy spectrum of the extended Dicke Hamiltonian in Eq. (3.2) for systems composed of up to $N = 6$ TLSs. A detailed analysis of Fig. 3.3(b), corresponding to the case of $N = 2$ emitters, reveals an avoided level crossing around $\eta = 0.65$ (highlighted in green), as already previously observed. This crossing involves the highest level of the $\tilde{c} = 1$ multiplet, namely $\big|\tilde{1}, \tilde{3}\big\rangle$, and the lowest level of the $\tilde{c} = 3$ multiplet, $\big|\tilde{3}, \tilde{1}\big\rangle$.

In the $N = 3$ case, shown Fig. 3.3(c), two avoided level crossings involving $\big|\tilde{1}, \tilde{3}\big\rangle$ are observed. The first, marked in orange, is analogous to $N = 2$ case and couples $\big|\tilde{1}, \tilde{3}\big\rangle$ to $\big|\tilde{3}, \tilde{1}\big\rangle$. The second, highlighted in red, is characterized by a narrower energy gap and involves the interaction with the state $\big|\tilde{3}, \tilde{3}\big\rangle$. These avoided level crossings are higher-order processes enabled by the interaction terms that do not conserve the number of excitations (namely, the counter-rotating terms,

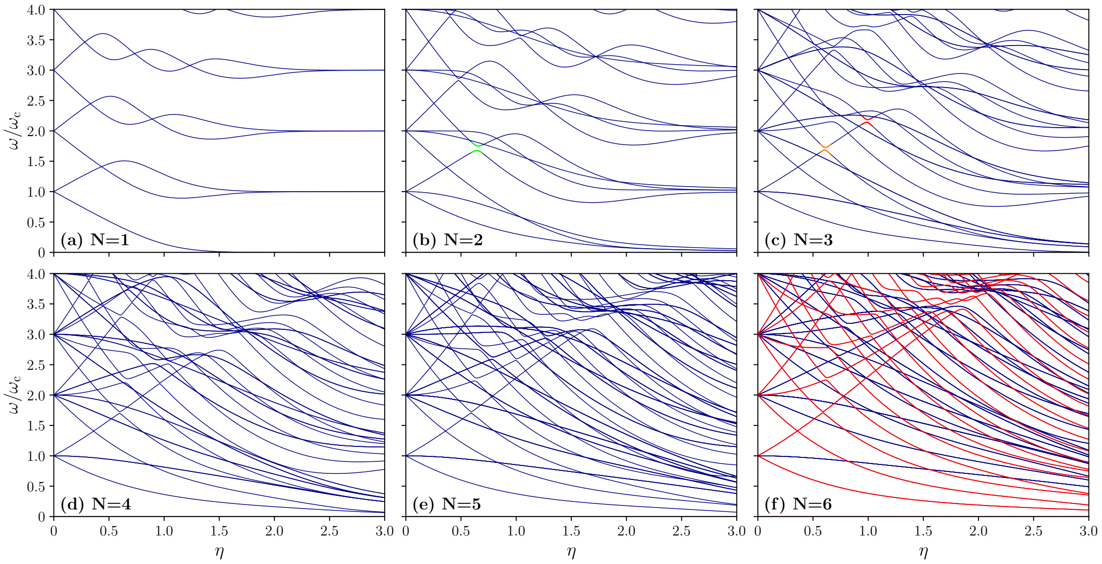

Figure 3.3: **(a-f)** Lowest energy eigenvalues of the generalized Dicke Hamiltonian in Eq. (3.2) for systems composed by $N = 1$ up to $N = 6$ TLSs, as a function of the normalized coupling strength $\eta = \lambda\sqrt{N}$. All the energy levels are taken with the ground state energy as reference. Increasing the number of quantum emitters, the number of energy levels rises exponentially as 2^N. Multi-dipole systems present avoided level crossings between energy levels corresponding to states with the same parity, highlighted in green (b) for N=2, and in orange and red (c) for $N = 3$. These avoided crossings become narrower when the number of TLSs increases. (f) The red-highlighted energy levels correspond to the Dicke states belonging to the maximum total angular momentum manifold, $j = N/2$.

which however conserve the parity), hence coupling states belonging to different excitation manifolds.

This pattern persists as the number of emitters increases. We notice that the avoided crossings become progressively narrower increasing the number of emitters, scaling as $1/\sqrt{N}$. In particular, for $N = 5$ and $N = 6$ in Fig. 3.3(e,f), the energy gaps of the avoided level crossings become extremely small, so much so that the levels appear to cross. These crossings will become exact in the thermodynamic limit, as we will see in the next section.

Finally, we observe that the red-highlighted energy levels in Fig. 3.3(f) correspond to the Dicke states belonging to the maximum total angular momentum manifold, $j = N/2$. These states are of particular interest because they are symmetric with respect to the exchange of any two atoms and thus embody the collective behavior of the atomic ensemble. As we will see in the next sections, these states play a crucial role in the thermodynamic limit and in the emergence of collective phenomena, especially in the emission spectra.

3.2 Many atoms and the thermodynamic limit

In this section, we extend the previous analysis to systems composed of many atoms (up to $N = 100$), where collective phenomena emerge. In particular, we explicitly study how the system approaches the thermodynamic limit. In this limit, the number of atoms N tends to infinity, while the coupling strength λ, scaling as $1/\sqrt{N}$, is compensated by the collective enhancement effects of the coupling due to the formation of the collective modes, so that the effective coupling $\eta = \lambda\sqrt{N}$ remains finite. As a consequence, the total interaction energy between the atomic ensemble and the bosonic field mode also remains finite in the thermodynamic limit. From an experimental perspective, for instance, this situation corresponds to a collection of natural atoms or nanoparticles coupled to the same cavity or resonator mode (see, *e.g.*, Ref. [139]), as we will discuss in more detail in Chapter 4.

3.2.1 Bosonization of the atomic ensemble and thermodynamic limit

In Section 3.1.1, we introduced Eq. (3.2) to describe systems with a finite number N of emitters interacting with a single-mode cavity electromagnetic field in the dipole gauge. We now extend this study, considering the thermodynamic limit ($N \to \infty$), while keeping the effective coupling η finite. It is well established that, in this limit, the collective behavior of the atomic ensemble dominates the system's dynamics, leading to the emergence of effective bosonic modes that describe the collective excitations of the atomic ensemble [21]. These collective modes naturally emerge from the symmetric states belonging to the maximum total angular momentum manifold, $j = N/2$, since they exhibit the strongest effective coupling to the bosonic mode.

A standard tool to introduce the collective modes is the Holstein-Primakoff mapping [11, 140, 141], which allows to represent the spin operators $\hat{J}_\alpha$ in terms of bosonic operators, $\hat{b}$ and $\hat{b}^\dagger$, satisfying the canonical commutation relations $[\hat{b}, \hat{b}^\dagger] = 1$. The Holstein-Primakoff transformations are defined as

$$\hat{J}_z = \hat{b}^\dagger \hat{b} - j\,, \tag{3.6a}$$

$$\hat{J}_+ = \hat{b}^\dagger \sqrt{2j - \hat{b}^\dagger \hat{b}}\,, \tag{3.6b}$$

$$\hat{J}_- = \sqrt{2j - \hat{b}^\dagger \hat{b}}\,\hat{b}\,, \tag{3.6c}$$

where $\hat{J}_\pm = \hat{J}_x \pm i\hat{J}_y$ are the raising and lowering operators, and j is the maximum total spin, which for a system of N identical TLSs is given by $j = N/2$. This mapping is particularly useful in the thermodynamic limit, where the number of atoms becomes very large. Indeed, if the system is not macroscopically excited, the number of bosonic excitations $\left\langle \hat{b}^\dagger \hat{b} \right\rangle$ is much smaller than the maximum total spin j, and thus we can approximate the square root in Eqs. (3.6b) and (3.6c) as $\sqrt{2j - \hat{b}^\dagger \hat{b}} \approx \sqrt{2j} = \sqrt{N}$. Applying this transformations to Eq. (3.2), we can express the dipole-gauge Hamiltonian for an infinite collection of TLSs in terms of bosonic operators as

$$\hat{\mathcal{H}}_D^{(\infty)} = \hbar\omega_c \hat{a}^\dagger \hat{a} + \hbar\omega_a \hat{b}^\dagger \hat{b} + i\hbar\eta\omega_a(\hat{a}^\dagger - \hat{a})(\hat{b}^\dagger + \hat{b}) + \hbar\eta^2\omega_a(\hat{b}^\dagger + \hat{b})^2, \tag{3.7}$$

where we used the relation $\eta = \lambda\sqrt{N}$. The last term of this equation originates from the self-polarization term in Eq. (3.2). We observe that the resulting Hamiltonian in Eq. (3.7) is formally equivalent to the Hopfield Hamiltonian for a single-mode electromagnetic resonator interacting with a bosonic polarization wave [128, 142], thus confirming that the Hopfield model provides the correct description of the transverse sector of a light-matter system in the thermodynamic limit.

An analogous procedure can be followed to obtain the Coulomb-gauge Hamiltonian in this limit. Importantly, we point out that it can also be derived by applying a suitable unitary transformation to the Hamiltonian in Eq. (3.7). For consistency, similiarly to what was done in Section 2.1.1 for the two-level truncation, to obtain the Coulomb gauge Hamiltonian in the thermodynamic limit we need to first apply the Holstein-Primakoff mapping directly to the exponent of the unitary operator $\hat{\mathcal{U}} = \exp\left(-2i\lambda(\hat{a} + \hat{a}^\dagger)\hat{J}_x\right)$ that connects the two gauges. In particular, using Eqs. (3.6), we obtain $\hat{\mathcal{U}} = \exp\left(-i\eta(\hat{a} + \hat{a}^\dagger)(\hat{b}^\dagger + \hat{b})\right)$ [87, 128]. By applying this operator to the Hamiltonian in Eq. (3.7), we obtain the Coulomb gauge Hamiltonian in the thermodynamic limit, which reads

$$\hat{\mathcal{H}}_C^{(\infty)} = \hbar\omega_c \hat{a}^\dagger \hat{a} + \hbar\omega_a \hat{b}^\dagger \hat{b} - i\hbar\eta\omega_a(\hat{b}^\dagger - \hat{b})(\hat{a}^\dagger + \hat{a}) + \hbar\eta^2\omega_a(\hat{a}^\dagger + \hat{a})^2\,, \tag{3.8}$$

where the last term represents the usual diamagnetic A^2 contribution in the Coulomb-gauge Hamiltonian.

3.2.2 Many-atom energy spectrum and convergence to the Hopfield model

Let us now analyze the energy spectra of the Hamiltonians in Eqs. (3.7) and (3.8), which are unitarily equivalent and thus yield identical results, and compare them with the results obtained for finite number of TLSs in Section 3.1.1. In particular, our primary focus is to examine how the energy spectrum converges to that of the Hopfield model in the thermodynamic limit.

Since the Hamiltonian in Eqs. (3.7) and (3.8) is quadratic in the bosonic operators, its energy spectrum can be obtained analytically through a Bogoliubov transformation [128, 142]. The resulting polaritonic eigenfrequencies are given by

$$E_\pm/\hbar = \omega_c\sqrt{\frac{1}{2}\left(1+\frac{\omega_a^2}{\omega_c^2}+2\eta^2 \pm \sqrt{\left(1-\frac{\omega_a^2}{\omega_c^2}\right)^2+4\eta^2\left(1+\frac{\omega_a}{\omega_c}\right)^2}\right)}\,, \tag{3.9}$$

where E_- and E_+ denote to the lower and upper polariton branches, respectively. The resulting energy spectrum is plotted in Fig. 3.4 as orange solid lines for the resonant case $\omega_a = \omega_c$, as a function of the normalized coupling strength η. We notice that the full energy spectrum is built from linear combinations of these polariton states, *i.e.* $E_{n_-,n_+} = n_-E_- + n_+E_+$, where n_- and n_+ are non-negative integers indicating the number of excitations in the lower and upper polariton branches, respectively.

Fig. 3.4 also shows the energy levels of the extended Dicke Hamiltonian in Eq. (3.2) belonging to the maximum angular momentum manifold, $j = N/2$, for systems composed of $N = 10, 50, 100$ TLSs. For comparison, the corresponding energy levels of the Hopfield model in Eqs. (3.7) and (3.8) are superimposed. As expected, increasing N, drives the spectrum of the extended Dicke model towards that of the Hopfield model, hence confirming that the latter correctly describe the physics of the system in the thermodynamic limit. The discrepancies between the two models (due to the finite number of emitters, although very large) are more pronounced in the USC and DSC regimes and for higher excited states, becoming progressively negligible as N grows. In addition, we observe that the avoided level crossings present in the energy spectra of the extended Dicke Hamiltonian for finite N become gradually narrower as N increases, ultimately turning into exact crossings in the thermodynamic limit.

Finally, we point out that, if the self-polarization term is omitted in Eq. (3.7), the standard Dicke Hamiltonian in its bosonized form would be recovered, *i.e.*

$$\hat{\mathcal{H}}^{(\infty)}_{\text{Dicke}} = \hbar\omega_c\hat{a}^\dagger\hat{a} + \hbar\omega_a\hat{b}^\dagger\hat{b} + \hbar\eta\omega_a(\hat{a}^\dagger+\hat{a})(\hat{b}^\dagger+\hat{b})\,, \tag{3.10}$$

where we applied the unitary transformation $\hat{a} \to -i\hat{a}$, as commonly done in the literature to express the Dicke Hamiltonian in a more symmetric form [21, 22]. A comprehensive analysis of this model, and in particular of its interaction with the external environment, especially near the critical point, will be presented in Chapter 5. Here, we limit ourselves to point out that the energy spectrum of this Hamiltonian can also be obtained analytically through a Bogoliubov transformation, and it exhibits a superradiant phase transition (SPT) at a critical coupling

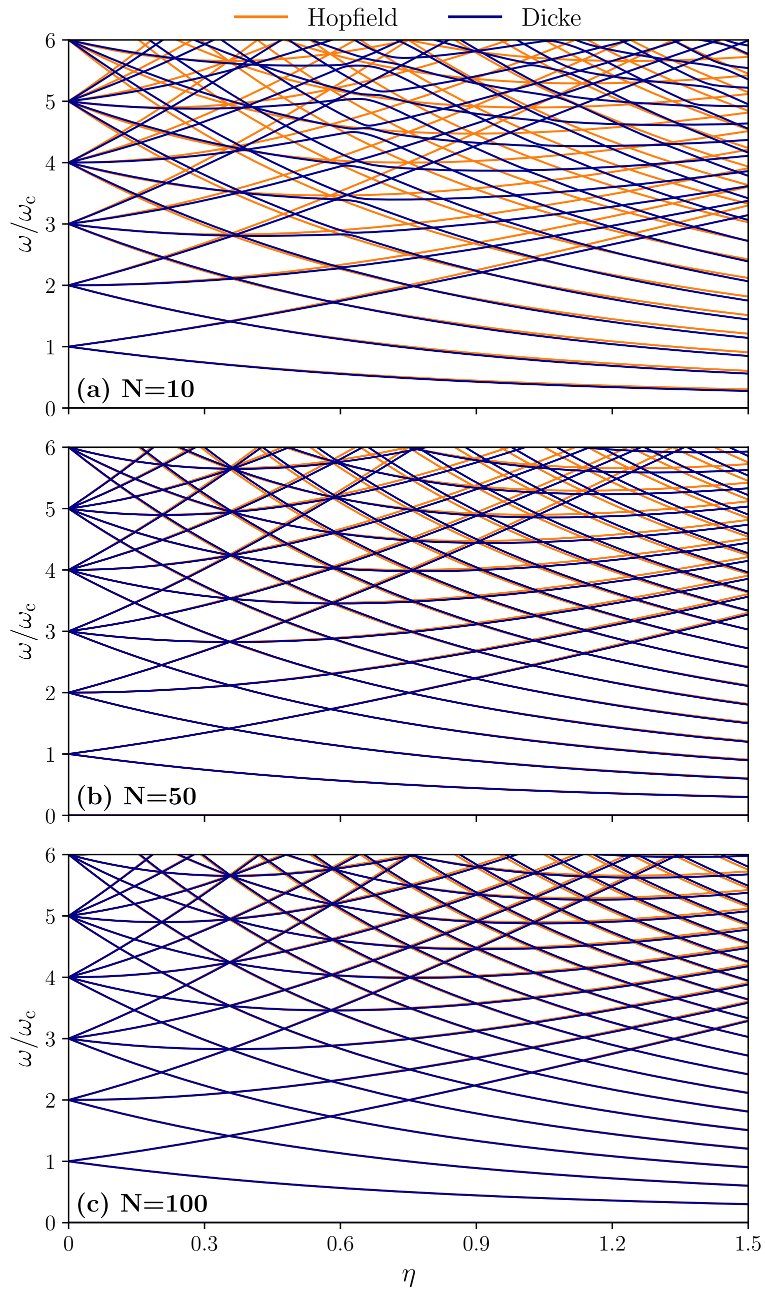

Figure 3.4: Lowest energy eigenvalues of the extended Dicke Hamiltonian belonging to the maximum angular momentum manifold (blue solid lines) for **(a)** $N = 10$, **(b)** $N = 50$, and **(c)** $N = 100$, as a function of the normalized coupling strength η. For comparison, the corresponding energy levels of the Hopfield model are also displayed (orange solid lines).

strength $\eta_c = \sqrt{\omega_c/4\omega_a}$ [19–21]. This transition is characterized by macroscopic occupations of the bosonic modes in the ground state of the system, which becomes two-fold degenerate above the critical coupling strength. Moreover, as discussed in Ref. [92], if the coefficient of the self-polarization term is treated as a free parameter, rather than being fixed by the Thomas-Reiche-Kuhn (TRK) sum rule [143], one obtains a family of models interpolating between the standard Dicke model and the Hopfield model. Indeed, they show that a superradiant phase transition can occur for sufficiently small values of the self-polarization coefficient.

3.3 Emission spectra

In this section, we investigate the incoherent emission spectra of the system and analyze how they evolve as the number of TLSs increases and the thermodynamic limit is approached. The theorical framework required to describe the interaction between the system and its environment in ultrastrongly-coupled systems, and in particular the calculation of emission spectra, has already been introduced in Section 2.2.1. Here, we briefly summarize the main results needed for the present discussion.

The dynamics of the system in the USC and DSC regimes can be accurately described within the generalized master equation (GME) formalism [85]. In this framework, the dynamics is governed by the master equation

$$\dot{\hat{\rho}}(t) = -\frac{i}{\hbar}[\hat{\mathcal{H}}, \hat{\rho}(t)] + \mathcal{L}_{\text{GME}}\hat{\rho}(t)\,, \tag{3.11}$$

where $\hat{\mathcal{H}}$ is the system's Hamiltonian, given in Eq. (3.2), and $\mathcal{L}_{\text{GME}}$ is the Liouvillian superoperator describing the dissipation processes (see also Eq. (2.24)). Its explicit form can be found in Ref. [85]. The operators appearing in the dissipators of $\mathcal{L}_{\text{GME}}$ determine the system-environment interaction, and thus directly affect the emission properties. In the following, we consider two different scenarios for the emitters: (i) individual atomic decay channels, $\hat{s}^{(j)}_{\text{ind}} = \hat{\sigma}^{(j)}_{-}$ for each j, and (ii) collective atomic decay channel, $\hat{s}_{\text{coll}} = \sum_j \hat{\sigma}^{(j)}_{-}/\sqrt{N}$. For the cavity mode, we consider a single dissipation channel, $\hat{s}_{\text{c}} = \hat{a}$.

The physical observable that couples the system to the external environment is the electric field operator $\hat{E}(r,t)$, and the photon-detection probability is proportional to the normally ordered correlation function of this operator [110, 112]. Importantly, in the USC and DSC regimes, the positive and negative frequency components of the electric field operator must be expressed in the dressed basis of the system, *i.e.* in terms of the eigenstates of the system's Hamiltonian [81, 82]. The emission spectrum is then given by the Fourier transform of the two-time correlation function of the positive and negative frequency components of the electric field operator, as described in Eq. (2.25). Namely,

$$S(\omega) \propto \mathrm{Re} \int_0^\infty \left\langle \hat{E}^-(t+\tau)\hat{E}^+(t) \right\rangle e^{-i\omega\tau} d\tau \,, \tag{3.12}$$

where $\langle \cdots \rangle = \mathrm{Tr}\{\hat{\rho}_{\mathrm{ss}}(t) \cdots\}$ denotes the expectation value over the system's steady state density matrix $\hat{\rho}_{\mathrm{ss}}(t)$, which is obtained by solving numerically the master equation in Eq. (3.11).

Throughout this section we assume the system is incoherently excited through the quantum emitters. Their continuous-wave incoherent pumping is modeled by coupling them to a thermal (ohmic) bath at an effective temperature $T_a > 0$ (in natural units, $\hbar = k_B = 1$). Unless stated otherwise, we set the cavity bath temperature to $T_c = 0$, while for the emitters we fix $T_a/\omega_c = 0.15$. The emission spectra are calculated as a function of the normalized coupling strength η, ranging from the weak to the DSC regimes. For each system we analyze, in addition to the cavity dissipation channel, the case of (i) purely individual atomic dissipation, (ii) purely collective atomic dissipation, and (iii) the coexistence of both channels. For all the numerical calculations of the emission spectra, we use the following bare damping rates: $\gamma_{\mathrm{c}} = 10^{-3}\omega_c$, $\gamma_{\mathrm{coll}} = 10^{-3}\omega_c$ (for the collective qubits reservoir), $\gamma_{\mathrm{ind}} = 10^{-3}\omega_c$ (for the individual qubits reservoirs). When both types of atomic reservoirs are present simultaneously, the dissipation rates γ_{ind} and γ_{coll} are halved to facilitate a consistent comparison.

3.3.1 Incoherent emission spectra for few atoms

Let us begin by analyzing the incoherent emission spectra of systems with a small number of TLSs. The single emitter case has already been examined in detail in Section 2.2.1. Therefore, in this subsection, we focus on the range $N = 2$ to $N = 6$.

We first focus on the $N = 2$ case, whose energy spectrum was already presented in Fig. 3.3(b). The corresponding incoherent emission spectra are shown in Fig. 3.5 for different effetive atomic temperatures $\tilde{T}_a = T_a/\omega_c$, in the resonant condition $\omega_a = \omega_c$ and at fixed normalized coupling strength $\eta = 0.3$. Only individual dissipation channels are considered. The orange line (rhombus marker) corresponds to the effective temperature $\tilde{T}_a = 0.15$, which will also be adopted for all subsequent emission spectra presented in this section. Although somewhat arbitrary, this value of the temperature represents a convenient compromise: it is sufficiently high to prevent an almost exclusive population of the ground state, yet low enough to prevent significant excitation of higher-energy states. As expected, increasing the temperature enables the population of higher excited levels, thus giving rise to additional emission lines. The peaks in Fig. 3.5 occur at the allowed transition frequencies of the system, which will be discussed in more detail below. For the moment, let us only highlight the presence of an emission line at the bare

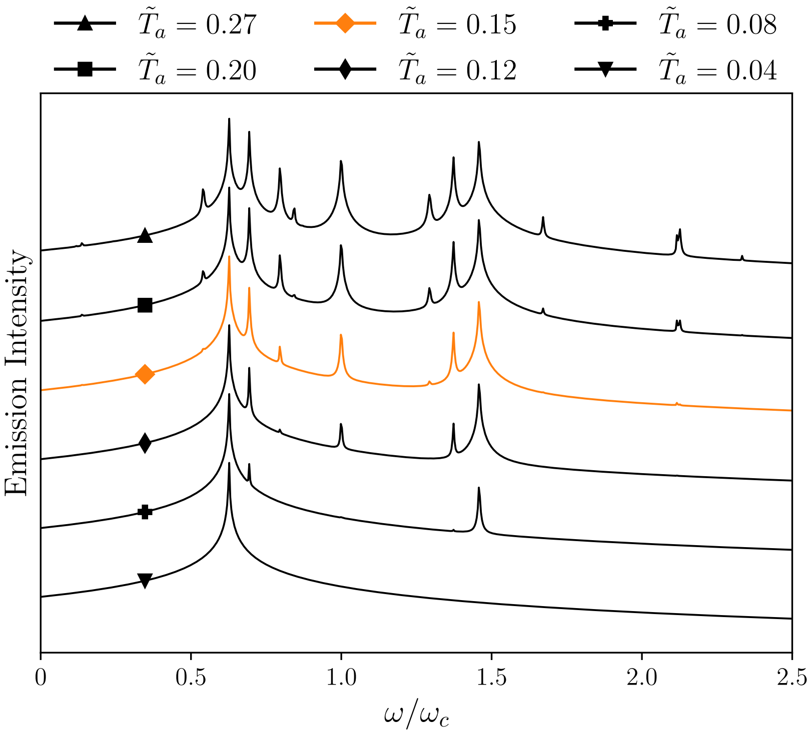

Figure 3.5: Incoherent emission spectra for a system composed of $N = 2$ TLSs for $\eta = 0.3$, with individual dissipation channels. The emission spectra are calculated at different effective temperatures, shown in the legend on top of the figure. For a better comparison, the emission spectra are vertically shifted along the emission intensity axis, which is in a logarithmic scale. The orange spectrum line corresponds to the temperature $\tilde{T}_a = T_a/\omega_c = 0.15$, which is used for all the other emission spectra. Notice the presence of the emission line at $\omega = \omega_c$ for high enough temperatures. We consider the resonant case $\omega_a = \omega_c$.

cavity frequency $\omega = \omega_c$, which becomes more pronounced at higher temperatures. This feature, present only when individual atomic dissipation channels are included, originates from the transitions between states involving antisymmetric matter states (dark states), such as the transitions $\left|\tilde{2}, \tilde{2}\right\rangle \to \left|\tilde{1}, \tilde{2}\right\rangle, \left|\tilde{3}, \tilde{2}\right\rangle \to \left|\tilde{2}, \tilde{2}\right\rangle$ and, more generally, $\left|\tilde{c}+1, \tilde{2}\right\rangle \to \left|\tilde{c}, \tilde{2}\right\rangle$. Obviously, at low temperature, the main contribution comes from the first of these transitions, namely $\left|\tilde{2}, \tilde{2}\right\rangle \to \left|\tilde{1}, \tilde{2}\right\rangle$. The appearance of this emission line is a direct consequence of the individual coupling of the quantum emitters to their respective baths, which enables the population of these (otherwise optically inactive) states, as well as their radiative decay into one another. Such states are characterized by $j = 0$, and therefore exist only for sys-

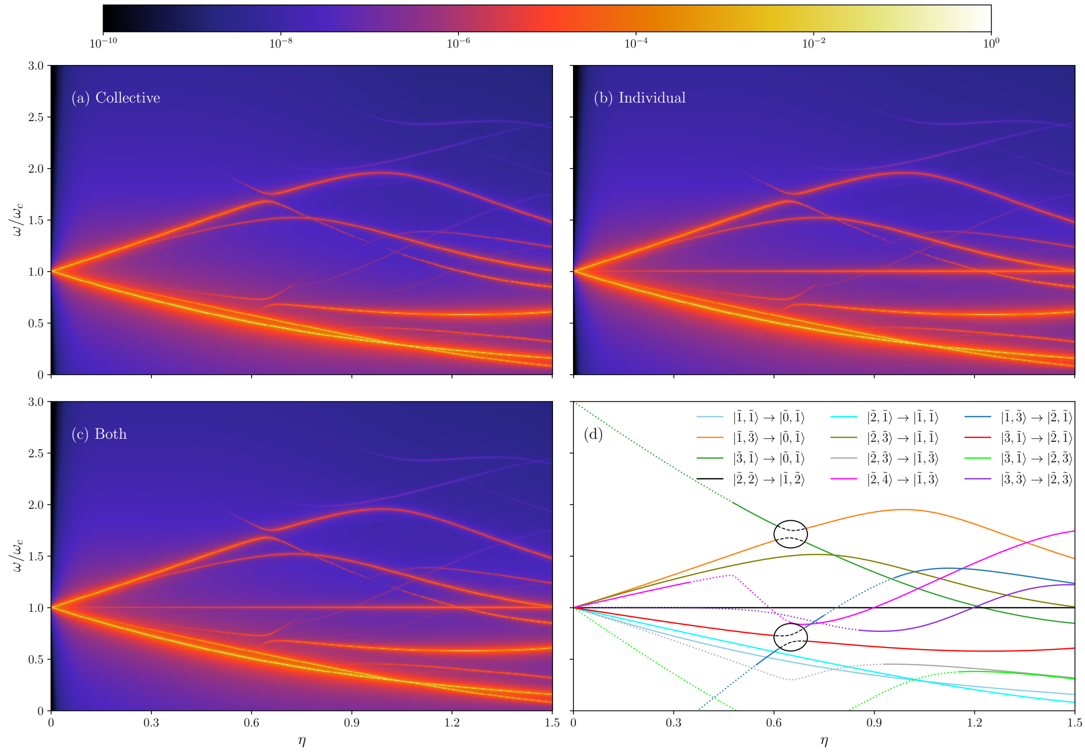

Figure 3.6: **(a-c)** Incoherent emission spectra for a system of $N = 2$ quantum emitters as a function of the normalized coupling strength η. The light-matter system interact with the reservoir in different configurations: (a) collective dissipation channel for the TLSs, (b) individual channels for each TLS, (c) a configuration where both are present. **(d)** Lowest level transitions' energies of the system as function of η. The solid curves represent the transition energies observable in the spectra (a-c), whereas the dotted curves correspond to transition lines that exhibit weak emission or are optically inactive.

tems with an even number of emitters. In the $N = 2$ case, these are antisymmetric two-qubit states with n photons, explicitly given by

$$|n\rangle \otimes \frac{1}{\sqrt{2}}(|1,0\rangle - |0,1\rangle)\,. \tag{3.13}$$

It is straightforward to verify that these states are also eigenstates of the interaction Hamiltonian with zero eigenvalue. Consequently, they remain unaffected by the light-matter coupling and give rise to energy levels that are independent of λ (or, equivalently, η).

To further consolidate this point, we now analyze the incoherent emission spectra for $N = 2$ TLSs, shown in Fig. 3.6, in presence of (a) collective, (b) individual, and (c) combined atomic dissipation channels, as functions of the normalized coupling strength η. This system exhibits a significantly different behavior compared to the single-emitter case presented in Fig. 2.4. In particular, as discussed below, increasing the number of emitters enlarges the Hilbert space, giving rise to a greater number of energy eigenstates and, consequently, to additional emission lines. Although the three cases in Fig. 3.6 share several common spectral features, a key distinction emerges: the appearance of a constant emission line at the frequency $\omega = \omega_c$ in the presence of individual-dissipation reservoirs (see Fig. 3.6(b,c)). This line, already visible at relatively small interaction strengths η, originates (as discussed above) from transitions involving antisymmetric matter states. It turns out that these transitions are forbidden for systems interacting with the bath collectively, explaining their absence in Fig. 3.6(a). The spectral features observed in Fig. 3.6(a-c) can be understood more clearly by comparing them with the lowest transition energies shown in Fig. 3.6(d) as a function of η. Solid curves describe the transition energies which can be observed in the spectra, while the dotted curves correspond to the dark or weakly emitting transitions. The most relevant features in the emission spectra are associated with transitions terminating in the ground state, or, at most, in the lower polariton state of the first excitation manifold. In the weak to moderate coupling regimes, the brightest emission lines correspond to the transitions $\left|\tilde{1}, \tilde{1}\right\rangle \to \left|\tilde{0}, \tilde{1}\right\rangle$ and $\left|\tilde{1}, \tilde{3}\right\rangle \to \left|\tilde{0}, \tilde{1}\right\rangle$. As the number of emitter increases,these transitions progressively evolve into the characteristic emission lines associated with the lower and upper polariton branches of the Hopfield model, respectively.

If more quantum emitters are included, the number of energy levels within a given spectral region also grows exponentially, adding complexity and making the system more challenging to analyze. However, at the effective temperature considered $\tilde{T}_a = 0.15$, many transitions are not sufficiently populated to be observed. As a result, the emission spectra tend to simplify, with a reduction in the number of prominent emission lines. As we will see, this behavior can be understood by noting that, for increasing N, the most active transitions of the system gradually acquire a harmonic-like character, as will be shown in Section 3.3.2, thus further hinting at the bosonization of the matter degrees of freedom in the thermodynamic limit.

Fig. 3.7 displays the emission spectra for systems composed of $N = 3$-6 emitters coupled to a single cavity mode. As for the $N = 2$ case, we consider configurations with either only individual dissipation channels (Fig. 3.7(a,d,g,j)) or collective reservoirs (Fig. 3.7(b,e,h,k)). When both types of dissipation channels are present simultaneously, the resulting spectra are qualitatively similar to those obtained with only individual dissipation channels, hence, for brevity, we omit them here. As the number of emitters increases, many emission lines become significantly less

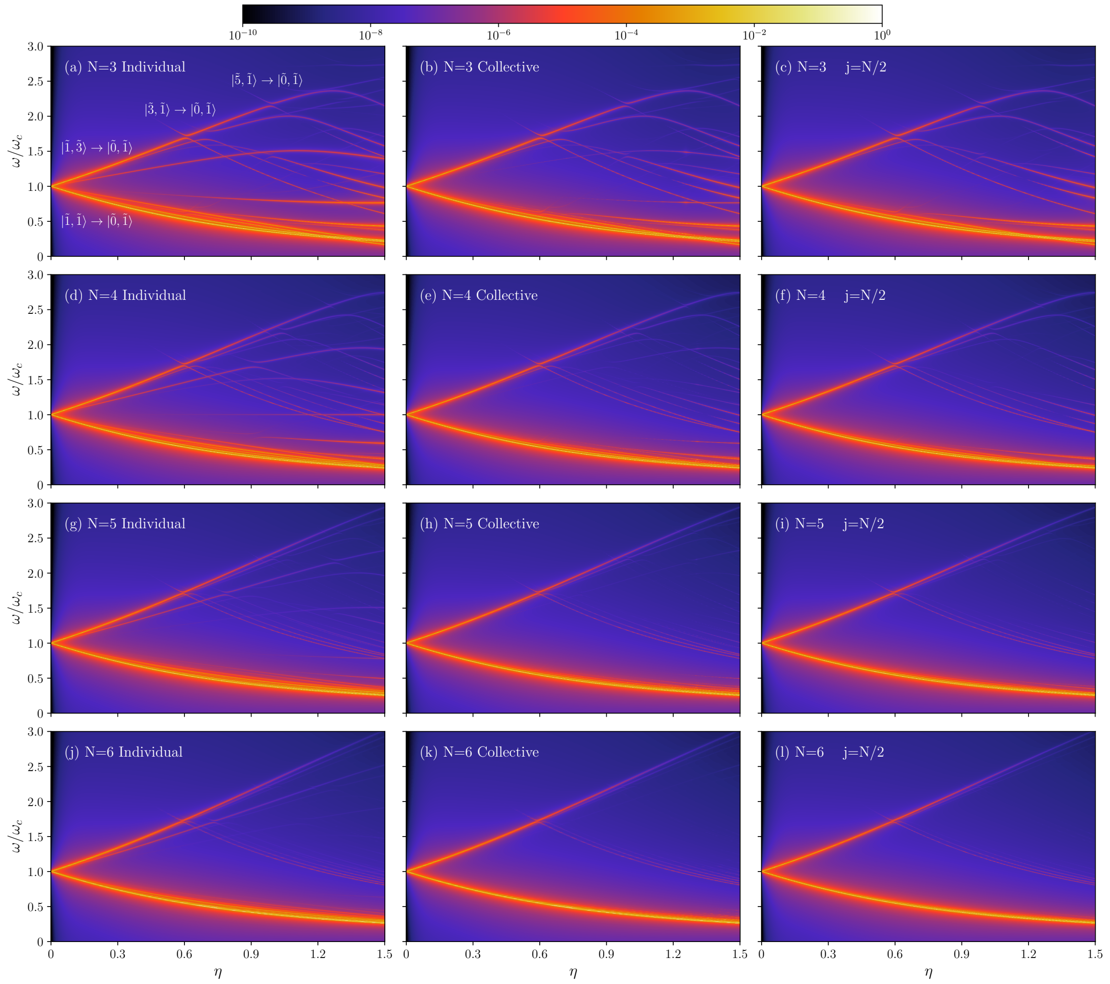

Figure 3.7: Incoherent emission spectra for systems composed of $N = 3$-6 as a function of the normalized coupling strength η. The emission spectra obtained considering: **(a,d,g,j)** individual reservoirs for the TLSs, **(b,e,h,k)** collective reservoir, and **(c,f,i,l)** collective reservoirs with transitions only between states of maximum total angular momentum $j = N/2$.

intense. In contrast, the transitions $\left|\tilde{1},\tilde{1}\right\rangle \rightarrow \left|\tilde{0},\tilde{1}\right\rangle$ and $\left|\tilde{1},\tilde{3}\right\rangle \rightarrow \left|\tilde{0},\tilde{1}\right\rangle$ consistently dominate the spectra as the brightest emission lines. We also observe several avoided level crossings along these emission lines, especially evident in the transition $\left|\tilde{1},\tilde{3}\right\rangle \rightarrow \left|\tilde{0},\tilde{1}\right\rangle$, caused by the interaction of states with the same parity but different excitation number. While the number of such avoided crossings increases with N, their width scales as $N^{-1/2}$, thus becoming progressively narrower. By $N = 6$, they are already barely distinguishable.

It is worth emphasizing that the brightest emission lines are associated with transitions between eigenstates belonging to the maximum angular momentum manifold, $j = N/2$. This naturally motivates us to focus on the emission spectra restricted to this manifold, which includes the ground and first excited states and couples most strongly to the photonic mode [21]. Such a restriction not only captures all the physically relevant spectral features but also brings a significant computational advantage when dealing with larger systems. In Fig. 3.7(c,f,i,l), we present the emission spectra obtained by restricting the matter Hilbert space to the $j = N/2$ manifold, for systems with $N = 3$-6 emitters coupled to collective reservoirs. We observe that, as N increases, the differences between the full and restricted spectra rapidly vanish. This is because the emission lines associated with $j < N/2$ manifolds become negligible in the limit $N \to \infty$. These observations justify restricting our analysis to the $j = N/2$ manifold in the following subsection, where we address the thermodynamic limit.

3.3.2 Incoherent emission spectra for many atoms and the thermodynamic limit

In this subsection, we examine the emission spectra of systems composed of a large number of emitters ($N = 10, 50, 100$), approaching the thermodynamic limit $N \to \infty$, whose energy spectra were already shown in Fig. 3.4. As mentioned earlier, our analysis is restricted to the maximum angular momentum manifold $j = N/2$, which is sufficient to capture all the relevant collective emission features for such large systems.

Fig. 3.8(a-c) display the incoherent emission spectra for systems with $N = 10, 50, 100$ emitters, as functions of the normalized coupling strength η, considering only collective dissipation channels. For comparison, Fig. 3.8(d) shows the emission spectrum in the thermodynamic limit, obtained from the Hopfield model in Eqs. (3.7) and (3.8). As illustrated in Fig. 3.8, the number of visible emission lines decreases rapidly as N increases, eventually leaving only the two most dominant emission lines, corresponding to the transitions $\left|\tilde{1}, \tilde{3}\right\rangle \to \left|\tilde{0}, \tilde{1}\right\rangle$ and $\left|\tilde{1}, \tilde{1}\right\rangle \to \left|\tilde{0}, \tilde{1}\right\rangle$. The avoided level crossings, still faintly visible for $N = 10$ (see Fig. 3.8(a)), disappear entirely for larger N.

The overall behavior displayed in these spectra for finite N already closely mimics that of the lower and upper polariton modes in the thermodynamic limit (see Fig. 3.8(d)). Indeed, as derived in Eqs. (3.7) and (3.8), the collective dynamics of the quantum emitter ensemble can be effectively described through bosonization, leading to the bosonic Hopfield model. The progressive disappearance of higher-order transitions is a clear manifestation of the system's tendency toward harmonicity as $N \to \infty$. These conclusions hold within the weak excitation regime

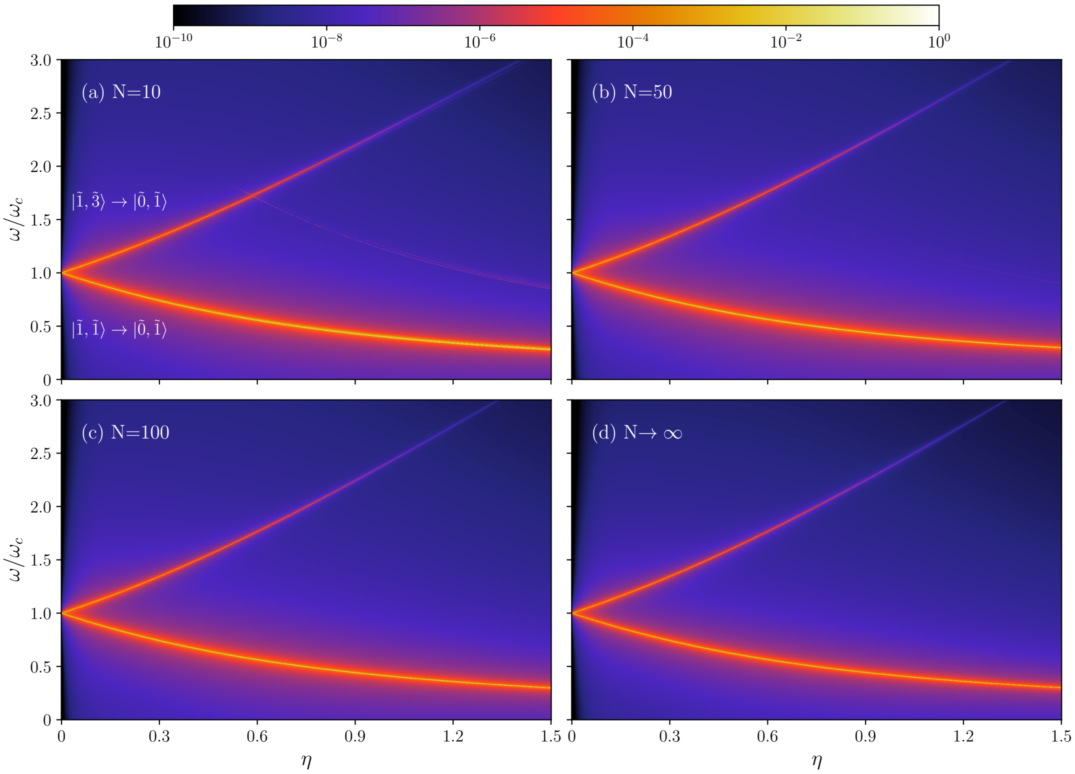

Figure 3.8: Incoherent emission spectra for systems of **(a)** $N = 10$, **(b)** $N = 50$, **(c)** $N = 100$ and **(d)** $N \to \infty$ (thermodynamic limit) TLSs as function of the normalized coupling strength η, considering a collective dissipation channel.

considered here. At higher effective temperatures, where more excited states become significantly populated, deviations from the Hopfield model may reemerge, and a larger number of emitters would be required to maintain the same level of agreement with the thermodynamic limit.

Chapter 4

Quantum phase transitions in ultrastrongly coupled light-matter systems: the role of electrostatic interactions

The occurrence of a potential quantum phase transition in systems composed of a large number of dipoles ultrastrongly coupled to a single-mode cavity field has been a topic of intense debate in the literature, with many theoretical predictions often in conflict. This controversy is further complicated by the presence of both no-go and counter no-go theorems, which often rely on simplified models that may not capture all relevant physical effects. In particular, many of these theorems are based on the role of the $\mathbf{A}^2$ term in the Coulomb-gauge light-matter Hamiltonian, or equivalently the $\mathbf{P}^2$ term of the multipolar gauge, as well as on the impact of the electrostatic interactions between dipoles, which are frequently neglected or treated in an oversimplified manner.

In this chapter, we aim to shed light on this long-standing debate by analyzing two specific arrangements of atoms, namely a three-dimensional cubic lattice and a cavity-embedded square-lattice layer. The latter provides a realistic model for single-mode cavity-QED setups with coupled dipoles in the thermodynamic limit. The predictions obtained from these models are shown to significantly differ from those of the standard Dicke model. In particular, we demonstrate that in the thermodynamic limit a realistic description leads to the introduction of renormalized Hopfield models. Moreover, we show that for sufficiently large atom-field coupling strengths, a ferroelectric phase transition can in principle occur, although its nature differs from the original superradiant phase transition predicted by the Dicke model. While the normal phase below the critical point can be accurately described using collective matter modes via a standard linearized Holstein-Primakoff approach, the description of the condensed phase beyond the critical point requires the inclusion of nonlinear terms in the Holstein-Primakoff mapping. Our theoretical predictions are further supported by experimental observations of the polaritonic spectrum in bulk crystals of gold nanoparticles. In such system, highly-localized gold nanoparticles interact strongly with light through localized surface plasmons, which are the collective oscillations of conduction electrons. Their large oscillator strength makes them excellent building blocks for engineered materials exhibiting ultrastrong light-matter interactions.

This chapter is organized as follows. In Section 4.1, we provide a brief historical overview of the occurrence of superradiant phase transitions in light-matter systems, highlighting the main controversies and debates in the literature. In Section 4.2, we introduce a theoretical model for a three-dimensional lattice of dipoles, explicitly taking into account the electrostatic dipole-dipole interactions. We derive a renormalized Hopfield-like Hamiltonian and analyze its polaritonic eigenmodes, discussing the possible occurrence of a quantum phase transition. Furthermore, we present experimental observations that support our theoretical predictions, demonstrating the relevance of our models in experimental realizations. Finally, in Section 4.3, we extend our analysis to a cavity-embedded planar layer of dipoles, deriving an effective light-matter Hamiltonian and examining its predictions for the polaritonic spectrum. The results presented in this chapter are based on Ref. [2], where detailed derivations and additional discussions can be found.

4.1 Historical overview of the occurrence of SPT in light-matter systems

The Dicke model, introduced in 1954 by R. H. Dicke [18], was originally formulated to describe the collective behavior of a large number of two-level atoms interacting with a common radiation field. A key prediction of the model is that when the coupling strength between the electromagnetic field and the atoms exceeds a critical value, the system undergoes a transition to a phase characterized by a macroscopic occupation of the cavity mode and a collectively ordered atomic state. This phenomenon, known as *superradiant phase transition* (SPT), has been extensively studied in various contexts, including cavity QED, circuit QED, and solid-state systems [19–22, 74, 144]. Early studies considered the Dicke model at finite temperature [19, 20, 74], predicting a classical phase transition, while later works extended the analysis to zero temperature [21, 144], revealing its quantum nature.

Since its formulation, the Dicke model has been the subject of intense theoretical and experimental investigations. In particular, the possibility of a quantum phase transition (QPT) between a normal state and a photon-condensate state within light-matter systems under the influence of electric dipolar interactions has been a long-standing debate for many decades [76, 145–154]. Even in recent years, several apparently conflicting no-go and counter no-go theorems have continued to dispute over the occurrence of a SPT in such systems [89–92, 130, 155, 156].

Notably, such debates are limited to the case of electric dipolar interactions, as there is a general consensus regarding the potential occurrence of a SPT in the presence of magnetic interactions, since in these systems the so-called $\mathbf{A}^2$ diamagnetic term in the Coulomb gauge Hamiltonian (or $\mathbf{P}^2$ self-polarization term in the multipolar gauge Hamiltonian), which prevents the SPT, is either negligible or totally absent [134, 157]. This originates from the fact that magnetic couplings arise from spin degrees of freedom and are typically described by Zeeman-like interactions, linear in the vector potential $\mathbf{A}$ [158]. In this case, these quadratic terms (if present) are not constrained by the Thomas-Reiche-Kuhn (TRK) sum rule [143], which instead applies to electric dipolar interactions. Very recently, a Dicke-like SPT has been experimentally observed in a magnonic system [159], where a magnon mode of ordered Fe^{3+} spins couples ultrastrongly to paramagnetic Er^{3+} spins, effectively realizing a Dicke-like model, where the Fe^{3+} mode plays the role of the bosonic mode while the Er^{3+} spins represent the two-level systems.

In contrast, for electric dipolar systems, the presence of the $\mathbf{A}^2$ or $\mathbf{P}^2$ terms has been shown to prevent the SPT [91, 146, 154]. These quadratic terms are not only required to preserve gauge invariance, but also ensure the correct recovery of fundamental classical limits [128, 154, 160]. Recent no-go theorems further argue that gauge invariance itself forbids any transition to a photon-condensate state when the cavity mode is assumed to be spatially uniform in the region where the dipoles are located [90, 91], or when magnetic interactions can be neglected [89].

On the other hand, several works argue that a SPT remains possible in many-dipole cavity-QED systems, grounded on the assumption that the system Hamiltonian can be mapped onto a Dicke-like model [78, 129, 130, 148, 149, 161]. This apparent possibility arises from a compensation mechanism between direct electrostatic dipole-dipole interactions and transverse polarization-field terms in the multipolar gauge. To make the situation even more intricate, there is no general agreement on the nature of this controversial QPT. According to [130], it corresponds to a ferroelectric-like spontaneous polarization of the dipoles, without a macroscopic transverse field. Conversely, Ref. [148] argues that any mean-field polarization in the displacement field, far from the dipoles, must be accompanied by a transverse electric field. Refs. [129, 161], instead, suggest that the nature of the

QPT is gauge dependent, being ferroelectric-like only in the Coulomb gauge. Still, several studies document consistent physical predictions based on this compensation [162, 163]. In contrast, Ref. [150] concludes that longitudinal dipole-dipole interactions cannot induce any QPT, at least in the idealized case of infinite, homogeneous, and isotropic ensembles of non-overlapping dipoles.

To shed light on these long-standing controversies, we investigate the interaction between the electromagnetic field and ordered lattices of atoms. Specifically, in our treatment, we consider isotropic, localized two-level atomic dipoles with threefold orientation degeneracy. Whitin the two-level approximation, a consistent atomic model requires accounting for the orientational degeneracy of one of the two levels (*e.g.*, the excited state), since the electric-dipole transitions are only allowed between states of different parity (such as between s and p orbitals). In analyzing these lattices, we explicitly take into account the discrete, non-overlapping topology of the system, which is often neglected during the different approximations and limiting procedures employed to derive the Dicke model. We begin with a cubic lattice array (an isotropic system in the long-wavelength limit) and subsequently examine a cavity-embedded planar layer with a square lattice.

In the thermodynamic limit, such dipole arrays are described by a light-matter Hamiltonian with a Hopfield-like structure, with an additional dipole-dipole interaction term. This contribution cannot be discarded and is explicitly retained here to provide a comprehensive description of the system. Accordingly, our approach yields a physically grounded model for single-mode cavity QED in the dipole approximation and in the thermodynamic limit. Importantly, the results of our analysis shows that, for sufficiently strong atom-field coupling, a ferroelectric QPT can in principle still emerge, although with different features with respect to the original Dicke SPT.

4.2 Theoretical models for a three-dimensional lattice of dipoles

Let us first consider the case of a three-dimensional lattice of atoms interacting with an electromagnetic field. For notational convenience, in the following, we will omit the $\hat{\cdot}$ symbol on the operators, as we are working entirely within the quantum regime and no ambiguity can arise.

The quantization of the electromagnetic field and its subsequent interaction with the matter subsystem can be carried out as described in Sections 1.2.2 and 1.3, respectively. Here, we briefly summarize the main steps of the derivation. As usual, the radiation field is quantized by the introduction of phtonic bosonic operators $a_{\mathbf{k},\lambda}$ for each mode $\mathbf{k}$ and polarization λ. The corresponding mode frequency is $\omega_k = v\,|\mathbf{k}|$, where $v = c/\sqrt{\epsilon_m}$ is the speed of light in a medium of relative dielectric constant ϵ_m. The vector potential of the electromagnetic field can then be expanded in plane waves as

$$\mathbf{A}(\mathbf{r}) = \sum_{\lambda}\sum_{\mathbf{k}} \mathcal{E}_k e^{i\mathbf{k}\cdot\mathbf{r}} a_{\mathbf{k},\lambda}\hat{\mathbf{e}}_\lambda + \text{H.c.}\,, \tag{4.1}$$

with $\mathcal{E}_k = \sqrt{\hbar/2\epsilon_0\epsilon_m V\omega_k}$, where V is the quantization volume, and $\hat{\mathbf{e}}_\lambda$ ($\lambda = 1, 2$) are the two polarization unit vectors orthogonal to $\hat{\mathbf{k}}$. The Hamiltonian of the free electromagnetic field then takes the standard form

$$H_{\text{ph}} = \hbar \sum_{\lambda,\mathbf{k}} \omega_k a^\dagger_{\mathbf{k},\lambda} a_{\mathbf{k},\lambda}\,. \tag{4.2}$$

On the other hand, the atoms are modeled as localized dipoles in the sites $\mathbf{R}_n$ of a lattice. For the sake of simplicity, we will consider single-electron atoms. Generalization to many-electron atoms does not affect the obtained results. We assume that the atoms are sufficiently far apart to neglect any overlap between their electronic wavefunctions. This allows us to treat the atoms as distinguishable particles, each described by its own position and momentum operators. Therefore, the bare Hamiltonian of N non-interacting identical atoms is given by

$$H_{\text{A}} = \sum_n \frac{\mathbf{p}_n^2}{2m} + V_{\text{C}}(\mathbf{r}_n)\,, \tag{4.3}$$

where $\mathbf{r}_n$ and $\mathbf{p}_n$ are the position and momentum operators of the electron of the n-th atom, satisfying the canonical commutation relations $[r_{n,\alpha}, p_{m,\beta}] = i\hbar\delta_{nm}\delta_{\alpha\beta}$, with $\alpha, \beta = x, y, z$. Here, m is the electron mass and $V_{\text{C}}(\mathbf{r}_n)$ is the *intra-atomic* Coulomb potential of the n-th atom, bounding each electron to its nucleus, which gives rise to the typical anharmonic atomic energy spectrum.

4.2.1 Dipole-dipole electrostatic interactions: the matter Hamiltonian

Before approaching the full light-matter Hamiltonian, it is useful to first focus only on the matter subsystem. As discussed in Section 1.1, the matter Hamiltonian must include not only the bare atomic Hamiltonian H_{A}, but also the electrostatic interactions between atoms of the lattice. These interactions turn out to play a central role in determining the collective resonance frequencies of the system and, ultimately, the possible occurrence of a QPT.

To this end, we begin by evaluating the contribution of the electrostatic interactions to the total Hamiltonian. In the long-wavelength approximation, and under the assumption of non-overlapping atomic wavefunctions, the total polarization density can be expressed as

$$\mathbf{P}(\mathbf{r}) = \sum_n \mathbf{P}_n(\mathbf{r}) = \sum_n \mathbf{d}_n \delta(\mathbf{r} - \mathbf{R}_n)\,, \tag{4.4}$$

where $\mathbf{d}_n$ is the total electric dipole of the n-th atom. The corresponding electrostatic *interatomic* interaction term in the Hamiltonian reduces to the dipole-dipole interaction, which is given by

$$H_{\mathrm{dip}} = \frac{1}{2}\sum_{n\neq m} V_{\mathrm{dip}}(\mathbf{R}_n, \mathbf{R}_m) = \frac{1}{8\pi\epsilon_0\epsilon_m}\sum_{n\neq m} \frac{\mathbf{d}_n\cdot\mathbf{d}_m - 3(\mathbf{d}_n\cdot\hat{\mathbf{r}}_{nm})(\mathbf{d}_m\cdot\hat{\mathbf{r}}_{nm})}{r_{nm}^3}\,, \tag{4.5}$$

with $\mathbf{r}_{nm} = \mathbf{R}_n - \mathbf{R}_m$ and $\hat{\mathbf{r}}_{nm} = \mathbf{r}_{nm}/r_{nm}$, where $r_{nm} = |\mathbf{r}_{nm}|$. Hence, the total matter Hamiltonian is given by

$$H_{\mathrm{matter}} = H_{\mathrm{A}} + H_{\mathrm{dip}}\,. \tag{4.6}$$

We now perform the two-level approximation to derive Dicke-like models, reducing the atomic states to just the ground and excited levels. Importantly, as previously mentioned, to ensure a consistent description of the atomic dipole degrees of freedom, we must take into account the orientation (threefold) degeneracy of the excited state, corresponding to three possible orthogonal orientations for the atomic dipole moment. Accordingly, we define generalized spin operators $\sigma_n^{x,y,z}$ for each atom, as detailed in Appendix Section B.1. This subtlety, often overlooked in simplified models, is crucial for a correct microscopic description.

In the thermodynamic limit ($N, V \to \infty$, at fixed density), the many-body dynamics can be bosonized using a generalized Holstein-Primakoff mapping (see Appendix Section B.2). Since we are considering a threefold degenerate excited state, we introduce three commuting bosonic operators $b_{n,\alpha}$ ($\alpha = x, y, z$) for each atom, which annihilate an excitation in the n-th atom with dipole orientation along the α-axis. In the low-excitation regime, where the number of atomic excitations is much smaller than the total number of atoms, these Holstein-Primakoff transformations can be linearized. This approximation is valid throughout the normal phase below the critical point of the QPT. As it will be shown shortly, above the critical point, however, nonlinear terms in the Holstein-Primakoff mapping must be included to accurately describe the condansates in the system.

In the end, the total Hamiltonian for the matter subsystem (according to the convention of “matter” adopted in this thesis) reads

$$H_{\mathrm{mat}} = \hbar\omega_0 \sum_{\alpha,\mathbf{k}} b_{\mathbf{k},\alpha}^\dagger b_{\mathbf{k},\alpha} + \hbar \sum_{\alpha,\beta,\mathbf{k}} \chi^2\omega_0 f_{\mathbf{k},\alpha,\beta}\left(b_{\mathbf{k},\alpha} + b_{-\mathbf{k},\alpha}^\dagger\right)\left(b_{-\mathbf{k},\beta} + b_{\mathbf{k},\beta}^\dagger\right)\,, \tag{4.7}$$

where the first term is the thermodynamic limit of the bare atomic Hamiltonian $H_{\rm A}$, with ω_0 being the atomic transition frequency between the ground and excited states, while the second term originates from the electrostatic dipole-dipole interaction in Eq. (4.5) in the thermodynamic limit (see Ref. [2] for a detailed derivation). The dimensionless structure factor $f_{\mathbf{k},\alpha,\beta}$ depends on the lattice geometry and, for a simple cubic lattice in the long-wavelength limit, is approximatively $f_{\mathbf{k},\alpha,\beta} \approx \left(3(\hat{\mathbf{k}}\cdot\hat{\mathbf{e}}_\alpha)(\hat{\mathbf{k}}\cdot\hat{\mathbf{e}}_\beta) - \delta_{\alpha\beta}\right)/3$. The interaction strength between the dipoles is given by $\chi = \sqrt{d^2N/2\hbar\epsilon_0\epsilon_m V\omega_0}$ [164]. The bosonic operators $b_{\mathbf{k},\alpha}$ are defined in the reciprocal space as $b_{\mathbf{k},\alpha} = (1/\sqrt{N})\sum_n b_{n,\alpha}e^{-i\mathbf{k}\cdot\mathbf{R}_n}$, and satisfy the canonical commutation relations $[b_{\mathbf{k},\alpha}, b^\dagger_{\mathbf{k}',\beta}] = \delta_{\mathbf{k}\mathbf{k}'}\delta_{\alpha\beta}$.

The matter Hamiltonian in Eq. (4.7) can be diagonalized through a Bogoliubov transformation [93], yielding

$$H_{\rm mat} = \hbar\sum_{\alpha,\mathbf{k}} \tilde{\omega}_{\mathbf{k},\alpha} c^\dagger_{\mathbf{k},\alpha} c_{\mathbf{k},\alpha}\,, \tag{4.8}$$

where $\tilde{\omega}_{\mathbf{k},\alpha} = \omega_0\sqrt{1+4\chi^2 f_{\mathbf{k},\alpha,\alpha}}$ is the renormalized matter frequency and $c_{\mathbf{k},\alpha}$ are the bosonic eigenoperators, which are linear combinations of the original operators $b_{\mathbf{k},\alpha}$ and $b^\dagger_{-\mathbf{k},\alpha}$. These new transverse eigenmodes describe the collective matter excitations which effectively couple with the radiation field, giving rise to a Hopfield-like description of the coupled light-matter system.

4.2.2 Light-matter interaction Hamiltonian: a renormalized Hopfield model

Let us now consider the interaction between the three-dimensional bulk lattice of atoms and the quantized electromagnetic field. When the matter system interacts with the radiation field solely through its polarization, *e.g.* assuming negligible magnetic interactions, the full light-matter Hamiltonian can be obtained either by applying the minimal coupling replacement in the Coulomb gauge, or (equivalently) by working in the multipolar gauge (see Section 1.3.4). In the following, we will adopt the multipolar gauge. Within the long-wavelength approximation, the multipolar-gauge Hamiltonian can be obtained by applying a suitable unitary transformation U to the bare photonic Hamiltonian. This transformation effectively performs a minimal coupling replacement on the photonic variables (see Eq. (2.6)), thus ensuring the gauge invariance of the theory [128]. The unitary operator U is defined as

$$U = \exp\left(\frac{i}{\hbar}\int \mathbf{A}(\mathbf{r})\cdot\mathbf{P}(\mathbf{r})d^3\mathbf{r}\right)\,. \tag{4.9}$$

By inserting the mode expansion for the vector potential and the definition of the polarization density in Eqs. (4.1) and (4.4), respectively, we obtain the explicit form of the unitary operator

$$U = \exp\left[\frac{i}{\hbar}\sum_{\lambda,\mathbf{k},n}\mathcal{E}_{\mathbf{k}}\left(e^{i\mathbf{k}\cdot\mathbf{R}_n}a_{\mathbf{k},\lambda} + e^{-i\mathbf{k}\cdot\mathbf{R}_n}a^\dagger_{\mathbf{k},\lambda}\right)\hat{\mathbf{e}}_\lambda\cdot\mathbf{d}_n\right] . \tag{4.10}$$

We can now apply the transfromation U to the bare photonic Hamiltonian in Eq. (4.2). Subsequently, we employ the two-level approximation for the atomic dipoles (Appendix Section B.1) and the generalized Holstein-Primakoff transformations (Appendix Section B.2). In the thermodynamic limit, this procedure yields the full light-matter Hamiltonian in the multipolar gauge, which reads

$$\begin{aligned} H = {} & \hbar\sum_{\lambda,\mathbf{k}}\omega_k a^\dagger_{\mathbf{k},\lambda}a_{\mathbf{k},\lambda} + \hbar\sum_{\alpha,\mathbf{k}}\tilde{\omega}_{\mathbf{k},\alpha}c^\dagger_{\mathbf{k},\alpha}c_{\mathbf{k},\alpha} \\ & + i\hbar\sum_{\alpha,\lambda,\mathbf{k}}\eta'\sqrt{\omega_k\tilde{\omega}^\perp_{\mathbf{k}}}\left(a^\dagger_{-\mathbf{k},\lambda}-a_{\mathbf{k},\lambda}\right)\left(c^\dagger_{\mathbf{k},\alpha}+c_{-\mathbf{k},\alpha}\right)(\hat{\mathbf{e}}_\lambda\cdot\hat{\mathbf{e}}_\alpha) \\ & + \hbar\sum_{\alpha,\beta,\lambda,\mathbf{k}}\eta'^2\tilde{\omega}^\perp_{\mathbf{k}}\left(c^\dagger_{\mathbf{k},\alpha}+c_{-\mathbf{k},\alpha}\right)\left(c^\dagger_{-\mathbf{k},\beta}+c_{\mathbf{k},\beta}\right)(\hat{\mathbf{e}}_\lambda\cdot\hat{\mathbf{e}}_\alpha)(\hat{\mathbf{e}}_\lambda\cdot\hat{\mathbf{e}}_\beta) , \end{aligned} \tag{4.11}$$

where $\tilde{\omega}^\perp_{\mathbf{k}} = \omega_0\sqrt{1+4\eta^2 f^\perp_{\mathbf{k}}}$ and $\eta' = \eta\,\omega_0/\tilde{\omega}^\perp_{\mathbf{k}}$ denote, respectively, the transverse resonance frequency and light-matter coupling, both renormalized by the dipole-dipole interaction. The bare light-matter coupling η is defined by $\eta = \sqrt{d^2N/2\hbar\epsilon_0\epsilon_m V\omega_0}$. As it can be easily verified, *only in the 3D case*, this expression coincides with χ, which is the dipole-dipole interaction strength introduced in Section 4.2.1. The parameters $f^\perp_{\mathbf{k}}$ and $f^\parallel_{\mathbf{k}}$ corresponds to the transverse and the longitudinal components of $f_{\mathbf{k},\alpha,\alpha}$, respectively (notice that $f^\perp_{\mathbf{k}} = -1/3$). The same Hamiltonian in Eq. (4.11) can equivalently be derived by first applying the two-level approximation and bosonization to the exponent of the unitary transformation in Eq. (4.10), and then applying the resulting operator to the bare photonic Hamiltonian in Eq. (4.2), as demonstrated in Appendix D of Ref. [2].

Notably, the Hamiltonian in Eq. (4.11) exhibits a Hopfield-like structure, with an additional dipole-dipole interaction term, included in the renormalized matter frequency $\tilde{\omega}^\perp_{\mathbf{k}}$ and light-matter coupling η'. This contribution is essential, as it plays a crucial role in determining the collective resonance frequencies of the system and, ultimately, the possible occurrence of a QPT, as it will be shown in the following subsection.

Moreover, we point out that we could have chosen to not perform the initial Bogoliubov transformation on the matter Hamiltonian in Eq. (4.7), as this step is not strictly necessary to diagonalize the full light-matter Hamiltonian in Eq. (4.11).

Indeed, this step was introduced merely for clarity sake, and to highlight the physical interpretation of the different contributions in Eq. (4.11). Had we not performed this transformation, the matter part of the Hamiltonian in Eq. (4.11) would have remained expressed in terms of the original bosonic operators $b_{\mathbf{k},\alpha}$, with the light-matter coupling and the $\mathbf{P}^2$ term expressed in terms of the bare quantities ω_0 and η, but with an additional dipole-dipole interaction term. In this alternative approach, the full light–matter Hamiltonian reads

$$\begin{aligned} H =&\hbar \sum_{\lambda,\mathbf{k}} \omega_k a^\dagger_{\mathbf{k},\lambda} a_{\mathbf{k},\lambda} + \hbar\omega_0 \sum_{\alpha,\mathbf{k}} b^\dagger_{\mathbf{k},\alpha} b_{\mathbf{k},\alpha} \\ &- i\hbar \sum_{\alpha,\lambda,\mathbf{k}} \eta\sqrt{\omega_k\omega_0} \left(a_{\mathbf{k},\lambda} - a^\dagger_{-\mathbf{k},\lambda}\right) \left(b_{-\mathbf{k},\alpha} + b^\dagger_{\mathbf{k},\alpha}\right) \left(\hat{\mathbf{e}}_\lambda \cdot \hat{\mathbf{e}}_\alpha\right) \\ &+ \hbar \sum_{\alpha,\beta,\lambda,\mathbf{k}} \eta\omega_0 \left(b_{-\mathbf{k},\alpha} + b^\dagger_{\mathbf{k},\alpha}\right) \left(b_{\mathbf{k},\beta} + b^\dagger_{-\mathbf{k},\beta}\right) \left(\hat{\mathbf{e}}_\lambda \cdot \hat{\mathbf{e}}_\alpha\right) \left(\hat{\mathbf{e}}_\lambda \cdot \hat{\mathbf{e}}_\beta\right) \\ &+ \hbar \sum_{\alpha,\beta,\mathbf{k}} \chi^2 \omega_0 f_{\mathbf{k},\alpha,\beta} \left(b_{-\mathbf{k},\alpha} + b^\dagger_{\mathbf{k},\alpha}\right) \left(b_{\mathbf{k},\beta} + b^\dagger_{-\mathbf{k},\beta}\right) . \end{aligned} \tag{4.12}$$

where η is the bare light-matter coupling in the dipolar gauge and the last term in Eq. (4.12) is the dipole-dipole interaction term, as defined above. In the following subsection, we will see that this Hamiltonian produces the same polaritonic eigenmodes as in Eq. (4.11), as expected by physical consistent models.

4.2.3 Dispersion relation and the occurence of a QPT

The Hamiltonian in Eq. (4.11) can be diagonalized through a Hopfield-Bogoliubov transformation [142], which yields the polaritonic eigenmodes of the coupled light-matter system. Due to the isotropy of the system, the two transverse modes are degenerate, and the corresponding dispersion relation is given by

$$\frac{\omega_k^2}{\Omega_\perp^2} = 1 + \frac{4\eta'^2 \tilde{\omega}^{\perp\,2}_{\mathbf{k}}}{\tilde{\omega}^{\perp\,2}_{\mathbf{k}} - \Omega_\perp^2} , \tag{4.13}$$

where $\Omega_\perp$ is the transverse polaritonic eigenfrequency. The longitudinal modes, in contrast, are decoupled from the transverse electromagnetic field and their dispersion relation is simply given by $\Omega_\parallel = \tilde{\omega}^\parallel_{\mathbf{k}}$. It is worth noting that the same dispersion relation in Eq. (4.13) can be also derived without performing the two-step Bogoliubov transformation. Indeed, we can directly diagonalize the full light-matter Hamiltonian in Eq. (4.12), which include explicitly the dipole-dipole interaction term, through a single Hopfield-Bogoliubov transformation. In this case, however, the physical interpretation of the results becomes less transparent, although equivalent.

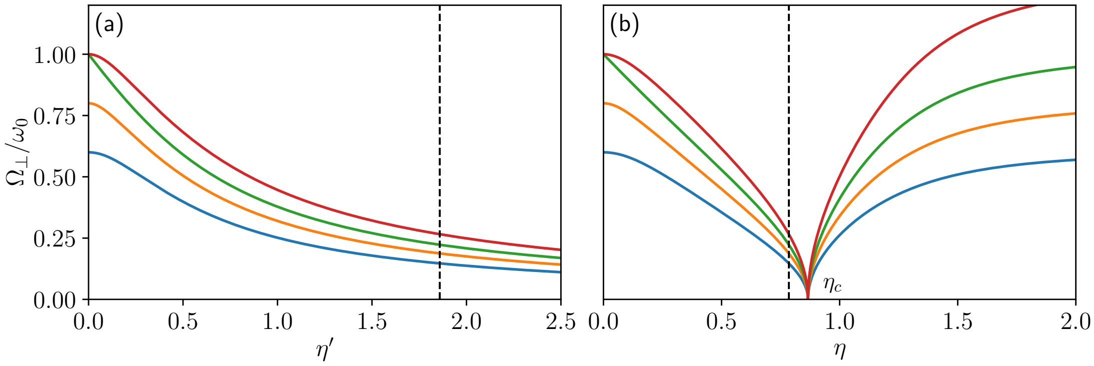

Figure 4.1: Lower polariton frequencies for different modes $\omega_k/\omega_0 = 0.6$ (blue), 0.8 (orange), 1 (green), 1.3 (red), as functions of **(a)** the renormalized coupling strength η' and **(b)** bare coupling strength η. The vertical dashed line indicates the coupling strength $\eta' = 1.83$ measured in Ref. [139], corresponding to $\eta = 0.78$. The softening of the lower polariton frequency for $\eta_c \approx \sqrt{3}/2$ (in isotropic systems) signals the occurrence of a QPT.

The dispersion relation in Eq. (4.13) has the same structure as that of a standard Hopfield model, but with renormalized matter frequency $\tilde{\omega}_{\mathbf{k}}^{\perp}$ and light-matter coupling η'. In Fig. 4.1, we show the lower branch of the transverse polaritonic dispersion relation as a function of both (a) the renormalized coupling η' and (b) the bare coupling η, for different photonic modes ω_k.

Let us now discuss the possibility for the system to undergo a QPT. Firstly, we recall that Eq. (4.13) can be formally obtained by diagonalizing a Hopfield-like model with effective coupling constant η'. As it is well known, such a model does not display any radiation-induced QPT for any finite value of η', as shown in Fig. 4.1(a) [92]. However, when expressed in terms of the bare light-matter coupling strength η, the model can exhibit a vanishing eigenfrequency. This behavior originates from the additional dipole-dipole interactions in the matter Hamiltonian in Eq. (4.7), which enable the occurrence of a QPT transition. Specifically, the softening of the transverse renormalized matter frequency $\tilde{\omega}_{\mathbf{k}}^{\perp}$ for increasing dipole-dipole interaction strengths $\chi\,(=\eta)$, induces the softening of the entire polaritonic mode, as illustrated in Fig. 4.1(b). This QPT takes place even in the absence of retardation effects and leads to a transverse polarization condensate, while no condensation occurs in the electric field, as it will be explicitly shown below (see also Appendix Section B.4). Consequently, this QPT should be classified as ferroelectric rather than superradiant. We emphasize that this distinction is not merely semantic, as this QPT is fundamentally different from the Dicke SPT, being driven by dipole-dipole interactions rather than by the coupling with the radiation field.

As a concrete example, for isotropic systems in the long-wavelength approximation, such as the one here considered, the QPT occurs for $\eta > \eta_c \approx \sqrt{3}/2$, as demonstrated by Fig. 4.1(b). In contrast, near the critical point, $\eta' = \eta\,\omega_0/\tilde{\omega}^{\perp}_{\mathbf{k}}$ is not a meaningful control parameter since it diverges for $\eta \to \eta_c$. This relation between η and η', and especially the behavior of the polaritonic eigenfrequencies as a function of η', clarifies why the Hopfield model remains a valid description even for many-dipole systems approaching a ferroelectric QPT.

Beyond the critical point, *i.e.* in the condensed phase, the effective bosonic Hamiltonian in Eq. (4.11) is no longer valid, as the low-excitation approximation necessary for the linearization of the generalized Holstein-Primakoff mapping breaks down. To accurately describe the system in this regime, higher-order terms in the Holstein-Primakoff transformation must be included [2, 21]. The explicit form and derivation of the full Hamiltonian in the condensed phase are reported in Appendix Section B.3. Here, we only present the corresponding transverse polaritonic dispersion relation in the condensed phase, which is given by

$$\frac{\omega_{\mathbf{k}}^2}{\Omega_\perp^2} = 1 + \frac{\omega_0^2/f^{\perp}_{\mathbf{k}}}{\omega_0^2\left(1 - 16\eta^4 {f^{\perp}_{\mathbf{k}}}^2\right) + \Omega_\perp^2}\,, \quad \text{for } \eta > \eta_c\,, \tag{4.14}$$

while Eq. (4.13) holds for $\eta \le \eta_c$. It is worth emphasizing that neither the critical point nor the ground-state transverse polarization in the condensed phase are affected by the coupling with the photon field, but are determined solely by the strength of dipolar interactions, as expected for a ferroelectric phase transition. Nevertheless, since this QPT involves transverse matter excitations, the explicit form of the transverse polaritons above the critical point is modified.

As mentioned above, the QPT occurring in this system is characterized by a spontaneous macroscopic transverse polarization of the dipoles in the ground state, $\langle \mathbf{P}^{\perp}_{\mathbf{k}} \rangle \neq 0$, which in turn induces a macroscopic occupation of $\langle \mathbf{D}_{\mathbf{k}} \rangle \neq 0$. The latter, *in the multipolar gauge*, is proportional to the field momentum, i.e. $\langle a_{\mathbf{k},\lambda} \rangle \neq 0$. This occurrence induced recent works [129, 161] to characterize the phase transition as ferroelectric or superradiant depending on the gauge choice. In contrast, our calculations (explicitly reported in Appendix Section B.4) show that $\langle \mathbf{D}_{\mathbf{k}} \rangle = \langle \mathbf{P}^{\perp}_{\mathbf{k}} \rangle$, which, from the definition of the displacement field, implies $\langle \mathbf{E}^{\perp}_{\mathbf{k}} \rangle = 0$. Therefore, the QPT is purely ferroelectric, with no superradiant component. Indeed, having $\langle a_{\mathbf{k},\lambda} \rangle \neq 0$ does not imply a macroscopic occupation of the transverse electric field or any photon condensation. It is important to emphasize that observables such as $\mathbf{D}(\mathbf{r})$ and the transverse electric field $\mathbf{E}^{\perp}(\mathbf{r})$ are the physical quantities, whose expectation values are not gauge dependent. Conversely, operators such as the field momentum and the bosonic operators are nonphysical quantities that serve only as calculation tools, and thus they are not suitable to characterize the nature of physical processes [27].

We now briefly examine a common cancellation procedure that is often invoked to justify the validity of the standard Dicke [129, 130, 147, 161]. This approach is based on the interplay between electrostatic dipole-dipole term in Eq. (4.7) and the interatomic part of the self-polarization term in the light-matter Hamiltonian, which originates from light-matter interaction itself. In particular, a key step of this procedure is the decomposition of the polarization field $\mathbf{P}(\mathbf{r})$ in its intra- and interatomic, longitudinal and transverse parts. After the compensation between the interatomic contributions, further approximations are applyied to obtain the Dicke model, namely a single-polarization single-mode reduction of the radiation and a strict two-level approximation of the dipoles (which neglects the orientational degrees of freedom). Under these assumptions, the remaining intra-atomic part of the self-polarization term becomes proportional to the identity operator. Following this procedure, one arrives at a Dicke-like Hamiltonian in the multipolar gauge for a single mode (see, *e.g.*, Ref. [129] for a detailed derivation):

$$H_{\text{Dicke}} = \hbar\omega_0 b^\dagger b + \hbar\omega_k a^\dagger a - i\hbar\eta\sqrt{\omega_k\omega_0}\left(a^\dagger - a\right)\left(b^\dagger + b\right) , \tag{4.15}$$

where, given the previous assumptions, subscripts on the operators are no longer necessary.

This model, in contrast with the Hopfield-like Hamiltonian in (4.11), predicts a light-induced QPT for a critical value of the coupling $\tilde{\eta}_c = 0.5$. Being the transition enabled by the photons, it can be classified as superradiant [21, 129]. Nonetheless, neglecting the dipole orientations in the description of realistic three-dimensional systems constitutes a significant oversimplification, leading to erroneous assessments of the interactions. Indeed, by ignoring the orientational degrees of freedom, contributions belonging to the transverse and longitudinal sectors of the Hamiltonian are mixed, resulting in an incorrect evaluation of the light-matter interaction.

In Fig. 4.2, we compare the lower polariton frequencies predicted by the three models here considered as functions of the bare coupling strength η: the renormalized Hopfield-like model in Eq. (4.13) (solid lines), the Dicke-like Hamiltonian in Eq. (4.15) (dashed lines), and a standard Hopfield model omitting the dipole-dipole interactions (dash-dotted lines). The different line colors correspond to different photonic modes ω_k. As clearly shown, for small values of η, which is the typical regime of experimental settings, all three models yield similar predictions. However, increasing the coupling strength, the differences between the models become more pronounced. It should be noted that having highly-localized dipoles in the USC regime is a challenging task to achieve. This explains why, so far, the validity of one model over the others has remained experimentally unverified.

As already stated, increasing the coupling strength induces significant discrepancies. Notably, only the renormalized Hopfield-like model predicts a QPT

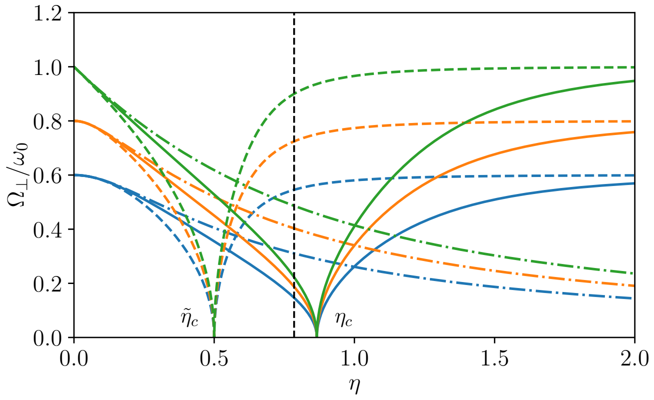

Figure 4.2: Comparison between the lower polariton frequencies obtained from the renormalized Hopfield-like model in Eq. (4.13) (solid lines), a Dicke-like model as in Eq. (4.15) (dashed lines), and a standard Hopfield model without dipole-dipole interactions (dash-dotted lines), as functions of the bare coupling strength η. The different colors correspond to different photonic modes: $\omega_k/\omega_0 = 0.6$ (blue), 0.8 (orange), 1 (green). The vertical dashed line indicates the coupling strength corresponding to $\eta = 0.78$ measured in Ref. [139].

at $\eta_c \approx \sqrt{3}/2$, whereas the Dicke-like model predicts a SPT at the lower value $\tilde{\eta}_c = 0.5$. In contrast, the standard Hopfield model without dipole-dipole interactions does not exhibit any QPT. The vertical dashed line in Fig. 4.2 marks the coupling strength $\eta = 0.78$ (corresponding to $\eta' = 1.83$), measured in a recent experiment reported in Ref. [139], which is the highest value reported in the literature for a three-dimensional lattice of dipoles. For such coupling strengths, the three models already yield fairly different predictions, making it possible to validate the adequacy of one model with respect to the others.

To this end, in Fig. 4.3, we compare the theoretical predictions for the transverse polaritonic frequencies obtained from the three models here presented with the experimental data reported in Ref. [139]. The experimental measurements of the lower polariton branch (black dots) show excellent agreement with the theoretical predictions of the Hopfield-like model including the dipolar interactions, hence demonstrating its validity. The data set reports measurements regarding a three-dimensional artificial crystal made of spatially separated gold nanoparticles, which achieved a record normalized light-matter coupling strength in the deep-strong coupling regime ($\eta' = 1.83$). This system falls within the assumptions of our model, since the nanoparticles are highly localized and their polarization fields can be safely considered as non-overlapping. The gold nanoparticles, each supporting triply-degenerate localized dipolar surface plasmons, couple through

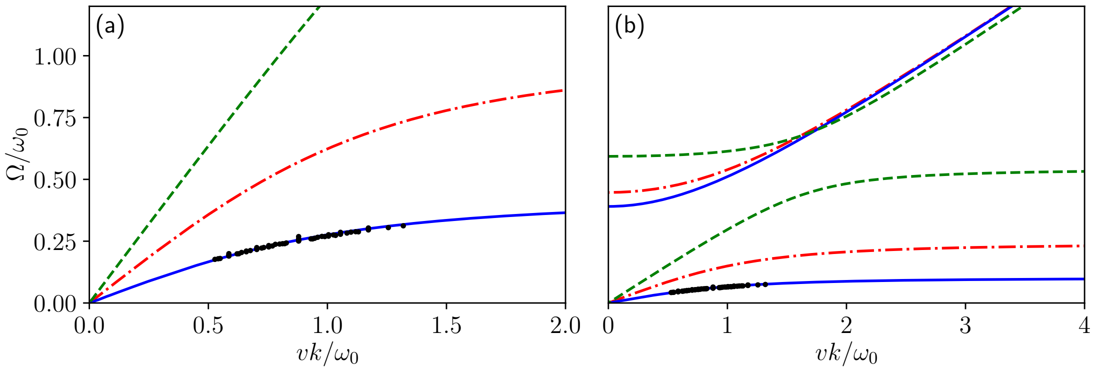

Figure 4.3: Comparison between the three theoretical models presented here and the experimental data in Ref. [139]: **(a)** region near the experimental data, **(b)** broader view including the upper polariton. As shown, the theoretical dispersion relations derived from the renormalized Hopfield-like in Eq. (4.11) (solid blue) perfectly fits the experimental data (black dots). In contrast, the curves derived from the Dicke-like model (dashed green) and from the Hopfield model neglecting the dipolar interaction (red dash-dotted) significantly differ from the experimental data. The relevant parameters are $\eta' = 1.83$, $\omega_0 = 1.83\ eV$ and $\epsilon_m = 1.96$, while the full set of parameters for the experimental curves can be found in Ref. [139].

dipole-dipole interactions, giving rise to collective plasmons that extend over the whole metamaterial [165]. These excitations can be effectively described in terms of collective bosonic operators, analogously to the atomic collective excitations in the thermodynamic limit discussed above. No experimental data are available for the upper polariton branch given its high energy, which collocates it above the onset of the gold interband transitions. Thanks to their structural properties and the high coupling strength achieved, these artificial gold crystals represent an ideal testbed for discerning among the different models considered, and thus help solving the long-standing debate about QPTs in many-dipoles systems. These experimental data have already been compared in Ref. [139] itself with a Hopfield model whose light-matter coupling strength was renormalized with respect to transverse matter polaritonic frequency, which corresponds to our η', indeed showing excellent agreement. However, possibly due to this parametrization, it was not pointed out there that a QPT could in principle occur at higher couplings. Here, we explicitly clarify the relation between the bare and renormalized parameters involved in the models.

The high coupling experimentally achieved ($\eta' = 1.83$, corresponding to $\eta = 0.78 > \tilde{\eta}_c$), according to the Dicke-like model, would imply a condensed phase and a dispersion relation (dashed green lines in Fig. 4.3) strongly different from the experimental dataset. We point out, however, that beyond the critical point, the dispersion relation for the atomic system and for the artificial crystal may present quantitative differences owing to the different nonlinear response of these systems. Furthermore, we notice that the achieved coupling strength $\eta = 0.78$ is close to the critical value $\eta_c \sim 0.87$, such that the consequent softening of $\tilde{\omega}^{\perp}_{\mathbf{k}}$, which dictates the asymptotic behavior of the lower polariton, can already be appreciated, both theoretically and in the experimental dataset. Nevertheless, realizing this QPT is experimentally challenging, as achieving the required high coupling strength necessitates densities approaching the point of system solidification [166, 167]. Indeed, owing to the small size of the fine structure constant, the dipole-dipole interaction strength $\chi \approx 10^{-3}\, r^2\lambda_0/a^3$ is usually far from the critical value χ_c, with $\lambda_0 = 2\pi v/\omega_0$ being the characteristic matter wavelength and r the mean atomic radius. Moreover, to avoid significant wavefunction overlap between emitters, the condition $4r < a$ must generally be satisfied.

These results provide further evidence of the crucial role played by electrostatic contributions in determining the correct polaritonic dispersion and the conditions for the occurence of a QPT, as well as its nature.

4.3 Theoretical models for a two-dimensional lattice of dipoles

In this section, we extend the analysis presented above to a two-dimensional lattice of dipoles embedded in a cavity, as schematically illustrated in Fig. 4.4. This configuration is particularly relevant for practical applications, as it can be experimentally realized by embedding a monolayer of dipoles within an optical cavity. The results of this analysis provide additional confirmation of the conclusions reached in the previous section, in particular concerning the impossibility of applying a compensation procedure to realistic dipolar arrangements.

The planar configuration of the dipoles naturally induces a decomposition of the vector potential in terms of $\mathbf{k}_\parallel$, the in-plane discrete component of the wave vector with corresponding quantization surface S, and its orthogonal component k_z, quantized by the length of the cavity L. Consequently, the photonic operators can be labeled as $a_{\mathbf{k}_\parallel, k_z, \lambda}$, where λ indicates the two transverse polarizations. Therefore, the mode expansion of the vector potential can be written as

$$\begin{aligned} A(\mathbf{r}) &= \sum_{\lambda,\mathbf{k}_\parallel} \sum_{k_z} \mathcal{E}_k\, e^{i\mathbf{k}_\parallel\cdot\mathbf{r}_\parallel}\, e^{ik_z z}\, a_{\mathbf{k}_\parallel,k_z,\lambda}\, \hat{\mathbf{e}}_\lambda + \text{H.c.} \\ &= \sum_{\lambda,\mathbf{k}_\parallel} \sum_{k_z>0} \mathcal{E}_k\, e^{i\mathbf{k}_\parallel\cdot\mathbf{r}_\parallel} \left(e^{ik_z z} a_{l,\mathbf{k}_\parallel,k_z,\lambda} + e^{-ik_z z} a_{r,\mathbf{k}_\parallel,k_z,\lambda} \right) \hat{\mathbf{e}}_\lambda + \text{H.c.}\,, \end{aligned} \tag{4.16}$$

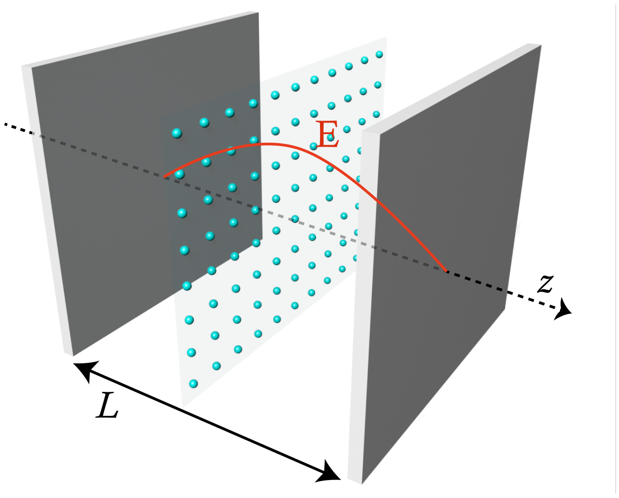

Figure 4.4: Schematic representation of a two-dimensional lattice of dipoles embedded in a cavity. We consider radiation modes orthogonal to the atomic layer (xy plane).

where $\mathcal{E}_k = \sqrt{\hbar/2\epsilon_0\epsilon_m\omega_k SL}$ and $\omega_k = v\sqrt{\mathbf{k}_\parallel{}^2 + k_z^2}$, with $v = c/\sqrt{\epsilon_m}$. In the second line of this decomposition, we introduced the left and right creation operators $a_{l(r),\mathbf{k}_\parallel,k_z,\lambda} \equiv a_{\mathbf{k}_\parallel,\pm k_z,\lambda}$, where the index $l\,(r)$ is associated with the $+(-)$ sign. If we consider only modes orthogonal to the planar surface, having $\mathbf{k}_\parallel = 0$ (and thus $\mathbf{k} = k_z\hat{\mathbf{z}}$), Eq. (4.16) considerably simplifies given that the two polarization vectors $\hat{\mathbf{e}}_\lambda$ now lie in the xy plane and the bosonic operators become independent on $\mathbf{k}_\parallel$, i.e. $a_{l(r),\mathbf{k}_\parallel=\mathbf{0},k_z,\lambda} \equiv a_{l(r),k_z,\lambda}$. Defining the even and odd radiation modes operators as $a_{e(o),k_z,\lambda} = \left(a_{l,k_z,\lambda} \pm a_{r,k_z,\lambda}\right)/\sqrt{2}$, the Hamiltonian of the free electromagnetic field reads [168]

$$H_{\text{ph}} = \hbar \sum_{j=e,o} \sum_{\lambda} \sum_{k_z>0} \omega_{k_z} a^\dagger_{j,k_z,\lambda} a_{j,k_z,\lambda}\,. \tag{4.17}$$

Following a procedure analogous to that applied to the three-dimensional dipole lattice, we first perform the two-level approximation including the dipole orientational degrees of freedom, as outlined in Appendix Section B.1, We then introduce bidimensional collective bosonic operators $b_{\mathbf{k}_\parallel,\alpha}$, defined for each orthogonal orientation $\alpha \in 1,2,3$, which reflect the bidimensionality of the layer. For incidence orthogonal to the planar surface ($\mathbf{k}_\parallel = 0$), the matter Hamiltonian takes the form

$$H_{\text{mat}} = \hbar\omega_0 \sum_{\alpha} b^\dagger_\alpha b_\alpha + \hbar \sum_{\alpha,\beta} \chi^2 \omega_0 f_{\mathbf{z},\alpha,\beta} \left(b_\alpha + b^\dagger_\alpha\right)\left(b_\beta + b^\dagger_\beta\right), \tag{4.18}$$

where $b_\alpha \equiv b_{\mathbf{k}_\parallel=0,\alpha}$ and the (structure-dependent) dipole-dipole interaction strength for a bidimensional square lattice is $\chi = \sqrt{d^2\mu/\hbar\epsilon_0\epsilon_m a^3\omega_0}$, with a being the lattice constant and $\mu \approx 6.78/4\pi$ (see Appendix C of Ref. [2] for details).

As in the three-dimensional case, the Hamiltonian in Eq. (4.18) can be diagonalized through a Bogoliubov transformation, which leads to the introduction of eigenoperators c_α with a corresponding renormalized frequency $\tilde{\omega}_\alpha = \omega_0\sqrt{1+4\chi^2 f_{\mathbf{z},\alpha,\alpha}}$. After including the interaction with the radiation field, the full light-matter Hamiltonian in the multipolar gauge can be written as

$$\begin{aligned} H =& \hbar \sum_{j=e,o}\sum_{\lambda}\sum_{k_z>0} \omega_{k_z} a^\dagger_{j,k_z,\lambda} a_{j,k_z,\lambda} + \hbar\sum_{\lambda}\tilde{\omega}_\lambda c^\dagger_\lambda c_\lambda \\ & - i\hbar \sum_{\lambda,k_z>0} \eta'\sqrt{\omega_{k_z}\tilde{\omega}^\perp}\left(a^\dagger_{e,k_z,\lambda} - a_{e,k_z,\lambda}\right)\left(c^\dagger_\lambda + c_\lambda\right) \\ & + \hbar \sum_{\lambda,k_z>0} \eta'^2\tilde{\omega}^\perp \left(c^\dagger_\lambda + c_\lambda\right)\left(c^\dagger_\lambda + c_\lambda\right)\,, \end{aligned} \tag{4.19}$$

where $\eta' = \eta\,\omega_0/\tilde{\omega}^\perp$ and $\tilde{\omega}^\perp$ are the renormalized light-matter coupling for the planar layer and transverse matter frequency, respectively, with $\eta = \sqrt{d^2N/\hbar\epsilon_0\epsilon_m SL\omega_0}$. In Eq. (4.19), without loss of generality, we have chosen the same basis for the dipole orientations and the radiation polarizations, *i.e.* $\hat{\mathbf{e}}_\alpha = \hat{\mathbf{e}}_\lambda$. We notice that only the even radiation modes couple with the matter field [168]. When considering a single cavity mode k_z and a single transverse polarization mode, the Hamiltonian in Eq. (4.19) reduces to that of a two coupled harmonic oscillators model, as the Dicke Hamiltonian in the thermodynamic limit, but with the additional self-polarization term.

From the total light-matter Hamiltonian in Eq. (4.19), we can derive the transverse dispersion relation through a Hopfield-Bogoliubov transformation, which reads

$$\frac{\Omega_\perp^2 - \tilde{\omega}^{\perp 2}}{2\tilde{\omega}^\perp} + 2\eta'^2\tilde{\omega}^\perp \sum_{k_z>0}\frac{\Omega_\perp^2}{\omega_{k_z}^2 - \Omega_\perp^2} = 0\,. \tag{4.20}$$

In the single-mode cavity approximation, such a relation reduces to the dispersion relation derived from a renormalized Hopfield-like model, as in the three-dimensional lattice. This result is to be expected due to the formal equivalence between the structures of the Hamiltonians in Eqs. (4.11) and (4.19).

Let us now highlight the subtle yet crucial differences between the three-dimensional and two-dimensional cases. In both arrangements, the dipole-dipole coupling strength χ scales as a^{-3}. However, the scaling of the light-matter coupling with the lattice constant differs. In particular, in the three-dimensional bulk, η can be directly related to the volumetric density ρ, leading to the proportionality $\eta^2 \propto \rho \propto a^{-3}$. In contrast, for a bidimensional layer, this relation no longer holds since the charges are arranged in a planar structure with a surface density

$\sigma \propto a^{-2}$. It is precisely the surface density that enters the expression for the light-matter coupling together with the cavity length L for this arrangement, such that $\eta^2 \propto \sigma/L \propto a^{-2}L^{-1}$. Consequently, in the bidimensional case, η cannot be straightforwardly connected to χ. Importantly, it is precisely the latter factor the one driving the QPT. Furthermore, we emphasize that in this case the cancellation procedure loses meaning, since the couplings that governing the dipole-dipole and the light-matter interactions, χ and η respectively, are different, despite both being dependent on the atomic dipole moment. Therefore, no perfect compensation can always be achieved.

In summary, together with the results of the previous section, these findings provide further evidence for the ferroelectric nature of the predicted QPT, as demonstrated by the following observations:

- the QPT occurs even without including the transverse coupling between matter and photons, and its inclusion neither shifts the critical point nor modifies the transverse polarization condensate;

- the critical parameter χ does not necessarily coincide with the light-matter coupling strength, despite both depending on the atomic dipole moment, as illustrated by the two-dimensional case, where in addition only χ depends on the cavity length;

- the QPT gives rise to a macroscopic transverse polarization of matter in the ground state, yet without any accompanying coherent macroscopic transverse electric or magnetic fields.

CHAPTER 5

Quantum phase transition in the open Dicke model: criticality in the presence of external baths

In this chapter, we study the critical behaviour of the open Dicke model in the presence of different types of baths, with particular focus on the vicinity of the critical point. This aspect is crucial for accurately reproducing experimental observations, especially in systems that are not driven-dissipative. Over the years, many approaches have been developed to study the driven-dissipative Dicke model, such as Lindblad master equations or Keldysh path integrals, which rely on well-established and widely-used approximations, including the Born-Markov approximation. However, if the system is not driven, many of these approximations fail in proximity of the critical point, thus preventing an accurate description of the critical behaviour. For instance, the Born-Markov approximation relies on the smallness of the ratio between the system-bath coupling strength and the relevant resonance frequencies of the systems, *i.e.* its eigenfrequencies. However, in proximity of the critical point, the lowest excitation energy of the system vanishes and the systems unavoidably enters first into the ultrastrong system-bath coupling regime, and subsequently the deep-strong coupling regime. As a consequence, the Born-Markov approximation becomes invalid.

In order to overcome these limitations, in this chapter we develop a general theoretical framework based on the quantum Langevin equations, valid in both the normal and superradiant phases. This method does not rely on approximations, and is thus well suited for describing equilibrium (non-driven) dissipative QPTs near their critical points. Furthermore, it enables the calculation of the spectral properties of the system when probed by a coherent weak tone, for arbitrary values of the critical parameters, different bath spectral densities (ohmic or non-ohmic), and arbitrary large damping rates. In our derivation, we consider the general case in which both the subsystems (harmonic and anharmonic) can interact with their respective reservoirs. The formalism can be straightforwardly extended to include additional loss channels, which have not been considered here for the sake of simplicity. Our findings show excellent agreement with recent experimental observations obtained in magnonic systems, where the SPT of a Dicke-like model was observed for the first time in a non-driven dissipative system.

This chapter is organized as follows. In Section 5.1, we briefly review the main properties of the standard Dicke model for an isolated system, deriving the effective Hamiltonians and the excitation energies in both the normal and superradiant phases. In Section 5.2, we extend this formalism to the open system case by including the interaction of each subsystem with its own thermal bath. We derive the quantum Langevin equations for both phases and study the critical behaviour of the system in presence of ohmic and non-ohmic baths. In Section 5.3, we compute the coherent emission spectra of the system when probed by a weak coherent tone, and analyze the effects of different types of baths on the spectral properties of the system, especially near the critical point. Finally, in Section 5.4, we investigate the ground-state squeezing of the system in vicinity of the critical point. The results presented in this chapter are based on Ref. [7].

5.1 SPT in the Standard Dicke model

In this section, we briefly summarize the main features of the standard Dicke model for an isolated system at zero temperature, in order to introduce the notations and the formalism that will be used in the following sections. We focus in particular on the properties of the Dicke model in the thermodynamic limit and on the associated superradiant phase tranition (SPT), as already mentioned in Section 1.5.2. Special attention will be devoted to the derivation of the effective Hamiltonians and of the eigenfrequencies of the system in both the normal and superradiant phases. In Section 5.2, we will then extend this formalism to the open system case, by including the coupling of each subsystem to its respective thermal bath. For notational convenience, in the following, we will omit the $\hat{}$ symbol on the operators, as we are working entirely within the quantum regime and no ambiguity can arise.

5.1.1 Standard Dicke model and its properties

The Dicke Hamiltonian, which describes a single bosonic mode with resonance frequency ω_a interacting with a collection of N identical two-level systems (TLSs) with transition frequency ω_b, is usually written as

$$H_{\text{sys}} = \hbar\omega_a a^\dagger a + \frac{\hbar\omega_b}{2}\sum_{i=1}^{N}\sigma_i^z + \frac{\hbar g}{\sqrt{N}}\left(a^\dagger + a\right)\sum_{i=1}^{N}\sigma_i^x\,, \tag{5.1}$$

where a is the bosonic annihilation operator, σ_i^α (with $\alpha = x, y, z$) are the usual Pauli operators associated to the i-th TLS and g is the coupling strength. This model does not include the $\mathbf{A}^2$ (or $\mathbf{P}^2$) term, which must be included when describing electric dipoles coupled to the electromagnetic field of a cavity in the Coulomb (dipole) gauge, as discussed in Chapter 3. Nevertheless, it is well-suited for systems displaying a Zeeman-like interaction, such as magnonic systems [157, 158].

Being an ubiquitous model in many areas of physics, the Dicke model has been extensively investigated and numerous generalizations have been proposed over the years. A first natural extension considers non-homogeneous couplings between the TLSs and the radiation field [22, 74]. Moreover, several extended versions of the Dicke model with additional interaction terms have been proposed, such as transverse spin-spin couplings (*e.g.* the introduction of the $\mathbf{P}^2$ term discussed in Chapter 3 and the Lipkin-Meshkov-Glick model [169]), longitudinal couplings [151], or the coupling to multiple bosonic modes [21, 170].

In this chapter, however, we will focus on the standard Dicke model in Eq. (5.1), which is the most basic model capturing the essential features of the SPT. Since all the TLSs are assumed to be identical, Eq. (5.1) can be equivalently rewritten by introducing collective spin operators $J^\alpha = \sum_i \sigma_i^\alpha/2$, satisfying the usual angular momentum algebra (notice that here we are not including the factor $\hbar$ into this definition, in contrast to the common convention). Therefore, the Dicke Hamiltonian can be expressed as

$$H_{\text{sys}} = \hbar\omega_a a^\dagger a + \hbar\omega_b J^z + \frac{\hbar g}{\sqrt{N}}\left(a^\dagger + a\right)\left(J^+ + J^-\right)\,, \tag{5.2}$$

where $J^\pm = J^x \pm iJ^y$ are the raising and lowering operators, respectively. It is straightforward to verify that the Dicke Hamiltonian presents a global $\mathbb{Z}_2$ symmetry, since it is invariant under the transformation $a \to -a$ and $J^\pm \to -J^\pm$. Formally, such symmetry can be expressed by noticing that the Hamiltonian commutes with the parity operator $\Pi = \exp\left[i\pi\left(a^\dagger a + J^z + N/2\right)\right]$, *i.e.* $[H_{\text{sys}}, \Pi] = 0$. This symmetry is associated to a conserved quantity, namely the parity of the total number of excitations. Indeed, every term in Eq. (5.2) preserves the total number of excitations with the exception of the counter-rotating terms $a^\dagger J^+$ and aJ^-, which however still create or annihilate two excitations at a time, thus conserving parity. The SPT occurring in the Dicke model corresponds to the spontaneous breaking of this $\mathbb{Z}_2$ symmetry [21]. For $g < g_c$, which is usually referred to as the *normal phase*, the ground state of the system respects this symmetry. On the contrary, for $g > g_c$, the systems enters the so-called *superradiant phase*, where the symmetry is spontaneously broken and the ground state becomes doubly degenerate. In this phase, both the bosonic mode and the collective spin acquire a macroscopic occupation in the ground state, either of which can serve as an order parameter for the SPT.

Another important property of the Dicke Hamiltonian in Eq. (5.2) is that it commutes with the total angular momentum operator $\mathbf{J}^2$. This allows the Hilbert space to be decomposed into independent sectors, each characterized by a different eigenvalue $j(j+1)$ of $\mathbf{J}^2$, with $j \in [j_0, N/2]$ in integer steps, where $j_0 = 0$ for N even and $j_0 = 1/2$ for N odd. The dimension of each spin-j sector is given by $D_j = (2j+1)N! \,/\, (N/2 - j)! \,(N/2 + j + 1)!$, so that the maximum angular momentum sector ($j = N/2$) has dimension $D_{N/2} = N + 1$. This block structure, derived by the division of the matter Hilbert space into the direct sum of these spin-j sectors, makes it possible to numerically diagonalize the Dicke Hamiltonian in each sector independently, greatly reducing the computational cost. This is particularly advantageous for large N, since the total dimension of the Hilbert space scales as 2^N, while the maximum angular momentum sector scales only linearly with N. Moreover, the numerical diagonalization can be further simplified by working in the so-called polaron frame, which has the advantage of reducing the number of bosonic excitations required to achieve convergence [171, 172].

Of particular interest is the thermodynamic limit of this model, which is obtained by letting $N \to \infty$. In this limit, the Dicke model undergoes a second-order QPT at a critical coupling strength $g_c = \sqrt{\omega_a \omega_b}/2$ [21, 92]. This value is in accordance with the mean-field result for finte termperature derived by Hepp and Lieb in their seminal work [19], which is given by $g_c = \sqrt{\omega_a \omega_b \coth(\hbar\omega_b/2k_B T)}/2$. In the zero-temperature limit, $\coth(\hbar\omega_b/2k_B T) \to 1$, recovering the previous result (see Section 1.5). Since our focus is on the quantum nature of this QPT, it is convenient to work directly at $T = 0$. In this case, both the ground state and the first excited state of the system lie in the maximum angular momentum manifold, which therefore becomes the most relevant for analyzing the SPT. Henceforth, we restrict our attention to this sector ($j = N/2$), which is composed by the states that couple most strongly with the bosonic field [21].

5.1.2 Effective bosonic Hamiltonian in the thermodynamic limit

We now employ the Holstein-Primakoff transformations [11, 140, 141] to derive two effective bosonic Hamiltonians, one for each phase of the system. We remind that the Holstein-Primakoff transformations map the angular momentum operators into bosonic operators b and $b^\dagger$ as

$$J^z = \left(b^\dagger b - \frac{N}{2}\right) , \tag{5.3a}$$

$$J^+ = b^\dagger \sqrt{N - b^\dagger b} \, , \tag{5.3b}$$

$$J^- = \sqrt{N - b^\dagger b} \, b \, . \tag{5.3c}$$

The bosonic vacuum $|0\rangle_b$ corresponds to the state with all TLSs in their ground state, *i.e.* $|0\rangle_b = |g\rangle^{\otimes N}$. By inserting these definitions into Eq. (5.2), we can rewrite the Dicke Hamiltonian in terms of bosonic operators only. We stress that this mapping is exact as long as we remain in the maximum angular momentum sector, since the dimension of such sector is $N+1$, which corresponds to the number of excitations allowed for the bosonic mode b. Therefore, the bosonic version of the Dicke Hamiltonian reads

$$\begin{aligned} H_{\text{sys}} =& \hbar\omega_a a^\dagger a + \hbar\omega_b b^\dagger b \\ &+ \hbar g \left(a^\dagger + a\right) \left(b^\dagger \sqrt{1 - \frac{b^\dagger b}{N}} + \sqrt{1 - \frac{b^\dagger b}{N}} \, b \right) . \end{aligned} \tag{5.4}$$

We now consider the thermodynamic limit of this Hamiltonian. As discussed above, in the normal phase ($g < g_c$), the ground state of the system is not macroscopically occupied, thus in the low-excitation regime we can linearize the operators in the Holstein-Primakoff maps, *i.e.* $b^\dagger\sqrt{1 - b^\dagger b/N} \simeq b^\dagger$ and $\sqrt{1 - b^\dagger b/N} \; b \simeq b$. This leads to the effective Hamiltonian in the normal phase

$$H_{\text{NP}} = \hbar\omega_a a^\dagger a + \hbar\omega_b b^\dagger b + \hbar g \left(a^\dagger + a\right) \left(b^\dagger + b\right) . \tag{5.5}$$

Such Hamiltonian can be straightforwardly diagonalized by considering the corresponding Hopfield-Bogoliubov matrix $\mathbf{A}_{\text{NP}}$, whose eigenvalues represent the excitation energies of the system, Ω. In the normal phase, such matrix reads

$$\mathbf{A}_{\text{NP}} = \begin{pmatrix} \omega_a & 0 & g & g \\ 0 & -\omega_a & -g & -g \\ g & g & \omega_b & 0 \\ -g & -g & 0 & -\omega_b \end{pmatrix} . \tag{5.6}$$

Therefore, the corresponding eigenfrequencies can be calculated by solving the eigenvalue problem $\mathbf{A}_{\text{NP}}\mathbf{v} = \Omega\mathbf{v}$, where $\mathbf{v}$ is the eigenvector associated to the eigenvalue Ω in the basis $\{a, a^\dagger, b, b^\dagger\}$. The two positive eigenvalues $\Omega_\pm$ are given by

$$\Omega_\pm^2 = \frac{1}{2}\left[\omega_a^2 + \omega_b^2 \pm \sqrt{(\omega_a^2 - \omega_b^2)^2 + 16 g^2 \omega_a \omega_b}\right] . \tag{5.7}$$

As previously discussed, and as can be directly verified from Eq. (5.7), the lowest excitation energy Ω_- vanishes in the limit $g \to g_c$, thereby signaling the occurence of the SPT. In contrast, in the superradiant phase ($g > g_c$), the effective Hamiltonian in Eq. (5.5) is no longer valid, since both fields acquire a macroscopic coherent occupation. To properly account for these condensates, the bosonic operators are shifted as

$$a \to a_{\mathrm{s}} + \sqrt{\alpha}\,, \qquad b \to b_{\mathrm{s}} - \sqrt{\beta}\,, \tag{5.8}$$

where α and β are c-number of order $O(N)$, while a_{s} and b_{s} are bosonic operators describing the fluctuations with respect to the respective mean value. By inserting these definitions into Eq. (5.4), we obtain a new Hamiltonian expressed in terms of the shifted bosonic operators, which reads (up to constant terms)

$$\begin{aligned} H_{\mathrm{sys}} =& \hbar\omega_a \left(a_{\mathrm{s}}^\dagger a_{\mathrm{s}} + \sqrt{\alpha}(a_{\mathrm{s}}^\dagger + a_{\mathrm{s}})\right) + \hbar\omega_b \left(b_{\mathrm{s}}^\dagger b_{\mathrm{s}} - \sqrt{\beta}(b_{\mathrm{s}}^\dagger + b_{\mathrm{s}})\right) \\ &+ \hbar g \sqrt{\frac{N-\beta}{N}} \left(a_{\mathrm{s}}^\dagger + a_{\mathrm{s}} + 2\sqrt{\alpha}\right) \left(b_{\mathrm{s}}^\dagger \sqrt{\xi} + \sqrt{\xi}\, b_{\mathrm{s}} - 2\sqrt{\beta}\sqrt{\xi}\right)\,, \end{aligned} \tag{5.9}$$

where, for notational convenience, we defined the operator

$$\sqrt{\xi} = \sqrt{1 - \frac{b_{\mathrm{s}}^\dagger b_{\mathrm{s}} - \sqrt{\beta}(b_{\mathrm{s}} + b_{\mathrm{s}}^\dagger)}{N-\beta}}\,. \tag{5.10}$$

We can now expand $\sqrt{\xi}$ in series of $1/N$ and substitute the resulting expression into Eq. (5.9). Retaining only terms up to the second order in the bosonic operators a_{s} and b_{s}, we finally obtain a quadratic Hamiltonian in the shifted bosonic operators, which still depends on the displacement parameters α and β. By imposing the equilibrium condition on the energy functional, corresponding to the vanishing of the linear terms in a_{s} and b_{s}, we obtain non-zero macroscopic mode occupations, which are given by [21]

$$\alpha = \frac{Ng^2}{\omega_a^2}\left(1 - \frac{1}{\lambda^2}\right)\,, \quad \beta = \frac{N}{2}\left(1 - \frac{1}{\lambda}\right)\,, \tag{5.11}$$

where $\lambda = 4g^2/\omega_a\omega_b = g^2/g_c^2$. Hence, the corresponding effective Hamiltonian in the superradiant phase reads

$$H_{\mathrm{SP}} = \omega_a a_{\mathrm{s}}^\dagger a_{\mathrm{s}} + \tilde{\omega}_b b_{\mathrm{s}}^\dagger b_{\mathrm{s}} + \tilde{g}(a_{\mathrm{s}} + a_{\mathrm{s}}^\dagger)(b_{\mathrm{s}} + b_{\mathrm{s}}^\dagger) + D(b_{\mathrm{s}} + b_{\mathrm{s}}^\dagger)^2\,, \tag{5.12}$$

where $\tilde{\omega}_b = \omega_b\,(\lambda+1)\,/2$, $\tilde{g} = g_c\sqrt{2/(\lambda+1)}$ and $D = \omega_b(\lambda-1)(3\lambda+1)/8(\lambda+1)$. The Hopfield-Bogoliubov matrix in the superradiant phase is thus given by

$$\mathbf{A}_{\mathrm{SP}} = \begin{pmatrix} \omega_a & 0 & \tilde{g} & \tilde{g} \\ 0 & -\omega_a & -\tilde{g} & -\tilde{g} \\ \tilde{g} & \tilde{g} & \tilde{\omega}_b + 2D & 2D \\ -\tilde{g} & -\tilde{g} & -2D & -\tilde{\omega}_b - 2D \end{pmatrix}\,. \tag{5.13}$$

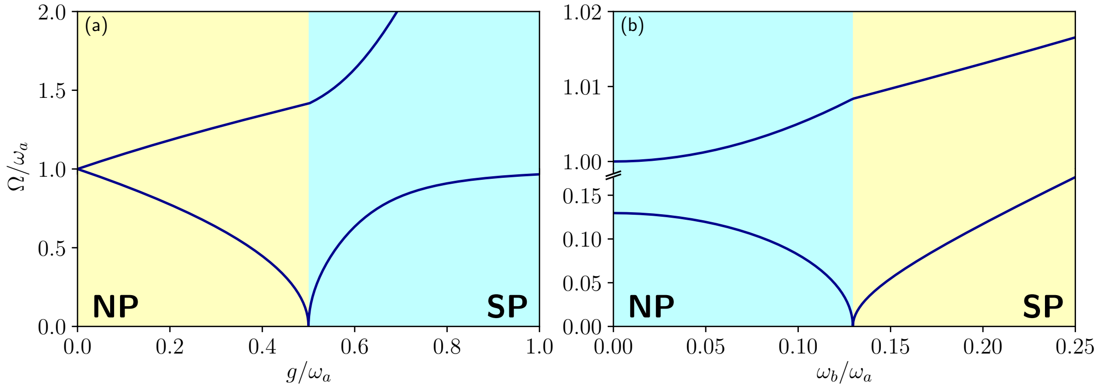

Figure 5.1: Upper and lower excitation energies for the isolated system in the normal (yellow background) and superradiant (cyan background) phases as a function of the **(a)** normalized coupling and **(b)** frequency ratio. Parameters: (a) $\omega_b/\omega_a = 1$, (b) $g/\omega_a = 0.18$.

The corresponding eigenfrequencies can be calculated analogously to the normal phase, which leads to the two positive eigenvalues $\Omega_\pm$ given by

$$\Omega_\pm^2 = \frac{1}{2}\left[\omega_a^2 + \lambda^2\omega_b^2 \pm \sqrt{(\omega_a^2 - \lambda^2\omega_b^2)^2 + 4\omega_a^2\omega_b^2}\right] . \tag{5.14}$$

In Fig. 5.1(a), the upper and lower excitation energies of the standard (closed system) Dicke model are plotted as a function of the normalized coupling strength g/ω_a. Similarly, Fig. 5.1(b) presents these excitation energies as a function of the frequency ratio ω_b/ω_a, which can be more easily controlled in a typical experimental realization [159].

5.2 Open Dicke model and its critical behaviour

In this section, we extend the well-established results of the previous section to include the interaction of the system with its external environment. This aspect is crucial for accurately reproducing experimental results, especially in systems that are not driven-dissipative. Indeed, the equilibrium SPT has been the subject of intense theoretical interest for decades, but its experimental demonstration still remains very challenging. Numerous non-equilibrium realizations of SPTs have been proposed over the years [144, 173]. Effective Dicke Hamiltonians in driven-dissipative systems have been reported, for example, in cold-atom systems driven by laser fields [174–178] and trapped ions [179]. However, despite strong analogies with the equilibrium SPT, such driven-dissipative transitions are inherently different phenomena [22, 180–183].

Theoretical proposals for the observation of equilibrium SPTs consider circuit QED systems [92, 152, 184–188], electron gases that either display a Rashba spin-orbit coupling [189] or interact with a spatially varying electromagnetic field [134, 190], and magnetic molecules coupled to superconducting microwave resonators via the Zeeman interaction [157, 191, 192]. Interesting related applications involve quantum computations in models exhibiting QPTs [193–195]. Recently, a proposal based on Er^{3+} spins collectively interacting with a magnonic field acting as the photonic mode [158] has led to the spectroscopic evidence of an equilibrium SPT [159].

In the following, we demonstrate that a large class of thermal baths, consisting of an infinite number of harmonic oscillators interacting with the system via a potential displaying a metastable minimum and with a *well-behaved* density of states (properly vanishing as $\omega \to 0$), does not affect the critical point with respect to the corresponding closed system. This finding, which aligns with the recent experimental results of Ref. [159], contrasts with earlier theoretical predictions obtained for driven-dissipative systems within master equation approaches [196–198]. We will also show that, in this case, the ground-state condensation occurring in the system influences the bath state, but not vice versa.

We begin by introducing a general theoretical framework based on the quantum Langevin equations, valid in both the normal and superradiant phases, which is approximation-free, thus particularly suitable for the description of non-driven dissipative QPTs near their critical points. In our derivation, we consider the general case in which both subsystems, A and B, interact with their respective external environments through the decay rates γ_a and γ_b (see Fig. 5.2). The formalism can be straightforwardly extended in the case of additional loss channels, such as additional input-output ports or non-radiative losses, which have not been included here for the sake of simplicity. The external baths are modeled as infinite, discrete collections of independent harmonic oscillators, coupled to the system Hamiltonian through their coordinates [111]. Hence, the total Hamiltonian takes the form

$$H = H_{\mathrm{sys}} + \frac{1}{2} \sum_{j=a,b} \sum_{n} \left[p_{jn}^2 + k_{jn} (q_{jn} - X_j)^2 \right] , \tag{5.15}$$

where q_{jn} and p_{jn} are the coordinate and momentum associated to the n-th mode of the j-th oscillator, respectively, and k_{jn} are the coupling constants determining the strength of the interaction between the system operator X_j and the n-th mode of the j-th bath. This form of coupling is physically well-grounded, as it admits a clear and straightforward interpretation: the bath coordinates q_{jn} are shifted from their unperturbed equilibrium position by the influence of the system coordinates X_j.

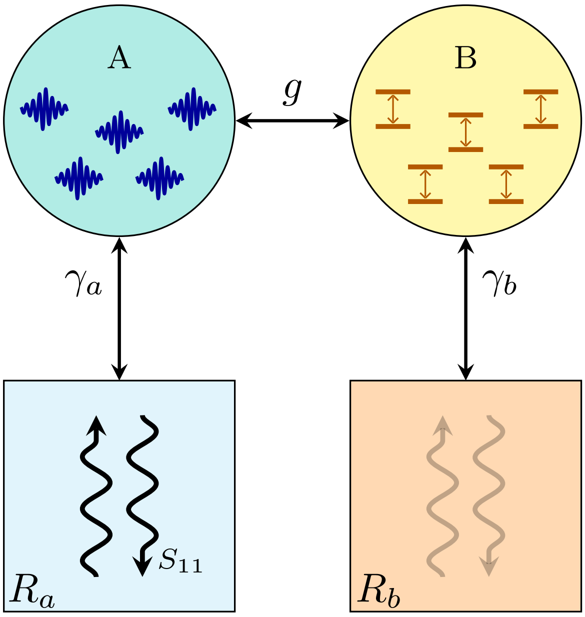

Figure 5.2: Schematic representation of the open Dicke model. A single bosonic mode interacts with a collection of N TLSs with coupling strength g. Each subsystem is coupled to its own thermal bath, characterized by a frequency-dependent coupling $\gamma_j(\omega)$, which may be ohmic or non-ohmic. The coupling of a subsystem with its own reservoir can also be regarded as an input-output port, through which the system can be excited and probed. In our analysis, we will explicitly consider a single tone coherent excitation of subsystem A and calculate the corresponding reflection coefficient S_{11}. The framework presented can be easily generalized to include the interaction with additional baths.

This interaction potential has the additional advantage of displaying a metastable energy minimum. On the other hand, another commonly employed form of the system-bath interaction term is given just by a sum of products between the system and bath coordinates, i.e. $q_{jn}X_j$. Differently from the expression in Eq. (5.15), the latter coupling term does not display an energy minimum and may therefore introduce additional instabilities into the system description. In what follows, we analyze the open-system dynamics by deriving the quantum Langevin equations directly from Eq. (5.15), without introducing any further approximation to the system-bath coupling. An equivalent alternative formulation involves the Fano-Hopfield-Bogoliubov diagonalization of the full Hamiltonian (see, *e.g.*, Refs. [168, 199]).

The system coordinates, X_j, that couple the external environments with the subsystems A and B are given by, respectively,

$$X_a = \sqrt{\frac{\hbar}{2\omega_a}} \left(a^\dagger + a\right) , \qquad X_b = \sqrt{\frac{\hbar}{2\omega_b}} \left(b^\dagger \sqrt{1 - \frac{b^\dagger b}{N}} + \sqrt{1 - \frac{b^\dagger b}{N}}\, b \right) . \tag{5.16}$$

These definitions will be used in the following to derive the quantum Langevin equations for both phases of the system.

5.2.1 Normal phase of the open Dicke model

In this subsection, we derive the quantum Langevin equations for the open Dicke model in the normal phase, while simultaneously identifying the critical point of the system. Indeed, in the thermodynamic limit, the ground state of the system in this phase is not macroscopically occupied, thus we can linearize the Holstein-Primakoff transformations in Eq. (5.3), as done in Section 5.1.2. Therefore, the system operator X_b can be approximated as $X_b \simeq \sqrt{\hbar/2\omega_b}(b^\dagger + b)$. We now derive the quantum Langevin equations for the bosonic operators a and b by following the procedure described in Ref. [111]. In particular, we use the standard form of the quantum Langevin equations for a generic system operator Y, which reads

$$\begin{aligned}\dot{Y}(t) &= \frac{i}{\hbar} \left[H_{sys}, Y(t)\right] \\ &\quad - \sum_{j=a,b} \frac{i}{2\hbar} \left[[X_j, Y] , \xi_j(t) - \int_{t_0}^{t} \dot{X}_j(t') f_j(t-t')\, dt' - f_j(t-t_0) X_j(t_0) \right]_+ ,\end{aligned} \tag{5.17}$$

where $[A, B]_+ = AB + BA$ is the anticommutator, $f_j(t) = \sum_n k_{jn} \cos(\omega_{jn} t)$ plays the role of a memory function, and t_0 is the initial time at which the system and baths are assumed to be uncorrelated. The noise operators $\xi_j(t)$ are defined as

$$\xi_j(t) = \sum_n \sqrt{\frac{\hbar k_{jn} \omega_{jn}}{2}} \left(c_{jn}^\dagger(t_0) e^{i\omega_{jn}(t-t_0)} + c_{jn}(t_0) e^{-i\omega_{jn}(t-t_0)} \right) , \tag{5.18}$$

which satisfy the commutation relations $[\xi_i(t), \xi_j(t')] = i\hbar f_j(t-t')\delta_{ij}$. The operators c_{jn} and $c_{jn}^\dagger$ are the annihilation and creation operators of the n-th mode of the j-th bath, respectively, and ω_{jn} are the corresponding mode frequencies. The first term on the right-hand side of Eq. (5.17) describes the closed-system dynamics, while the second term takes into account the effects of the external baths on the system evolution. The latter includes both a noise contribution, described by the operators $\xi_j(t)$, and a dissipation contribution, which is non-local in time and depends on the memory functions $f_j(t)$, which are directly related to the spectral density of the baths.

We now specialize Eq. (5.17) to the system's bosonic operators, obtaining the following set of quantum Langevin equations

$$\dot{a} = -i\omega_a a - ig(b^\dagger + b) - \frac{i}{2\omega_a}\int_{t_0}^{t} f_a(t-t')[\dot{a}^\dagger(t') + \dot{a}(t')]dt' + \frac{i}{\sqrt{2\hbar\omega_a}}\xi_a \tag{5.19a}$$

$$\dot{a}^\dagger = i\omega_a a^\dagger + ig(b^\dagger + b) + \frac{i}{2\omega_a}\int_{t_0}^{t} f_a(t-t')[\dot{a}^\dagger(t') + \dot{a}(t')]dt' - \frac{i}{\sqrt{2\hbar\omega_a}}\xi_a \tag{5.19b}$$

$$\dot{b} = -i\omega_b b - ig(a^\dagger + a) - \frac{i}{2\omega_b}\int_{t_0}^{t} f_b(t-t')[\dot{b}^\dagger(t') + \dot{b}(t')]dt' + \frac{i}{\sqrt{2\hbar\omega_b}}\xi_b \tag{5.19c}$$

$$\dot{b}^\dagger = i\omega_b b^\dagger + ig(a^\dagger + a) + \frac{i}{2\omega_b}\int_{t_0}^{t} f_b(t-t')[\dot{b}^\dagger(t') + \dot{b}(t')]dt' - \frac{i}{\sqrt{2\hbar\omega_b}}\xi_b \tag{5.19d}$$

where we omitted the time dependence of the operators for the sake of clarity, aside from the memory functions. We analyze these equations in the frequency domain, assuming that the initial condition is set in the distant past, i.e., $t_0 \to -\infty$. The aforementioned assumption, combined with the constraint that $f(t)$ is generally a highly localized function around the zero of its argument (a Dirac delta function for an ohmic bath), allows the last term in Eq. (5.17) to be safely neglected. We define the decay rate function $\gamma_j(\omega)$ as the Fourier transform of $\theta(t)f_j(t)$, where $\theta(t)$ is the Heaviside step function, needed to ensures causality. Although in general $\gamma_j(\omega)$ is a complex-valued function, it must satisfy the property $\gamma_j^*(\omega) = \gamma_j(-\omega)$, since $f_j(t)$ is real-valued function. For the purposes of this paper, we assume $\gamma_j(\omega)$ itself to be real. Nonetheless, in explicit calculations, there is no restriction against taking it as complex.

Therefore, by taking the Fourier transform of Eqs. (5.19), we obtain the following set of quantum Langevin equations in the frequency domain for the normal phase, which can be written compactly in matrix form as

$$-i\omega\tilde{\mathbf{v}}(\omega) = -i\left(\mathbf{A}_{\mathrm{NP}} - \frac{i}{2}\mathbf{\Gamma}_{\mathrm{NP}}(\omega)\right)\tilde{\mathbf{v}}(\omega) + \tilde{\mathbf{F}}_{\mathrm{in}}(\omega)\,, \tag{5.20}$$

where $\tilde{\mathbf{v}} = (\tilde{a}, \tilde{a}^\dagger, \tilde{b}, \tilde{b}^\dagger)^T$ is the vector of the Fourier-transformed bosonic operators and $\tilde{\mathbf{F}}_{\mathrm{in}}$ is the Langevin force vector of the input fields in the frequency domain, whose components are given by

$$\tilde{\mathbf{F}}_{\mathrm{in}} = \left(\frac{i}{\sqrt{2\hbar\omega_a}}\tilde{\xi}_a,\; -\frac{i}{\sqrt{2\hbar\omega_a}}\tilde{\xi}_a,\; \frac{i}{\sqrt{2\hbar\omega_b}}\tilde{\xi}_b,\; -\frac{i}{\sqrt{2\hbar\omega_b}}\tilde{\xi}_b\right)^T\,. \tag{5.21}$$

The decay matrix $\mathbf{\Gamma}$ depends on how the losses of the system are modeled, which in turn are microscopically linked to the bath-system couplings k_{jn}. To simplify the notation, from now on we will omit the explicit dependence on ω whenever it is not strictly necessary. By introducing the matrix $\mathbf{M}(\mathbf{A},\mathbf{\Gamma}) = \mathbf{A} - i\mathbf{\Gamma}/2 - \omega\mathbf{I}$, Eq. (5.20) can be compactly written as

$$i\mathbf{M}(\mathbf{A},\mathbf{\Gamma})\tilde{\mathbf{v}} = \tilde{\mathbf{F}}_{\text{in}}\,. \tag{5.22}$$

An analogous procedure can be followed to derive the quantum Langevin equations for the output fields, by taking into account the final condition at $t_f \to +\infty$, rather than the initial condition at $t_0 \to -\infty$. The resulting quantum Langevin equations are similiar to Eq. (5.20), with the only difference that the sign of the decay matrix is reversed and the Langevin force vector now describes the output fields. Therefore, the matrix form of quantum Langevin equations for the output fields in the frequency domain reads

$$i\mathbf{M}(\mathbf{A},-\mathbf{\Gamma})\tilde{\mathbf{v}} = \tilde{\mathbf{F}}_{\text{out}}\,. \tag{5.23}$$

We remark that Eqs. (5.22) and (5.23) are exact and valid for any form of the decay rates $\gamma_j(\omega)$, thus allowing us to describe both ohmic and non-ohmic baths. In the next subsection, we show that this same form of the quantum Langevin equations holds also in the superradiant phase, with the only difference that the Hopfield-Bogoliubov and decay matrices are replaced by their superradiant counterparts, $\mathbf{A}_{\text{SP}}$ and $\mathbf{\Gamma}_{\text{SP}}$, respectively. For the specific cases of only one bath for each of the two subsystems A and B, as shown in Fig. 5.2, the resulting decay matrix $\mathbf{\Gamma}$ in the normal phase can be expressed as

$$\mathbf{\Gamma}_{\text{NP}} = \begin{pmatrix} \gamma_a & -\gamma_a & 0 & 0 \\ -\gamma_a & \gamma_a & 0 & 0 \\ 0 & 0 & \gamma_b & -\gamma_b \\ 0 & 0 & -\gamma_b & \gamma_b \end{pmatrix}. \tag{5.24}$$

The off-diagonal elements originates from the counter-rotating terms in the system-bath interaction in Eq. (5.15).

We can now use Eq. (5.22) to determine the excitation energies of the open system. If the system is not coherently driven, the mean values of the input fields vanish. Consequently, by averaging Eq. (5.22) and imposing the compatibility constraint on the system of equations, we obtain

$$\zeta_{\text{NP}}(\omega;\omega_a,\omega_b,\gamma_a,\gamma_b) \equiv \det\left[\mathbf{M}(\omega;\mathbf{A}_{\text{NP}},\mathbf{\Gamma}_{\text{NP}})\right] = 0\,. \tag{5.25}$$

The roots of this characteristic polynomial $\zeta_{\text{NP}}(\omega)$, denoted by Ω, correspond to the complex eigenfrequencies of the equilibrium open Dicke model, since by construction they are the eigenvalues of the non-Hermitian matrix $\mathbf{A}_{\text{NP}} - i\mathbf{\Gamma}_{\text{NP}}/2$. The evolution of these complex eigenvalues as a function of the coupling strength g determines the critical properties of the open system. A detailed discussion on their behaviour, together with a discussion of their main features, will be presented in Section 5.2.3. At this stage, we simply observe that the critical point of the open system can be identified in a similar way to the closed Dicke model, namely through the vanishing of one of the complex eigenfrequencies. Remarkably, this occurs at the same critical coupling strength as in the closed case, *i.e.* $g_c = \sqrt{\omega_a \omega_b}/2$. Beyond this critical point, the ground state of the system acquires a macroscopic occupation, requiring a revised description of the system. These implications will be addressed in the following subsection.

5.2.2 Superradiant phase of the open Dicke model

To properly describe the properties of the open Dicke model in the superradiant phase, it is essential to account for the condensates that develop in the system's ground state. A comprehensive and consistent treatment requires a direct analysis of the total Hamiltonian in Eq. (5.15), which includes both system and bath variables. This approach ensures a proper account of the mutual influence between the system and its environment, which becomes relevant in the strong system-bath coupling regime. This methodology significantly differs from previous studies, which typically rely on either the minimization of the effective system's degrees of freedom through a master equation approach [196, 198] or the analytic continuation of the system's Green function [200]. Such treatments effectively disregard possible modifications of the reservoirs induced by the QPT. In contrast, the framework adopted here enables a more comprehensive description of the open-system dynamics, capturing key effects that can emerge due to the strong system-bath interactions, which becomes inevitable in the vicinity of an equilibrium QPT.

To analyze the superradiant phase, we follow a procedure analogous to that adopted for the standard Dicke model, but with a crucial refinement: we shift both the system and bath bosonic operators, in order to accomodate a possible condensation of the bath modes as well. Specifically, we introduce the following shifted operators

$$\begin{aligned} a &= a_s + \sqrt{\alpha}\,, & b &= b_s - \sqrt{\beta}\,, \\ c_{an} &= c_{\mathrm{s},an} + \sqrt{\sigma_{an}}\,, & c_{bn} &= c_{\mathrm{s},bn} - \sqrt{\sigma_{bn}}\,, \end{aligned} \tag{5.26}$$

where $c_{jn} = (\omega_{jn} q_{jn} + i p_{jn}) / \sqrt{2\hbar\omega_{jn}}$ are the bosonic operators of the j-th bath. We emphasize that the baths can have different dimensionalities. In the superradiant phase, the system operators X_b can no longer be approximated as linear functions of the bosonic operators, as done in the normal phase, but should be expressed in terms of the shifted operators and subsequently expanded in series in the total Hamiltonian. A complete derivation of the effective Hamiltonian in the superradiant phase, obtained by inserting the definitions in Eq. (5.26) into

Eq. (5.15) and expanding up to second order in the shifted operators, is presented in Appendix C. The resulting non-zero macroscopic occupations α, β, σ_{an}, and σ_{bn} can be determined by imposing the equilibrium condition on the energy functional, which corresponds to the vanishing of the linear terms in the shifted operators. This procedure leads to the following expressions for the macroscopic occupations:

$$\begin{aligned} \alpha &= \frac{Ng^2}{\omega_a^2}\left(1-\frac{1}{\lambda^2}\right), & \beta &= \frac{N}{2}\left(1-\frac{1}{\lambda}\right), \\ \sigma_{an} &= \frac{k_{an}}{\omega_{an}\omega_a}\alpha\,, & \sigma_{bn} &= \frac{k_{bn}}{\omega_{bn}\omega_b}\frac{\lambda+1}{2\lambda}\beta\,. \end{aligned} \tag{5.27}$$

Notably, this minimization procedure reveals that the open Dicke model predicts a macroscopic ground state condensation in the superradiant phase which is exactly the same as in the isolated system, as evidenced by the same values of α and β as in Eq. (5.11). These results highlight what can be described as a *resilience* of the condensate against the effects of system-bath coupling. Furthermore, although the ground state condensation of the system remains unaffected by the presence of the baths, it nevertheless induces a macroscopic occupation in the bath fields. This phenomenon is to be expected in equilibrium conditions and can be interpreted as the baths inheriting a property of the system, much like a material develops magnetization when placed in contact with a magnet. The resilience of the QPT to the interaction of the system with the external baths can be ultimately traced to the specific form of the system-bath coupling introduced in Eq. (5.15). Indeed, the form of the microscopic system-bath interaction can significantly influence the predicted outcomes. For instance, in the present case, the compensation among some of the terms involved in the minimization process, which in turn plays a crucial role in determining the macroscopic mode occupations, is directly tied to this choice.

The resulting effective Hamiltonian in the superradiant phase can be compactly expressed as

$$H = H_{\mathrm{SP}} + \frac{1}{2}\sum_{j=a,b}\sum_{n}\left[p_{jn}^2 + \tilde{k}_{jn}\left(q_{\mathrm{s},jn} - x_j\right)^2\right], \tag{5.28}$$

where $q_{\mathrm{s},jn} = \sqrt{\hbar\omega_{jn}/2k_{jn}}\left(c_{\mathrm{s},jn}^\dagger + c_{\mathrm{s},jn}\right)$ are the coordinate fluctuation operators. Likewise, the effective system coordinates coupled to the baths are given by $x_a = \sqrt{\hbar/2\omega_a}(a_{\mathrm{s}}^\dagger + a_{\mathrm{s}})$ and $x_b = \sqrt{2\hbar/\omega_b(\lambda+1)^2}(b_{\mathrm{s}}^\dagger + b_{\mathrm{s}})$, while the effective coupling constants are $\tilde{k}_{an} = k_{an}$ and $\tilde{k}_{bn} = k_{bn}\left(\lambda+1\right)/2\lambda$. The effects of condensation are incorporated through the λ-dependent factors. As shown in Appendix Section C.2, the quantum Langevin equations in the superradiant phase preserve the same structure as in Eq. (5.23), upon the introduction of the decay matrix $\mathbf{\Gamma}_{\mathrm{SP}}$, obtained by the replacement $\gamma_b \to \tilde{\gamma}_b = 2\gamma_b/\lambda(\lambda+1)$ in $\mathbf{\Gamma}_{\mathrm{NP}}$ in Eq. (5.24). The effective loss rate of subsystem B, $\tilde{\gamma}_b$, coincides with the bare damping rate γ_b at the critical point but gradually decreases to zero as the coupling strength increases. This behavior arises from saturation effects, which become increasingly significant and are determined by the values of the condensates. Similarly to the normal phase, the excitation energies in the superradiant phase can be calculated by computing the roots of the characteristic polynomial $\zeta_{\mathrm{SP}}(\omega) = \det\left[\mathbf{M}(\omega; \mathbf{A}_{\mathrm{SP}}, \mathbf{\Gamma}_{\mathrm{SP}})\right]$.

5.2.3 Excitation energies and critical point of the open Dicke model

In this subsection, we analyze in detail the excitation energies of the open Dicke model, obtained as the complex eigenvalues of the non-Hermitian matrix $\mathbf{A} - i\mathbf{\Gamma}/2$. As already mentioned, they correspond to the roots of the characteristic polynomial $\zeta_{\mathrm{NP}}(\omega)$, defined in Eq. (5.25) for the normal phase, and $\zeta_{\mathrm{SP}}(\omega)$ for the superradiant phase.

Fig. 5.3 displays the real and imaginary parts of the complex excitation energies as a function of the normalized coupling strength g/ω_a for ohmic baths. In particular, Fig. 5.3(a) displays the real parts of the upper and lower excitation energies of the open Dicke model (red lines), compared with those of the closed Dicke model (blue lines). Fig. 5.3(c), on the other hand, presents the opposite of the imaginary parts of the upper (gray line) and lower (orange line) excitation energies of the open Dicke model. Finally, Fig. 5.3(b) is a zoom of Fig. 5.3(a,c) near the critical point.

The most notable distinction from the excitation spectra of the closed Dicke model is the emergence of a *gap* region between the normal and superradiant phases (Fig. 5.3(b)), where the real part of the lower polariton becomes zero while its imaginary part splits. We identify the critical point of the QPT with the vanishing of the imaginary part of a complex excitation energy, which necessarily coincides with the vanishing of the total complex eigenfrequency. It is important to highlight that extending the normal-phase excitation frequencies beyond the critical point would incorrectly predict a positive imaginary component for the lower mode, violating the principle of causality, which requires the response functions to not have any poles in the upper half of the complex frequency plane. Indeed, in the next section, we will show that the poles of a causal response function in the frequency domain (the reflection coefficient S_{11}) actually coincide with these complex excitation energies, thereby validating the present analysis. Remarkably, it can be shown that the critical point in this equilibrium open Dicke model coincides with that of the corresponding closed Dicke model, provided the dissipation rates are *well-behaved*, even if not ohmic. To clarify this point, we analyze the behavior of the complex excitation energies in the normal phase by examining the

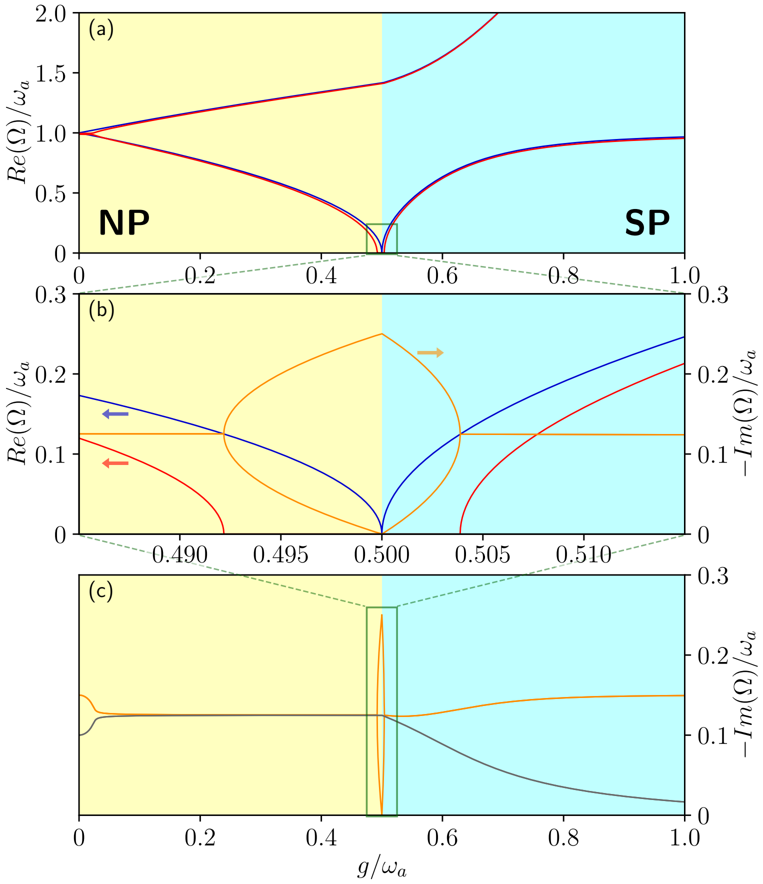

Figure 5.3: **(a)** Real parts of the upper and lower excitation energies as a function of the normalized coupling in the closed (blue) and open (red) Dicke models. **(b)** Inset zooming near the critical point of the lower polaritons of both the closed and open Dicke models. **(c)** Negative imaginary parts of the upper (gray) and lower (orange) excitation energies. In panel (b) the imaginary part of the upper polariton is not shown for the sake of clarity, as it is almost constant. Parameters used: $\omega_a = \omega_b = 1$, $\gamma_a = 0.3$, $\gamma_b = 0.2$.

explicit expression of $\zeta_{\mathrm{NP}}(\omega)$, given by

$$\begin{aligned}\zeta_{\mathrm{NP}}(\omega) = \omega^4 &+ i(\gamma_a + \gamma_b)\omega^3 - (\omega_a^2 + \omega_b^2 + \gamma_a\gamma_b)\omega^2 \\ &- i(\omega_a^2\gamma_b + \omega_b^2\gamma_a)\omega - 4g^2\omega_a\omega_b + \omega_a^2\omega_b^2\,.\end{aligned} \tag{5.29}$$

As can be readily observed, in the limit $\omega \to 0$ (i.e., near the QPT), only the constant terms in Eq. (5.29) are relevant, provided the damping rates are physically meaningful. By this, we refer to the constraint that $\omega\gamma(\omega)$ must vanish as $\omega \to 0$, though the rate at which it approaches zero may vary [201]. These constant terms vanish when the coupling strength reaches $g = \sqrt{\omega_a \omega_b}/2 = g_c$, which coincides with the critical coupling of the SPT in the closed Dicke model, thus demonstrating the resilience of the SPT against the coupling with the external environments. This result sharply constrasts with previous findings obtained using a master equation approach, where a finite gap between the excitations of the normal and superradiant phases emerged, thus preventing the identification of a well-defined critical point [196–198].

Another peculiar feature is the behavior in the energy spectrum at low coupling strengths, where the imaginary parts of the upper and lower excitation energies split (see Fig. 5.3(c)), while their real parts tends to converge. This characteristic behavior marks the transition between the weak and strong coupling regimes. Notably, if one of the channel effectively acts as a gain that compensates for the system's losses, i.e. $\gamma_b = -\gamma_a$, the effective Hamiltonian in the normal phase would display $\mathcal{PT}$ symmetry and the transition would have been associated to an exceptional point [202–207].

Although Eq. (5.29) remains valid for any well-behaved dissipation rates, the case of constant decay rates ($\gamma_j(\omega) \equiv \gamma_{0j}$, for frequencies well below a high-frequency cutoff) is of particular interest. This corresponds to the ohmic dissipation described in Ref. [201], as it yields the familiar velocity-dependent damping term of a classical damped harmonic oscillator. Indeed, considering as an example the decoupled oscillator A (thus $g = 0$), the frequency-domain equation of motion reads $-i\omega \tilde{P}_a = -\omega_a^2 \tilde{X}_a - i\omega\gamma_a \tilde{X}_a + \tilde{\xi}_a$ and we can identify the familiar damping term proportional to $\dot{X}_a$ in the time domain. Since the damping rates must satisfy the condition $\gamma_j^*(\omega) = \gamma_j(-\omega)$, we model their low-frequency behavior as $\gamma_j(\omega) = \gamma_{0j}|\omega|^s$, where $s = 0$ corresponds to the ohmic case. Baths with $-1 < s < 0$, where the damping rate vanishes more slowly as $\omega \to 0$ than in the ohmic case, are classified as subohmic, while those with $s > 0$ are referred to as superohmic. Pathological cases with $s \leq -1$ are excluded from the present analysis. Remarkably, due to the form of $\gamma_j(\omega)$, the behavior of $\zeta_{\mathrm{NP}}(\omega)$ near the QPT remains qualitatively unaffected, leaving the critical point unchanged even in presence of non-ohmic baths.

Fig. 5.4 shows the real (red) and imaginary (blue) parts of the lower eigenfrequency for subohmic (Fig. 5.4(a), dotted lines) and superohmic (Fig. 5.4(b), dash-dotted lines) baths, in comparison with the ohmic case (solid lines). The damping rates are intentionally set to high values to emphasize the relative differences between the various types of baths. This choice is allowed by the fact that our approach does not impose any constraints on the smallness of the damping rates, enabling an unrestricted exploration of their effects. We can notice that, while the critical point remains unchanged, the behavior of the imaginary parts

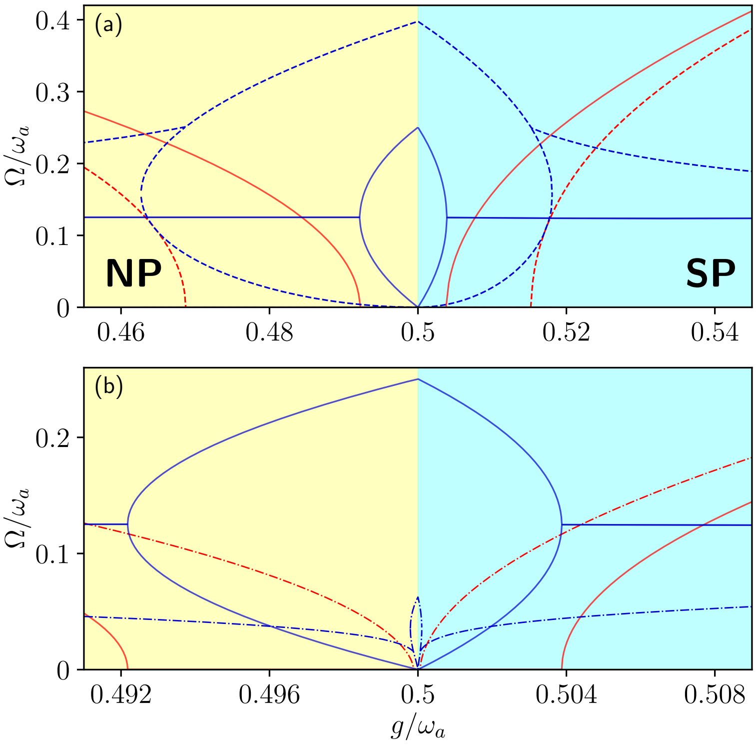

Figure 5.4: Comparison of the real (red) and imaginary (blue) parts of the lower excitation energy for ohmic baths (solid lines) with those for **(a)** subohmic baths (dotted lines) and **(b)** superohmic baths (dashed lines), plotted as functions of the normalized coupling strength g/ω_a. Notice the different scale of the g axis between the two panels. Parameters used: $\omega_a = \omega_b = 1$, $\gamma_{0a} = 0.3$, $\gamma_{0b} = 0.2$.

of the excitation energies is significantly influenced by the nature of the baths. In particular, although being qualitatively similar, the imaginary parts of the excitation energies for subohmic and superohmic baths exhibit narrower and broader profiles, respectively, compared to the ohmic case.

5.3 Coherent emission spectra

The theoretical framework previously presented, as discussed in the previous section, offers several advantages in analyzing the open Dicke model. Beyond its applicability across a broad range of parameters, thanks to the absence of approximations, and the possibility of addressing non-ohmic baths, it also allows for the analytical calculation of reflection and transmission spectra for both ohmic and non-ohmic environments. In this section, we develop the theoretical framework required for such analysis and subsequently analytically compute, as examples, the coherent reflection spectra of the open Dicke model in both phases of the system, for ohmic and non-ohmic baths.

We start by introducing the input and output fields associated with each bath, following the approach outlined in Refs. [111, 208]. In particular, we define the input and output fields in the time domain as

$$C_{\mathrm{in},j}(t) = \int_0^\infty \sqrt{\frac{\hbar}{4\pi\omega}} \left(\tilde{c}_{\mathrm{in},j}(\omega) e^{-i\omega t} + \tilde{c}^\dagger_{\mathrm{in},j}(\omega) e^{i\omega t} \right) d\omega \,, \tag{5.30}$$

with a similar relation holding for the output fields, $C_{\mathrm{out},j}(t)$. The creation and annihilation operators, in which these fields are decomposed, satisfy the canonical commutation relations $\left[\tilde{c}_{\mathrm{in/out},j}(\omega')\,,\tilde{c}^\dagger_{\mathrm{in/out},k}(\omega'')\right] = \delta_{jk}\delta(\omega'-\omega'')$ and are strictly related to the baths noise operators, as we will discuss in the following. For convenience, we adopted the continuum limit on the bath degrees of freedom. We observe that, in absence of the RWA, both co-rotating and counter-rotating terms in $C_{\mathrm{in},j}(t)$ must be considered. It can be shown that, in the normal phase, the Langevin forces are proportional to the fields in the frequency domain, *i.e.* $\tilde{F}_{\mathrm{in/out},j}(\omega) \propto \sqrt{\gamma_j/\omega_j}\,\tilde{C}_{\mathrm{in/out},j}(\omega)$. A similar relation holds in the superradiant phase, upon the introduction of a prefactor $2/(\lambda+1)$ preceding $\tilde{C}_{\mathrm{in/out},b}$. A detailed discussion on the derivation and properties of the input and output fields is provided in Appendix D of Ref. [7]. The input-output relations [29, 111, 208] can be obtained by combining Eqs. (5.22) and (5.23), reformulated in terms of the input and output fields $\tilde{C}_{\mathrm{in/out},j}$, which yields

$$\begin{pmatrix} \tilde{C}_{\mathrm{out},j} \\ -\tilde{C}_{\mathrm{out},j} \end{pmatrix} = \sum_k \sqrt{\frac{\omega_j}{\omega_k}\frac{\gamma_k}{\gamma_j}}\, \mathbf{M}\left(\mathbf{A},-\mathbf{\Gamma}\right)\mathbf{M}\left(\mathbf{A},\mathbf{\Gamma}\right)^{-1}\Big|_{jk} \begin{pmatrix} \tilde{C}_{\mathrm{in},k} \\ -\tilde{C}_{\mathrm{in},k} \end{pmatrix} \,, \tag{5.31}$$

where $\mathbf{M}\left(\mathbf{A},-\mathbf{\Gamma}\right)\mathbf{M}\left(\mathbf{A},\mathbf{\Gamma}\right)^{-1}\Big|_{jk}$ is the (j,k)-th 2×2 block for $j,k = 1,2\,(=a,b)$, as we are considering both the co-rotating and counter-rotating terms. Thus, we can now introduce the scattering matrix $\mathbf{S}(\omega)$, whose elements are defined by

$$S_{jk} = \left.\frac{\langle \tilde{C}_{\mathrm{out},j}\rangle}{\langle \tilde{C}_{\mathrm{in},k}\rangle}\right|_{\langle \tilde{C}_{\mathrm{in},i}\rangle = 0 \text{ for } i\neq k} \tag{5.32}$$

As already highlighted, a key advantage of this approach lies in the absence of any approximation in the derivation of Eq. (5.32), which makes it suitable for describing the system properties across all range of the parameters, including highly nontrivial cases such as those in the proximity of the critical point or in presence of strong dissipation.

As illustrative examples, in the following sections we compute coherent reflection spectra through port a, *i.e.* S_{11}, obtained by evaluating Eq. (5.32) for $j = k = 1$, which leads to

$$\begin{aligned} S_{11} &= \left.\frac{\langle \tilde{C}_{\mathrm{out},a}\rangle}{\langle \tilde{C}_{\mathrm{in},a}\rangle}\right|_{\langle \tilde{C}_{\mathrm{in},b}\rangle = 0} \\ &= \left(\frac{1}{\sqrt{2}}, -\frac{1}{\sqrt{2}}\right) \mathbf{M}\left(\mathbf{A}, -\mathbf{\Gamma}\right) \mathbf{M}\left(\mathbf{A}, \mathbf{\Gamma}\right)^{-1}\Big|_{11} \begin{pmatrix} 1/\sqrt{2} \\ -1/\sqrt{2} \end{pmatrix} \\ &= \frac{\zeta(\omega_a, \omega_b, -\gamma_a, \gamma_b)}{\zeta(\omega_a, \omega_b, \gamma_a, \gamma_b)} \,. \end{aligned} \tag{5.33}$$

As already previously mentioned, the denominator in this expression corresponds to the characteristic polynomial of the open Dicke model and thus the poles of S_{11} coincide with the complex excitation energies of the system. We are not employing any subscripts to distinguish between the normal and superradiant phases, as Eq. (5.33) is valid in both phases, provided the appropriate Hopfield-Bogoliubov and decay matrices are used. Furthermore, Eq. (5.33) is valid for both ohmic and non-ohmic baths. Spectra associated with alternative input-output channels, such as the transmission spectrum S_{12}, can be readily obtained by appropriately applying Eq. (5.32).

5.3.1 Ohmic emission spectra

In this subsection, we focus our attention on the analysis of ohmic spectra ($s = 0$), which corresponds to assuming constant damping rates, i.e. $\gamma_j(\omega) = \gamma_{0j}$ in Eq. (5.33). While maintaining constant damping rates over a broad spectral range is not entirely realistic, here our main interest lies in the low-frequency region, where the softening of the lower polariton occurs near the critical point. Nevertheless, the theoretical framework employed here allows for the incorporation of more complex frequency-dependent damping rates without any issues, as we will demonstrate in the next subsection.

In Fig. 5.5, we plot the reflection spectra for an ohmic bath over a wide range of parameters, taking advantage of the opportunities our treatment allows for. A key feature observed is the presence of a coupling-dependent Lamb shift, which displaces the reflection minima relative to the eigenfrequencies of the isolated system (green solid lines). However, while the Lamb shift is appreciable far from the critical point, it vanishes in the vicinity of g_c, as highlighted in the inset of panel (a) and panels (e-f). Simultaneously, the left-side broadening of the asymmetric Lorentzian profile shrinks to zero at the same rate as the minima, ensuring a consistent spectral description even in the low-frequency regime. We point out

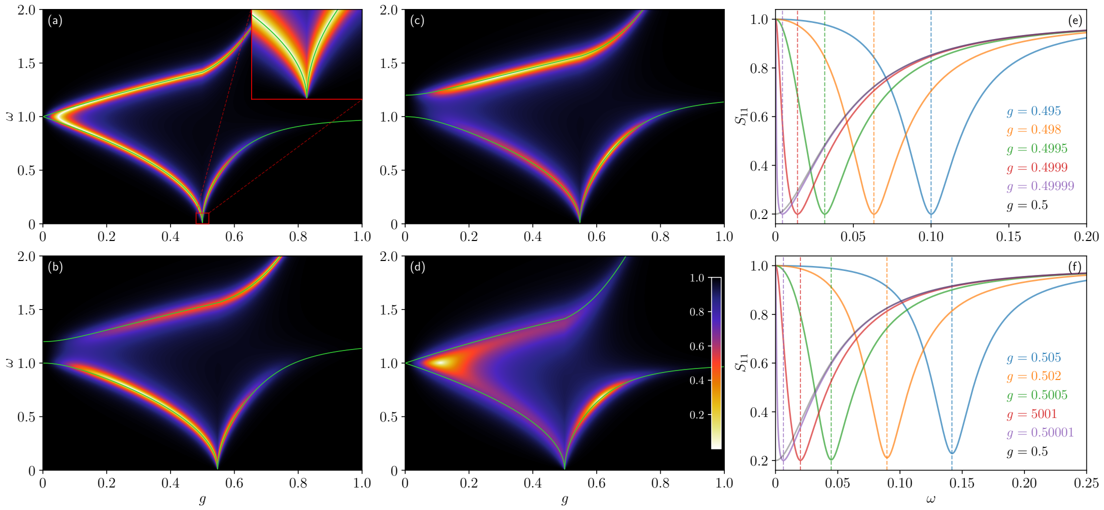

Figure 5.5: **(a-d)** 2D ohmic reflection spectra S_{11}, with an inset near the critical point in (a). The corresponding close-system excitation energies Ω are superimposed on the plots (green lines). **(e,f)** 1D spectra in the proximity of the critical point. Vertical lines represent the corresponding closed-system lower excitation energies Ω_{-}, showing excellent agreement with the minima of the reflection spectra, both in (e) normal and (f) superradiant phases. Parameters used: (a) $\omega_a = \omega_b = 1$, $\gamma_a = \gamma_b = 0.1$; (b) $\omega_a = 1.2$, $\omega_b = 1$, $\gamma_a = 0.2$, $\gamma_b = 0.1$; (c) $\omega_a = 1.2$, $\omega_b = 1$, $\gamma_a = 0.1$, $\gamma_b = 0.2$; (d) $\omega_a = \omega_b = 1$, $\gamma_a = 0.1$, $\gamma_b = 0.5$; (e-f) $\omega_a = \omega_b = 1$, $\gamma_a = 0.05$, $\gamma_b = 0.075$.

that the reflection spectrum exactly at the critical point is not entirely physically meaningful for the lower polariton, as it exhibits a reflectivity different from 1 at $\omega = 0$. However, this does not pose a practical issue in experiments and applications, since the critical point represents a singular set of zero measure in the coupling parameter space and cannot be precisely accessed due to various intrinsic system noises. Indeed, for any coupling $g = g_c \pm \epsilon$, where ϵ is a arbitrary small positive quantity, the spectra remain well-behaved. While panel (a) represents a resonant system ($\omega_a = \omega_b = 1$), a comparison of panels (b) and (c) provides additional insight: both depict detuned systems ($\omega_a = 1.2, \omega_b = 1$), but in panel (b) the subsystem A has an higher damping rate compared to B ($\gamma_a = 0.2, \gamma_b = 0.1$), whereas panel (c) illustrates the opposite scenario. The most striking consequence is the difference in the depth of the reflection minima for the upper and lower excitation energies, which is to be expected due to the different nature of the polaritons at low and high coupling strengths. Panel (d) showcases a more extreme scenario where $\gamma_b = 0.5$, placing it well outside the parameter range where the Born-Markov approximation remains valid, regardless of the coupling strength. In this case, we observe a considerable Lamb shift, particularly for the upper excitation energy and for weak couplings in the lower branch. However, even in this extreme situation, the Lamb shift vanishes when approaching the critical point for the lower polariton. Finally, panels (e,f) present 1D reflection spectra near the critical point (solid lines), alongside the excitation energies of the closed Dicke model described by Eqs. (5.7) and (5.14) (vertical dashed lines). Remarkably, these plots confirm that, in the proximity of the critical point, the usual interpretation of the real and imaginary parts of the complex eigenfrequencies as reflection minima and linewidths, respectively, breaks down. Indeed, since the two quantities become comparable in magnitude, the reflection minima are instead better determined by the closed-system excitation energies. This feature explains why, even near a QPT, experimental fits remain accurate when compared with the conventional closed-system eigenfrequencies (see, e.g., the theoretical description and related fit in Ref. [159]). Furthermore, this analysis aligns with the previous observation of the vanishing of the Lamb shift near the critical point, both from (e) below and (f) above.

5.3.2 Non-ohmic emission spectra

In this subsection, we explore the impact of non-ohmic baths on the reflection spectra of the open Dicke model. As previously discussed, our theoretical framework allows for the consideration of arbitrary frequency-dependent damping rates without any restrictions. In particular, as illustrative examples, we consider $s = -0.5$ for the subohmic and $s = 0.5$ for the superohmic cases, and calculate the corresponding reflection spectra using Eq. (5.33). Spectra for other types of baths or different channels can be straightforwardly computed using the same procedure.

In Fig. 5.6(a,b), we present subohmic reflection spectra, utilizing the same parameters as those used in panels (a) and (c) of Fig. 5.5, respectively. Similarly, Fig. 5.6(c,d) displays superohmic reflection spectra for the corresponding parameter set. In the subohmic spectra, we observe a broadening of the full width at half maximum (FWHM) for the lower polariton and a narrowing for the upper polariton compared to the ohmic case. This behavior arises from the frequency-dependent scaling of the damping, $\gamma_j(\omega) = \gamma_{0j}/\sqrt{|\omega|}$, which amplifies losses at low frequencies while reducing them at high frequencies. Conversely, in the superohmic case, characterized by $\gamma_j(\omega) = \gamma_{0j}\sqrt{|\omega|}$, losses are enhanced at high frequencies and suppressed at low frequencies. This behavior is particularly evident in the insets near the critical point shown in Fig. 5.6(a,c), especially when compared to the inset of Fig. 5.5(a) for the ohmic bath. The range of all three insets is the same to better highlight the differences in spectral characteristics. Fig. 5.6(e,f) display 1D lower polariton spectra for coupling strengths close to the critical point, showing the differences between various baths both (e) below and (f) above the

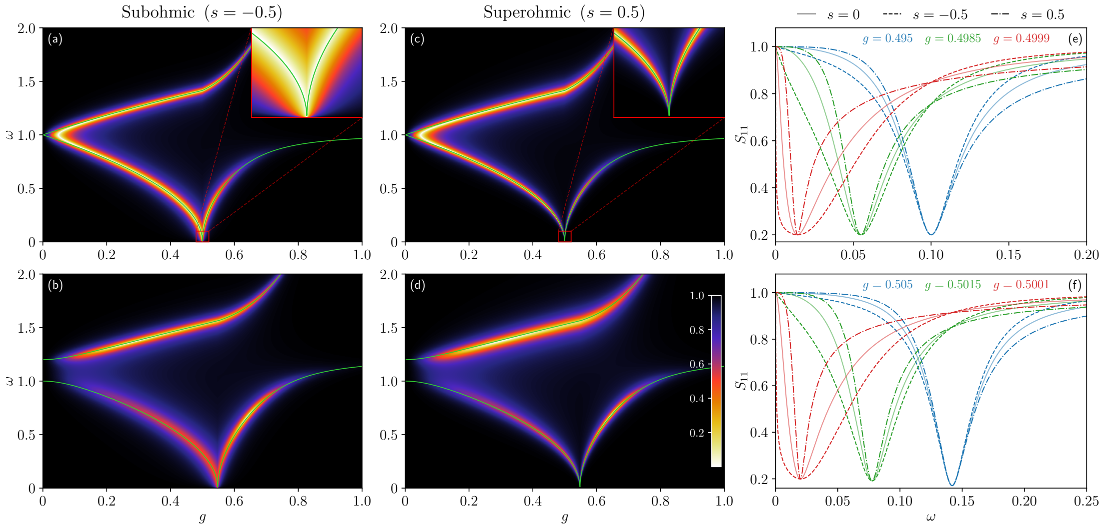

Figure 5.6: **(a-d)** 2D reflection spectra S_{11} for subohmic (a,b) and superohmic (c,d) baths, with the corresponding close-system excitation energies Ω (green lines). The insets near the critical point highlight the differences in the spectral behavior. **(e,f)** Comparison of the 1D spectra in the proximity of the critical point, both in (e) normal and (f) superradiant phases, for different coupling strengths in the three cases studied: ohmic (solid), subohmic (dashed) and superohmic (dash-dotted). The constants γ_{0j} have been chosen such that the damping rates of the lower excitation energies $\gamma_j(\Omega_-)$ for the blue lines would be equal, allowing for a better comparison between the lineshapes. Parameters used: (a,c) $\omega_a = \omega_b = 1$, $\gamma_{0a} = \gamma_{0b} = 0.1$; (b,d) $\omega_a = 1.2$, $\omega_b = 1$, $\gamma_{0a} = 0.1$, $\gamma_{0b} = 0.2$; (e,f) $\omega_a = \omega_b = 1$, $\gamma_{0a} = 0.05$, $\gamma_{0b} = 0.075$ for the ohmic case, while in the subohmic and superohmic cases the dampings have been respectively divided or multiplied by a factor 3.162 in the normal phase and 2.656 in the superradiant phase.

QPT. The most notable difference lies in the distinct lineshapes between different baths, which cannot be solely attributed to variations in FWHM. Instead, it directly arises from the frequency dependence of $\gamma_j(\omega)$, leading to a highly asymmetric Lorentzian behavior. To better illustrate this feature, the damping rates in Fig. 5.6(e,f) have been deliberately chosen to differ across the three cases, while coinciding at a specific point. Specifically, the values of γ_{0j} for the different baths have been adjusted so that the damping rates evaluated at the lower eigenfrequency, i.e. $\gamma_j(\Omega_-)$, are all equal for specific coupling strengths near the critical point ($g = 0.495$ and $g = 0.505$ for the normal and superradiant phases, respectively, corresponding to the blue lines). This ensures a fair comparison of the spectral asymmetry originating from the frequency dependence of $\gamma_j(\omega)$.

5.4 Squeezing near the critical point and its observability

Fundamental concepts as squeezing and entanglement have been extensively studied in quantum optics for several decades. Their relevance has further increased with the development of various fields, including quantum computing and quantum cryptography, as well as in many-body systems displaying QPTs near their criticality [209–211]. It has been demonstrated that the ground state of the Dicke model exhibits two-mode squeezing, which becomes perfect at the critical point of the QPT [21, 212]. This result may have significant implications for sensing applications [213], since intrinsic squeezing has the potential to enhance the robustness of quantum sensing and information processing against photon loss and decoherence [214, 215]. Typically, squeezing is observed in signals with appreciable intensity; however, the ground state, by definition, does not radiate. Nonetheless, recent advancements in nonlinear optical techniques, in particular electro-optic sampling, have enabled the probing of vacuum fluctuations [216–218]. Since the detection of a signal necessarily requires considering an open system, the investigation of the open Dicke model becomes essential in this context. In this section, we explore the presence of squeezing in the ground state of the open Dicke model and discuss its potential observability. Specifically, while focusing on the normal phase, we will present results obtained in the dispersive regime, leaving a more general treatment to Appendix E of Ref. [7].

In electro-optic sampling, the measured output field results from the convolution of the input field with the field inside the system, each oscillating at its respective eigenfrequency. This principle is strictly correlated to energy conservation [219]. Consequently, when defining the field quadratures, it is essential to express them in terms of physical operators oscillating at the actual system eigenfrequencies, rather than in terms of bare operators (a and b), which do not possess a well-defined frequency due to the presence of counter-rotating terms in the interaction and therefore contain contributions from both positive and negative frequencies [82, 220]. The correct construction of the quadratures thus requires decomposing fields into their positive- and negative-frequency components, denoted $X^+(\omega)$ and $X^-(\omega)$, respectively.

As an illustrative example, let us consider the case in which the measurement apparatus is placed outside the reference system, assumed here to be a single-mode electromagnetic resonator coupled to a magnetic material. Probing vacuum fluctuations implies providing the free vacuum field as input state and analyzing how its interaction with the system modifies the state. In light of the aforementioned considerations, we define the positive- and negative-frequency operators as

$$X^+(\omega) = \tilde{C}_{\mathrm{out},a}(\omega)\,, \qquad X^-(\omega) = \tilde{C}^\dagger_{\mathrm{out},a}(\omega)\,. \tag{5.34}$$

The corresponding ϕ-dependent quadrature operator is therefore given by

$$X_\phi(\omega) = e^{i\phi} X^+(\omega) + e^{-i\phi} X^-(\omega)\,, \tag{5.35}$$

whose ground-state variance is $(\Delta X_\phi)^2 \equiv \langle 0| (X_\phi)^2 |0\rangle - \langle 0| X_\phi |0\rangle^2 = \langle 0| (X_\phi)^2 |0\rangle$.

To highlight the fundamental physics without heavy mathematical treatment, in this section we analyze the problem within the dispersive regime [221]. We refer the reader to Appendix E of Ref. [7] for a more general treatment, which does not rely on this approximation. In the dispersive limit, $\omega_b \gg \omega_a$, the spin dynamics can be traced out through the use of a suitable Schrieffer-Wolff transformation [124, 125], resulting in an effective Hamiltonian in the normal phase

$$H_{\mathrm{SW}} = \hbar\omega_a a^\dagger a - \frac{\hbar g^2}{4\omega_b}\left(a^\dagger + a\right)^2 + \frac{1}{2}\sum_n \left[p_{an}^2 + k_{an}(q_{an} - X_a)^2\right]\,, \tag{5.36}$$

where the coupling operator X_a is the same as in Eq. (5.15). Notably, it can be verified that the application of the Schrieffer-Wolff transformation does not alter the coupling between the system and the thermal bath, k_{an}.

Proceeding in a similar manner as in the previous sections, we derive the input-output relation for the effective Hamiltonian in Eq. (5.36), which reads

$$\tilde{C}_{\mathrm{out},a}(\omega) = \frac{\omega(\omega - i\gamma_a)\omega_b + \omega_a(4g^2 - \omega_a\omega_b)}{\omega(\omega + i\gamma_a)\omega_b + \omega_a(4g^2 - \omega_a\omega_b)}\,\tilde{C}_{\mathrm{in},a}(\omega)\,. \tag{5.37}$$

As expected, this equation coicides with the dispersive limit of Eq. (5.31). Indeed, by taking the dispersive limit of the $(1,1)$-th block in Eq. (5.31), *i.e.* of $\mathbf{M}(\mathbf{A}, -\boldsymbol{\Gamma})\,\mathbf{M}(\mathbf{A}, \boldsymbol{\Gamma})^{-1}\big|_{11}$, we recover exactly the prefactor in Eq. (5.37). In turn, the input field can be expressed in terms of the bath operators as

$$\tilde{C}_{\mathrm{in},a}(\omega) = i\sqrt{\frac{\hbar}{2\omega}}\tilde{c}_{\mathrm{in},a}(\omega)\,, \tag{5.38}$$

for $\omega > 0$, whereas it is proportional to the creation operator $\tilde{c}^\dagger_{\mathrm{in},a}(\omega)$ for $\omega < 0$, as it can be verified by taking the Fourier transform of Eq. (5.30). Inserting Eqs. (5.37) and (5.38) into Eq. (5.34) and recalling that $\tilde{c}_{\mathrm{in},a}(\omega)\,|0\rangle = 0$ by definition, we obtain

$$(\Delta X_\phi)^2 = \langle 0| X^+(\omega) X^-(\omega) |0\rangle = \frac{\hbar}{2\omega}\,. \tag{5.39}$$

The resulting variance $(\Delta X_\phi)^2$ is independent of the angle ϕ, thus demonstrating that the squeezing in the ground state cannot be detected using these techniques. Eq. (5.39) is strictly related to the experimental scheme employed in electro-optical detection. The impossibility of accessing ground-state squeezing aligns with the findings of Ref. [220]. It is worth noting, however, that their analysis focused on systems where counter-rotating terms were included only in the system Hamiltonian, while the system-bath interaction was simplified using the RWA. Furthermore, their detection model was based on homodyne detection rather than on electro-optic sampling.

On the contrary, we expect that strong two-mode squeezing and quantum entanglement could be observable near the critical point if a non-adiabatic time modulation of either the coupling strength g or of one of the two bare frequencies $\omega_{a/b}$ is implemented. Such a physical process is in close analogy with the dynamical Casimir effect observed in superconducting circuits [222, 223] and quantum vacuum radiation in polariton systems [224], in the absence of QPTs. Instead, the theoretical framework presented here also provides the means for investigating these dynamical modulations in the proximity of a critical point, which could greatly enhance the generation of quantum correlations, entanglement and squeezing.

Chapter 6

Conclusions

This thesis explores various ultrastrongly-coupled systems and their properties, with particular focus on quantum phase transitions, spectral features, and effective models. In particular, it is structured in chapters that progressively build on each other, starting from Chapter 1, which provided all the basics and theoretical tools necessary to understand the subsequent chapters.

Chapter 2 was devoted to the simplest case of a single two-level emitter coupled to a single mode of the electromagnetic field in the ultrastrong coupling (USC) regime, which can be described by the quantum Rabi model (QRM). In particular, we investigated the properties of this model in both cavity and circuit quantum electrodynamics (QED) implementations, highlighting how the coherent and incoherent emission spectra may differ significantly in the USC regime. Specifically, we studied circuit QED systems described by an extended QRM with parity-symmetry breaking terms, which are coupled to the external environment either inductively or capacitively. We showed that this two coupling mechanisms lead to significantly different emission spectra, especially in the USC regime, for both coherent and incoherent emission. We explained these differences in terms of the dynamical variables that couple the system with the external environment, being either the flux or the charge operator of the qubit, further highlighting the importance of correctly identifying the interaction mechanism. We then compared these results with cavity QED spectra, finding that they coincide with those of capacitively coupled circuit QED setups. In the same chapter, we also investigated the influence of higher-energy levels of the matter subsystem (which, by definition, are neglected in a two-level description) on the system's behavior in the USC regime. This led us to the introduction of the renormalized QRM (RQRM), through which we were able to incorporate the effects of these higher-energy levels into the system's parameters while still retaining a two-level description. To this end, we employed a slightly variation of the Schrieffer-Wolff transformation, which allowed us to obtain analytical expressions for the renormalized parameters of the RQRM, both in cavity and circuit QED. These results were validated numerically by exactly diagonalizing the full Hamiltonian, demonstrating a significant improvement in accuracy of the RQRM over the standard QRM, particularly in the USC regime. Beyond the energy spectrum, we also analyzed the gauge invariance of the RQRM, showing that it is possibly to recover a notion of gauge invariance, inspired by that defined in truncated Hilbert spaces introduced in Refs. [77, 87]. Finally, we discussed how the renormalization affects the system's observables and how higher-order correction can further improve the accuracy, though at the cost of losing the analyticity of the treatment.

Chapter 3 extended the previous analysis to systems composed of multiple two-level emitters coupled to a single mode of the electromagnetic field, which can be described by an extended Dicke model including the additional self-polarization term. In this chapter, the electrostatic interactions between the emitters are still not taken into account, which will be instead addressed later. We explored the evolution of the system properties, such as energy levels and emission spectra, as a function of the number of emitters, and how these results converge toward those of the Hopfield model in the thermodynamic limit. We also studied how different coupling mechanisms between the emitters and the external environment, either individual or collective, affect the system's emission spectra, showing that collective coupling can lead to the emergence of an emission line at the cavity frequency which can be traced back to the presence of the dark states, that are not optically active in the case of individual emitter-bath couplings.

In Chapter 4, we investigated the impact of the electrostatic interactions between the emitters, which are often neglected in simpler models, on the system's behavior. This topic has been the subject of much controversy in recent years, especially regarding the occurrence of a superradiant phase transition (SPT) in such systems, with many works arguing both for and against its occurrence (see Section 4.1 for a brief review of the literature on this topic). In this chapter, we demonstrated that these electrostatic interactions can indeed induce a quantum phase transition (QPT) in the system, which however has different characteristics from the standard SPT predicted by the Dicke model. To further support these results, we investigated two realistic arrangement of the emitters: a three-dimensional lattice of spatially separated and highly localized dipoles and a two-dimensional dipole layer embedded in a cavity. Especially in the latter case, by carefully modeling the system, we showed that a supposed compensation between the dipole-dipole interactions and the inter-atomic contribution of the self-polarization term is indeed not possible. This mechanism was in fact at the basis of many arguments supporting the occurrence of a SPT in such systems.

Finally, Chapter 5 was devoted to the study of the open Dicke model, and specifically to the impact of external baths on the occurrence of the SPT in equilibrium conditions. This topic is of great importance, as in realistic implementations the system is always coupled to an external environment, which in principle could modify its behavior. Unlike most of the existing literature, which concentrates on driven-dissipative versions, this chapter is focused on the equilibrium case, where many of the usual approximations (such as the Born-Markov approximation) break down, especially in the vicinity of the critical point. To overcome these limitations, we employed an approch based on the quantum Langevin equations, which allowed us to exactly solve the system in the thermodynamic limit, even in the presence of strong coupling with the environment or in presence of non-ohmic baths. Remarkably, we found that the presence of the baths does not modify the critical point with respect to the closed system, in striking contrast to previous works on driven-dissipative systems. Furthermore, the macroscopic occupations in the superradiant phase are also unaffected by the presence of the baths, while the baths themselves on the other hand acquire macroscopic occupations of their modes in the superradiant phase. This formalism also allowed us to analytically study the coherent emission spectra of the open Dicke model, which we analyzed for different types of baths, both ohmic and non-ohmic. In the end, we discussed the possibility of observing squeezing in the vicinity of the critical point.

In conclusion, this thesis aims to contribute to the understanding of the properties of ultrastrongly-coupled light-matter systems, both closed and open, ranging from single-emitter to many-emitter configurations and their thermodynamic limit. Particular emphasis was placed on the occurrence of quantum phase transitions and on the spectral properties of these systems, which were analyzed in detail. Furthermore, we introduced effective models that can accurately describe these systems while maintaining simple analytical forms, thus offering reliable tools for both the theoretical analysis and its physical interpretation. Overall, I hope that the results presented in this thesis will prove useful for future theoretical and experimental research in this rapidly evolving field.

However, this thesis does not cover all the works I contributed to during my PhD, as some of them did not directly fit into the main narrative. In particular, I would like to breafly discuss the publication reported in Ref. [6], which, although not involving ultrastrongly coupled systems, is sitll relevant to the field of light-matter interactions.

In this work, carried out in collaboration with an experimental group from the University of Modena and Reggio Emilia, we reported the observation of Perfect Absorption (PA) in a system consisting of molecular spin centers coherently coupled to a planar microwave resonator at millikelvin temperatures and in the single-photon regime. Two different samples of molecular spin ensembles were investigated: (i) a spin ensemble with a single dominant transition, consisting of diluted α, γ-bisdiphenylene-β-phenylallyl (BDPA) organic radical spins, and (ii) a sample with multiple hyperfine transitions due to the presence of a large nuclear spin ($I = 7/2$), which consists of a diluted tetraphenylporphyrinato oxovandium(IV) complex (VOTPP) spins. The platform employed allows for a fine tuning of the spin-photon coupling and to control the effective dissipation of the two subsystems towards the environment, by adjusting either the distance between the spin samples and the resonator or between the probing antenna and the resonator, respectively. The central result of this work was the observation of PA in a system of molecular spin ensembles at cryogenic temperatures, supported by a theoretical description within the framework of non-Hermitian physics.

From the theoretical standpoint, we developed a model based on the input-output formalism and its mapping to effective non-Hermitian Hamiltonians, that was able to accurately reproduce the experimental results. Since the interactions were mainly due to the magnetic component of the coplanar waveguide resonator field, which interacts with the spins via their magnetic dipole moment, a Dicke-like model was employed to describe the system. For the BDPA sample, this reduces to the standard Dicke Hamiltonian, while the VOTPP sample required a generalized multi-level, multi-coupling Dicke Hamiltonian to account for the different hyperfine transitions and their corresponding coupling strengths. Both these models have been solved in the thermodynamic limit through the use of the Holstein-Primakoff transformations. Importantly, the coupling strengths achieved in this platform never achieved the USC regime, thus justifying the use of the rotating wave approximation in the Hamiltonian description.

Subsequently, we focused on the analysis of the open system properties and, in particular, on the development of a framework able to predict the presence of PA. In general, PA occurs when there is a dip in the reflection spectrum reaching zero reflectivity. We reported its observation both in the weak and strong coupling regimes and demonstrated how this phenomenon can be easily explained in terms of non-Hermitian physics. In particular, we showed that PA occurs when the imaginary part of a complex eigenvalue of an effective non-Hermitian Hamiltonian vanishes. These findings constitues a generalization of the results presented in, *e.g.*, Ref. [225], where the effective non-Hermitian Hamiltonian exhibited $\mathcal{PT}$-symmetry. In contrast, being our Hamiltonian composed of more than two interacting subsystems, the very notion of $\mathcal{PT}$-symmetry is not applicable, thus requiring a more general framework.

Specifically, we showed that the presence PA can be linked with the emergence of a Hermitian subspace in the effective non-Hermitian Hamiltonian describing the system, characterized by a real eigenvalues, *i.e.* vanishing of the corresponding imaginary part. This generalizes the concept of $\mathcal{PT}$-symmetry and provides a

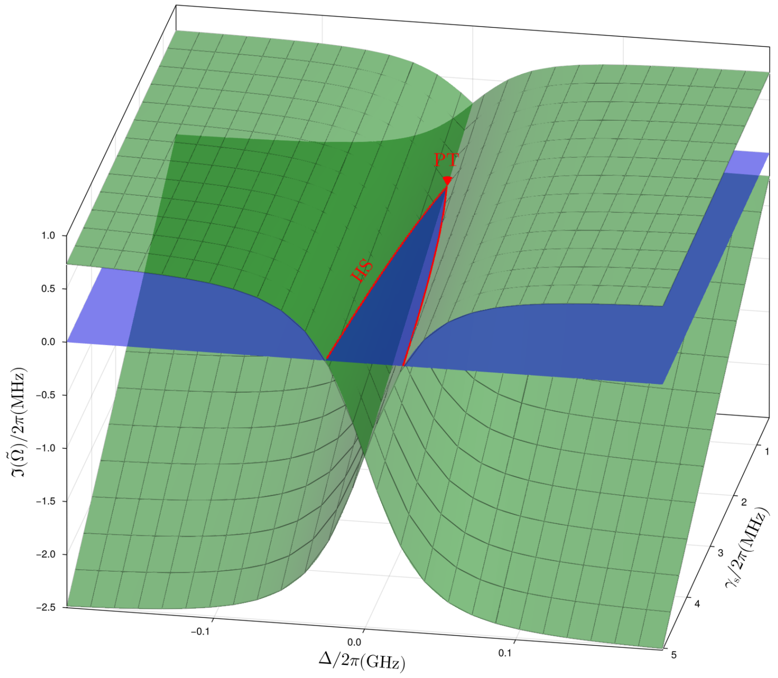

Figure 6.1: Surface plot illustrating the imaginary part of the complex eigenvalues of the effective non-Hermitian Hamiltonian in the case of two interacting bosons, as a function of the detuning Δ and the spins decay rate γ_s. The two red lines indicate where an Hermitian subspace is realized, *i.e.*, the intersection with the $\mathrm{Im}(\tilde{\Omega}) = 0$ plane (in blue), where one of the eigenvalues becomes real. These lines coalesce at the point $(\gamma_\mathrm{s}, \Delta) = (\gamma_\mathrm{c}, 0)$, marked by the red triangle, corresponding to the PT symmetry condition, where γ_c is the effective gain of the cavity.

broader criterion for PA. Furthermore, we demonstrated (both theoretically and experimentally) that these Hermitian subspaces can be engineered through the resonator-spin detuning, which controls the composition of the polaritons in terms of its photon and spin contents. Importantly, given the previous considerations, the realization of Hermitian subspaces is of easier experimental realization with respect to the realization of exceptional points, which instead requires a much finer tuning of the system parameters. Fig. 6.1 illustrates this concept for the case of two interacting bosons, namely a single resonator mode and a single spin transition of the BDPA sample. The surface plot shows the imaginary part of the complex eigenvalues $\tilde{\Omega}$ of the effective non-Hermitian Hamiltonian for such a systems, as a function of the detuning Δ and the spins decay rate γ_s. The red lines indicate the realization of Hermitian subspaces, where one of the eigenvalues

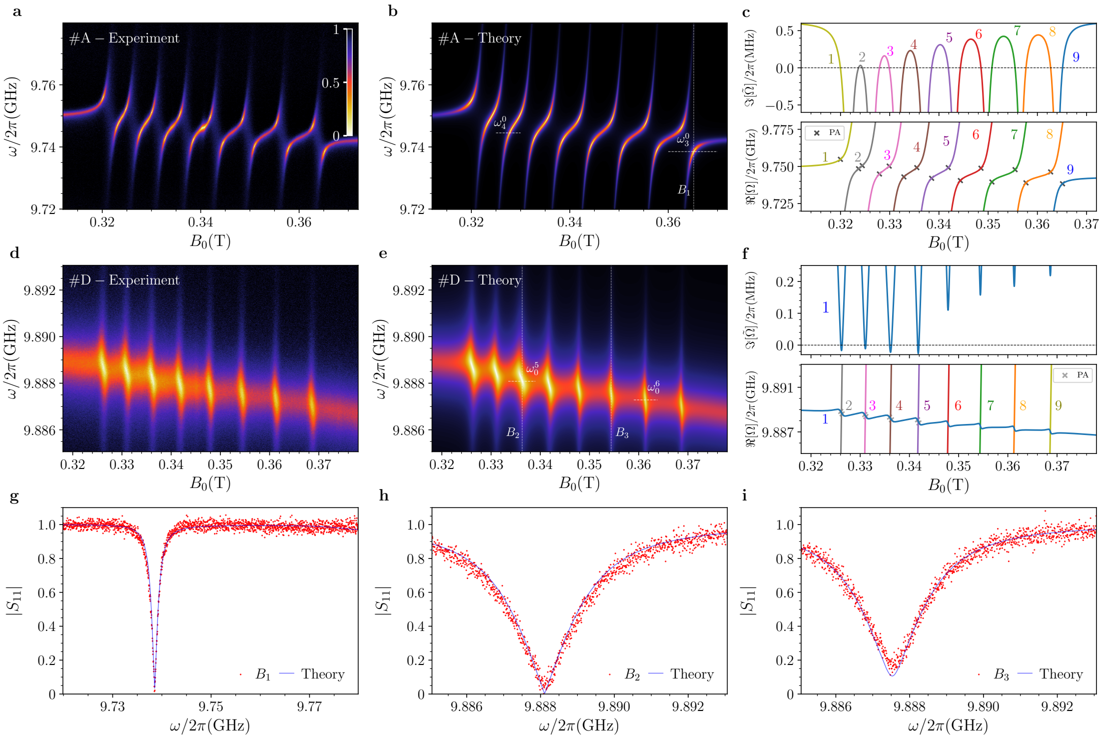

Figure 6.2: **(a,d)** Normalized reflection maps measured for the VOTPP crystal as a function of the externally applyed static magnetic field B_0 and driving frequency. PA is observed in proximity of multiple hyperfine levels. The strongest (position $\#A$) and the weakest (position $\#D$) coupling regimes are shown, respectively. **b,e** Simulated reflection maps obtained by fitting the maps in panels (a,d). **(c,f)** (Upper panels) Imaginary parts of the complex frequencies as a function of the magnetic field B_0, for each polariton frequency. The horizontal black dotted line corresponds to the the vanishing of the imaginary part, *i.e.* the PA condition.(Lower panels) Real parts of the polariton frequencies with the predicted PA points, showing excellent agreement with the experimental data. **(g,h,i)** Experimental (red dots) and theoretical (blue lines) normalized reflection data in correspondence of the vertical lines B_1, B_2, and B_3, displaying (g,h) perfect absorption dips and one (i) not satisfying this condition.

becomes purely real, i.e., $\mathrm{Im}(\tilde{\Omega}) = 0$ (in blue). These two lines coalesce at the point $(\gamma_s, \Delta) = (\gamma_c, 0)$, where γ_c is the effective gain of the cavity (effective feeding due to the drive minus intrinsic losses). This point, marked by the red triangle, corresponds to the $\mathcal{PT}$-symmetry condition. This figure clearly illustrates how that Hermitian subspaces, and thus the presence of PA, can be achieved for a wide range of parameters, not only at the $\mathcal{PT}$-symmetry point.

The theoretical predictions were found to be in excellent agreement with the experimental results, both in the weak and strong coupling regimes, thus confirming the validity of our model. Fig. 6.2 shows the experimental and theoretical reflection maps for the VOTPP sample, which exhibits multiple hyperfine transitions. The left-most panels (a,d) display the experimental normalized reflection maps as a function of the externally applied static magnetic field B_0 and driving frequency, clearly showing the possibility to achieve PA in both coupling regimes. The middle panels (b,e) show the corresponding theoretical simulations, which perfectly reproduce the experimental results. The right-most panels (c,f) present the imaginary (upper panels) and real (lower panels) parts of the complex polariton frequencies, $\tilde{\Omega}_j$, as a function of the magnetic field B_0. The horizontal black dotted line at $\mathrm{Im}(\tilde{\Omega}) = 0$ identifies the PA condition, while the corresponding markers in the lower panels highlight the predicted PA points, in excellent correspondence with the experimental dips in the reflection spectra. Finally, panels (g,h,i) show three representative vertical cuts of the normalized reflection data in correspondence of the dips at three values of the magnetic field B_1, B_2, and B_3, further consolidating the excellent agreement between the experimental data (red dots) and theoretical fit (blue lines). The first two panels (g,h) display perfect absorption dips, while the last one (i) does not satisfy the PA condition.

Since these results were obtained in the linear response regime, future studies could explore the possibility of achieving PA in purely quantum systems, such as those described by the quantum Rabi model, where nonlinear quantum effects could play a crucial role.

Appendix A

Derivation of the RQRM in cavity and circuit QED

In this Appendix, we provide additional details on the derivation of the Renormalized Quantum Rabi Model (RQRM) presented in Section 2.3. We first introduce the general framework of the Schrieffer-Wolff transformation, which is used to include the contributions of the higher-energy levels into an effective low-energy Hamiltonian. Subsequently, we apply this method to the derivation of the RQRM for both cases studied in Section 2.3, namely a cavity QED setup where a natural atom interacts with a single-mode cavity field, and a circuit QED setup where a superconducting qubit is coupled to a resonator.

A.1 Schrieffer-Wolff transformation

The standard Schrieffer-Wolff (SW) transformation is a perturbative method that allows for the derivation of an effective Hamiltonian in a low-energy manifold by eliminating the interactions with higher-energy states [11, 124, 125]. This technique has been widely employed in various fields of physics, including condensed matter, quantum optics, and quantum information. In the context of cavity and circuit QED, the SW transformation has been used to derive effective models for systems operating in the dispersive regime [221]. This approach assumes the Hamiltonian to be divisible into two parts: a term belonging to the low-energy manifold, and a perturbative term that couples the low-energy manifold with the high-energy one. More formally, let the total Hamiltonian be expressed as

$$\hat{H} = \hat{H}_0 + \hat{H}_1 \,, \tag{A.1}$$

where $\hat{H}_0$ is the term lying in the low-energy manifold (plus eventual diagonal elements of $\hat{H}_1$), while $\hat{H}_1$ includes the contributions that links the low-energy manifold with the high-energy one and the terms residing in the high-energy subspace itself. As we will see in the next subsection, for our system, we will identify $\hat{H}_0 = \hat{H}_{0'} + \hat{H}^{\mathrm{L}}_{\mathrm{int,D}}$ and $\hat{H}_1 = \hat{H}^{\mathrm{H}}_{\mathrm{int,D}}$. The SW procedure consists in finding a suitable unitary transformation $\hat{U} = e^{\hat{S}}$ (where $\hat{S}$ must be an anti-Hermitian operator for $\hat{U}$ to be unitary), which allows for the truncation of the Hilbert space to the low-energy manifold to incorporate the effects of the high-energy states perturbatively. To this end, we apply the Baker-Campbell-Hausdorff formula, which transformes the Hamiltonian into

$$\hat{H}^{\mathrm{std}} = e^{\hat{S}} \hat{H} e^{-\hat{S}} = \hat{H} + \left[\hat{H}, \hat{S}\right] + \frac{1}{2}\left[\left[\hat{H}, \hat{S}\right], \hat{S}\right] + \cdots . \tag{A.2}$$

If we consider $\hat{H}_1$ to be proportional to a small parameter, we can truncate the series in Eq. (A.2) at the second order in this parameter. The goal of the SW transformation is to find $\hat{S}$ such that the transformed Hamiltonian $\hat{H}^{\mathrm{std}}$ does not include any coupling term between the low-energy and high-energy manifolds, at least up to the second order in the perturbation parameter, after the projection into the low-energy manifold. This can be achieved by choosing the SW generator, $\hat{S}$, such that it satisfies the condition

$$\hat{H}_1 + \left[\hat{H}_0, \hat{S}\right] = 0 . \tag{A.3}$$

The effective Hamiltonian can thus be expressed as

$$\hat{H}^{\mathrm{std}}_{\mathrm{eff}} \simeq \hat{H}_0 + \hat{H}_1 + \left[\hat{H}_0, \hat{S}\right] + \left[\hat{H}_1, \hat{S}\right] + \frac{1}{2}\left[\left[\hat{H}_0, \hat{S}\right], \hat{S}\right] , \tag{A.4}$$

where we have truncated the series at the second order in the perturbation parameter. By applying the condition in Eq. (A.3), we can simplify Eq. (A.4) to

$$\hat{H}^{\mathrm{std}}_{\mathrm{eff}} = \hat{H}_0 + \frac{1}{2}\left[\hat{H}_1, \hat{S}\right] . \tag{A.5}$$

This equation provides the effective Hamiltonian up to the second order in the perturbation parameter. The next step consists in projecting this effective Hamiltonian into the low-energy manifold by applying the projector $\hat{P}$, which leads to

$$\hat{\mathcal{H}}^{\mathrm{std}}_{\mathrm{eff}} = \hat{P} \hat{H}^{\mathrm{std}}_{\mathrm{eff}} \hat{P} = \hat{\mathcal{H}}_0 + \frac{1}{2} \hat{\mathcal{P}} \left[\hat{H}_1, \hat{S}\right] \hat{\mathcal{P}} , \tag{A.6}$$

where $\hat{\mathcal{H}}_0 = \hat{P} \hat{H}_0 \hat{P}$, which almost coincides with the $\hat{H}_0$ Hamiltonian itself, except for the diagonal higher-energy terms induced by the projection of $\hat{H}_1$. Eq. (A.6) represents the standard SW effective Hamiltonian.

From the condition in Eq. (A.3), we can explicitly write the matrix elements of the generator as

$$\langle n|\hat{S}|m\rangle = \frac{\langle n|\hat{H}_1|m\rangle}{E_m - E_n}\,, \tag{A.7}$$

where E_n and $|n\rangle$ are the eigenvalues and eigenvectors of $\hat{H}_0$, respectively. An explicit expression of the last term in Eq. (A.6) can be provided by using Eq. (A.7), namely

$$\begin{aligned}
\frac{1}{2}\langle n|\left[\hat{H}_1, \hat{S}\right]|m\rangle &= \frac{1}{2}\langle n|\hat{H}_1\hat{S} - \hat{S}\hat{H}_1|m\rangle \\
&= \frac{1}{2}\sum_l \left[\langle n|\hat{H}_1|l\rangle\,\langle l|\hat{S}|m\rangle - \langle n|\hat{S}|l\rangle\,\langle l|\hat{H}_1|m\rangle\right] \\
&= \frac{1}{2}\sum_l \langle n|\hat{H}_1|l\rangle\,\langle l|\hat{H}_1|m\rangle\left[\frac{1}{E_m - E_l} + \frac{1}{E_n - E_l}\right]. \qquad \text{(A.8)}
\end{aligned}$$

Therefore, by performing the two-level truncation on the atomic bare basis, *i.e.* by applying the projector $\hat{P}$, we obtain the effective Hamiltonian:

$$\begin{aligned}
\hat{\mathcal{H}}^{\rm std}_{\rm eff} &= \sum_n E_n \hat{P}\,|n\rangle\!\langle n|\,\hat{P} \\
&\quad + \frac{1}{2}\sum_{n,m}\sum_l \langle n|\hat{H}_1|l\rangle\,\langle l|\hat{H}_1|m\rangle\left[\frac{1}{E_m - E_l} + \frac{1}{E_n - E_l}\right]\hat{P}\,|n\rangle\!\langle m|\,\hat{P}\,. \qquad \text{(A.9)}
\end{aligned}$$

While this approach treats the low-energy subspace unperturbatively, it requires the knowledge of the eigenvalues and eigenvectors of $\hat{H}_0$. In the case of the QRM, although being integrable, finding their analytical form is challenging [50], as they involve transcendental equations and confluent Heun functions. Indeed, $\hat{H}_0$ is usually diagonalized numerically, and therefore also $\hat{\mathcal{H}}^{\rm std}_{\rm eff}$. This poses a clear limitation of this approach.

On the contrary, in order to obtain the RQRM, we slightly modify the standard SW procedure. In particular, we only require

$$\hat{H}^{\rm H}_{\rm int,D} + \left[\hat{H}_{0'}, \hat{S}\right] = 0\,, \tag{A.10}$$

as it will be clear in the next subsection. This choice allows us to achieve an analytical expression for the generator $\hat{S}$, as $\hat{H}_{0'}$ is already diagonal.

A.2 Derivation of the RQRM in cavity QED

In this subsection, we present the derivation of the RQRM in the cavity QED setting introduced in Section 2.3.1.

We consider the full Hamiltonian expressed in the dipole gauge in Eq. (2.33), as the perturbative expansion of the SW transformation is not suitable in the Coulomb gauge due to the growth of the interaction term, as already discussed in Section 2.1.1. Let us firstly rewrite this dipole-gauge Hamiltonian in the basis of the bare atomic eigenstates, which yields

$$\hat{H}_{\mathrm{D}} = \hbar\omega_c\hat{a}^\dagger\hat{a} + \hbar\sum_j \omega_j \left|j\right\rangle\!\left\langle j\right| - i\hbar\sum_{j,k} g_{jk} \left|j\right\rangle\!\left\langle k\right| \left(\hat{a} - \hat{a}^\dagger\right) + \hbar\sum_{j,k} \frac{G_{jk}}{\omega_c} \left|j\right\rangle\!\left\langle k\right| \tag{A.11}$$

where the coupling constants have been defined in Eq. (2.34). We now divide the full Hamiltonian into three terms:

$$\hat{H}_{\mathrm{D}} = \hat{H}_{0'} + \hat{H}^{\mathrm{L}}_{\mathrm{int,D}} + \hat{H}^{\mathrm{H}}_{\mathrm{int,D}}\,, \tag{A.12}$$

where

$$\hat{H}_{0'} = \sum_j \hbar\omega'_j \left|j\right\rangle\!\left\langle j\right| + \hbar\omega_c\hat{a}^\dagger\hat{a} \tag{A.13}$$

is the quasi-free Hamiltonian, which includes the high-energy frequencies renormalized by the diagonal contributions of the $\hat{x}^2$ term, i.e.

$$\omega'_j = \begin{cases} \omega_j & \text{if } j \leq 1, \\ \omega_j + \frac{G_{jj}}{\omega_c} & \text{if } j > 1 \end{cases}\,. \tag{A.14}$$

The remaining terms of the light-matter interaction are divided into the low-energy and high-energy terms given by, respectively,

$$\hat{H}^{\mathrm{L}}_{\mathrm{int,D}} = -\,i\hbar\sum_{j,k\in\mathcal{S}} g_{jk} \left|j\right\rangle\!\left\langle k\right| \left(\hat{a} - \hat{a}^\dagger\right) + \hbar\sum_{j,k\in\mathcal{S}} \frac{G_{jk}}{\omega_c} \left|j\right\rangle\!\left\langle k\right|\,, \tag{A.15}$$

$$\hat{H}^{\mathrm{H}}_{\mathrm{int,D}} = -\,i\hbar\sum_{j,k\in\overline{\mathcal{S}}} g_{jk} \left|j\right\rangle\!\left\langle k\right| \left(\hat{a} - \hat{a}^\dagger\right) + \hbar\sum_{j,k\neq j\in\overline{\mathcal{S}}} \frac{G_{jk}}{\omega_c} \left|j\right\rangle\!\left\langle k\right|\,, \tag{A.16}$$

where $\mathcal{S} = \{0,1\}^2$ is the low-energy manifold corresponding to the ground and first excited atomic states, and $\overline{\mathcal{S}} = \mathbb{N}^2 \setminus \mathcal{S}$ is its complementary subspace. This implies that $\hat{H}^{\mathrm{L}}_{\mathrm{int,D}}$ has elements only in the low-energy subspace, while $\hat{H}^{\mathrm{H}}_{\mathrm{int,D}}$ contains elements in the high-energy subspace.

While the low-energy interaction term cannot be treated perturbatively, the high-energy interaction term $\hat{H}^{\mathrm{H}}_{\mathrm{int,D}}$ can be regarded as a perturbation on $\hat{H}_{0'}$. Specifically, we assume that the cavity and the high-energy transitions are in the dispersive regime with the cavity, i.e. $\left|g_{jk}/(\omega'_{jk} - \omega_c)\right| \ll 1$. Under this condition, we employ the SW transformation to derive the effective influence of the high-energy terms on the low-energy subspace.

To this end, we introduce the generator of the SW transformation, $\hat{S}$, which can be expanded as (see Eq. (A.2))

$$e^{-\hat{S}}\hat{H}_{\mathrm{D}}e^{\hat{S}} = \hat{H}_{\mathrm{D}} + \left[\hat{H}_{\mathrm{D}}, \hat{S}\right] + \frac{1}{2}\left[\left[\hat{H}_{\mathrm{D}}, \hat{S}\right], \hat{S}\right] + \dots \,, \tag{A.17}$$

By truncating the series to the second order in the perturbation, and subsequently projecting into the two-level subspace, we obtain the effective Hamiltonian in the truncated Hilbert space

$$\begin{aligned}\hat{\mathcal{H}}_{\mathrm{D}}^{\mathrm{eff}} = \hat{P}\Big\{&\hat{H}_{0'} + \hat{H}^{\mathrm{L}}_{\mathrm{int,D}} + \hat{H}^{\mathrm{H}}_{\mathrm{int,D}} \\ &+\left[\hat{H}_{0'}, \hat{S}\right] + \left[\hat{H}^{\mathrm{L}}_{\mathrm{int,D}}, \hat{S}\right] + \left[\hat{H}^{\mathrm{H}}_{\mathrm{int,D}}, \hat{S}\right] + \frac{1}{2}\left[\left[\hat{H}_{0'}, \hat{S}\right], \hat{S}\right]\Big\}\hat{P}\,,\end{aligned} \tag{A.18}$$

with $\hat{P} = \sum_{j=0}^{1} |j\rangle\langle j|$ the projector onto the two-level subspace. We point out that the series is consistently truncated up to the second order in A_0, which is the parameter varied in the plots of the main text. We choose the generator $\hat{S}$ such that

$$\left[\hat{H}_{0'}, \hat{S}\right] = -\hat{H}^{\mathrm{H}}_{\mathrm{int,D}}\,, \tag{A.19}$$

in order to eliminate the high-energy terms from the effective Hamiltonian, while still treating the low-energy contribution $\hat{H}^{\mathrm{L}}_{\mathrm{int,D}}$ exactly. This leads to the following expression for the generator

$$\hat{S} = i\sum_{j,k\in\overline{\mathcal{S}}}\frac{g_{jk}}{\Delta_{jk}}\left[\omega'_{jk}\left(\hat{a}-\hat{a}^{\dagger}\right) + \omega_c\left(\hat{a}+\hat{a}^{\dagger}\right)\right]|j\rangle\langle k| - \frac{1}{\omega_c}\sum_{j,k\neq j\in\overline{\mathcal{S}}}\frac{G_{jk}}{\omega'_{jk}}|j\rangle\langle k|\,, \tag{A.20}$$

and, consequently, the effective Hamiltonian becomes

$$\hat{\mathcal{H}}_{\mathrm{D}}^{\mathrm{eff}} = \hat{P}\left\{\hat{H}_{0'} + \hat{H}^{\mathrm{L}}_{\mathrm{int,D}} + \frac{1}{2}\left[\hat{H}^{\mathrm{H}}_{\mathrm{int,D}}, \hat{S}\right] + \left[\hat{H}^{\mathrm{L}}_{\mathrm{int,D}}, \hat{S}\right]\right\}\hat{P}\,. \tag{A.21}$$

We notice that $\hat{P}\left[\hat{H}^{\mathrm{L}}_{\mathrm{int,D}}, \hat{S}\right]\hat{P} = 0$, because $\hat{H}^{\mathrm{L}}_{\mathrm{int,D}}$ is only composed of terms acting on the two-level subspace, and $\hat{S}$ is composed of terms acting only on its complementary subspace, resulting in a first-order zero contribution in the low-energy subspace. Finally, by explicitly expanding the other terms, we get the following effective Hamiltonian, up to an identity term

$$\begin{aligned}\hat{\mathcal{H}}_{\mathrm{D}}^{\mathrm{eff}} =&\hbar\omega_c\hat{a}^{\dagger}\hat{a} + \hbar\left(\frac{\omega_{10}}{2} + \frac{G_{11}-G_{00}}{2\omega_c} + A_-\right)\hat{\sigma}_z \\ &+ \hbar\left(B_+ + B_-\hat{\sigma}_z\right)\left(\hat{a}-\hat{a}^{\dagger}\right)^2 \\ &- i\hbar\left(g_{01} + C_{01}\right)\hat{\sigma}_x\left(\hat{a}-\hat{a}^{\dagger}\right) - \hbar D_{01}\hat{\sigma}_y\left(\hat{a}+\hat{a}^{\dagger}\right)\,,\end{aligned} \tag{A.22}$$

where $A_\pm = A_{11} \pm A_{00}$ and $B_\pm = B_{11} \pm B_{00}$, with the following definitions for the coefficients:

$$A_{jk} = \sum_{l>1}^{\infty} \left[\frac{g_{jl} g_{lk}}{2} \frac{\omega_c}{\Delta_{lk}} - \frac{G_{jl} G_{lk}}{4\omega_c^2} \left(\frac{1}{\omega'_{lk}} + \frac{1}{\omega'_{lj}} \right) \right] \tag{A.23}$$

$$B_{jk} = \sum_{l>1}^{\infty} \frac{g_{jl} g_{lk}}{4} \left(\frac{\omega'_{lk}}{\Delta_{lk}} + \frac{\omega'_{lj}}{\Delta_{lj}} \right) \tag{A.24}$$

$$C_{jk} = \sum_{l>1}^{\infty} \frac{1}{2\omega_c} \left(g_{jl} \frac{G_{lk}}{\omega'_{kl}} + g_{lk} \frac{G_{jl}}{\omega'_{jl}} + \frac{g_{lk}}{\Delta_{lk}} G_{jl} \omega'_{kl} + \frac{g_{jl}}{\Delta_{jl}} G_{lk} \omega'_{jl} \right) \tag{A.25}$$

$$D_{jk} = \sum_{l>1}^{\infty} \frac{1}{2} \left(\frac{g_{jl}}{\Delta_{jl}} G_{lk} - \frac{g_{lk}}{\Delta_{lk}} G_{jl} \right) . \tag{A.26}$$

The effective Hamiltonian Eq. (A.22), which coincides with Eq. (2.35) upon the introduction of the renormalized parameters, describes the low-energy physics of the system in the dipole gauge. However, many of these terms become negligible for increasing anharmonicities. Specifically, we notice that D_{jk} scales as $g_{jl} g_{kl}^2 / \omega_{jl}^2$, where j and k are states in the low-energy subspace and l belongs to the high-energy subspace, while the remaining coefficients scale linearly. Consequently, D_{jk} approaches zero more rapidly compared to the other coefficients. Furthermore, although the individual terms B_{jj} are non-negligible, their difference $B_{11} - B_{00} = B_-$ also scales quadratically with the nonlinearity. With these considerations, we finally get the reduced effective Hamiltonian in Eq. (2.36).

A.3 Derivation of the RQRM in circuit QED

In this subsection, we present the derivation of the RQRM in the circuit QED setting, namely a fluxonium qubit coupled to a electromagnetic resonator, introduced in Section 2.3.2, using an analogous procedure as the one employed in the previous subsection.

We first rewrite the Hamiltonian in Eq. (2.38) by using the bosonic operator $\hat{a}$ for the bare mode of the harmonic resonator in Eq. (2.40), while employing the unperturbed states of the fluxonium Hamiltonian in Eq. (2.39) for the anharmonic variables. Therefore, the resulting Hamiltonian reads

$$\hat{H}_{\text{fl-res}} = \hbar\omega_c \hat{a}^\dagger \hat{a} + \hbar \sum_j \omega_j |j\rangle\langle j| - \frac{\phi_{\text{zpf}}}{L_2} \sum_{j,k} \phi_{jk} |j\rangle\langle k| \left(\hat{a} + \hat{a}^\dagger \right) + \frac{1}{2L_2} \sum_{j,k} \Phi_{jk} |j\rangle\langle k| \, . \tag{A.27}$$

By the introduction of the coupling strengths g_{jk} and G_{jk} as in Eq. (2.42), the Hamiltonian in Eq. (A.27) reads

$$\hat{H}_{\text{fl-res}} = \hbar\omega_c\hat{a}^\dagger\hat{a} + \hbar\sum_j \omega_j |j\rangle\langle j| - \hbar\sum_{j,k} g_{jk} |j\rangle\langle k| \left(\hat{a}+\hat{a}^\dagger\right) + \hbar\sum_{j,k} \frac{G_{jk}}{\omega_c} |j\rangle\langle k| \ . \quad (\text{A.28})$$

Both the generator $\hat{S}$ of the SW transformation and the effective Hamiltonian can be determined by using a key observation: Hamiltonian in Eq. (A.28) is structurally equivalent to the dipole gauge Hamiltonian of the cavity QED case in Eq. (A.11), upon the application of the unitary transformation $\hat{T} = \exp\left(i\pi\hat{a}^\dagger\hat{a}/2\right)$, as $\hat{H}_{\text{fl-res}} \equiv \hat{T}\hat{H}_{\text{D}}\hat{T}^\dagger$, with the only difference lying in the definitions of the coupling constants. This unitary transformation $\hat{T}$ interchanges the roles of the position and momentum operators of the resonator, as the only formal difference between the two Hamiltonians lies in the nature of the coupling term, as already mentioned in the main text. Therefore, upon the application of the unitary transformation $\hat{T}$ to Eq. (A.20), the SW generator for the Hamiltonian of a fluxonium-resonator circuit can be written as

$$\hat{S} = \sum_{j,k\in\overline{S}} \frac{g_{jk}}{\Delta_{jk}} \left[\omega'_{jk}\left(\hat{a}+\hat{a}^\dagger\right) + \omega_c\left(\hat{a}-\hat{a}^\dagger\right)\right] |j\rangle\langle k| - \frac{1}{\omega_c} \sum_{j,k\neq j\in\overline{S}} \frac{G_{jk}}{\omega'_{jk}} |j\rangle\langle k| \ . \quad (\text{A.29})$$

Hence, following the same procedure as in the cavity QED case presented in the previous section, the renormalized Hamiltonian is given by

$$\begin{aligned}
\hat{\mathcal{H}}^{\text{eff}}_{\text{fl-res}} =& \hbar\omega_c\hat{a}^\dagger\hat{a} + \hbar\left(\frac{\omega_{10}}{2} + \frac{G_{11}-G_{00}}{2\omega_c} + A_-\right)\hat{\sigma}_z + \hbar\left(\frac{G_{01}}{\omega_c} + A_{10} + A_{01}\right)\hat{\sigma}_x \\
& - \hbar\left(\frac{\tilde{g}_{11}+\tilde{g}_{00}}{2}\hat{I} + \frac{\tilde{g}_{11}-\tilde{g}_{00}}{2}\hat{\sigma}_z + \tilde{g}_{01}\hat{\sigma}_x\right)\left(\hat{a}+\hat{a}^\dagger\right) \\
& - \hbar\left(B_+\hat{I} + B_-\hat{\sigma}_z + 2B_{01}\hat{\sigma}_x\right)\left(\hat{a}+\hat{a}^\dagger\right)^2 \\
& + i\hbar\left(A_{10}-A_{01}\right)\hat{\sigma}_y\left(\hat{a}^2 - \hat{a}^{\dagger 2}\right) - i\hbar D_{01}\hat{\sigma}_y\left(\hat{a}-\hat{a}^\dagger\right) \ , \qquad (\text{A.30})
\end{aligned}$$

where $\tilde{g}_{jk} = g_{jk} + C_{jk}$ and the coefficients are identical to those of natural atoms, as no *a priori* selection rules have been employed in the derivation of the coefficients. However, in evaluating the effective Hamiltonian for the cavity QED setting in Eq. (A.22), it has been taken into account that the parity of the potential leads to the vanishing of the coupling constants g_{jk} between states of the same parity. As a consequence, G_{jk} vanishes between states of different parity. On the other hand, in the circuit QED case, where such symmetry can be broken, several additional terms appear in the renormalized Hamiltonian in Eq. (A.30).

Appendix B

Two-level approximation with threefold degeneracy and generalized Holstein-Primakoff transformations

In this Appendix, we provide additional details on the two-level approximation with threefold degeneracy and the generalized Holstein-Primakoff transformations used in Chapter 4. We first introduce the two-level approximation with a threefold degeneracy of the excited state, due to the orientational degree of freedom of the dipole moment, which leads to the introduction of generalized spin operators. Subsequently, we present generalized Holstein-Primakoff transformations that allow us to express these spin operators in terms of bosonic operators, which take into account the threefold degeneracy, facilitating the analysis of the system in the thermodynamic limit. As an application, we derive the effective bosonic Hamiltonian for a collection of isotropic dipoles interacting with the electromagnetic field, in the ferroelectric phase, where non-linear terms in the expansion of the generalized Holstein-Primakoff must be retained, as discussed in Chapter 4. Finally, we calculate the ground state occupations of the fields in this phase.

B.1 Two-level approximation with threefold degeneracy of the excited state

In this subsection, we introduce the two-level approximation considering the threefold degeneracy of the excited state. Let us consider isotropic atoms with inversion symmetry. Owing to isotropy and electric-dipole selection rules, a consistent two-level model requires that the excited state is threefold degenerated, while the ground state is unique (p-like and s-like orbitals, respectively). We denote with $\left|-\right\rangle_n$ the ground state of the n-th atom, while we use $\left|+_\alpha\right\rangle_n$ for the excited states in the three different orientations $\alpha \in \{1,2,3\}$, which are orthogonal to each other. Therefore, we can define generalized orientation-dependent Pauli operators, describing the transitions from the ground to the respective orientation. In particular, we define the operator $S^z_n = \hbar\,\sigma^z_n/2$ (where $n = 1,\dots,N$ is the index of the atom) such that it satisfies the usual relations for spin-$\frac{1}{2}$ systems

$$\begin{aligned} S^z \left|-\right\rangle &= -\frac{\hbar}{2}\left|-\right\rangle \\ S^z \left|+_\alpha\right\rangle &= \frac{\hbar}{2}\left|+_\alpha\right\rangle \end{aligned} \qquad \forall\,\alpha \in \{1,2,3\}\ , \tag{B.1}$$

where momentarily we dropped the atomic index n for notational convenience. Compactly, we can write the previous relations as an eigenvalue equation, *i.e.* $S^z \left|m_\alpha\right\rangle = \hbar m \left|m_\alpha\right\rangle$, where $\left|m_\alpha\right\rangle \in \{\left|-\right\rangle, \left|+_\alpha\right\rangle\}$ and $m \in \{-\frac{1}{2}, \frac{1}{2}\}$ are the respective eigenvalues. Analogously, we define the orientation-dependent raising and lowering operators $S^\pm_\alpha = \hbar\sigma^\pm_\alpha$ which raise or lower the state in the corresponding direction α, characterized by the following properties

$$\begin{aligned} S^+_\alpha \left|-\right\rangle &= \hbar \left|+_\alpha\right\rangle \\ S^+_\alpha \left|+_\beta\right\rangle &= 0 \\ S^-_\alpha \left|-\right\rangle &= 0 \\ S^-_\alpha \left|+_\beta\right\rangle &= \delta_{\alpha\beta}\hbar \left|-\right\rangle \end{aligned} \qquad \forall\,\alpha,\beta \in \{1,2,3\}\ , \tag{B.2}$$

In the basis $\{\left|+_1\right\rangle, \left|+_2\right\rangle, \left|+_3\right\rangle, \left|-\right\rangle\}$, these Pauli operators have the following matrix representation:

$$\sigma^-_\alpha = \begin{pmatrix} 0 & 0 & 0 & 0 \\ 0 & 0 & 0 & 0 \\ 0 & 0 & 0 & 0 \\ \delta_{\alpha 1} & \delta_{\alpha 2} & \delta_{\alpha 3} & 0 \end{pmatrix}, \tag{B.3}$$

$$\sigma^+_\alpha = \left(\sigma^-_\alpha\right)^\dagger\ , \tag{B.4}$$

$$\sigma^x_\alpha = \sigma^-_\alpha + \sigma^+_\alpha\ , \tag{B.5}$$

$$\sigma^y_\alpha = i\left(\sigma^-_\alpha - \sigma^+_\alpha\right)\ , \tag{B.6}$$

$$\sigma^z = \begin{pmatrix} 1 & 0 & 0 & 0 \\ 0 & 1 & 0 & 0 \\ 0 & 0 & 1 & 0 \\ 0 & 0 & 0 & -1 \end{pmatrix}. \tag{B.7}$$

It can be shown that these operators satisfy generalized commutation relations expected from angular-momentum-like operators. In particular, the relation $[S^z, S^\pm_\alpha] = \pm\hbar S^\pm_\alpha$ holds. Using these notions, we can express the dipole moment operator of the n-th atom as

$$\mathbf{d}_n = \sum_\alpha d_{n,\alpha}\hat{\mathbf{e}}_\alpha = \sum_\alpha d\sigma^x_{n,\alpha}\hat{\mathbf{e}}_\alpha = \sum_\alpha d\left(\sigma^-_{n,\alpha} + \sigma^+_{n,\alpha}\right)\hat{\mathbf{e}}_\alpha\,, \tag{B.8}$$

where $\hat{\mathbf{e}}_\alpha$ is the unit vector in the α direction. We considered the dipole moment having the same modulus in the different directions, due to the isotropy of the atoms. Notice that the definition in (B.8) is consistent with the selection rules prohibiting the transition between states of the same parity.

B.2 Generalized Holstein-Primakoff transformations

In this subsection, we introduce generalized Holstein-Primakoff transformations (which have a similar form to the standard Holstein-Primakoff mapping [11, 140, 141]) that allow us to express the generalized spin operators introduced in the previous subsection in terms of bosonic operators. Initially, we will bosonize a two-level system with a threefold degenerated excited state, and successively extend the mapping to a collection of such systems.

To this end, let us first derive a closed form for the action of $S^\pm_\alpha$ on a generic state $|m_\beta\rangle$. We notice that, by definition, $S^\pm_\alpha|m_\beta\rangle = c^\pm_{\alpha\beta}|m \pm 1_\beta\rangle$, where the coefficients $c^\pm_{\alpha\beta}$ can be determined by the following relation

$$\begin{aligned}|c^\pm_{\alpha\beta}|^2 = \| S^\pm_\alpha |m_\beta\rangle \|^2 &= \langle m_\beta| S^\mp_\alpha S^\pm_\alpha |m_\beta\rangle \\ &= \hbar^2\left[s\left(s+\delta_{\alpha\beta}\right) - m\left(m \pm \delta_{\alpha\beta}\right)\right]\,,\end{aligned} \tag{B.9}$$

where in our case $s = 1/2$. Thus, in accordance with the Condon-Shortley phase convention, we select the coefficients to be real and positive, namely

$$\begin{aligned}c^\pm_{\alpha\beta} &= \hbar\sqrt{s\left(s+\delta_{\alpha\beta}\right) - m\left(m \pm \delta_{\alpha\beta}\right)} \\ &= \hbar\sqrt{\left(s \mp m\right)\left(s \pm m + \delta_{\alpha\beta}\right)}\ .\end{aligned} \tag{B.10}$$

Introducing the operator $N = s + S^z/\hbar$, which represent the number of excitations in the system, we observe that the eigenvectors of S^z can be relabeled, as they are evidently also eigenvectors of N with a shifted eigenvalue. Thus, we write $N|n_\alpha\rangle = n|n_\alpha\rangle$, with $n = \frac{1}{2} + m \in \{0,1\}$. We notice that $n = 0$ if the system is in the ground state, while $n = 1$ if the system is in its excited state, consistently with the physical interpretation of the N. From Eqs. (B.1), (B.2) and (B.10), the actions of S^z and $S^{\pm}_{\alpha}$ on $|n_{\beta}\rangle$ in terms of the excitation number therefore are

$$\begin{aligned} S^z\,|n_\beta\rangle &= \hbar\left(n-\frac{1}{2}\right)|n_\beta\rangle\ , &&\text{(B.11)}\\ S^+_\alpha\,|n_\beta\rangle &= \hbar\sqrt{n+\delta_{\alpha\beta}}\sqrt{1-n}\,|n+1_\beta\rangle \\ &= \hbar\delta_{\alpha\beta}\sqrt{n+1}\sqrt{1-n}\,|n+1_\beta\rangle\ , &&\text{(B.12)}\\ S^-_\alpha\,|n_\beta\rangle &= \hbar\sqrt{1-(n-\delta_{\alpha\beta})}\sqrt{n}\,|n-1_\beta\rangle \\ &= \hbar\delta_{\alpha\beta}\sqrt{1-(n-1)}\sqrt{n}\,|n-1_\beta\rangle\ , &&\text{(B.13)} \end{aligned}$$

where in the last steps of Eqs. (B.12) and (B.13) we exploited the isomorphism between the two members. These relations are indeed consistent with the physical interpretation of $S^{\pm}_{\alpha}$, since we expect the operator $S^+_\alpha(S^-_\alpha)$ to be able to increase (decrease) the quantum number only in the α-direction.

We can now define commuting bosonic operators for the different orientations, indicated by b_α, which satisfy the usual bosonic properties

$$\begin{aligned} b_\alpha\,|n_\beta\rangle &= \delta_{\alpha\beta}\,\sqrt{n}\,|n-1_\beta\rangle\ , &&\text{(B.14)}\\ b^\dagger_\alpha\,|n_\beta\rangle &= \delta_{\alpha\beta}\,\sqrt{n+1}\,|n+1_\beta\rangle\ , &&\text{(B.15)}\\ b^\dagger_\alpha b_\alpha\,|n_\beta\rangle &= \delta_{\alpha\beta}\,n\,|n_\beta\rangle\ , &&\text{(B.16)}\\ \left[b_\alpha, b^\dagger_\beta\right] &= \delta_{\alpha\beta}\,. &&\text{(B.17)} \end{aligned}$$

Therefore, using the previous relations in Eqs. (B.11-B.13), we can establish the generalized Holstein-Primakoff transformations for a single two-level system, relating the generalized spin and bosonic operators, as

$$\begin{aligned} S^+_\alpha &= \hbar b^\dagger_\alpha\sqrt{1-\sum_\beta b^\dagger_\beta b_\beta}\,, &&\text{(B.18)}\\ S^-_\alpha &= \hbar\sqrt{1-\sum_\beta b^\dagger_\beta b_\beta}\; b_\alpha\,, &&\text{(B.19)}\\ S^z &= \hbar\left(\sum_\beta b^\dagger_\beta b_\beta-\frac{1}{2}\right)\,. &&\text{(B.20)} \end{aligned}$$

In the limit of low excitations in the system (corresponding to a low average excitation per site), we can expand the radicals in Eqs. (B.18) and (B.19) and retain only the lowest power term in each expression, which yields to

$$S^{-(+)}_\alpha \approx \hbar b^{(\dagger)}_\alpha\,. \tag{B.21}$$

Finally, we consider a collection of N spin-$\frac{1}{2}$ identical systems and construct collective operators in the three-dimensional $\mathbf{k}$-space. In particular, labeling with $b_{n,\alpha}$ the bosonic operator associated with the n-th site, we define the collective bosonic operators $b_{\mathbf{k},\alpha}$ as

$$b_{\mathbf{k},\alpha} = \frac{1}{\sqrt{N}} \sum_n e^{-i\mathbf{k}\cdot\mathbf{R}_n} b_{n,\alpha} \,. \tag{B.22}$$

It can be readily verified that these operators obey the commutation relations $[b_{\mathbf{k},\alpha}, b_{\mathbf{k}',\beta}] = \delta_{\mathbf{k}\mathbf{k}'}\delta_{\alpha\beta}$. In the derivation of the Hamiltonians, we will make use of the relation $\sum_n b^\dagger_{n,\alpha} b_{n,\alpha} = \sum_{\mathbf{k}} b^\dagger_{\mathbf{k},\alpha} b_{\mathbf{k},\alpha}$, which can be easily demonstrated. Furthermore, using Eqs. (B.21) and (B.22), we derive the relations for the low-excitation regime

$$\sum_{n=1}^{N} e^{-(+)i\mathbf{k}\cdot\mathbf{R}_n} S^{-(+)}_{n,\alpha} = \hbar\sqrt{N} b^{(\dagger)}_{\mathbf{k},\alpha} \,. \tag{B.23}$$

B.3 Effective bosonic Hamiltonian in the ferroelectric phase

In this subsection, we apply the previous results to derive the effective bosonic Hamiltonian for a collection of isotropic dipoles interacting with the electromagnetic field in the ferroelectric phase, where non-linear terms in the expansion of the generalized Holstein-Primakoff must be retained. In particular, after the expansion of the radicals in Eqs. (B.18) and (B.19), we keep terms up to the second order, and subsequently minimaze the resulting Hamiltonian to determine the mean-field macroscopic occupations of the modes.

Specifically, in order to account for these macroscopic occupations, we shift the bosonic radiation and matter operators of each mode as

$$a_{\mathbf{k},\lambda} = \tilde{a}_{\mathbf{k},\lambda} - iA_{\mathbf{k},\lambda} \,, \tag{B.24}$$

$$b_{\mathbf{k},\alpha} = \tilde{b}_{\mathbf{k},\alpha} + B_{\mathbf{k},\alpha} \,, \tag{B.25}$$

where the real parameters $A_{\mathbf{k},\lambda}$ and $B_{\mathbf{k},\alpha}$ are linked to the macroscopic mean field mode occupation. Therefore, we expect them to be zero in the normal phase and of order $O(\sqrt{N})$ beyond the phase transition. After substituting these relations into the full light-matter Hamiltonian in the dipole gauge in Eq. (4.12), expanding the square root contribution in the generalized Holstein-Primakoff mapping and retaining only the terms up to second order, the resulting condensed phase

Hamiltonian, in the thermodynamic limit, is given by

$$
\begin{aligned}
H \;=\;& \hbar \sum_{\lambda,\mathbf{k}} \omega_k \tilde{a}^\dagger_{\mathbf{k},\lambda} \tilde{a}_{\mathbf{k},\lambda} \\
&+ \hbar \sum_{\alpha,\mathbf{k}} \left[\omega_0 + 2\frac{\tilde{g}_k}{\tilde{N}_k}\omega_k \sum_{\lambda,\beta} A_{\mathbf{k},\lambda} B_{\mathbf{k},\beta} e_{\lambda_\beta} - 4\frac{\tilde{g}_k^2}{\tilde{N}_k}\omega_k \tilde{f}_{\mathbf{k},\beta,\gamma} \sum_{\beta,\gamma} B_{\mathbf{k},\beta} B_{\mathbf{k},\gamma} \right] \tilde{b}^\dagger_{\mathbf{k},\alpha} \tilde{b}_{\mathbf{k},\alpha} \\
&- i\hbar \sum_{\lambda,\mathbf{k}} \left[2\tilde{g}_k \omega_k \sum_{\alpha} B_{\mathbf{k},\alpha} e_{\lambda_\alpha} - \omega_k A_{\mathbf{k},\lambda} \right] \left(\tilde{a}_{\mathbf{k},\lambda} - \tilde{a}^\dagger_{-\mathbf{k},\lambda} \right) \\
&- \hbar \sum_{\alpha,\mathbf{k}} \left[2\tilde{g}_k \omega_k \sum_{\lambda} A_{\mathbf{k},\lambda} e_{\lambda_\alpha} - \left(\omega_0 + 2\frac{\tilde{g}_k}{\tilde{N}_k}\omega_k \sum_{\lambda,\beta} A_{\mathbf{k},\lambda} B_{\mathbf{k},\beta} e_{\lambda_\beta} \right) B_{\mathbf{k},\alpha} \right. \\
&\qquad \left. + 4\tilde{g}_k^2 \omega_k \left(\frac{B_{\mathbf{k},\alpha}}{\tilde{N}_k} \sum_{\beta,\gamma} B_{\mathbf{k},\beta} B_{\mathbf{k},\gamma} \tilde{f}_{\mathbf{k},\beta,\gamma} - \sum_{\beta} B_{\mathbf{k},\beta} \tilde{f}_{\mathbf{k},\alpha,\beta} \right) \right] \left(\tilde{b}_{\mathbf{k},\alpha} + \tilde{b}^\dagger_{-\mathbf{k},\alpha} \right) \\
&- i\hbar \sum_{\alpha,\lambda,\mathbf{k}} \left[\frac{\tilde{g}_k}{\tilde{N}_k}\omega_k \left(\tilde{N}_k e_{\lambda_\alpha} - B_{\mathbf{k},\alpha} \sum_{\beta} B_{\mathbf{k},\beta} e_{\lambda_\beta} \right) \right] \left(\tilde{a}_{\mathbf{k},\lambda} - \tilde{a}^\dagger_{-\mathbf{k},\lambda} \right) \left(\tilde{b}_{-\mathbf{k},\alpha} + \tilde{b}^\dagger_{\mathbf{k},\alpha} \right) \\
&+ \hbar \sum_{\alpha,\beta,\lambda,\mathbf{k}} \frac{\tilde{g}_k}{\tilde{N}_k}\omega_k \left[\frac{A_{\mathbf{k},\lambda} B_{\mathbf{k},\alpha}}{2\tilde{N}_k} \left(2\tilde{N}_k e_{\lambda_\beta} + B_{\mathbf{k},\beta} \sum_{\gamma} B_{\mathbf{k},\gamma} e_{\lambda_\gamma} \right) \right. \\
&\qquad \left. + \left(\tilde{N}_k \tilde{f}_{\mathbf{k},\alpha,\beta} - 4B_{\mathbf{k},\alpha} \sum_{\gamma} \tilde{f}_{\mathbf{k},\beta,\gamma} B_{\mathbf{k},\gamma} \right) \right] \left(\tilde{b}_{-\mathbf{k},\alpha} + \tilde{b}^\dagger_{\mathbf{k},\alpha} \right) \left(\tilde{b}_{\mathbf{k},\beta} + \tilde{b}^\dagger_{-\mathbf{k},\beta} \right)
\end{aligned}
\tag{B.26}
$$

where $\tilde{g}_k = g_k \sqrt{\tilde{N}_k / N}$, $\tilde{N}_k = N - \sum_\alpha B^2_{\mathbf{k},\alpha}$ and $\tilde{f}_{\mathbf{k},\alpha,\beta} = \sum_\lambda e_{\lambda_\alpha} e_{\lambda_\beta} + f_{\mathbf{k},\alpha,\beta}$, with $e_{\lambda_\alpha} = \hat{\mathbf{e}}_\lambda \cdot \hat{\mathbf{e}}_\alpha$. The parameters $A_{\mathbf{k},\lambda}$ and $B_{\mathbf{k},\alpha}$, at equilibrium, are fixed by the stationary condition of the energy functional, which in turn is equivalent to impose the vanishing of the linear terms in the shifted bosonic operators. Thus, for each mode $\mathbf{k}$, we have the resulting system of two coupled equations in the two parameters $A_{\mathbf{k},\lambda}$ and $B_{\mathbf{k},\alpha}$:

$$
\begin{cases}
2\tilde{g}_k \omega_k \sum_\alpha B_{\mathbf{k},\alpha} e_{\lambda_\alpha} - \omega_k A_{\mathbf{k},\lambda} & = 0 \\
2\tilde{g}_k \omega_k \left(\sum_\lambda A_{\mathbf{k},\lambda} e_{\lambda_\alpha} - \frac{B_{\mathbf{k},\alpha}}{\tilde{N}_k} \sum_{\lambda,\beta} A_{\mathbf{k},\lambda} B_{\mathbf{k},\beta} e_{\lambda_\beta} \right) - \omega_0 B_{\mathbf{k},\alpha} & \\
+4\tilde{g}_k^2 \omega_k \left(\frac{B_{\mathbf{k},\alpha}}{\tilde{N}_k} \sum_{\beta,\gamma} B_{\mathbf{k},\beta} B_{\mathbf{k},\gamma} \tilde{f}_{\mathbf{k},\beta,\gamma} - \sum_\beta B_{\mathbf{k},\beta} \tilde{f}_{\mathbf{k},\alpha,\beta} \right) & = 0\,.
\end{cases}
\tag{B.27}
$$

We now focus our attention on the transverse mode solutions, since those are the ones coupling with the radiation field. This system of Eqs. (B.27) admits, beside the trivial solution $A_{\mathbf{k},\lambda} = B_{\mathbf{k},\alpha} = 0$ corresponding to the normal phase where no condensation occurs, a nontrivial solution which is defined by the conditions

$$\begin{aligned}\sum_{\alpha} B_{\mathbf{k},\alpha}^2 &= \frac{N}{2}\left(1+\frac{1}{4\eta^2 f_{\mathbf{k}}^{\perp}}\right), &\text{(B.28)}\\ A_{\mathbf{k},\lambda} &= 2\tilde{g}_k \sum_{\alpha} B_{\mathbf{k},\alpha} e_{\lambda_\alpha}. &\text{(B.29)}\end{aligned}$$

Inserting these values of the parameters in (B.26), we obtain the Hamiltonian describing the condensed phase at the equilibrium

$$\begin{aligned}H_{\mathrm{cp}} &= \hbar\sum_{\lambda,\mathbf{k}} \omega_k \tilde{a}_{\mathbf{k},\lambda}^{\dagger}\tilde{a}_{\mathbf{k},\lambda} + \hbar\sum_{\alpha,\mathbf{k}} \omega_0 \frac{1-4\eta^2 f_{\mathbf{k}}^{\perp}}{2} \tilde{b}_{\mathbf{k},\alpha}^{\dagger}\tilde{b}_{\mathbf{k},\alpha}\\ &- i\hbar\sum_{\alpha,\lambda,\mathbf{k}} \left[\frac{\tilde{g}_k}{\tilde{N}_k}\omega_k\left(\tilde{N}_k e_{\lambda_\alpha} - B_{\mathbf{k},\alpha}\sum_{\beta} B_{\mathbf{k},\beta} e_{\lambda_\beta}\right)\right]\left(\tilde{a}_{\mathbf{k},\lambda} - \tilde{a}_{-\mathbf{k},\lambda}^{\dagger}\right)\left(\tilde{b}_{-\mathbf{k},\alpha} + \tilde{b}_{\mathbf{k},\alpha}^{\dagger}\right)\\ &+ \hbar\sum_{\alpha,\mathbf{k}} \eta^2\omega_0\left(1+f_{\mathbf{k}}^{\perp}\right)\frac{4\eta^2 f_{\mathbf{k}}^{\perp}-1}{8\eta^2 f_{\mathbf{k}}^{\perp}}\left(\tilde{b}_{-\mathbf{k},\alpha} + \tilde{b}_{\mathbf{k},\alpha}^{\dagger}\right)\left(\tilde{b}_{\mathbf{k},\alpha} + \tilde{b}_{-\mathbf{k},\alpha}^{\dagger}\right)\\ &+ \hbar\sum_{\alpha,\beta,\mathbf{k}} \frac{\eta^2\omega_0}{N}\left[\frac{12\eta^2 f_{\mathbf{k}}^{\perp}-1}{4\eta^2 f_{\mathbf{k}}^{\perp}-1} - 4\left(1+f_{\mathbf{k}}^{\perp}\right)\right] B_{\mathbf{k},\alpha}B_{\mathbf{k},\beta}\times\\ &\qquad\left(\tilde{b}_{-\mathbf{k},\alpha} + \tilde{b}_{\mathbf{k},\alpha}^{\dagger}\right)\left(\tilde{b}_{\mathbf{k},\beta} + \tilde{b}_{-\mathbf{k},\beta}^{\dagger}\right). \qquad\text{(B.30)}\end{aligned}$$

The dispersion relation derived by this Hamiltonian (B.30) can be calculated by means of a Bogoliubov transformation, analogously to what was done in the normal phase. In particular, we obtain the following dispersion relation for the transverse mode solutions

$$\frac{\omega_{\mathbf{k}}^2}{\Omega_{\perp}^2} = 1 + \frac{\omega_0^2/f_{\mathbf{k}}^{\perp}}{\omega_0^2\left(1-16\eta^4 {f_{\mathbf{k}}^{\perp}}^2\right)+\Omega_{\perp}^2}, \qquad\text{(B.31)}$$

which coincides with the one reported in Eq. (4.14) of the main text. Therefore, combining Eqs. (4.13) and (B.31), we obtain the dispersion relations before and after the QPT

$$\begin{cases}\dfrac{\omega_{\mathbf{k}}^2}{\Omega_{\perp}^2} = 1 + \dfrac{4\eta^2\omega_0^2}{\omega_0^2\left(1+4\eta^2 f_{\mathbf{k}}^{\perp}\right)-\Omega_{\perp}^2} & \eta < \eta_c,\\[2ex] \dfrac{\omega_{\mathbf{k}}^2}{\Omega_{\perp}^2} = 1 + \dfrac{\omega_0^2/f_{\mathbf{k}}^{\perp}}{\omega_0^2\left(1-16\eta^4 {f_{\mathbf{k}}^{\perp}}^2\right)+\Omega_{\perp}^2} & \eta > \eta_c,\end{cases} \qquad\text{(B.32)}$$

where the critical coupling is given by $\eta_c = \sqrt{3}/2$ (we remind that $f_{\mathbf{k}}^{\perp} = -1/3$ in the bulk case).

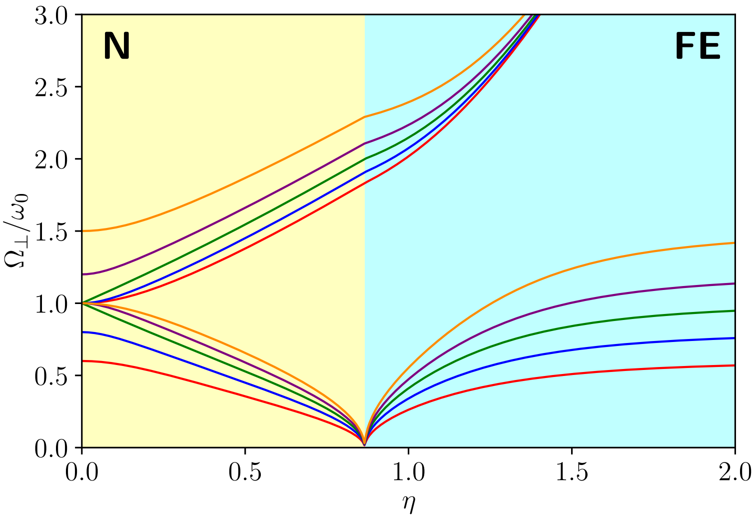

Figure B.1: Upper and lower polaritons as functions of η for different modes: $\omega_k/\omega_0 = 0.6$ (red), 0.8 (blue), 1 (green), 1.2 (purple), 1.5 (yellow). The polaritons in the normal (yellow background) and ferroelectric (cyan background) phases are calculated by Eqs. (4.13) and (B.31), respectively.

In Fig. B.1, we plot the upper and lower polariton branches as functions of the coupling strength η for different values of the bare photon frequency ω_k. We can observe that, at the critical point $\eta_c = \sqrt{3}/2$, the lower polariton frequency vanishes for all the modes, consistently with the softening mechanism of QTPs. Beyond this point, in the condensed phase, the lower polariton branch increases again with η, as described by Eq. (B.31). In the next subsection, we will analyze the macroscopic occupations of the physical fields occurring after the QPT, and effectively demonstrate that this phase can be classified as a ferroelectric.

B.4 Macroscopic ground state occupations in the ferroelectric phase

In this subsection, we analyze the macroscopic ground state occupations of the physical fields occurring after the QPT in terms of mean mode occupation derived in the previous subsection. In particular, we demonstrate that the electric displacement field $\mathbf{D}(r)$ has a mean mode occupation, $\langle \mathbf{D}_\mathbf{k} \rangle$, which is equal to the mean mode occupation of the transverse polarization field, $\langle \mathbf{P}^\perp_\mathbf{k} \rangle$.

To this end, we firstly remind that, in the multipolar gauge, the radiation field canonical momentum is $\mathbf{\Pi}(\mathbf{r}) = -\mathbf{D}(\mathbf{r})$, which leads to the expansion of the displacement field in terms of the bosonic operators as

$$\mathbf{D}(\mathbf{r}) = -\mathbf{\Pi}(\mathbf{r}) = i\epsilon_m \sum_{\lambda,\mathbf{k}} \sqrt{\frac{\hbar\omega_k}{2\epsilon_m V}} \left(e^{i\mathbf{k}\cdot\mathbf{r}} a_{\mathbf{k},\lambda} - e^{-i\mathbf{k}\cdot\mathbf{r}} a^{\dagger}_{\mathbf{k},\lambda}\right) \mathbf{e}_{\lambda}. \tag{B.33}$$

We can now insert the shifted bosonic operator $\tilde{a}_{\mathbf{k},\lambda}$, defined in (B.24), which physically represents the fluctuations around $A_{\mathbf{k},\lambda}$, into this equation. Therefore, by averaging out these fluctuations, the mean value of mode $\mathbf{k}$ of the displacement field is given by

$$\langle \mathbf{D}_{\mathbf{k}} \rangle = \epsilon_m \sum_{\lambda} \sqrt{\frac{\hbar\omega_k}{2\epsilon_m V}} \left(e^{i\mathbf{k}\cdot\mathbf{r}} + e^{-i\mathbf{k}\cdot\mathbf{r}}\right) A_{\mathbf{k},\lambda} \mathbf{e}_{\lambda}, \tag{B.34}$$

where we considered that, by definition, $\langle \tilde{a}_{\mathbf{k},\lambda} \rangle = 0$. Using relation (B.29), this mean value can be rewritten after some algebraic manipulations as

$$\langle \mathbf{D}_{\mathbf{k}} \rangle = \frac{d\sqrt{N}}{V} \sum_{\alpha} \sqrt{\frac{1}{2}\left(1 - \frac{1}{4\eta^2 f^{\perp}_{\mathbf{k}}}\right)} \left(e^{i\mathbf{k}\cdot\mathbf{r}} + e^{-i\mathbf{k}\cdot\mathbf{r}}\right) B_{\mathbf{k},\alpha} \mathbf{e}_{\alpha}, \tag{B.35}$$

where $B_{\mathbf{k},\alpha}$ is defined by (B.28).

On the other hand, we can write the polarization field in terms of the bosonic operators as

$$\begin{aligned}\mathbf{P}(\mathbf{r}) = \frac{d\sqrt{N}}{V} \sum_{\alpha,\mathbf{k}} \Bigg(& e^{i\mathbf{k}\cdot\mathbf{r}} \sqrt{1 - \frac{1}{N}\sum_{\beta} b^{\dagger}_{\mathbf{k},\beta} b_{\mathbf{k},\beta}}\; b_{\mathbf{k},\alpha} \\ & + e^{-i\mathbf{k}\cdot\mathbf{r}} b_{\mathbf{k},\alpha} \sqrt{1 - \frac{1}{N}\sum_{\beta} b^{\dagger}_{\mathbf{k},\beta} b_{\mathbf{k},\beta}} \Bigg) \mathbf{e}_{\alpha}.\end{aligned} \tag{B.36}$$

Using (B.25) and taking the mean value of (B.36), recalling that $\langle \tilde{b}_{\mathbf{k},\alpha} \rangle = 0$, we obtain the mean mode occupation of the transverse polarization field

$$\begin{aligned}\langle \mathbf{P}^{\perp}_{\mathbf{k}} \rangle &= \frac{d\sqrt{N}}{V} \sum_{\alpha} \left(e^{i\mathbf{k}\cdot\mathbf{r}} + e^{-i\mathbf{k}\cdot\mathbf{r}}\right) B_{\mathbf{k},\alpha} \sqrt{1 - \frac{1}{N}\sum_{\beta} B_{\mathbf{k},\beta}}\; \mathbf{e}_{\alpha} \\ &= \frac{d\sqrt{N}}{V} \sum_{\alpha} \sqrt{\frac{1}{2}\left(1 - \frac{1}{4\eta^2 f^{\perp}_{\mathbf{k}}}\right)} \left(e^{i\mathbf{k}\cdot\mathbf{r}} + e^{-i\mathbf{k}\cdot\mathbf{r}}\right) B_{\mathbf{k},\alpha} \mathbf{e}_{\alpha}.\end{aligned} \tag{B.37}$$

Therefore, by comparison of Eqs. (B.35) and (B.37), we conclude that the mean mode occupations of the displacement and transverse polarization fields are equal, *i.e.* $\langle \mathbf{D}_{\mathbf{k}} \rangle = \langle \mathbf{P}^{\perp}_{\mathbf{k}} \rangle$.

Moreover, given the definition of the displacement field $\mathbf{D}(\mathbf{r}) = \epsilon_m \mathbf{E}^{\perp}(\mathbf{r}) + \mathbf{P}^{\perp}(\mathbf{r})$, by taking the mean value of this relation in $\mathbf{k}$-space, we easily conclude that the mean mode occupation of the transverse electric field, $\langle \mathbf{E}^{\perp}_{\mathbf{k}} \rangle$, must be zero. Moreover, we remark that the same mean field mode occupations are predicted even by applying the same procedure directly only to the matter Hamiltonian, further confirming the ferroelectricity of the QPT. In fact, the mean occupation of the matter field is dictated only by the strength of dipolar interactions and not on the interaction with the radiation field.

As a final note, it is instructive to point out that if the factor $f_{\mathbf{k},\alpha,\beta}$ is regarded as a free parameter, we can recover relevant known models and their critical behaviors. For instance, the Dicke model can be recovered by restricting the study only to the transverse modes and considering $f^{\perp}_{\mathbf{k},\alpha,\beta} = -\delta_{\alpha\beta}$ (implying $\tilde{f}^{\perp}_{\mathbf{k},\alpha,\beta} = 0$). As a consequence, relation (B.31) reduces to the already known Dicke dispersion relation beyond the SPT [21]. Another notable case is $f^{\perp}_{\mathbf{k},\alpha,\beta} = 0$, corresponding to a pure Hopfield model neglecting the dipole-dipole interactions. For such a model, the system of equations (B.27) admits only the trivial solution, which is consistent with the well-known impossibility for a pure Hopfield Hamiltonian to undergo a phase transition.

Appendix C

Effective Hamiltonian in the superradiant phase of the open Dicke model and quantum Langevin equations

In this Appendix, we provide additional details on the derivation of the effective Hamiltonian in the superradiant phase of the open Dicke model in Eq. (5.28), as well as the calculation of the mean-field condensates of both the system and bath modes. This approach is based on the minimization of the total system-bath Hamiltonian, ensuring a self-consistent treatment that also accounts for possible modifications of the bath's degrees of freedom. This represents a fundamental distinction from previous theoretical methods, which typically assume a weak system-bath coupling and rely on corresponding approximations. Finally, we will derive the quantum Langevin equations used to compute the input-output relations of the system in the superradiant phase.

C.1 Derivation of the effective Hamiltonian in the superradiant phase

In this subsection, we focus on the derivation of the effective Hamiltonian in the superradiant phase of the open Dicke model and the corresponding mean-field condensates of both the system and bath modes. Therefore, to accurately describe the superradiant phase, it is essential to account for the macroscopic coherent occupation of both the system fields and the eventual induced macroscopic occupation that could arise in the baths. Thus, the bosonic operators have to be shifted as defined in Eq. (5.26) of the main text. The system coordinates, to which the bath operators couple, in the superradiant phase are $X_a = \sqrt{\hbar/2\omega_a}(a_\mathrm{s}^\dagger + a_\mathrm{s} + 2\sqrt{\alpha})$ and $X_b = \sqrt{\hbar/2\omega_a}\sqrt{(\lambda+1)/2\lambda}(b_\mathrm{s}^\dagger\sqrt{\xi} + \sqrt{\xi}\,b_\mathrm{s} - 2\sqrt{\beta}\sqrt{\xi})$ for systems A and B, respectively, where $\xi = 1 - [b_\mathrm{s}^\dagger b_\mathrm{s} - \sqrt{\beta}(b_\mathrm{s}^\dagger + b_\mathrm{s})](N-\beta)^{-1}$ (as in Eq. (5.10)).

Upon substituting these definitions into the total Hamiltonian in Eq. (5.15), and successively considering the thermodynamic limit and expanding up to the second order in the bosonic operators the square roots contributions, we obtain the total Hamiltonian in terms of the shifted bosonic operators (up to constant terms)

$$\begin{aligned}
\frac{H}{\hbar} &= \omega_a a_\mathrm{s}^\dagger a_\mathrm{s} + \left[2g\sqrt{\frac{\alpha\beta}{N(N-\beta)}} + \omega_b\right] b_\mathrm{s}^\dagger b_\mathrm{s} - \left[2g\sqrt{\frac{\beta(N-\beta)}{N}} - \omega_a\sqrt{\alpha}\right](a_\mathrm{s}^\dagger + a_\mathrm{s}) \\
&\quad + \left[2g(N-2\beta)\sqrt{\frac{\alpha}{N(N-\beta)}} - \omega_b\sqrt{\beta}\right](b_\mathrm{s}^\dagger + b_\mathrm{s}) \\
&\quad + \frac{g(2N-\beta)}{2(N-\beta)}\sqrt{\frac{\alpha\beta}{N(N-\beta)}}\left(b_\mathrm{s}^\dagger + b_\mathrm{s}\right)^2 + g(N-2\beta)\sqrt{\frac{1}{N(N-\beta)}}(a_\mathrm{s}^\dagger + a_\mathrm{s})(b_\mathrm{s}^\dagger + b_\mathrm{s}) \\
&\quad + \sum_n \Bigg\{\omega_{an} c_{\mathrm{s},an}^\dagger c_{\mathrm{s},an} - \frac{1}{2}\sqrt{\frac{k_{an}\omega_{an}}{\omega_a}}\left(c_{\mathrm{s},an}^\dagger + c_{\mathrm{s},an}\right)\left(a_\mathrm{s}^\dagger + a_\mathrm{s}\right) + \frac{k_{an}}{4\omega_a}\left(a_\mathrm{s}^\dagger + a_\mathrm{s}\right)^2 \\
&\qquad + \sqrt{\frac{k_{an}}{\omega_a}}\left(\sqrt{\frac{k_{an}\alpha}{\omega_a}} - \sqrt{\omega_{an}\sigma_{an}}\right)\left(a_\mathrm{s}^\dagger + a_\mathrm{s}\right) \\
&\qquad + \sqrt{\omega_{an}}\left(\sqrt{\omega_{an}\sigma_{an}} - \sqrt{\frac{k_{an}\alpha}{\omega_a}}\right)\left(c_{\mathrm{s},an}^\dagger + c_{\mathrm{s},an}\right)\Bigg\} \\
&\quad + \sum_n \Bigg\{\omega_{bn} c_{\mathrm{s},bn}^\dagger c_{\mathrm{s},bn} - \frac{1}{2}\sqrt{\frac{k_{bn}\omega_{bn}}{\omega_b}}\left(1 - \frac{\beta}{N-\beta}\right)\left(c_{\mathrm{s},bn}^\dagger + c_{\mathrm{s},bn}\right)\left(b_\mathrm{s}^\dagger + b_\mathrm{s}\right) \\
&\qquad + \frac{\beta}{N-\beta}\sqrt{\frac{k_{bn}}{\omega_b}}\left(\sqrt{\frac{\omega_{bn}\sigma_{bn}}{\beta}} - \sqrt{\frac{k_{bn}}{\omega_b}}\right) b_\mathrm{s}^\dagger b_\mathrm{s} \\
&\qquad + \left[\frac{2N-\beta}{4(N-\beta)^2}\sqrt{\frac{k_{bn}\omega_{bn}\sigma_{bn}\beta}{\omega_b}} + \frac{k_{bn}}{4\omega_b}\left(1 - \frac{4\beta}{N-\beta}\right)\right]\left(b_\mathrm{s}^\dagger + b_\mathrm{s}\right)^2 \\
&\qquad - \sqrt{\frac{k_{bn}}{\omega_b}}\left(1 - \frac{\beta}{N-\beta}\right)\left(\sqrt{\frac{k_{bn}\beta}{\omega_b}} - \sqrt{\omega_{bn}\sigma_{bn}}\right)\left(b_\mathrm{s}^\dagger + b_\mathrm{s}\right) \\
&\qquad - \sqrt{\omega_{bn}}\left(\sqrt{\omega_{bn}\sigma_{bn}} - \sqrt{\frac{k_{bn}\beta}{\omega_b}}\right)\left(c_{\mathrm{s},bn}^\dagger + c_{\mathrm{s},bn}\right)\Bigg\}\,.
\end{aligned} \tag{C.1}$$

We now proceed to the minimization of this Hamiltonian, corresponding to the vanishing of the linear terms in the bosonic operators in Eq. (C.1), which leads to a set of coupled equations for the mean-field condensates α, β, σ_{an} and σ_{bn}. The solution of this system of equations is given by the trivial solution $\alpha = \beta = \sigma_{an} = \sigma_{bn} = 0$ for $g < g_c$, corresponding to the normal phase, and by the non-trivial solution for $g > g_c$, corresponding to the non-zero macroscopic occupations of the superradiant phase, which are given by

$$\begin{aligned} \alpha &= \frac{Ng^2}{\omega_a^2}\left(1-\frac{1}{\lambda^2}\right), & \beta &= \frac{N}{2}\left(1-\frac{1}{\lambda}\right), \\ \sigma_{an} &= \frac{k_{an}}{\omega_{an}\omega_a}\alpha\,, & \sigma_{bn} &= \frac{k_{bn}}{\omega_{bn}\omega_b}\frac{\lambda+1}{2\lambda}\beta\,, \end{aligned} \tag{C.2}$$

where $\lambda = 4g^2/(\omega_a\omega_b)$, as in the closed Dicke model presented in Section 5.1. Inserting these equilibrium values into Eq. (C.1) and grupping the terms, the effective total Hamiltonian for the superradiant phase can be written in the compact form

$$H = H_{\text{SP}} + \frac{1}{2}\sum_{j=a,b}\sum_{n}\left[p_{jn}^2 + \tilde{k}_{jn}\left(q_{\text{s},jn} - x_j\right)^2\right], \tag{C.3}$$

coinciding with Eq. (5.28) of the main text. In writing this equation, we have defined the following quantities: $q_{\text{s},jn} = \sqrt{\hbar\omega_{jn}/2k_{jn}}\left(c_{\text{s},jn}^\dagger + c_{\text{s},jn}\right)$ are the coordinate fluctuation operators of the j-th bath, $x_a = \sqrt{\hbar/2\omega_a}(a_{\text{s}}^\dagger + a_{\text{s}})$ and $x_b = \sqrt{2\hbar/\omega_b(\lambda+1)^2}(b_{\text{s}}^\dagger + b_{\text{s}})$ are the displaced coordinates of the system, and $\tilde{k}_{an} = k_{an}$ and $\tilde{k}_{bn} = k_{bn}\left(\lambda+1\right)/2\lambda$ are the effective coupling constants. The effects of condensation are incorporated through the λ-dependent factors.

C.2 Quantum Langevin equations in the superradiant phase

To calculate the quantum Langevin equation in the superradiant phase, we apply the same methodology applyed in Section 5.2, but now using the effective Hamiltonian of the superradiant phase in Eq. (5.28). Indeed, it can be observed that the Hamiltonians in Eqs. (5.15) and (5.28) for the two phases have the same formal structure, with the only difference being that the bare bosonic operators are replaced by the shifted ones. Hence, the Langevin equations in the superradiant phase retain a similiar form to those in the normal phase, and can be expressed as

$$\dot{a}_\mathrm{s} = -\,i\omega_a a_\mathrm{s} - i\tilde{g}(b_\mathrm{s}^\dagger + b_\mathrm{s}) + \frac{1}{2}\int_{-t_0}^{t} f_a(t-t')(a_\mathrm{s}^\dagger(t') - a_\mathrm{s}(t'))dt' + \frac{i}{\sqrt{2\hbar\omega_a}}\xi_a \tag{C.4a}$$

$$\dot{a}_\mathrm{s}^\dagger = i\omega_a a_\mathrm{s}^\dagger + i\tilde{g}(b_\mathrm{s}^\dagger + b_\mathrm{s}) - \frac{1}{2}\int_{-t_0}^{t} f_a(t-t')(a_\mathrm{s}^\dagger(t') - a_\mathrm{s}(t'))dt' - \frac{i}{\sqrt{2\hbar\omega_a}}\xi_a \tag{C.4b}$$

$$\begin{aligned}\dot{b}_\mathrm{s} = &-\,i\tilde{\omega}_b b_\mathrm{s} - i\tilde{g}(a_\mathrm{s}^\dagger + a_\mathrm{s}) - 2iD(b_\mathrm{s}^\dagger + b_\mathrm{s}) + \frac{i}{\sqrt{2\hbar\tilde{\omega}_b}}\sqrt{\frac{2}{\lambda(\lambda+1)}}\xi_b \\ &+ \frac{1}{2}\frac{2}{\lambda(\lambda+1)}\int_{-t_0}^{t} f_b(t-t')(b_\mathrm{s}^\dagger(t') - b_\mathrm{s}(t'))dt'\end{aligned} \tag{C.4c}$$

$$\begin{aligned}\dot{b}_\mathrm{s}^\dagger = &\; i\tilde{\omega}_b b_\mathrm{s}^\dagger + i\tilde{g}(a_\mathrm{s}^\dagger + a_\mathrm{s}) + 2iD(b_\mathrm{s}^\dagger + b_\mathrm{s}) - \frac{i}{\sqrt{2\hbar\tilde{\omega}_b}}\sqrt{\frac{2}{\lambda(\lambda+1)}}\xi_b \\ &- \frac{1}{2}\frac{2}{\lambda(\lambda+1)}\int_{-t_0}^{t} f_b(t-t')(b_\mathrm{s}^\dagger(t') - b_\mathrm{s}(t'))dt'\end{aligned} \tag{C.4d}$$

where $\tilde{\omega}_b$, $\tilde{g}$ and D are defined in Section 5.1.1. The previous system of equations can be reformulated within the frequency domain in a compact form as

$$-i\omega\begin{pmatrix}\tilde{a}_\mathrm{s}\\ \tilde{a}_\mathrm{s}^\dagger\\ \tilde{b}_\mathrm{s}\\ \tilde{b}_\mathrm{s}^\dagger\end{pmatrix} = -i\left(\mathbf{A}_\mathrm{SP} - \frac{i}{2}\mathbf{\Gamma}_\mathrm{SP}\right)\begin{pmatrix}\tilde{a}_\mathrm{s}\\ \tilde{a}_\mathrm{s}^\dagger\\ \tilde{b}_\mathrm{s}\\ \tilde{b}_\mathrm{s}^\dagger\end{pmatrix} + \begin{pmatrix}\frac{i}{\sqrt{2\hbar\omega_a}}\tilde{\xi}_a\\ \frac{-i}{\sqrt{2\hbar\omega_a}}\tilde{\xi}_a\\ \frac{i}{\sqrt{\hbar\tilde{\omega}_b\lambda(\lambda+1)}}\tilde{\xi}_b\\ \frac{-i}{\sqrt{\hbar\tilde{\omega}_b\lambda(\lambda+1)}}\tilde{\xi}_b\end{pmatrix}, \tag{C.5}$$

which coincides with Eq. (5.20), which describes the normal phase, except for the replacement of the matrices $\mathbf{A}_\mathrm{NP}$ and $\mathbf{\Gamma}_\mathrm{NP}$ with $\mathbf{A}_\mathrm{SP}$ and $\mathbf{\Gamma}_\mathrm{SP}$, respectively.

Bibliography

[1] A. Sergi, D. Lamberto, A. Migliore, and A. Messina, “Quantum-Classical Hybrid Systems and Ehrenfest’s Theorem”, Entropy **25**, 602 (2023).

[2] D. Lamberto, O. Di Stefano, S. Hughes, F. Nori, and S. Savasta, “Quantum phase transitions in many-dipole light-matter systems”, Phys. Rev. Res. **7**, 013271 (2025).

[3] S. Napoli, A. Mercurio, D. Lamberto, A. Zappalà, O. Di Stefano, and S. Savasta, “Circuit QED spectra in the ultrastrong coupling regime: How they differ from cavity QED”, Phys. Rev. Res. **7**, 033037 (2025).

[4] D. Lamberto, A. Mercurio, O. D. Stefano, V. Savona, and S. Savasta, “Renormalization and low-energy effective models in cavity and circuit quantum electrodynamics”, Commun. Phys. **8**, 430 (2025).

[5] A. Zappalà, A. Mercurio, D. Lamberto, S. Napoli, O. Di Stefano, and S. Savasta, “From Few to Many Emitters Cavity QED: Energy Levels and Emission Spectra From Weak to Deep-Strong Coupling”, arXiv:2506.18763 (2025), to appear on Phys. Rev. A.

[6] C. Bonizzoni, D. Lamberto, S. Napoli, S. Gunzler, D. Rieger, F. Santanni, A. Ghirri, W. Wernsdorfer, S. Savasta, and M. Affronte, “Observation of Perfect Absorption in Hyperfine Levels of Molecular Spins with Hermitian Subspaces”, arXiv:2505.05966 (2025), to appear on Nature Communications.

[7] D. Lamberto, G. Orlando, and S. Savasta, “Superradiant Quantum Phase Transition in Open Systems: System-Bath Interaction at the Critical Point”, arXiv:2411.16514 (2025).

[8] R. Stassi, S. Abo, D. Lamberto, Y.-H. Chen, A. Miranowicz, S. Savasta, and F. Nori, “Noise Protected Logical Qubit in a Open Chain of Superconducting Qubits with Ultrastrong Interactions”, arXiv:2509.17903 (2025).

[9] C. Kittel, *Introduction to Solid State Physics*, 8th (Wiley, Hoboken, NJ, 2004).

[10] N. W. Ashcroft and N. D. Mermin, *Solid State Physics* (Harcourt College Publishers, New York, 1976).

[11] G. Grosso and G. Pastori Parravicini, *Solid state physics* (Academic Press, San Diego, 2000).

[12] S. M. Girvin and K. Yang, *Modern Condensed Matter Physics* (Cambridge University Press, Cambridge, 2019).

[13] J. M. Yeomans, *Statistical Mechanics of Phase Transitions* (Cambridge University Press, Cambridge, 1992).

[14] M. Baus and C. Tejero, *Equilibrium Statistical Physics* (Springer, Cham, 2021).

[15] P. M. Chaikin and T. C. Lubensky, *Principles of Condensed Matter Physics* (Cambridge University Press, Cambridge, 2012).

[16] S. Sachdev, *Quantum Phase Transitions* (Cambridge University Press, Cambridge, 2011).

[17] L. D. Carr, ed., *Understanding Quantum Phase Transitions* (CRC Press, Boca Raton, FL, 2010).

[18] R. H. Dicke, “Coherence in spontaneous radiation processes”, Phys. Rev. **93**, 99 (1954).

[19] K. Hepp and E. H. Lieb, “On the superradiant phase transition for molecules in a quantized radiation field: the Dicke maser model”, Ann. Phys. (N.Y.) **76**, 360–404 (1973).

[20] Y. Wang and F. Hioe, “Phase transition in the Dicke model of superradiance”, Phys. Rev. A **7**, 831 (1973).

[21] C. Emary and T. Brandes, “Chaos and the quantum phase transition in the Dicke model”, Phys. Rev. E **67**, 066203 (2003).

[22] P. Kirton, S. Mazzucchi, S. De Liberato, J. Keeling, and I. Carusotto, “Introduction to the Dicke model: From equilibrium to nonequilibrium, and vice versa”, Adv. Quantum Technol. **2**, 1800043 (2019).

[23] J. J. Sakurai and J. Napolitano, *Modern quantum mechanics* (Cambridge University Press, 2020).

[24] C. Cohen-Tannoudji, B. Diu, and F. Laloë, *Quantum mechanics* (Wiley-VCH, 1992).

[25] H. Goldstein, C. Poole, and J. Safko, *Classical Mechanics* (Addison-Wesley, 2011).

[26] P. Lambropoulos and D. Petrosyan, *Fundamentals of quantum optics and quantum information* (Springer, Berlin, 2007).

[27] M. O. Scully and M. S. Zubairy, *Quantum optics* (Cambridge University Press, 1997).

[28] L. Mandel and E. Wolf, *Optical coherence and quantum optics* (Cambridge University Press, 1995).

[29] D. F. Walls and G. J. Milburn, *Quantum optics* (Springer Science & Business Media, 2008).

[30] T. Niemczyk, F. Deppe, H. Huebl, E. P. Menzel, F. Hocke, M. J. Schwarz, J. J. Garcia-Ripoll, D. Zueco, T. Hümmer, E. Solano, A. Marx, and R. Gross, “Circuit quantum electrodynamics in the ultrastrong-coupling regime”, Nat. Phys. **6**, 772–776 (2010).

[31] J. Q. You and F. Nori, “Superconducting circuits and quantum information”, Phys. Today **58**, 42–47 (2005).

[32] J. Q. You and F. Nori, “Atomic physics and quantum optics using superconducting circuits”, Nature **474**, 589–597 (2011).

[33] J. M. Fink, M. Göppl, M. Baur, R. Bianchetti, P. J. Leek, A. Blais, and A. Wallraff, “Climbing the Jaynes–Cummings ladder and observing its nonlinearity in a cavity QED system”, Nature **454**, 315–318 (2008).

[34] J. D. Jackson, *Classical electrodynamics* (Wiley, 1999).

[35] D. J. Griffiths, *Introduction to Electrodynamics* (Cambridge University Press, 2018).

[36] M. Babiker and R. Loudon, “Derivation of the Power-Zienau-Woolley Hamiltonian in quantum electrodynamics by gauge transformation”, Proceedings of the Royal Society of London. A. Mathematical and Physical Sciences **385**, 439–460 (1983).

[37] C. Cohen-Tannoudji, J. Dupont-Roc, and G. Grynberg, *Photons and Atoms: Introduction to Quantum Electrodynamics* (Wiley, New York, 1989).

[38] C. Cohen-Tannoudji, J. Dupont-Roc, and G. Grynberg, *Atom-Photon Interactions: Basic Process and Appilcations* (Wiley, 1998).

[39] E. A. Power and S. Zienau, “Coulomb gauge in non-relativistic quantum electro-dynamics and the shape of spectral lines”, Philos. Trans. R. Soc. Lond. A, Math. Phys. Sci. **251**, 427–454 (1959).

[40] R. G. Woolley, “Molecular quantum electrodynamics”, Proc. R. Soc. Lond. A Math. Phys. Sci. **321**, 557–572 (1971).

[41] A. F. Kockum, A. Miranowicz, S. De Liberato, S. Savasta, and F. Nori, “Ultrastrong coupling between light and matter”, Nat. Rev. Phys. **1**, 19–40 (2019).

[42] P. Forn-Díaz, L. Lamata, E. Rico, J. Kono, and E. Solano, “Ultrastrong coupling regimes of light-matter interaction”, Rev. Mod. Phys. **91**, 025005 (2019).

[43] I. I. Rabi, “On the Process of Space Quantization”, Phys. Rev. **49**, 324–328 (1936).

[44] E. T. Jaynes and F. W. Cummings, “Comparison of Quantum and Semiclassical Radiation Theories with Application to the Beam Maser”, Proc. IEEE **51**, 89–109 (1963).

[45] B. W. Shore and P. L. Knight, “The Jaynes-Cummings Model”, Journal of Modern Optics **40**, 1195–1238 (1993).

[46] W.-H. Chang, W.-Y. Chen, H.-S. Chang, T.-P. Hsieh, J.-I. Chyi, and T.-M. Hsu, “Efficient Single-Photon Sources Based on Low-Density Quantum Dots in Photonic-Crystal Nanocavities”, Phys. Rev. Lett. **96**, 117401 (2006).

[47] E. M. Purcell, “Spontaneous Emission Probabilities at Radio Frequencies”, Phys. Rev. **69**, 681 (1946).

[48] M. Brune, F. Schmidt-Kaler, A. Maali, J. Dreyer, E. Hagley, J. M. Raimond, and S. Haroche, “Quantum Rabi Oscillation: A Direct Test of Field Quantization in a Cavity”, Phys. Rev. Lett. **76**, 1800–1803 (1996).

[49] Y. Kaluzny, P. Goy, M. Gross, J. M. Raimond, and S. Haroche, “Observation of Self-Induced Rabi Oscillations in Two-Level Atoms Excited Inside a Resonant Cavity: The Ringing Regime of Superradiance”, Phys. Rev. Lett. **51**, 1175–1178 (1983).

[50] D. Braak, “Integrability of the Rabi Model”, Phys. Rev. Lett. **107**, 100401 (2011).

[51] F. Bloch and A. Siegert, “Magnetic Resonance for Nonrotating Fields”, Phys. Rev. **57**, 522–527 (1940).

[52] A. Bayer, M. Pozimski, S. Schambeck, D. Schuh, R. Huber, D. Bougeard, and C. Lange, “Terahertz light-matter interaction beyond unity coupling strength”, Nano Lett. **17**, 6340–6344 (2017).

[53] G. Günter, A. A. Anappara, J. Hees, A. Sell, G. Biasiol, L. Sorba, S. De Liberato, C. Ciuti, A. Tredicucci, A. Leitenstorfer, and R. Huber, "Sub-cycle switch-on of ultrastrong light-matter interaction", Nature **458**, 178–181 (2009).

[54] T. Schwartz, J. A. Hutchison, C. Genet, and T. W. Ebbesen, "Reversible Switching of Ultrastrong Light-Molecule Coupling", Phys. Rev. Lett. **106**, 196405 (2011).

[55] Y. Ashida, A. İmamoğlu, and E. Demler, "Cavity Quantum Electrodynamics at Arbitrary Light-Matter Coupling Strengths", Phys. Rev. Lett. **126**, 153603 (2021).

[56] S. De Liberato, "Light-Matter Decoupling in the Deep Strong Coupling Regime: The Breakdown of the Purcell Effect", Phys. Rev. Lett. **112**, 016401 (2014).

[57] P. Forn-Díaz, J. Lisenfeld, D. Marcos, J. J. García-Ripoll, E. Solano, C. J. P. M. Harmans, and J. E. Mooij, "Observation of the Bloch-Siegert Shift in a Qubit-Oscillator System in the Ultrastrong Coupling Regime", Phys. Rev. Lett. **105**, 237001 (2010).

[58] Y. Todorov, A. M. Andrews, R. Colombelli, S. De Liberato, C. Ciuti, P. Klang, G. Strasser, and C. Sirtori, "Ultrastrong Light-Matter Coupling Regime with Polariton Dots", Phys. Rev. Lett. **105**, 196402 (2010).

[59] V. Macrì, F. Nori, S. Savasta, and D. Zueco, "Spin squeezing by one-photon–two-atom excitation processes in atomic ensembles", Phys. Rev. A **101**, 053818 (2020).

[60] G. Scalari, C. Maissen, D. Turčinková, D. Hagenmüller, S. D. Liberato, C. Ciuti, C. Reichl, D. Schuh, W. Wegscheider, M. Beck, and J. Faist, "Ultrastrong Coupling of the Cyclotron Transition of a 2D Electron Gas to a THz Metamaterial", Science **335**, 1323–1326 (2012).

[61] M. Geiser, F. Castellano, G. Scalari, M. Beck, L. Nevou, and J. Faist, "Ultrastrong Coupling Regime and Plasmon Polaritons in Parabolic Semiconductor Quantum Wells", Phys. Rev. Lett. **108**, 106402 (2012).

[62] L. Garziano, V. Macrì, R. Stassi, O. Di Stefano, F. Nori, and S. Savasta, "One Photon Can Simultaneously Excite Two or More Atoms", Phys. Rev. Lett. **117**, 043601 (2016).

[63] L. Garziano, R. Stassi, V. Macrì, A. F. Kockum, S. Savasta, and F. Nori, "Multiphoton quantum Rabi oscillations in ultrastrong cavity QED", Phys. Rev. A **92**, 063830 (2015).

[64] K. K. W. Ma and C. K. Law, "Three-photon resonance and adiabatic passage in the large-detuning Rabi model", Phys. Rev. A **92**, 023842 (2015).

[65] A. Baust, E. Hoffmann, M. Haeberlein, M. J. Schwarz, P. Eder, J. Goetz, F. Wulschner, E. Xie, L. Zhong, F. Quijandría, D. Zueco, J.-J. G. Ripoll, L. García-Álvarez, G. Romero, E. Solano, K. G. Fedorov, E. P. Menzel, F. Deppe, A. Marx, and R. Gross, "Ultrastrong coupling in two-resonator circuit QED", Phys. Rev. B **93**, 214501 (2016).

[66] R. Stassi, V. Macrì, A. F. Kockum, O. Di Stefano, A. Miranowicz, S. Savasta, and F. Nori, "Quantum nonlinear optics without photons", Phys. Rev. A **96**, 023818 (2017).

[67] E. Sanchez-Burillo, D. Zueco, J. J. Garcia-Ripoll, and L. Martin-Moreno, "Scattering in the Ultrastrong Regime: Nonlinear Optics with One Photon", Phys. Rev. Lett. **113**, 263604 (2014).

[68] L. A. Martínez-Martínez, R. F. Ribeiro, J. Campos-González-Angulo, and J. Yuen-Zhou, "Can Ultrastrong Coupling Change Ground-State Chemical Reactions?", ACS Photonics **5**, 167–176 (2018).

[69] G. Flower, M. Goryachev, J. Bourhill, and M. E. Tobar, "Experimental implementations of cavity-magnon systems: from ultra strong coupling to applications in precision measurement", New J. Phys. **21**, 095004 (2019).

[70] M. Jeannin, G. M. Nesurini, S. Suffit, D. Gacemi, A. Vasanelli, L. Li, A. G. Davies, E. Linfield, C. Sirtori, and Y. Todorov, "Ultrastrong Light–Matter Coupling in Deeply Subwavelength THz LC Resonators", ACS Photonics **6**, 1207–1215 (2019).

[71] S.-P. Wang, G.-Q. Zhang, Y. Wang, Z. Chen, T. Li, J. S. Tsai, S.-Y. Zhu, and J. Q. You, "Photon-Dressed Bloch-Siegert Shift in an Ultrastrongly Coupled Circuit Quantum Electrodynamical System", Phys. Rev. Appl. **13**, 054063 (2020).

[72] M.-J. Hwang, R. Puebla, and M. B. Plenio, "Quantum Phase Transition and Universal Dynamics in the Rabi Model", Phys. Rev. Lett. **115**, 180404 (2015).

[73] M.-L. Cai, Z.-D. Liu, W.-D. Zhao, Y.-K. Wu, Q.-X. Mei, Y. Jiang, L. He, X. Zhang, Z.-C. Zhou, and L.-M. Duan, "Observation of a quantum phase transition in the quantum Rabi model with a single trapped ion", Nat. Commun. **12**, 1126 (2021).

[74] F. Hioe and Y. Wang, "Phase transition in the Dicke model of superradiance. II", Phys. Rev. A **8**, 1440 (1973).

[75] J. M. Raimond, M. Brune, and S. Haroche, "Manipulating quantum entanglement with atoms and photons in a cavity", Rev. Mod. Phys. **73**, 565–582 (2001).

[76] D. De Bernardis, P. Pilar, T. Jaako, S. De Liberato, and P. Rabl, "Breakdown of gauge invariance in ultrastrong-coupling cavity QED", Phys. Rev. A **98**, 053819 (2018).

[77] S. Savasta, O. Di Stefano, A. Settineri, D. Zueco, S. Hughes, and F. Nori, "Gauge principle and gauge invariance in two-level systems", Phys. Rev. A **103**, 053703 (2021).

[78] A. Stokes and A. Nazir, "Gauge ambiguities imply Jaynes-Cummings physics remains valid in ultrastrong coupling QED", Nat. Commun. **10**, `10.1038/s41467-018-08101-0` (2019).

[79] M. A. D. Taylor, A. Mandal, W. Zhou, and P. Huo, "Resolution of Gauge Ambiguities in Molecular Cavity Quantum Electrodynamics", Phys. Rev. Lett. **125**, 123602 (2020).

[80] O. Dmytruk and M. Schiró, "Gauge fixing for strongly correlated electrons coupled to quantum light", Phys. Rev. B **103**, 075131 (2021).

[81] A. Settineri, O. Di Stefano, D. Zueco, S. Hughes, S. Savasta, and F. Nori, "Gauge freedom, quantum measurements, and time-dependent interactions in cavity QED", Phys. Rev. Res. **3**, 023079 (2021).

[82] A. Ridolfo, M. Leib, S. Savasta, and M. J. Hartmann, "Photon Blockade in the Ultrastrong Coupling Regime", Phys. Rev. Lett. **109**, 193602 (2012).

[83] A. Mercurio, V. Macrì, C. Gustin, S. Hughes, S. Savasta, and F. Nori, "Regimes of cavity QED under incoherent excitation: From weak to deep strong coupling", Phys. Rev. Res. **4**, 023048 (2022).

[84] F. Beaudoin, J. M. Gambetta, and A. Blais, "Dissipation and ultrastrong coupling in circuit QED", Phys. Rev. A **84**, 043832 (2011).

[85] A. Settineri, V. Macrì, A. Ridolfo, O. Di Stefano, A. F. Kockum, F. Nori, and S. Savasta, "Dissipation and thermal noise in hybrid quantum systems in the ultrastrong-coupling regime", Phys. Rev. A **98**, 053834 (2018).

[86] A. Mercurio, S. Abo, F. Mauceri, E. Russo, V. Macrì, A. Miranowicz, S. Savasta, and O. Di Stefano, "Pure Dephasing of Light-Matter Systems in the Ultrastrong and Deep-Strong Coupling Regimes", Phys. Rev. Lett. **130**, 123601 (2023).

[87] O. Di Stefano, A. Settineri, V. Macrì, L. Garziano, R. Stassi, and S. Savasta, "Resolution of gauge ambiguities in ultrastrong-coupling cavity QED", Nat. Phys. **15**, 803–808 (2019).

[88] G. Arwas, V. E. Manucharyan, and C. Ciuti, "Metrics and properties of optimal gauges in multimode cavity QED", Phys. Rev. A **108**, 023714 (2023).

[89] G. Andolina, F. Pellegrino, A. Mercurio, O. Di Stefano, M. Polini, and S. Savasta, "A non-perturbative no-go theorem for photon condensation in approximate models", Eur. Phys. J. Plus **137**, 1–14 (2022).

[90] G. M. Andolina, F. M. D. Pellegrino, V. Giovannetti, A. H. MacDonald, and M. Polini, "Cavity quantum electrodynamics of strongly correlated electron systems: A no-go theorem for photon condensation", Phys. Rev. B **100**, 121109 (2019).

[91] J. M. Knight, Y. Aharonov, and G. T. C. Hsieh, "Are super-radiant phase transitions possible?", Phys. Rev. A **17**, 1454–1462 (1978).

[92] P. Nataf and C. Ciuti, "No-go theorem for superradiant quantum phase transitions in cavity QED and counter-example in circuit QED", Nat. Commun. **1**, 1–6 (2010).

[93] N. Bogoljubov, "On a new method in the theory of superconductivity", Il nuovo cimento **7**, 794–805 (1957).

[94] U. Vool and M. Devoret, "Introduction to quantum electromagnetic circuits", Int. J. Circuit Theory Appl. **45**, 897–934 (2017).

[95] A. Blais, A. L. Grimsmo, S. M. Girvin, and A. Wallraff, "Circuit quantum electrodynamics", Rev. Mod. Phys. **93**, 025005 (2021).

[96] V. E. Manucharyan, J. Koch, L. I. Glazman, and M. H. Devoret, "Fluxonium: Single Cooper-Pair Circuit Free of Charge Offsets", Science **326**, 113–116 (2009).

[97] V. E. Manucharyan, A. Baksic, and C. Ciuti, "Resilience of the quantum Rabi model in circuit QED", J. Phys. A: Math. Theor. **50**, 294001 (2017).

[98] F. Yoshihara, S. Ashhab, T. Fuse, M. Bamba, and K. Semba, "Hamiltonian of a flux qubit-LC oscillator circuit in the deep-strong-coupling regime", Sci. Rep. **12**, `10.1038/s41598-022-10203-1` (2022).

[99] F. Yoshihara, T. Fuse, S. Ashhab, K. Kakuyanagi, S. Saito, and K. Semba, "Superconducting qubit–oscillator circuit beyond the ultrastrong-coupling regime", Nat. Phys. **13**, 44–47 (2017).

[100] F. Yoshihara, T. Fuse, S. Ashhab, K. Kakuyanagi, S. Saito, and K. Semba, "Characteristic spectra of circuit quantum electrodynamics systems from the ultrastrong- to the deep-strong-coupling regime", Phys. Rev. A **95**, 053824 (2017).

[101] D. Ballester, G. Romero, J. J. García-Ripoll, F. Deppe, and E. Solano, "Quantum Simulation of the Ultrastrong-Coupling Dynamics in Circuit Quantum Electrodynamics", Phys. Rev. X **2**, 021007 (2012).

[102] J. E. Mooij, T. P. Orlando, L. Levitov, L. Tian, C. H. van der Wal, and S. Lloyd, "Josephson Persistent-Current Qubit", Science **285**, 1036–1039 (1999).

[103] Z. Chen, Y. Wang, T. Li, L. Tian, Y. Qiu, K. Inomata, F. Yoshihara, S. Han, F. Nori, J. S. Tsai, and J. Q. You, "Single-photon-driven high-order sideband transitions in an ultrastrongly coupled circuit quantum electrodynamics system", Phys. Rev. A **96**, 012325 (2017).

[104] I. Chiorescu, P. Bertet, K. Semba, Y. Nakamura, C. J. P. M. Harmans, and J. E. Mooij, "Coherent dynamics of a flux qubit coupled to a harmonic oscillator", Nature **431**, 159–162 (2004).

[105] F. Yan, S. Gustavsson, A. Kamal, J. Birenbaum, A. P. Sears, D. Hover, T. J. Gudmundsen, D. Rosenberg, G. O. Samach, S. J. Weber, J. L. Yoder, T. P. Orlando, J. Clarke, A. B. Kerman, and W. D. Oliver, "The flux qubit revisited to enhance coherence and reproducibility", Nat. Commun. **7**, 1–8 (2016).

[106] S. Saito, T. Meno, M. Ueda, H. Tanaka, K. Semba, and H. Takayanagi, "Parametric control of a superconducting flux qubit", Phys. Rev. Lett. **96**, 107001 (2006).

[107] S.-P. Wang, A. Ridolfo, T. Li, S. Savasta, F. Nori, Y. Nakamura, and J. Q. You, "Probing the symmetry breaking of a light-matter system by an ancillary qubit", Nat. Commun. **14**, `10.1038/s41467-023-40097-0` (2023).

[108] N. Wiener, "Generalized harmonic analysis", Acta Mathematica **55**, 117–258 (1930).

[109] A. Khinchin, "Correlation theory of stationary stochastic processes", Mathematical Annals **109**, 604–615 (1934).

[110] H. J. Carmichael, *Statistical methods in quantum optics 1: master equations and Fokker-Planck equations* (Springer, 1999).

[111] C. Gardiner and P. Zoller, *Quantum noise: a handbook of Markovian and non-Markovian quantum stochastic methods with applications to quantum optics* (Springer Science & Business Media, 2004).

[112] R. J. Glauber, "The Quantum Theory of Optical Coherence", Phys. Rev. **130**, 2529–2539 (1963).

[113] A. Mercurio, Y. T. Huang, L. X. Cai, Y. N. Chen, V. Savona, and F. Nori, "QuantumToolbox.jl: An efficient Julia framework for simulating open quantum systems", ArXiv preprint, `10.48550/arXiv.2504.21440` (2025).

[114] J. R. Johansson, P. D. Nation, and F. Nori, “QuTiP: An open-source Python framework for the dynamics of open quantum systems”, Comput. Phys. Commun. **183**, 1760–1772 (2012).

[115] J. R. Johansson, P. D. Nation, and F. Nori, “QuTiP 2: A Python framework for the dynamics of open quantum systems”, Comput. Phys. Commun. **184**, 1234–1240 (2013).

[116] J. J. García-Ripoll, B. Peropadre, and S. De Liberato, “Light-matter decoupling and A^2 term detection in superconducting circuits”, Sci. Rep. **5**, 16055 (2015).

[117] C. Gustin, S. Franke, and S. Hughes, “Gauge-invariant theory of truncated quantum light-matter interactions in arbitrary media”, Phys. Rev. A **107**, 013722 (2023).

[118] C. Sánchez Muñoz, A. Frisk Kockum, A. Miranowicz, and F. Nori, “Simulating ultrastrong-coupling processes breaking parity conservation in Jaynes-Cummings systems”, Phys. Rev. A **102**, 033716 (2020).

[119] R. Grimshaw, *Nonlinear Ordinary Differential Equations* (CRC Press, Boca Raton, 1993).

[120] V. Macrì, A. Mercurio, F. Nori, S. Savasta, and C. Sánchez Muñoz, “Spontaneous Scattering of Raman Photons from Cavity-QED Systems in the Ultrastrong Coupling Regime”, Phys. Rev. Lett. **129**, 273602 (2022).

[121] W. Salmon, C. Gustin, A. Settineri, O. D. Stefano, D. Zueco, S. Savasta, F. Nori, and S. Hughes, “Gauge-independent emission spectra and quantum correlations in the ultrastrong coupling regime of open system cavity-QED”, Nanophotonics **11**, 1573–1590 (2022).

[122] W. E. Lamb, “Fine Structure of the Hydrogen Atom. III”, Phys. Rev. **85**, 259–276 (1952).

[123] F. Bassani, J. J. Forney, and A. Quattropani, “Choice of Gauge in Two-Photon Transitions: $1s-2s$ Transition in Atomic Hydrogen”, Phys. Rev. Lett. **39**, 1070–1073 (1977).

[124] J. R. Schrieffer and P. A. Wolff, “Relation between the Anderson and Kondo Hamiltonians”, Phys. Rev. **149**, 491–492 (1966).

[125] S. Bravyi, D. P. DiVincenzo, and D. Loss, “Schrieffer-Wolff transformation for quantum many-body systems”, Ann. Phys. (N.Y.) **326**, 2793–2826 (2011).

[126] R. A. Mencia, W.-J. Lin, H. Cho, M. G. Vavilov, and V. E. Manucharyan, “Integer Fluxonium Qubit”, PRX Quantum **5**, `10.1103/prxquantum.5.040318` (2024).

[127] L. B. Nguyen, Y.-H. Lin, A. Somoroff, R. Mencia, N. Grabon, and V. E. Manucharyan, “High-Coherence Fluxonium Qubit”, Phys. Rev. X **9**, `10.1103/physrevx.9.041041` (2019).

[128] L. Garziano, A. Settineri, O. Di Stefano, S. Savasta, and F. Nori, “Gauge invariance of the Dicke and Hopfield models”, Phys. Rev. A **102**, 023718 (2020).

[129] A. Stokes and A. Nazir, “Uniqueness of the Phase Transition in Many-Dipole Cavity Quantum Electrodynamical Systems”, Phys. Rev. Lett. **125**, 143603 (2020).

[130] J. Keeling, “Coulomb interactions, gauge invariance, and phase transitions of the Dicke model”, J. Phys. Condens. Matter **19**, 295213 (2007).

[131] C. Emary and T. Brandes, “Quantum chaos triggered by precursors of a quantum phase transition: The Dicke model”, Phys. Rev. Lett. **90**, 044101 (2003).

[132] V. Bužek, M. Orszag, and M. Roško, “Instability and Entanglement of the Ground State of the Dicke Model”, Phys. Rev. Lett. **94**, 163601 (2005).

[133] K. Rzazewski, K. Wódkiewicz, and W. Żakowicz, “Phase transitions, two-level atoms, and the A^2 term”, Phys. Rev. Lett. **35**, 432 (1975).

[134] G. M. Andolina, F. M. D. Pellegrino, V. Giovannetti, A. H. MacDonald, and M. Polini, “Theory of photon condensation in a spatially varying electromagnetic field”, Phys. Rev. B **102**, 125137 (2020).

[135] F. Mila and K. P. Schmidt, “Strong-Coupling Expansion and Effective Hamiltonians”, in *Introduction to frustrated magnetism* (Springer Berlin Heidelberg, 2010), pp. 537–559.

[136] P. Fulde, *Electron correlations in molecules and solids*, Vol. 100 (Springer Science & Business Media, 2012).

[137] H.-P. Breuer and F. Petruccione, *The Theory of Open Quantum Systems*, Oxford Graduate Texts (Oxford University Press, 2002).

[138] M. Tavis and F. W. Cummings, “Exact Solution for an N-Molecule—Radiation-Field Hamiltonian”, Phys. Rev. **170**, 379–384 (1968).

[139] N. S. Mueller, Y. Okamura, B. G. M. Vieira, S. Juergensen, H. Lange, E. B. Barros, F. Schulz, and S. Reich, “Deep strong light-matter coupling in plasmonic nanoparticle crystals”, Nature **583**, 780–784 (2020).

[140] T. Holstein and H. Primakoff, “Field Dependence of the Intrinsic Domain Magnetization of a Ferromagnet”, Phys. Rev. **58**, 1098–1113 (1940).

[141] D. V. Kapor, M. J. Škrinjar, and S. D. Stojanović, “Relation between spin-coherent states and boson-coherent states in the theory of magnetism”, Phys. Rev. B **44**, 2227–2230 (1991).

[142] J. J. Hopfield, “Theory of the Contribution of Excitons to the Complex Dielectric Constant of Crystals”, Phys. Rev. **112**, 1555–1567 (1958).

[143] S. Savasta, O. D. Stefano, and F. Nori, “Thomas-Reiche-Kuhn (TRK) sum rule for interacting photons”, Nanophotonics **10**, 465–476 (2021).

[144] F. Dimer, B. Estienne, A. S. Parkins, and H. J. Carmichael, “Proposed realization of the Dicke-model quantum phase transition in an optical cavity QED system”, Phys. Rev. A **75**, 013804 (2007).

[145] K. Rzażewski, K. Wódkiewicz, and W. Żakowicz, “Phase Transitions, Two-Level Atoms, and the A^2 Term”, Phys. Rev. Lett. **35**, 432–434 (1975).

[146] M. Yamanoi, “Influence of omitting the A^2 term in the conventional photon-matter-Hamiltonian on the photon-field equation”, Phys. Lett. A **58**, 437–439 (1976).

[147] M. Yamanoi and M. Takatsuji, *Coherence and Quantum Optics IV: Proceedings of the Fourth Rochester Conference on Coherence and Quantum Optics* (Plenum Press, New York, 1978), pp. 839–850.

[148] A. Vukics and P. Domokos, “Adequacy of the Dicke model in cavity QED: A counter-no-go statement”, Phys. Rev. A **86**, 053807 (2012).

[149] A. Vukics, T. Grießer, and P. Domokos, “Elimination of the A-Square Problem from Cavity QED”, Phys. Rev. Lett. **112**, 073601 (2014).

[150] M. Bamba and T. Ogawa, “Stability of polarizable materials against superradiant phase transition”, Phys. Rev. A **90**, 063825 (2014).

[151] T. Jaako, Z.-L. Xiang, J. J. Garcia-Ripoll, and P. Rabl, “Ultrastrong-coupling phenomena beyond the Dicke model”, Phys. Rev. A **94**, 033850 (2016).

[152] D. De Bernardis, T. Jaako, and P. Rabl, “Cavity quantum electrodynamics in the nonperturbative regime”, Phys. Rev. A **97**, 043820 (2018).

[153] Y. Ashida, A. İmamoğlu, J. Faist, D. Jaksch, A. Cavalleri, and E. Demler, “Quantum Electrodynamic Control of Matter: Cavity-Enhanced Ferroelectric Phase Transition”, Phys. Rev. X **10**, 041027 (2020).

[154] C. Sch́afer, M. Ruggenthaler, V. Rokaj, and A. Rubio, “Relevance of the quadratic diamagnetic and self-polarization terms in cavity quantum electrodynamics”, ACS photonics **7**, 975–990 (2020).

[155] G. Mazza and A. Georges, “Superradiant Quantum Materials”, Phys. Rev. Lett. **122**, 017401 (2019).

[156] K. Lenk and M. Eckstein, “Collective excitations of the $U(1)$-symmetric exciton insulator in a cavity”, Phys. Rev. B **102**, 205129 (2020).

[157] J. Román-Roche, F. Luis, and D. Zueco, “Photon Condensation and Enhanced Magnetism in Cavity QED”, Phys. Rev. Lett. **127**, 167201 (2021).

[158] M. Bamba, X. Li, N. Marquez Peraca, and J. Kono, “Magnonic superradiant phase transition”, Commun. Phys. **5**, 3 (2022).

[159] D. Kim, S. Dasgupta, X. Ma, J.-M. Park, H.-T. Wei, X. Li, L. Luo, J. Doumani, W. Yang, D. Cheng, R. H. J. Kim, H. O. Everitt, S. Kimura, H. Nojiri, J. Wang, S. Cao, M. Bamba, K. R. A. Hazzard, and J. Kono, “Observation of the magnonic Dicke superradiant phase transition”, Sci. Adv. **11**, eadt1691 (2025).

[160] S. Hughes, C. Gustin, and F. Nori, “Reconciling quantum and classical spectral theories of ultrastrong coupling: role of cavity bath coupling and gauge corrections”, Opt. Quantum **2**, 133–139 (2024).

[161] A. Stokes and A. Nazir, “Implications of gauge freedom for nonrelativistic quantum electrodynamics”, Rev. Mod. Phys. **94**, 045003 (2022).

[162] G. J. Daniels, R. D. Jenkins, D. S. Bradshaw, and D. L. Andrews, “Resonance energy transfer: The unified theory revisited”, J. Chem. Phys. **119**, 2264–2274 (2003).

[163] G. A. Jones and D. S. Bradshaw, “Resonance Energy Transfer: From Fundamental Theory to Recent Applications”, Front. Phys. **7**, `10.3389/fphy.2019.00100` (2019).

[164] M. H. Cohen and F. Keffer, “Dipolar Sums in the Primitive Cubic Lattices”, Phys. Rev. **99**, 1128–1134 (1955).

[165] S. Lamowski, C.-R. Mann, F. Hellbach, E. Mariani, G. Weick, and F. Pauly, “Plasmon polaritons in cubic lattices of spherical metallic nanoparticles”, Phys. Rev. B **97**, 125409 (2018).

[166] A. Vukics, T. Grießer, and P. Domokos, “Fundamental limitation of ultrastrong coupling between light and atoms”, Phys. Rev. A **92**, 043835 (2015).

[167] T. Grießer, A. Vukics, and P. Domokos, “Depolarization shift of the superradiant phase transition”, Phys. Rev. A **94**, 033815 (2016).

[168] S. Savasta and R. Girlanda, “Quantum description of the input and output electromagnetic fields in a polarizable confined system”, Phys. Rev. A **53**, 2716–2726 (1996).

[169] H. Lipkin, N. Meshkov, and A. Glick, “Validity of many-body approximation methods for a solvable model: (I). Exact solutions and perturbation theory”, Nucl. Phys. **62**, 188–198 (1965).

[170] J. Fan, Z. Yang, Y. Zhang, J. Ma, G. Chen, and S. Jia, "Hidden continuous symmetry and Nambu-Goldstone mode in a two-mode Dicke model", Phys. Rev. A **89**, 023812 (2014).

[171] Q.-H. Chen, Y.-Y. Zhang, T. Liu, and K.-L. Wang, "Numerically exact solution to the finite-size Dicke model", Phys. Rev. A **78**, 051801 (2008).

[172] P. Pilar, D. De Bernardis, and P. Rabl, "Thermodynamics of ultrastrongly coupled light-matter systems", Quantum **4**, 335 (2020).

[173] P. Kirton and J. Keeling, "Superradiant and lasing states in driven-dissipative Dicke models", New J. Phys. **20**, 015009 (2018).

[174] K. Baumann, C. Guerlin, F. Brennecke, and T. Esslinger, "Dicke quantum phase transition with a superfluid gas in an optical cavity", Nature **464**, 1301–1306 (2010).

[175] D. Nagy, G. Kónya, G. Szirmai, and P. Domokos, "Dicke-Model Phase Transition in the Quantum Motion of a Bose-Einstein Condensate in an Optical Cavity", Phys. Rev. Lett. **104**, 130401 (2010).

[176] D. Nagy and P. Domokos, "Nonequilibrium Quantum Criticality and Non-Markovian Environment: Critical Exponent of a Quantum Phase Transition", Phys. Rev. Lett. **115**, 043601 (2015).

[177] D. Nagy and P. Domokos, "Critical exponent of quantum phase transitions driven by colored noise", Phys. Rev. A **94**, 063862 (2016).

[178] Z. Zhiqiang, C. H. Lee, R. Kumar, K. Arnold, S. J. Masson, A. Parkins, and M. Barrett, "Nonequilibrium phase transition in a spin-1 Dicke model", Optica **4**, 424–429 (2017).

[179] S. Genway, W. Li, C. Ates, B. P. Lanyon, and I. Lesanovsky, "Generalized Dicke Nonequilibrium Dynamics in Trapped Ions", Phys. Rev. Lett. **112**, 023603 (2014).

[180] Á. L. Corps and A. Relaño, "Theory of Dynamical Phase Transitions in Quantum Systems with Symmetry-Breaking Eigenstates", Phys. Rev. Lett. **130**, 100402 (2023).

[181] M. Heyl, "Scaling and Universality at Dynamical Quantum Phase Transitions", Phys. Rev. Lett. **115**, 140602 (2015).

[182] M. Heyl, "Dynamical quantum phase transitions: a review", Rep. Prog. Phys. **81**, 054001 (2018).

[183] A. A. Zvyagin, "Dynamical quantum phase transitions (Review Article)", Low Temp. Phys. **42**, 971–994 (2016).

[184] O. Viehmann, J. von Delft, and F. Marquardt, “Superradiant Phase Transitions and the Standard Description of Circuit QED”, Phys. Rev. Lett. **107**, 113602 (2011).

[185] N. Lambert, Y. Matsuzaki, K. Kakuyanagi, N. Ishida, S. Saito, and F. Nori, “Superradiance with an ensemble of superconducting flux qubits”, Phys. Rev. B **94**, 224510 (2016).

[186] M. Bamba, K. Inomata, and Y. Nakamura, “Superradiant Phase Transition in a Superconducting Circuit in Thermal Equilibrium”, Phys. Rev. Lett. **117**, 173601 (2016).

[187] P. Forn-Díaz, J. J. García-Ripoll, B. Peropadre, J.-L. Orgiazzi, M. Yurtalan, R. Belyansky, C. M. Wilson, and A. Lupascu, “Ultrastrong coupling of a single artificial atom to an electromagnetic continuum in the nonperturbative regime”, Nat. Phys. **13**, 39–43 (2017).

[188] S. Ashhab, Y. Matsuzaki, K. Kakuyanagi, S. Saito, F. Yoshihara, T. Fuse, and K. Semba, “Spectrum of the Dicke model in a superconducting qubit-oscillator system”, Phys. Rev. A **99**, 063822 (2019).

[189] P. Nataf, T. Champel, G. Blatter, and D. M. Basko, “Rashba Cavity QED: A Route Towards the Superradiant Quantum Phase Transition”, Phys. Rev. Lett. **123**, 207402 (2019).

[190] D. Guerci, P. Simon, and C. Mora, “Superradiant Phase Transition in Electronic Systems and Emergent Topological Phases”, Phys. Rev. Lett. **125**, 257604 (2020).

[191] A. Mercurio, G. M. Andolina, F. M. D. Pellegrino, O. Di Stefano, P. Jarillo-Herrero, C. Felser, F. H. L. Koppens, S. Savasta, and M. Polini, “Photon condensation, Van Vleck paramagnetism, and chiral cavities”, Phys. Rev. Res. **6**, 013303 (2024).

[192] A. Ghirri, C. Bonizzoni, M. Maksutoglu, A. Mercurio, O. Di Stefano, S. Savasta, and M. Affronte, “Ultrastrong Magnon-Photon Coupling Achieved by Magnetic Films in Contact with Superconducting Resonators”, Phys. Rev. Appl. **20**, 024039 (2023).

[193] T. Albash and D. A. Lidar, “Adiabatic quantum computation”, Rev. Mod. Phys. **90**, 015002 (2018).

[194] H. Bernien, S. Schwartz, A. Keesling, H. Levine, A. Omran, H. Pichler, S. Choi, A. S. Zibrov, M. Endres, G. M., V. Vuletić, and M. D. Lukin, “Probing many-body dynamics on a 51-atom quantum simulator”, Nature **551**, 579–584 (2017).

[195] J. G. Bohnet, B. C. Sawyer, J. W. Britton, M. L. Wall, A. M. Rey, M. Foss-Feig, and J. J. Bollinger, “Quantum spin dynamics and entanglement generation with hundreds of trapped ions”, Science **352**, 1297–1301 (2016).

[196] W. Kopylov, C. Emary, and T. Brandes, “Counting statistics of the Dicke superradiance phase transition”, Phys. Rev. A **87**, 043840 (2013).

[197] E. G. D. Torre, S. Diehl, M. D. Lukin, S. Sachdev, and P. Strack, “Keldysh approach for nonequilibrium phase transitions in quantum optics: Beyond the Dicke model in optical cavities”, Phys. Rev. A **87**, 023831 (2013).

[198] F. Brange, N. Lambert, F. Nori, and C. Flindt, “Lee-Yang theory of the superradiant phase transition in the open Dicke model”, Phys. Rev. Res. **6**, 033181 (2024).

[199] E. Cortese and S. De Liberato, “Exact solution of polaritonic systems with arbitrary light and matter frequency-dependent losses”, J. Chem. Phys. **156**, 084106 (2022).

[200] J. Román-Roche, Á. Gómez-León, F. Luis, and D. Zueco, “Linear response theory for cavity QED materials at arbitrary light-matter coupling strengths”, Phys. Rev. B **111**, 035156 (2025).

[201] A. J. Leggett, S. Chakravarty, A. T. Dorsey, M. P. A. Fisher, A. Garg, and W. Zwerger, “Dynamics of the dissipative two-state system”, Rev. Mod. Phys. **59**, 1–85 (1987).

[202] C. M. Bender and S. Boettcher, “Real Spectra in Non-Hermitian Hamiltonians Having $\mathcal{PT}$ Symmetry”, Phys. Rev. Lett. **80**, 5243–5246 (1998).

[203] C. M. Bender, “Making sense of non-Hermitian Hamiltonians”, Rep. Prog. Phys. **70**, 947 (2007).

[204] L. Feng, R. El-Ganainy, and L. Ge, “Non-Hermitian photonics based on parity–time symmetry”, Nat. Photonics **11**, 752–762 (2017).

[205] S. Longhi, “Bloch Oscillations in Complex Crystals with $\mathcal{PT}$ Symmetry”, Phys. Rev. Lett. **103**, 123601 (2009).

[206] J. Wenner, Y. Yin, Y. Chen, R. Barends, B. Chiaro, E. Jeffrey, J. Kelly, A. Megrant, J. Y. Mutus, C. Neill, P. J. J. O’Malley, P. Roushan, D. Sank, A. Vainsencher, T. C. White, A. N. Korotkov, A. N. Cleland, and J. M. Martinis, “Catching Time-Reversed Microwave Coherent State Photons with 99.4% Absorption Efficiency”, Phys. Rev. Lett. **112**, 210501 (2014).

[207] Y. Sun, W. Tan, H.-q. Li, J. Li, and H. Chen, “Experimental Demonstration of a Coherent Perfect Absorber with PT Phase Transition”, Phys. Rev. Lett. **112**, 143903 (2014).

[208] B. Yurke and J. S. Denker, “Quantum network theory”, Phys. Rev. A **29**, 1419–1437 (1984).

[209] J. A. Hertz, “Quantum critical phenomena”, Phys. Rev. B **14**, 1165–1184 (1976).

[210] A. Osterloh, L. Amico, G. Falci, and R. Fazio, “Scaling of entanglement close to a quantum phase transition”, Nature **416**, 608–610 (2002).

[211] G. Vidal, J. I. Latorre, E. Rico, and A. Kitaev, “Entanglement in Quantum Critical Phenomena”, Phys. Rev. Lett. **90**, 227902 (2003).

[212] K. Hayashida, T. Makihara, N. Marquez Peraca, D. Fallas Padilla, H. Pu, J. Kono, and M. Bamba, “Perfect intrinsic squeezing at the superradiant phase transition critical point”, Sci. Rep. **13**, 2526 (2023).

[213] C. Hotter, H. Ritsch, and K. Gietka, “Combining Critical and Quantum Metrology”, Phys. Rev. Lett. **132**, 060801 (2024).

[214] C. L. Degen, F. Reinhard, and P. Cappellaro, “Quantum sensing”, Rev. Mod. Phys. **89**, 035002 (2017).

[215] S. L. Braunstein and P. van Loock, “Quantum information with continuous variables”, Rev. Mod. Phys. **77**, 513–577 (2005).

[216] I.-C. Benea-Chelmus, F. F. Settembrini, G. Scalari, and J. Faist, “Electric field correlation measurements on the electromagnetic vacuum state”, Nature **568**, 202–206 (2019).

[217] C. Riek, D. V. Seletskiy, A. S. Moskalenko, J. Schmidt, P. Krauspe, S. Eckart, S. Eggert, G. Burkard, and A. Leitenstorfer, “Direct sampling of electric-field vacuum fluctuations”, Science **350**, 420–423 (2015).

[218] F. Lindel, R. Bennett, and S. Y. Buhmann, “Theory of polaritonic quantum-vacuum detection”, Phys. Rev. A **102**, 041701 (2020).

[219] A. S. Moskalenko, C. Riek, D. V. Seletskiy, G. Burkard, and A. Leitenstorfer, “Paraxial Theory of Direct Electro-optic Sampling of the Quantum Vacuum”, Phys. Rev. Lett. **115**, 263601 (2015).

[220] R. Stassi, S. Savasta, L. Garziano, B. Spagnolo, and F. Nori, “Output field-quadrature measurements and squeezing in ultrastrong cavity-QED”, New J. Phys. **18**, 123005 (2016).

[221] D. Zueco, G. M. Reuther, S. Kohler, and P. Hänggi, “Qubit-oscillator dynamics in the dispersive regime: Analytical theory beyond the rotating-wave approximation”, Phys. Rev. A **80**, 033846 (2009).

[222] J. R. Johansson, G. Johansson, C. M. Wilson, and F. Nori, “Dynamical Casimir Effect in a Superconducting Coplanar Waveguide”, Phys. Rev. Lett. **103**, 147003 (2009).

[223] C. M. Wilson, G. Johansson, A. Pourkabirian, M. Simoen, J. R. Johansson, T. Duty, F. Nori, and P. Delsing, “Observation of the dynamical Casimir effect in a superconducting circuit”, Nature **479**, 376–379 (2011).

[224] S. De Liberato, C. Ciuti, and I. Carusotto, “Quantum Vacuum Radiation Spectra from a Semiconductor Microcavity with a Time-Modulated Vacuum Rabi Frequency”, Phys. Rev. Lett. **98**, 103602 (2007).

[225] D. Zhang, X.-Q. Luo, Y.-P. Wang, T.-F. Li, and J. Q. You, “Observation of the exceptional point in cavity magnon-polaritons”, Nat. Commun. **8**, 1368– (2017).